UNIVERSITY OF SOUTHAMPTON

FACULTY OF ENGINEERING AND THE ENVIRONMENT

Institute of Sound and Vibration Research

ON THE DETECTION OF SHALLOW BURIED OBJECTS USING SEISMIC WAVE REFLECTIONS

by

Benjamin David Papandreou

Thesis for the degree of Doctor of Philosophy

MAY 2011

UNIVERSITY OF SOUTHAMPTON

ABSTRACT

FACULTY OF ENGINEERING AND THE ENVIRONMENT

INSTITUTE OF SOUND AND VIBRATION RESEARCH

Doctor of Philosophy

ON THE DETECTION OF SHALLOW BURIED OBJECTS USING SEISMIC WAVE REFLECTIONS

By Benjamin David Papandreou

This thesis is concerned with a methodology for the detection of shallow (of order 1 metre) objects buried in soil using seismic waves. Possible objects of interest include infrastructure, archaeological artefacts and ordinance.

A mathematical analysis of an idealised system is performed to gain understanding of both seismic wave propagation and the generation of these waves by surface sources. The mathematical techniques used in the existing analysis of a point vertical source are applied to the desired problem of a point horizontal surface traction. Results are displayed in a graphically concise form.

An experimental methodology, capable of forming two-dimensional images through the ground, is described. The use of shear waves is shown preferable. The advantages and implementation of using time extended, rather than impulsive, excitation signals are described. Additional signal processing techniques, such as generalised cross-correlation functions, are also detailed.

Simple numerical simulations are undertaken with the aim of both validating the post-processing algorithms and evaluating its robustness against non-ideal conditions. Simulated time histories are created by defining signals in the frequency domain and then modifying their amplitude and phase to replicate attenuation and propagation. Non-ideal conditions focus mainly on variation in the wavespeed as a function of depth. Simulations indicate that the imaging method fails for sufficiently large variations of wavespeed, particularly for objects buried below significant discontinuities in material properties.

As shear waves are used for the imaging method, a source was designed and constructed to preferentially generate shear waves and was verified using field experimentation. The imaging methodology is applied to data from three experimental sites and is able to detect the target objects with some success. Problems, however, remain with the measurement of a wavespeed that is consistent and indicative of the propagation speed at depth, and in consistently obtaining a sufficiently large reflected wave from the object.

Table of Contents

Declaration of Authorship

I, Benjamin David Papandreou, declare that the thesis entitled ON THE DETECTION OF SHALLOW BURIED OBJECTS USING SEISMIC WAVE REFLECTIONS and the work presented in the thesis are both my own, and have been generated by me as the result of my own original research. I confirm that:

- this work was done wholly or mainly while in candidature for a research degree at this University;
- where any part of this thesis has previously been submitted for a degree or any other qualification at this University or any other institution, this has been clearly stated;
- where I have consulted the published work of others, this is always clearly attributed;
- where I have quoted from the work of others, the source is always given. With the exception of such quotations, this thesis is entirely my own work;
- I have acknowledged all main sources of help;
- where the thesis is based on work done by myself jointly with others, I have made clear exactly what was done by others and what I have contributed myself;
- parts of this work have been published as:
    - Papandreou, B., Rustighi, E. and Brennan, M.J., *On the detection of shallow buried objects using seismic wave reflections*, in *Proceedings of the 16th International Congress on Sound and Vibration: Recent Developments in Acoustics, Noise and Vibration (ICSV16)*. 2009 Krakow, Poland.
    - Papandreou, B., Brennan, M.J., Rustighi, E., On *the Detection of Objects Buried at Shallow Depth Using Seismic Wave Reflections*. Journal of the Acoustical Society of America, 2011. **129**(3): p. 1366-1374.

Signed: ……..

Date:…….

Acknowledgements

I would like to give my sincere thanks to my supervisors, Mike Brennan and Emiliano Rustighi, for their guidance and advice during my PhD. Their knowledge and patience has made the completion of this project possible.

I gratefully acknowledge the financial support provided by the Defence and Science Technology Laboratories and the Diawa Anglo-Japanese Foundation.

Special thanks go to Jen Muggleton and Professor Tsuneyoshi Sugimoto (and his students) for the use of their experimental facilities and their help during field trials.

Thanks also go to the members of my internal review panels, Paul White, Chris Jones and Neil Ferguson for their helpful comments during the project.

I would like express my gratitude to Steve Dorney and Tony Curran for their organisation and encouragement with regard to university outreach activities. Such activities were an enjoyable and productive break for the project, and gave me the opportunity to work with many interesting people I would not have otherwise met.

On a personal note, I am deeply indebted to Hans and Jenifer Guelbert, Stephen and Moya Rolls, and Nora Kowschuk for their generous help throughout the project.

A final thank you goes to all my family and friends that have patiently feigned interested when I discussed details of the project with them. I know that most people aren't really interested in research into shallow seismic vibrations, and their willingness to listen regardless is gratefully acknowledged.

Abbreviations and Definitions

CDP	Common depth point.
FIR	Finite impulse response.
GCC	Generalised cross-correlation.
GPR	Ground penetrating radar.
horz.	Horizontal.
LDV	Laser Doppler vibrometer.
MUSIC	Mulitple signal classification.
NMO	Normal move out.
P	Compressional.
PHAT	Phase transform.
RAY	Rayleigh.
RMS	Root mean squared.
SASW	Spectral analysis of surface waves.
SCOT	Smoothed coherence transform.
SH	Shear horizontal.
SV	Shear vertical.
vert.	Vertical.

Table of Symbols

a	Source radius.
b_2	Coefficient in method of steepest descent.
c	General wavespeed.
c_p, c_s, c_R	Compressional, shear and Rayleigh wavespeeds.
d	Propagation distance.
d_{ref}	Geometric attenuation reference distance.
$d_{D,i}$	Source-sensor separation via a direct path.
$d_{Rl,i}$	Source-sensor separation via a reflected path.
f	Frequency.
$f(\xi)$	Arbitrary function of variable ξ.
$f_1(\xi), f_2(\xi)$	Real and imaging parts of $f(\xi)$.
$g(\xi)$	Arbitrary function of variable ξ.
$\mathbf{h}$	Elastic vector potential.
j	$\sqrt{-1}$.
k	General wavenumber.
k_p, k_s, k_R	Compressional, shear and Rayleigh wavenumbers.
m	Order of Bessel or Hankel function.
n	Geometric attenuation power.
$\mathbf{n}$	Normal vector.
p	Exponential decay function occurring in Rayleigh wave analysis.
q	Exponential decay function occurring in Rayleigh wave analysis.
r	Radius in cylindrical or polar coordinates.
s_1	Reference geophone time history.
s_i	*i*-th geophone time history.
$\mathbf{s}$	Vector defining contour.
t	Time variable.
u	Alternative variable used in method of steepest descent.
$\mathbf{u}$	Deformation displacement vector.
u_x, u_y, u_z	Cartesian components of deformation displacement vector.

u_r, u_θ, u_z	Cylindrical components of deformation displacement vector.
u_R, u_θ, u_φ	Spherical components of deformation displacement vector.
$\mathbf{x}$	Position vector.
x, y, z	Cartesian components of position vector components.
$x_{g,i}$	Position of the *i*-th geophone on the surface.
x_s	Position of seismic source on the surface.
x_t, y_t, z_t	Position of target object in Cartesian coordinates.
z_l	Depth of a discontinuity in the medium.
A_η	Fractional change in amplitude from hysteretic damping.
A_g	Fractional change in amplitude from geometric damping.
C	Integration contour.
C'	Modified integration contour.
F	Rayleigh equation.
F_0	Normalised Rayleigh equation.
G	Function of $\xi(u)$ in method of steepest descent.
$\mathrm{H}_m^{(1)}$	*m*-th order Hankel function of the first kind.
I	Value of integration.
J_m	*m*-th order Bessel function.
N	Number of elements in numerically simulated target object.
N_e	Number of elements to target object in numerical simulations.
R	Radius in spherical coordinates; Reflection coefficient.
$R_{1,i}$	Cross-correlation function between reference and *i*-th geophone.
$S_{1,i}$	Cross-spectral density function between reference and *i*-th geophone.
$S_{1,1}, S_{i,i}$	Auto-spectral density of reference and *i*-th geophone signals.
T	Time length of signal; Transmission coefficient.
W	Power radiated.
X	Function of non-dimensional variable in Rayleigh wave intensities.
Z_R	Ratio of wave impedances.
α	Coefficients in Rayleigh wave intensity expressions.

β	Frequency domain representation of simulated signal.
β_2	Polar angle in method of steepest descent.
β_i	Frequency domain representation of the *i*-th geophone.
γ	Phase angle of β.
γ_{1i}	Coherence function between reference and *i*-th geophone.
$\delta(x)$	Dirac delta function.
δ_{ij}	Kronecker delta.
δ_s	Distance between source and single sensor.
δ_t	Distance between source and target.
ε	Ratio of compressional to shear wavespeeds.
ζ	Real component of complex variable ξ.
η	Loss factor.
θ	Polar angle variable.
θ_c	Critical angle of refraction.
θ_e	Angle subtended by an object in numerical simulations.
θ_i	Angle of incidence of propagation path at a material discontinuity.
$\theta_{min}, \theta_{min}$	Angle of shallowest and steepest descent.
θ_r	Angle of reflection of propagation path at a material discontinuity.
θ_t	Angle of transmission of propagation path at a material discontinuity.
ς	Imaginary component of complex variable ξ.
κ	Generic variable.
κ_0	Arbitrary fixed value of generic variable.
λ	First Lame constant.
μ	Second Lame constant, also known as shear modulus.
ν	Poisson's ratio.
ξ	Complex wavenumber variable.
ξ_p	Value of wavenumber variable at the real root of the Rayleigh equation.
ρ	Density.
σ	Ratio of shear to compressional wavespeeds.
τ	Time lag.
τ_i	Propagation time between source and *i*-th geophone.

τ_{ij}	Stress acting on *i*-th plane in *j*-th direction.
τ_0	Input stress.
φ	Azimuthal angle variable.
χ	Ratio of Rayleigh to shear wavespeeds.
$\psi, \psi_{PHAT}, \psi_{SCOT}$	Generic, PHAT and SCOT GCC weighting functions.
ω	Angular frequency.
Γ	Ratio of angle subtended by simulated target object to π.
$\Delta x, \Delta z, \Delta\tau$	Incremental increase in x, z and τ.
K	Function of generic variable κ.
Λ	Rayleigh wavelength.
Φ	Elastic scalar potential.
Ψ	Intensity.

Superscripts

*	Complex conjugation.
′	First order differentiation for function of a single variable.
″	Second order differentiation for function of a single variable.
~	Hilbert transform.
–	Fourier transformed quantity.
^	Unit vector.

Subscripts

D	Direct wave quantity.
P	Compressional wave quantity.
Rl	Reflected wave quantity.
RAY	Rayleigh wave quantity.
SH	Shear horizontal wave quantity.
SV	Shear vertical wave quantity.

Other Symbols

∇	Dell.
∇^2	Laplacian.
$\otimes$	Convolution.
$\bullet$	Dot (scalar) product.

$\times$	Cross (vector) product.
$\Re$	Real part.
$\Im$	Imaginary part.

1. Introduction and Literature Review

Chapter 1

Introduction and Literature Review

1.1 Background

The problem under consideration in this thesis is that of the detection of objects buried in soil at shallow depths, of the order of one metre, using seismic waves. A wide variety of possible target objects exists including ordinance, archaeological artefacts, water distribution pipes and other buried infrastructure. The problem of object detection, and the associated problem of identification of the objects, is an established one with many existing technologies offering solutions.

A review of these technologies is presented in this chapter. This begins with a review of the two main electromagnetic technologies – metal detectors and ground penetrating radar (GPR), which is contained in Section 1.2. A brief overview of target detection in water is then presented in Section 1.3. The established technologies used for the detection of deep underground surfaces (primarily for hydrocarbon exploration) are detailed in Section 1.4. This is divided into an explanation of the basic technique in Section 1.4.1 and a review of some of the improvements to the basic method that have occurred over the years in Section 1.4.2. The application of seismic techniques to shallower depths is discussed in Section 1.5. This includes refraction surveys, methods focusing on the detection of target resonances, the application of the techniques of Section 1.4 to shallow depths and seismic methods that specifically aim to detect point-like shallow buried objects. The aims and objectives of the PhD are given in Section 1.6, with Section 1.7 detailing the approach taken throughout this thesis to enable these aims and objectives to be met. Finally, Section 1.8 contains the contributions of the thesis.

1.2 Electromagnetic Techniques in Soil

The use of electromagnetic devices to detect objects in soil is widespread and well established. Many different methods of using the electromagnetic phenomenon to detect and identify objects have been developed, but the focus of this section is to review the two most important technologies - metal detectors and GPR. A brief outline of the physical principles behind their operation, practical application and limitations are given in Sections 1.2.1 and 1.2.2 respectively. The fundamental principles of electromagnetism relevant to these methods are not included, as they can be found in any standard text on the subject, for example [1, 2].

1.2.1 Metal Detectors

Metal detectors rely on electromagnetic induction to detect objects. The electromagnetic principle of relevance is that a time varying electric field will induce a time varying magnetic field and vice versa. Metal detectors emit an electromagnetic field which propagates away from the detector. Upon reaching a conductive object the electromagnetic field induces currents to form within the object. The electromagnetic field associated with the induced currents then propagates back to the detector where it induces a current within a receiver coil [3, 4]. In the simplest case an audio signal is triggered when the current in the receiver coil exceeds a given threshold to alert the operator of the presence of a conductive material.

Metal detectors have a long history, and their ability to detect conductive objects has given them a myriad of applications. The earliest documented use was a device constructed in haste by Alexander Graham Bell 1881 in an attempt to find a bullet lodged in the U.S. President Garfield (it was unsuccessful) [5]. Applications relevant to this thesis include the detection of natural metal deposits in the ground, archaeology [6], and both military and humanitarian landmine detection [3, 7]. The latter application has particular significance, as much of the recent literature on the use of metal detectors is concerned with it.

An obvious limiting constraint on the application of metal detectors is that the target object must be conductive. This immediately excludes detection of non-metallic modern infrastructure, which is commonly made of plastic [8], as well as archaeological structures and studies of non-magnetic soil structure. This is a fundamental constraint that cannot be overcome with modifications or enhancements to the technique.

The level of the current generation in the conductive object varies as a function of its surface area. This means that smaller targets will generate a smaller electromagnetic field and are therefore harder to detect. This problem is of relevance for detection of ‘non-metallic’ landmines, which despite their

name do usually contain small amounts of metal, often possessing a metallic firing pin [9]. The problem can be overcome by increasing the sensitivity of the metal detector. This, however, amplifies a further constraint with basic metal detectors: their inability to discriminate between objects. Although this applies to all applications of metal detectors, it is particularly important for the detection of shallow objects, as there is often metallic 'clutter', or objects that are of no interest, near to the surface. The definition of clutter varies with the circumstance. What is clutter to a landmine detector may be the desired target of an archaeologist. With regard to landmine detection, the high levels of metallic clutter at shallow depths in conflict zones means that for every mine detected there will be several thousand detections of clutter [4].

The motivation of object discrimination in landmine detection has led to the development of additional signal processing. The simplistic use of an audio indicator utilises only the magnitude of the received electromagnetic signal. Techniques exploiting the phase information from the returned signal have been developed to aid in clutter discrimination. A new method for discriminating from clutter is electromagnetic induction spectroscopy [10, 11]. This method uses input magnetic fields of frequency varying over a large bandwidth, typically tens of hertz to tens of kilohertz, and has been applied specifically with the aim of detecting landmines. The level of current formation within the target has a complex dependency on the materials of which it is composed, its size and its orientation; hence detectable objects have very different levels of response over the frequency range used.

Unfortunately the differences in received signals are great even between individual types of landmine, and there is no common distinguishing feature which allows for discrimination of landmines from clutter. A library of landmine signatures would need to be collected in order to give the method value, although efforts have been made to numerically calculate these responses from basic target information [12]. This is difficult as the signatures vary substantially depending on the environment in which they are situated. Furthermore this limits the use to general shallow buried object detection, as in most applications such detailed properties of the target will not be known.

Metal detectors are adversely affected by the type of soil under interrogation. If the soil has notable magnetic properties then a secondary magnetic field will result from the magnetisation of the material, lowering the signal to noise ratio of the measurement [13]. Furthermore, if there is large spatial variation in the magnetic properties of the material then false alarms may result [14]. If the soil is conductive (for example due to moisture content) the operation of the metal detector will also be degraded, with both the penetration depth and amplitude of the return signal reduced [15]. In normal operating conditions metal detectors can only find large metallic objects to a depth of about half a metre, and smaller targets such as landmines within the first few tens of centimetres [3]. These depths are reduced further still in the presence of moisture.

To conclude, the basic metal detector has been used with success over many decades for the detection of metallic objects buried at a shallow depth. Recently, efforts have been made to advance metal detector technology such that it is capable of identifying the objects it detects. Although these efforts have met with some success, the fundamental limitations on the operation of metal detectors remain, such as the requirement for the target object to be conductive and for the background material to possess minimal electromagnetic properties.

1.2.2 Ground Penetrating Radar

Ground penetrating radar is a technology that uses the reflection of electromagnetic waves to form images. The technology is more recent than metal detectors, with the first successful efforts not undertaken until the 1950s [16]. Ground penetrating radar does not require an object to be conductive to be detected; rather that it has sufficiently different electromagnetic properties from the surrounding material. This enables a wider range of targets to be detected than with metal detectors. For example, GPR is a standard technique in modern archaeology [6] as it enables the detection and mapping of buried structures. Other applications include mapping non-conductive geological structures and contaminates [17] and the detection of buried infrastructure [18].

The operation of GPR is well described in the literature [19, 20]. High frequency (of order 1 MHz to 10 GHz depending on the situation) electromagnetic waves are inputted to the system. Reflections of the waves occur at discontinuities or gradients of the permittivity of the material (a parameter associated with its electromagnetic properties). Reflections are measured via an antenna located next to the source. There are several different versions of the method, some for example using very short (of order nanosecond) pulses, whilst others use time extended signals whose frequency content is either continuously or discontinuously varying [18].

Limitations on depth are caused by attenuation of the transmitted and reflected electromagnetic radiation. Conductive materials increase the attenuation and thus limit operational depths. This is because conductive materials contain free charges that when subject to external electromagnetic fields move to oppose the external field by creation of an internal electromagnetic field. This creates evanescent waves whose amplitude decays in relation to the incident wave. A fundamental trade off occurs between the ability of GPR to detect small and closely spaced targets and the ability of GPR to detect targets at depth [21]. The constraints placed on the method by the presence of conductivity influences the applications of the method. GPR has, for example, excellent performance in surveys in ice and snow due to the low conductivity and ideal electromagnetic properties, with penetration depths of several kilometres possible [22].

Ground penetrating radar has proved to be successful in the detection of both shallow buried surfaces and objects. The fundamental limitation imposed on the method is that the buried object of interest must have sufficiently different electromagnetic properties from the surrounding media for an adequate reflection of the electromagnetic radiation to occur, and that attenuation must be low enough to enable the required high frequency wave propagation.

1.3 Sonar

Sonar is the technology used for the detection of objects in water. Consequently, the physical processes and specific difficulties faced in its implementation are not directly applicable to the problem considered in this thesis. The technology is, however, well developed, and its use of linear sensor arrays means that sonar signal processing techniques are worthy of examination when considering object detection in soil. This section begins with a brief overview of the operation of the basic types of sonar before focusing on the signal processing techniques employed. Details of the technologies specific to object detection in water, such as underwater transducers, are omitted.

Sonar is an acronym (from SOund and NAvigation Ranging) although its widespread use has led to relaxation of its capitalisation. With the use of radar techniques in water prohibited by the electromagnetic properties of seawater, only acoustic waves have the potential to propagate the required distances. Development of sonar technology began in the 1910's with both the safety of shipping from ice (spurred by the sinking of the Titanic) and the ability to detect submarines in the 1st World War being primary motivations [23]. The latter of these, sonar for military purposes, came to dominate the funding and development of the technology over the following decades. More recently attention has focused on the environmental impact of sonar, with specific research into the effects of sonar on marine wildlife [24].

Sonar can be separated into two types: passive and active. Both attempt to detect, localise and track objects in water using acoustic energy. Passive sonar relies exclusively on the acoustic energy radiated by the object whilst active sonar generates an acoustic wave whose reflection is then measured and used to gain information about the target. Passive sonar is not applicable to the problem of the detection of objects in soil as none of the targets under consideration radiate acoustic energy. Application of passive sonar to the detection of non-radiating subsurfaces has been shown possible, with the ability to map the seabed and some subsurfaces structures demonstrated experimentally [25, 26]. The sound source in these cases is primarily breaking of sea waves. This type of technique is therefore not applicable in soil as it is not possible for sufficient energy from ambient sources to propagate the required distances for the detection of objects of interest in this thesis.

Active sonar technologies are sufficiently similar to the problem of detection of shallow buried objects in soil to justify meaningful examination. As the generation and radiation of acoustic energy in water and soil are very different, the attention of this review is on the literature relating to the signal processing. Common to both passive and active systems is the use of sensor arrays. These have been towed from naval vessels since the beginnings of naval sonar [27]. As each sensor is, in general, omnidirectional, the use of sensor arrays is essential in order to obtain directivity information. Furthermore, the use of multiple sensors allows for a significant increase in the signal-to-noise ratio.

The most basic form of sonar for the detection and localisation of targets exploits the directivity of a linear array of sensors [28, 29] and is known as beamforming. An array of omnidirectional sensors whose outputs are summed will naturally exhibit directivity in a certain frequency range. For an array length much smaller than the incident wavelength the overall array directivity will be approximately omnidirectional as all measured waves will arrive approximately in phase. As incident wavelengths become of comparable order to the array length the additional propagation time between sensors leads to cancellation of the waves from some directions. For certain frequency to array length ratios a single, albeit relatively wide, dominant peak can be formed in the array directivity pattern.

To detect and localise targets to a specific direction (although not distance) the amount of energy in the measured signal can be plotted as a function of the direction of this main peak. Rather than physically move the sensor array, phase shifts can be introduced into the measured sensor signals prior to summation in a process known as beam steering. To reduce the energy measured by the sensor array at directions other than within the main peak the amplitude of the measured signals can also be adjusted in a process known as array shading. Whilst this increases the main width peak it also increases the signal-to-noise ratio.

Many improved methods of array signal processing have been suggested and successfully implemented over the decades of development of sonar. A brief description of two illustrative examples is given here, with detailed reviews available in the literature [30-32]. Both of these require the cross-correlation functions between each set of sensors to be calculated and arranged in a single matrix, known as the correlation matrix. Aspects of sonar of no relevance to the problem in this thesis, such as the use of Doppler shift to estimate target velocity, are omitted.

Capon [33] introduced a method that sought to minimise the amount of energy from directions other than the main peak by seeking to adjust both the amplitude and phase of the array element's weighting. The desired state, that of the minimisation of the output power of the array whilst keeping the power output in the direction of the main beam constant, is imposed mathematically with the correlation matrix then inversed to obtain the optimal weightings. This enables an increase in the

resolution over basic beamforming, although Capon's method is susceptible to coherent noise (such as unwanted reflections).

An illustration of the complexity of the array signal processing is provided by the development of eigenvector based techniques. These rely on finding the eigenvectors of the correlation matrix and using this to form a subspace. The amplitude of the associated eigenvalues can then be used to find the direction of the signals from the target object. The first method to use the eigenvectors of the correlation matrix was introduced by Schmitt as the MUSIC (MUltiple SIgnal Classification) algorithm [34], although there are now many variations to this technique [30, 31]. Whilst the MUSIC algorithm offered a significant improvement in performance, limitations remain, particularly on target resolution in circumstances with coherent signals.

To conclude, although many aspects of sonar technology are relevant only to propagation in water, the use of sensors arrays and the associated signal processing means that sonar methods offer the possibility of adaptation to the problem of object detection in soil.

1.4 Deep Geophysics

The standard technique used to explore deep subsurface structures for the purpose of hydrocarbon exploration uses seismic wave reflections. Depths of interest range from a few hundred metres to many kilometres. Section 1.4.1 describes the basic seismic reflection surveying method. The financial motivation for detection and accurate mapping of hydrocarbon reserves has facilitated greater developments into the basic technique, with seismic reflection surveys having matured to become highly complicated but commonly used procedures. Some of the developments to the method are described in Section 1.4.2. Whilst this section concerns only seismic methods for detection of deep subsurfaces, rather than shallow objects, the applicability of many of the principles and signal processing techniques makes them worthy of attention. Conclusions are drawn in Section 1.4.3.

1.4.1 Basic Seismic Reflection Surveying

The history and development of seismic reflection surveying is closely linked to the exploration of oil and other hydrocarbons. The earliest use of seismic reflections for surveying purposes was by R.A. Fressenden in 1917 [35]. Early seismic reflection surveys were limited by a lack of recording technology and simply attempted to detect reflections using single sensors. Both the increase in available technology and the desire to find increasingly well covered hydrocarbon reserves drove development. During the 1930's multiple sensors were first used to increase signal-to-noise ratios [36]. By the late 1950's recording technology had advanced to allow for manual post-processing, and

methods using sensor arrays with multiple source locations had been developed [37, 38]. A method known as the common depth point (CDP) stack has become the most utilised of these. A brief description of the CDP stack shall be given in this section (see [39-42] for further details), with Section 1.4.2 detailing some of the many developments and modifications to the CDP method that have taken place over the decades.

The CDP stack uses an array of linearly spaced sensors. Seismic disturbances are generated and the response at each sensor measured, with the process repeated for many source locations along a measurement line. For each point on the surface the measured time histories corresponding to a source-sensor arrangement symmetric about the point are considered. An example arrangement is shown in Figure 1.1. The purpose of this grouping is that all the time histories share a common mid-point where the reflection from a horizontal surface would occur. Whilst this is only true for horizontal surfaces it provides a good initial approximation. Note that Figure 1.1 indicates which source-sensor pair's time histories are considered for post-processing analysis at the mid-point - the actual measurement procedure goes through the different source locations in turn and then selects the relevant data channels in post-processing.

The purpose of selecting data from source-sensor arrangements where the reflector is mid-way between them is so that this data can be summed to reinforce the reflected signal at this point. Prior to any summation, account must be taken of the additional propagation time that occurs because of the increased horizontal source-sensor distances. This time is called the normal move out (NMO), and is defined as the difference between the two way travel time for a given source-sensor pair and the minimum possible two way travel time to the reflector at the mid-point. It is a function of both the horizontal distance from the mid-point and the depth of the reflector. Calculation of the NMO relies on knowledge (or an estimate) of the wavespeed in the medium. Provided this can be estimated, NMO corrections can be applied to each set of data. Summation of all of the data from the source-sensor arrangements with the common mid-point should produce a constructive summation with background noise and correlated contamination (such as surface waves) cancelling.

This procedure is repeated for all mid-points, and the resulting time histories are plotted in a single figure called a seismogram. The summed trace is plotted vertically, with the time ordinate increasing in a downwards direction, and the horizontal location of the trace determined by the mid-point common to all of its constituent source-sensor pairs. Examples of such plots are shown in Figure 1.2. The high density and long length of the measurement array are typical.

1.4.2 Improvements to Basic Seismic Reflection Surveying

The increasing financial motivation of finding hydrocarbons reserves, coupled with the fact that many of the more easily detected reserves have already been exploited, has lead to continued development of the basic seismic reflection surveying technique. Readily available computing power has also allowed for much greater processing of the measured signals. Several of the improvements are described in this section.

1.4.2.1 Static Corrections

When considering wave propagation to the depths required for hydrocarbon exploration it is important to compensate for the effects of the near surface layer of geological material, often referred to as the 'weathered layer'. This is typically the layer of soil which overlies harder bedrock. The wavespeed in this material is considerably lower than in the underlying layers, and the weathered layer also usually exhibits greater lateral heterogeneity in terms of both thickness and material properties. Thus, although the propagation distance in the weathered layer may be relatively small (typically of the order of tens of metres), the large propagation time and variability mean that it can have significant effects on the quality of the imaging methods.

The effects of the both the presence and the variability of the weathered layer are compensated for by using static corrections [43]. This involves shifting the measured time histories to compensate for the additional propagation time spent in the weathered layer. Static correction time shifts due to variability in the surface height profile of the weathered layer can be accurately estimated using modern GPS systems. The thickness and propagation speeds can be estimated from a variety of techniques [44], including from refraction surveys (see Section 1.5.1) and more direct time-travel measurements [40]. These direct measurements involve the burying of either a source or sensor and measuring the time taken for propagation between the source and sensors [45]. The measurements must be repeated over many surface locations to achieve adequate static correction.

1.4.2.2 Data Migration

An assumption within the CDP method is that the reflections measured on a seismograph occur directly beneath the location of each respective element of the seismograph. This assumption is valid only for the case of a flat horizontal subsurface. This assumption is often violated in practice, with subsurfaces commonly containing dips, bumps and discontinuities [42]. These features are often of the greatest interest in hydrocarbon exploration as these can signify possible deposit locations. The technique that has been developed to relax this assumption, and thus accurately image irregular subsurfaces, is called migration.

Migration of seismic data is currently applied as standard and has undergone significant development in terms of its complexity, theoretical foundations and implementation since it was first applied over 60 years ago [46]. Interested readers are referred to some of the in-depth tutorials on the subject [47-49]. It can be shown that the result of diffraction from a point is a hyperbolic response in the seismograph [46]. By summing the values of the traces of the seismograph over this hyperbola the image of the point object is restored in the seismograph. Performing this procedure for each trace enables the imaging of irregular dips and non-horizontal layers.

Whilst the original methods of migration came from geometric and graphic principles, as the procedure became more developed in the early 1970's it was placed on firmer theoretical foundations by Claerbout [50]. Claerbout began by considering the seismic wave equation with the measured time histories as boundary conditions. This method used relatively few assumptions and gave more rigor to migration processing [48]. Greater understanding has lead to further improvements, such as forming the problem such that approximations to Kirchhoff integrals could be used in the solution, or using solutions to the discretised wave equations. These techniques have led to industry standard techniques known as Kirchhoff migration and finite-difference migration respectively [47], with these methods still subject to refinement and improvement [51]. Although these different types of seismic data migration have developed over time, they have the same general form, with the different techniques coming down to implementation from this form [52].

An example of the application of migration to actual seismic data is shown in Figures 1.2 (a) and 1.2 (b). The former of these shows a seismograph prior to application of data migration, and the latter with migration applied. Comparison of the figures illustrates the function of migration: the irregularities of the lowest subsurfaces are clearly visible once the migration techniques have been applied.

1.4.2.3 Filtering of the Seismic Data

In addition to shifting or migrating data, filtering of the data can also improve the image. Filtering removes information not useful to the imaging process by removing data that does not correspond to a reflection from a subsurface. Filtering in the frequency domain is commonly applied for the removal of noise outside the frequency range of the input signal. As this can not be a reflection from a subsurface the frequency components outside this range can be filtered out prior to processing. Bandpass filtering can also be applied with the frequency limits of the filtering varying as a function of depth. This is because increasing depth means increasing propagation distance and thus increasing attenuation of the higher frequencies due to attenuation with propagation. Deeper sections of an image

can therefore be filtered with a lower upper frequency limit [40], as the higher frequency regions will correspond to noise rather than reflections from subsurfaces.

Seismic reflection surveys generally use large numbers of sensors. This enables spatial Fourier transforms to be applied in addition to the frequency domain transforms described above. For this method to be viable it is important that there is a sufficiently large number of sensors, and that the sensors are close enough to prevent spatial aliasing at the wavenumbers of interest [53]. A widely employed type of filtering is velocity (or 'pie-slice') filtering [40, 54]. For this, both frequency and spatial Fourier transforms are applied so that the data is presented in the frequency-wavenumber space. Gradients in this space correspond to specific wave propagation velocities. Thus by removing appropriate portions of the signal from the frequency-wavenumber space, waves propagating at certain velocities are removed. Filtering in this domain is further improved by the use of windowing functions, analogous to the windowing functions used in standard frequency domain filtering.

An example of this application could be to remove the presence of the surface Rayleigh wave in measurements to increase the visibility of reflections from subsurfaces. Other unwanted wave types, such as waves propagating through the air or along refraction paths, could also be removed. An example is shown in Figure 1.3. Figure 1.3 (a) shows data from a marine seismic survey. Waves propagating directly through the water (rather than reflecting from subsurfaces) dominate, producing the straight line that virtually obscures the curved line representing the reflection from a subsurface. Figure 1.3 (b) shows the same data after velocity filtering of the water wave. The curved line corresponding to the subsurface is now more clearly visible.

1.4.2.4 Three and Four Dimensional Surveys

Thus far only two dimensional seismic reflection surveys have been considered. By using two dimensional arrays of surface sensors and sources it is possible to extend the experimental and processing methods, including migration, to three-dimensions [40, 41]. Three-dimensional seismic surveys offer the ability to image complex structures that may not be obvious in two dimensional slices, and therefore allow for easier interpretation of possible targets of interest to hydrocarbon explorations, such as domes and traps [55]. Its disadvantages are the considerably higher financial, experimental time and computing costs.

A further development from three-dimensional surveys is the addition of time dependence into the surveys, known as four-dimensional surveys. For these surveys three-dimensional surveys are taken in the same location at intervals over a period of time to evaluate changes in the subsurface structure. The principle application is in tracking the properties of hydrocarbon reservoirs during extraction.

This is possible because seismic reflections depend upon properties such as rock saturation [56]. Images from data measured at different times are subtracted to make the changes in structures clearly visible.

The main difficultly with four-dimensional surveying is in keeping all measurement parameters the same over long periods of time, as relatively small changes in measurement and environmental parameters can lead to substantial changes in resulting images [56]. Some effects can be compensated for in post-processing, whilst others, such as variation in location of source and sensor locations, simply mandate that measurements are performed with great rigor. The use of multiple experimental measurements over a long period of time obviously greatly increases the cost of the seismic reflection survey.

1.4.2.5 Truck Mounted Vibrators

The primary source for early seismic reflection surveys was dynamite. This was readily available and capable of producing an approximately impulsive input with sufficient amplitude. Over time safety and environmental concerns, as well as difficulty with repeatability, have meant that dynamite has been increasingly replaced by other sources [40]. One such method worthy of mention is that using truck mounted vibrators.

Truck mounted vibrators were initially developed by the Continental Oil Company in the late 1950s and were known by the trademarked name of Vibroseis [57]. The trademark has since lapsed, but the method has grown in popularity. It allows for quick measurement with a repeatable and controllable input and can be used in urban or other areas where the use of explosives is not a possibility. Although this method has a lower excitation force than provided by explosives, it is possible to use multiple source vehicles to compensate. A photograph of a modern vehicle for use with this method is shown in Figure 1.4. A disadvantage of this method is the high cost of these vehicles and equipment.

As truck mounted vibrators are capable of producing arbitrary waveforms, appropriate waveforms must be chosen. Any signal could, in theory, be used provided it contained the required frequency content. The most commonly used input waveform is a linear sweep [39], although non-linear sweeps have been considered [58]. The techniques for forming and improving seismic survey images cannot be directly applied to the time histories measured when using non-impulsive excitation, which must first be correlated with the input signal (see Chapter 3 for further details on cross-correlation). Application of the previously described techniques are then possible with only relatively minor additional considerations [59]. The use of truck mounted vibrators illustrates the development of the

basic seismic reflection survey method not only in post-processing, but also in the experimental methodology itself.

1.4.2.6 Anisotropy

The continuing development of techniques for the mapping of hydrocarbon reserves has lead to the exploitation of anisotropy in the ground. Anisotropy is defined as the variation in propagation wavespeeds as a function of the propagation direction. An excellent review of the chronological development of this technique has been given by Helibig & Thomsen [60]. Historically, anisotropy has been viewed as a problem within seismic reflection surveys, responsible for complicating conceptualisations of the wave propagations and causing anomalous results. More recently, however, the positive use of anisotropy have been explored [61-63].

The utility of anisotropy in hydrocarbon exploration is that rocks naturally contain cracks and fractures which, through suitably designed experimental investigations, allow for the estimation of the permeability of the material, and in turn an indication of the possibility of hydrocarbon reserves being present. Such surveys require measurements of all three orientations of displacement to be taken at the surface, as well more complex analysis. Despite this extra cost their utility has meant that their application has become more common [60].

1.4.3 Deep Geophysics Conclusions

The use of seismic reflection surveys for exploration at large depths is well established with the technology developed over many decades of well financed research. Basic methods involve the use of large sensor arrays with many source locations. Many signal processing techniques such as frequency filtering, velocity filtering and data migration are applied to signals prior to summation. These techniques are applied as standard across the hydrocarbon industry with great success. The financial motivations for improved imaging techniques has lead to continued development of the technology, such as inclusions of material anisotropy, with further developments undoubtedly continuing into the future.

1.5 Shallow Seismic Techniques

The application of seismic techniques to the problem of hydrocarbon exploration has been reviewed in Section 1.4. The techniques described were typically used for detection and mapping at depths of the order of kilometres. Attention now focuses on seismic techniques capable of detection and imaging at considerably shallower depths; typically less than a few tens of metres. The different

technologies described in this section utilise seismic waves in different ways. Section 1.5.1 examines the application of seismic wave refractions, whilst Section 1.5.2 reviews the technologies that use seismic energy to excite the structural resonances of objects buried very close to the surface. The attempts that have been made to apply the techniques described in Section 1.4 directly to shallow depths are discussed in Section 1.5.3. Finally, methods that are designed specifically for the purpose of point-like objects are detailed in Section 1.5.4.

1.5.1 Refraction Surveys

An alternate use of seismic waves for subsurface investigations is to make use of the refraction of waves along subsurface boundaries, as opposed to the reflection of the seismic waves described in the preceding section. The use of seismic wave refractions is even older than that of reflections, with the first documented use in 1845 by R. Mallet [35] (using dishes of mercury resting on the ground as seismic sensors). Refraction methods are capable of detecting the presence and properties of subsurfaces - not point-like objects. Applications include calculation of wavespeeds in the upper (weathered) geological layers for the purposes of static correction in seismic reflection surveys [44] (see Section 1.4.2.1), mineral exploration and civil engineering investigations of ground structures prior to building works [41].

When a seismic wave is incident upon a discontinuity in a propagation medium, refraction will occur. The propagation path of the incident wave will alter by an amount governed by Snell's Law [64]. If the incident wave is entering a medium with a higher propagation speed, as is usually the case in geophysics, then it will be bent away from the line normal to the material boundary. For given propagation speeds, a sufficiently large angle of incidence will cause the refracted wave to propagate along the boundary between the two media. This angle is known as the critical angle. As the refracted wave travels along the boundary it radiates energy upwards towards the surface. A diagram illustrating this process is shown in Figure 1.5.

As the wavespeed is higher in the lower medium (as it must be for the refraction along the boundary to occur), for a sufficient horizontal source-sensor separation the refracted wave is detected before the direct wave. Thus plotting the time of first detection at the sensor as a function of the source-sensor separation should, for the very simple case described, give the relationship between two linear regions joined discontinuously. Features of this plot, such as gradients and axis intercepts, enables estimation of both the distance to the lower layer and the propagation wavespeeds in both layers [65].

Seismic refraction surveying has developed to account for complex deviations from the simple assumption of two different materials separated by a horizontal boundary. The case of multiple

horizontal layers can be treated by, as in the case of two layers, plotting the time of first measurement at a sensor as a function of the source-sensor separation. With multiple layers present each additional layer will cause an additional discontinuously joined linear region in the plot. As the number of layers rises, however, it becomes increasingly difficult to accurately distinguish between the separate linear regions of the plot, with the accuracy of estimated ground properties reducing accordingly. An empirical maximum of four layers is observed [40].

In practice, the assumption of horizontal layers is unlikely to be fulfilled. Further improvements to the analysis of seismic refraction surveys allow for non-horizontal planar layer boundaries and irregular, non-planar layer boundaries. Various methods, such as the plus-minus interpretation methods [66, 67], generalised reciprocal method [68] and ray tracing methods [69] have been developed. Technical details are not of direct relevance in this thesis and thus lie outside the scope of this review, and interested readers should refer to the appropriate references.

A fundamental assumption of the method is that seismic wave propagation speeds increase through the geological layers. If, however, there is a layer which has a lower wavespeed than the layer above it then it is not possible for there to be refractions along the layer; the propagation path will instead bend towards the line normal to the layer interface. This is referred to as a ‘hidden layer’ [41, 70] as it does not appear on refraction surveys. Moreover, the additional propagation time that comes from propagating through this low velocity layer will lead to the impression that the layer below it is at greater depth than it really is.

Another scenario also often referred to as a ‘hidden layer’ is where the propagation velocity in the layers increases with depth, as required, but one intermediate layer is relatively thin [71]. Any refraction along the boundary of this layer arrives at times very similar to the refractions from the previous boundary. This can prevent their interpretation as separate events, and can happen for surprisingly thick intermediary layers [72]. Although there are methods for overcoming the problem of hidden layers the application of these solution relies on the knowledge that such a layer is present. This is obviously not usually the case.

Seismic refraction surveys, whilst useful for the detection and characterisation of geological layering, are not applicable for the detection of shallow buried objects. A basic understanding is useful, however, as ignorance of the additional propagation paths provided by seismic refractions from geological layers can lead to the interpretation of refraction events as reflection events. Furthermore, although the use of seismic refraction surveying cannot be used for the detection of buried objects it has the potential to be useful in the measurement of wave propagation speeds as a function of depth.

1.5.2 Detection of Target Resonance

This section concerns a method that has been specifically designed to detect anti-personal mines. Several variants of the method exist, but the basic concept is that seismic energy is used to excite an object buried at a very shallow depth. Providing the object has a sufficiently strong resonance in the range of excitation then its motion causes the ground above the object to vibrate. The amplitude of this ground movement is detected and displayed graphically to indicate the location of targets. This method is viable as landmines possess structural resonances inherent to their design [73]. A key advantage of this technique is that, unlike metal detectors and GPR, it naturally includes target discrimination. The excitation frequencies are chosen to correspond to those in the range of the structural resonances of landmines. Clutter objects such as metal debris or rocks are unlikely to have resonant frequencies in this range. An example experimental image is shown in Figure 1.6 (a), with the buried object arrangement photographed in Figure 1.6 (b). The method is capable of clearly detecting the landmines and not the clutter objects.

Different methods of excitation of the target object and measurement of the subsequent displacements have been used by different groups of researchers. Researchers at the Georgia Institute of Technology have used seismic sources in contact with the surface of the ground as an excitation mechanism [74-76], with the source designed to preferentially excite surface Rayleigh waves. The use of a seismic wave excitation allows the operators stand-off (the distance between the device and operators from the area under investigation), a preferable arrangement for detection of explosive devices. Attenuation of the Rayleigh waves due to damping, geometric spreading, and the effect of irregularities in the surface of the ground [77] does, however, limit the range of the technique.

Another method of excitation is that of acoustic to seismic coupling, which uses an acoustic source located above the surface of the ground to induce seismic vibrations. This method of excitation was used as far back as the 1970's [78] as an excitation method for shallow seismic detection. Theoretical and experimental development has continued [79, 80], with implementation for the purposes of mine detection now performed by several different researchers [81-84]. Unlike the seismic source, acoustic to seismic excitation eliminates the need for the source to be in contact with the ground: this is again a positive attribute when considering the detection of landmines.

Excitation using acoustic to seismic coupling may initially appear counter-intuitive as the large impedance discontinuity between the air and the ground can be expected to reflect most of the acoustic energy impinged upon it. Provided, however, that the soil is porous, the input impedance to the ground will be lower than for a body of homogeneous material. Physically this can be attributed to acoustic waves propagating into the pores of the material; as first established mathematically by Biot [85]. The transfer of energy from the pore wave propagation to seismic vibrations via viscous drag

results in a significant lowering of the ground impedance. However, even taking this extra coupling into account, the transmission coefficient remains low.

Acoustic to seismic excitation does have some disadvantages, mainly resulting from the difficulty in transmitting energy between the two media. This can require large acoustic sources capable of emitting sound pressure levels of up to 130 dB at 1 m [83], reducing the practical application of the method in the field due to both transportation and power consumption constraints. The acoustic source must be located close to the ground to prevent geometric attenuation from reducing the signal level, reducing much advantage in the stand-off. Finally, as the excitation of seismic waves from incident acoustic waves varies with the impedance of the ground the level of transmission will depend on both soil and environmental conditions. Fully saturated soil, with its porous structure water filled, will significantly reduce transmission. Lateral variations in soil properties have also been shown to cause impedance variations that lead to false detections [86].

Discussion now moves to the methods used for the detection of the ground motion. One such method is that of electromagnetic radar [74]. This measures the reflection of electromagnetic waves from the surface of the ground and is capable of detecting the very small displacements involved with good accuracy. An advantage of this type of detection is that it can also be used as a GPR (see Section 1.2.2), allowing the possibility of multiple detection methods being used to confirm the existence of a target object. The use of electromagnetic radar does, however, lead to the possibility of soil with magnetic properties or large amounts of moisture reducing the applicability of the detection method, as described in the aforementioned section.

An alternate non-contact method to detect the motion of the excited landmine is the laser Doppler vibrometer (LDV). This shines a monochromatic laser on the vibrating surface which is reflected and measured at the LDV. Variations in the velocity of the surface cause small changes in the frequency of the reflected laser due to Doppler shift. These small variations are measured by the interference produced when the signal is summed with a reference beam. This method is capable of producing accurate results, but difficulties can arise in isolating the vibration of the LDV unit from the ground vibrations [87]. This may limit the applicability of the measurement method in difficult field conditions. The application of an LDV can also be slow as it can only measure one point at a time, and must therefore be scanned over the required area.

A final method of detecting ground vibrations, and perhaps the simplest, uses a matrix of contact sensors that are placed directly on the ground. This requires careful consideration and measurement of the force exerted on the ground, as if this force is too large it will detonate the landmine. Direct contact sensors, such as accelerometers, can be obtained relatively cheaply and allows for

simultaneous measurement of many points. The method still remains relatively slow and as such the researchers investigating this method recommend it for target confirmation, rather than location [88].

The method of detection using target resonances, whilst useful for the specific application of landmine detection, is not suitable for modification to the general problem of shallow buried object detection using seismic waves. This is because it relies on the target being close to the surface and having a strong resonance: depths range from flush with the surface to a few tens of centimetres. The method is constrained to such shallow depths because of the reduction in the ability of the excitation methods to excite the target object, either because of the decay of Rayleigh waves with depth or the rapid reduction in amplitude of acoustically induced seismic waves. Even if the target receives adequate energy in the frequency range of its resonances, if it is buried too deeply then the consequent motion at the surface will be insufficient to allow for detection by any of the outlined methods.

An additional development is the exploitation of non-linearity in the interaction between the landmine and the surrounding soil [89]. This method was introduced by Donskoy [90], and relies on the target object possessing a resonance. Above the resonant frequency the target surface and the surrounding soil move out of phase with each other, causing them to separate. This causes a non-linear change in stiffness in the oscillation as the separation will only occur in part of the vibration. This is achieved even for reasonably low levels of excitation. Clutter items, such as rocks, typically have resonances well outside of the frequency range of excitation. The surface of these objects moves in phase with the adjacent soil and linear transmission of the vibration can occur. Thus clutter discrimination is reliably achieved.

When a non-linear system is excited simultaneously with two sinusoids of different frequencies, sum and difference tones are produced. This has been experimentally and theoretically verified for landmines [91, 92]. Therefore when a target with a strong resonance is excited simultaneously with two frequencies, one or more other predictable frequencies can be measured to indicate the presence of the target. Measurements are made in a similar manner to those described by Sabatier et al. previously, with excitation provided using acoustic-to-seismic coupling and measurements made using an LDV.

This method has the advantage that the measured output signal can be bandpass filtered to focus on the known desired frequencies, as the output will always contain frequencies different from the input frequencies due to the non-linearity of the system. This enables the removal of the relatively large input to the system. Field tests have been performed and the non-linear physics has been analysed using lumped parameter models, both indicating the validity of the method. Clutter rejection is, as expected, excellent.

The reliance on non-linear coupling between the target and the soil constrains the method to the detection of target objects with strong resonances. Furthermore, this reliance is subject to the interaction between the object and the surrounding material. The effects of variability in soil conditions or difficult field conditions have not been fully assessed, and may pose serious problems to the practical applicability of the method.

1.5.3 Application of Deep Surveying Techniques to 'Ultra-Shallow' Depths

This section is concerned with the application of the techniques devised for hydrocarbon exploration, generally with little modification from their description in Section 1.4, to shallow depths. The terms 'shallow' or 'ultra-shallow' detection occur frequently in the literature with no fixed definition of the depths that they refer to. The targets of interest are subsurfaces or buried structures rather than point-like objects. Applications vary from environmental geophysics, such as the location and mapping of water tables [93] and fractures [94], to engineering, where knowledge of near-surface geological layering is required prior to the construction of foundations. Serious efforts to apply seismic reflection techniques to shallower depths were not undertaken until the mid 1980's [95]. The application of methods designed and widely utilised for deep hydrocarbon exploration to shallower depths is a natural extension and methods are often simply copied from deeper techniques. However, differences in the problem prevent the scaling down of the experiments [53].

Numerous applications of shallow seismic reflection surveys have been documented in the literature [96-98], but perhaps the fullest application of processing techniques developed for deeper reflection seismology to ultra-shallow depths is provided by Schmelzbach et al. [99]. A particular problem in this case was the domination of direct waves (both surface and those confined to the near surface regions) in the measured signals. In all seismic reflection surveys waves will be detected at the sensor due to both the seismic waves propagating directly from the source to sensor and from reflections. In deep seismic reflection surveys the difference in travel time between the direct and reflected paths is large, with direct waves often removable directly in the time domain. If there is overlapping in the time domain then the reflected wave has usually propagated through materials with much higher propagation speeds than the direct wave, enabling application of the velocity filtering described in Section 1.4.2.3. For shallow depths, however, the direct and reflected waves are much closer together in time, with the possibility of them overlapping in the time domain much higher. Furthermore, the similarity in their propagation speeds reduces the effectiveness of velocity filtering. The high level of data processing did enable Schmelzbach et al. [99] to produce moderate results despite this, with some reflections from subsurfaces visible. Agreement could not be obtained with other experiments performed at the same site using different imaging methods.

There are several important differences between deep and shallow seismic reflection surveys. It is common for shallow seismic reflection surveys to use sources with much higher frequency content that the deeper surveying techniques. In part this is more from a desire to maximise the bandwidth of the input signal. This is not plausible in deeper circumstances due to the much longer propagation distances and thus much higher attenuation of these frequencies. Maximisation of the bandwidth of signals is particularly important when using non-impulsive input signals which require the application of cross-correlation functions in post-processing. When using impulsive signals it is still important to use signals that contain higher frequencies (typically a few hundred hertz) than those used in deeper work. This is because when analysing measurements made using impulsive signals, it is necessary for the signal being used to be shorter than the time delays involved [53] to prevent overlapping of measurements in the time domain.

The use of higher frequencies allows for possible discrimination of surface waves from reflected waves. This has been experimentally exploited by some authors, with subsequent theoretical backing also provided [77]. Whilst this seems perhaps too dependent on undulations in the ground's surface for general application, it nevertheless illustrates the variations between deep and shallow seismic reflection surveying.

A further, and problematic difference, noted by many working in the field of shallow seismic work is the large variation of wavespeed near to the surface. This has been observed both experimentally [93, 100, 101] and demonstrated theoretically [102]. This is caused by the presence of unconsolidated media near the surface, with material density and stiffness increasing with depth due to increasing overburden pressure. Although variations in wavespeed are present in the deeper seismic reflection surveys both the severity of this increase and the large lateral variations at shallow depths can cause difficulties that would not be found in deeper work.

A final illustrative example of a shallow seismic reflection survey is provided by Deidda & Balia [103]. This seismic reflection survey used a large concrete substructure, approximately 30 m long and buried at a depth of 3 m. A cross-sectional diagram of the arrangement is shown in Figure 1.7 (a). The concrete block was buried specifically for the purposes of reflection survey experimentation. Standard techniques were applied to make the CDP stack shown in Figure 1.7(b). The CDP stack can be seen to accurately map the buried concrete, although this is made somewhat easier as the material between the concrete and the surface was simply filled back in with the excavated material, thus ensuring relative lateral and vertical homogeneity.

Whilst this survey has great utility for large buried substructures, it is not applicable to the detection of buried targets. The CDP method fundamentally assumes that the object is not point-like but a

surface, with the migration techniques described in Section 1.4.2 required to image discontinuities. In the aforementioned example survey by Deidda and Balia the CDP stack fails to image at these discontinuities, with migration techniques failing to improve the situation. A comment, general to all of the surveys discussed in this section, is that a large number of source and sensors locations are required to form the images. In the Deddia and Belia example 144 excitation locations were required. This high measurement density is required for the resolution of the image, as this directly affects the number of vertical traces that go into the image. It was also required for the application of velocity filtering or other post-processing techniques that require the application of spatial Fourier transforms.

An important feature of the survey by Deddia and Belia was their use of horizontally polarized shear waves as the seismic wave chosen for detection. In deep geophysics compressional waves are used for detection with very few exceptions. Comparative studies between the use of different wave types have been made, with the use of shear waves shown to be desirable in certain circumstances [94]. The advantages of shear waves include their ability to be generated with a minimum generation of other unwanted wave types, that their propagation is more consistent in water saturated soils, and that they do not exhibit conversion into other wave types at the interaction with material boundaries. Shallow reflection surveys using shear waves are, however, still not widespread [95].

In the preceding discussion of shallow seismic detection work, little mention has been given as to the types of seismic sources used. As the seismic sources used in this thesis are examined in some detail in Chapter 5, it is relevant to discuss the sources used by previous authors. Although there are exceptions [104], sources are generally poorly described and characterised.

Where compressional waves are being used these are usually generated from impulses. These impulses are either generated by striking a base plate placed on the ground with a sledgehammer [96, 99] or using shotguns or other explosives [97, 99]. Shear waves were generated by striking the ends of a base plate with sledgehammers, with the base plate coupled to the ground either using prongs [103] or by driving a vehicle onto the base plate [96].

To conclude, work on shallow seismic reflection surveys aimed at the mapping of substructures has been ongoing and shown positive developments, including with the use of shear waves. Established hydrocarbon techniques cannot simply be scaled down due various additional effects, including poor time separation between surface and reflected waves, large variations in near-surface wavespeed and the implications of the use of higher frequencies. The seismic sources used are usually poorly defined and characterised. Despite the success of some seismic reflection surveys the method is fundamentally not applicable to the detection of shallow buried point-like objects.

1.5.4 Seismic Reflection Surveys for Point-Like Targets

Unlike the previous section on seismic reflection surveys this section looks at techniques specifically designed for the detection of point-like objects. Applications are varied and include buried infrastructure, such as water and gas pipes, archaeological artefacts and unexploded ordinance. Particular focus is naturally on areas where other technologies prove ineffective. Buried infrastructure, for example, is now mainly constructed of plastic piping [8] and cannot be detected by metal detectors, and GPR often performs poorly in wet or difficult soil conditions.

Work has been undertaken by Sugimoto et al. from the Toin University of Yokohama for some time. Early work used an impulsive excitation source to generate shear waves [105]. Horizontally polarised shear waves were chosen because of the similarity of their wavespeed with the surface wavespeed (see Chapter 3, Section 3.2.2) for further details. Various improvements were applied to the method such as frequency filtering, enveloping and attempts to counteract attenuation in the time domain [106-108]. This method has had some success. An example image is shown in Figure 1.8. This survey was taken over a buried concrete pipe, with the measurement line perpendicular to the run of the pipe. A cross-sectional image of the pipe is successfully formed. Experiments were performed with Professor Sugimoto as part of the work for thesis, and consequently more details of his work can be found in Section 6.4. The shear source used in this work consisted of a transducer coupled to the ground via a platform such that bending motion was induced in the platform. This is described in more detail in the discussion of the experiments conducted with Sugimoto.

Some additional studies have been performed by Grice & Pinnington [109]. For these a laboratory rig was constructed consisting of a large tanks filled with sand. The tank had several targets buried at different depths with attached sensors. Work focussed on attempting to measure reflections from the target using time-extended signals and autocorrelation functions [110], analogous to the excitation technique described in the reflection seismic surveying Section 1.4.2. The results were generally poor, with the main difficultly being the high levels of reflection from side-walls of the tank, despite the fitting of anechoic terminations. This illustrates a difficulty in attempting to perform seismic reflection surveys in the laboratory: although they have the advantage of much greater control, for example in ensuring homogeneity of the material, because phase (time delay) information is crucial, reflections from the walls of the tank prove prohibitive. This can be contrasted with laboratory experiments examining the method of detecting of target resonances, described in Section 1.5.2, in which reflections from the surroundings are actually beneficial. This is because these methods are concerned with magnitude (amplitude) information, and thus reverberation in the containing structure serves to increase the amount of seismic energy exciting the target.

Other attempts to use similar principles have met with limited success. Despite this, some aspects of their work can prove useful. For example, House and Pape [111] developed a method for measuring acoustic energy over a two dimensional grid in an attempt to obtain images of a target's rough shape. Whilst the methods used are not of relevance for this thesis, they did attempt to overcome the high levels of attenuation in the ground by inputting time extended signals whose energy increased as a function of frequency. This has the potential to maximise the bandwidth of the reflected signal, and thus improve the resultant correlation functions [112].

Whilst technologies using seismic wave reflections to detect point-like objects exist and have had some success, they remain poorly developed. This gap in the knowledge forms the basis of the research described in this thesis.

1.6 Aims and Objectives

The overall aim of this thesis is the development of a method to detect objects buried at very shallow depths, of the order of 1 m, using seismic waves. Based on the literature review given in the preceding part of this chapter, there is a sufficient gap in the literature to allow for progression of current knowledge.

The tasks necessary to achieve the stated aim can be subdivided into the following objectives:

- Examine mathematically the generation of various wave types by surface seismic sources.
- Develop an experimental procedure for the detection of shallow buried objects and investigate the application of further signal processing techniques to improve this method.
- Perform computer simulations to validate this method.
- Use computer simulations to investigate the effects of potential difficulties, such as soil layer structures and measurement inaccuracies.
- Design and experimentally validate a source suitable for emission of seismic waves for shallow object detection.
- Experimentally validate the procedure on targets buried in known locations.

The approach taken in fulfilling these objectives is given in the following section.

1.7 Overview and Approach

The work undertaken for this thesis to fulfil the aims and objectives stated in Section 1.6 begins in Chapter 2 with a mathematical examination of an elastic half space. The aim throughout the chapter is to form a basic understanding of different types of wave propagation and their generation in some simple circumstances. A large portion of Chapter 2 is concerned with how the direction of forces applied at the surface of an idealised elastic half space affects the relative proportion of the generated wave types. This is important when considering seismic reflection techniques as care must be taken to understand the seismic waves generated by the source if there is to be accurate analysis of the measured seismic waves. Final results are presented in a graphically simple way.

The details of the experimental methodology for the shallow seismic reflection method used in this thesis are given in Chapter 3. The basic method using impulsive excitation is described in detail, before modifications are made to allow for the inclusion of time extended signals. Additions to the signal processing, such as the inclusion of generalised cross-correlation functions, are also described.

To validate the methodology prior to field work numerical simulations are performed in Chapter 4. These are conceptually simple and involve the formation of simulated time histories in the frequency domain. The numerical simulations are then used to evaluate anticipated sources of experimental error and other possible anomalies, such as variations of wavespeed with depth, which have the potential to affect the performance of the method.

The design of the seismic source used in the experiments is described in Chapter 5 and its properties are experimentally evaluated. Two different types of shear wave source were constructed and simple measurements of surface amplitude components performed to chose the optimal source. Experiments using both surface and buried sensors were then undertaken to compare the shear source with a point vertical source. This comparison enables the wave types generated by the source to be compared with the mathematical analysis of Chapter 2.

Chapter 6 contains the experimental results and analysis from the application of the imaging method described in Chapter 3 and evaluated numerically in Chapter 4. Experiments were performed at multiple test sites. Each test site is described and the experimental results shown. Concluding remarks on the performance of the imaging method at the different test sites are given.

Finally, Chapter 7 concludes the thesis and offers suggestions for future work.

1.8 Contributions

The original contributions of this thesis to the existing knowledge are:

- A mathematical analysis of the energy partition between wave types generated by a point seismic source oscillating parallel to the surface of a homogeneous, isotropic elastic half-space. Previous work has calculated this energy partition for a point source oscillating perpendicular to the surface of the ground. The clear form of graphical representation of the mathematical results used in the previous work is first reproduced and then applied to the new results.

- Improved physical insight in the use of the imaging technique used for the detection of objects buried at shallow depth. This includes the use of imaging artefacts caused by surface waves to verify the wavespeed value used in the imaging method.

- Development of a numerical simulation to simulate time histories measured on the surface using a frequency domain based method. This method is conceptually simply but has not, to the author's knowledge, been used previously. A basic numerical simulation was initially developed, to which additional complications, such as variation of wavespeeds as a function of depth, were then added to enable more realistic simulated results.

- Design of a seismic source that preferentially generates shear using an inertial electromagnetic shaker. The design of this source was verified by experiments using both buried and surface sensors.

- The inclusion of spatial filtering and the smoothed coherence transform variant of the cross-correlation functions in the imaging method. Spatial filtering, whilst simple to implement, can give a marked improvement in the imaging method's results. The smoothed coherence transform (or another such generalised cross-correlation function that 'pre-whitens' signals prior to calculation) is essential for overcoming the effects of attenuation.

- Experiments were performed at multiple sites to test the validity of the experimental method, the numerically simulated results and the theoretical analysis.

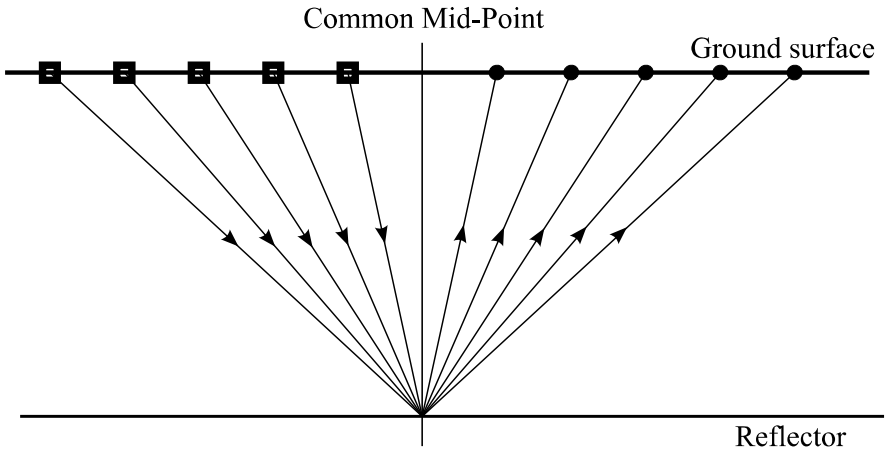

Figure 1.1 - Diagram of a typical source-sensor arrangement used to form a trace in the CDP method. In the diagram squares represent source locations and circles sensor locations. Note that measurements are performed at each source location in turn (not simultaneously). The data from the paired sources and sensors in this diagram are then selected to form a large data set suitable for post-processing.

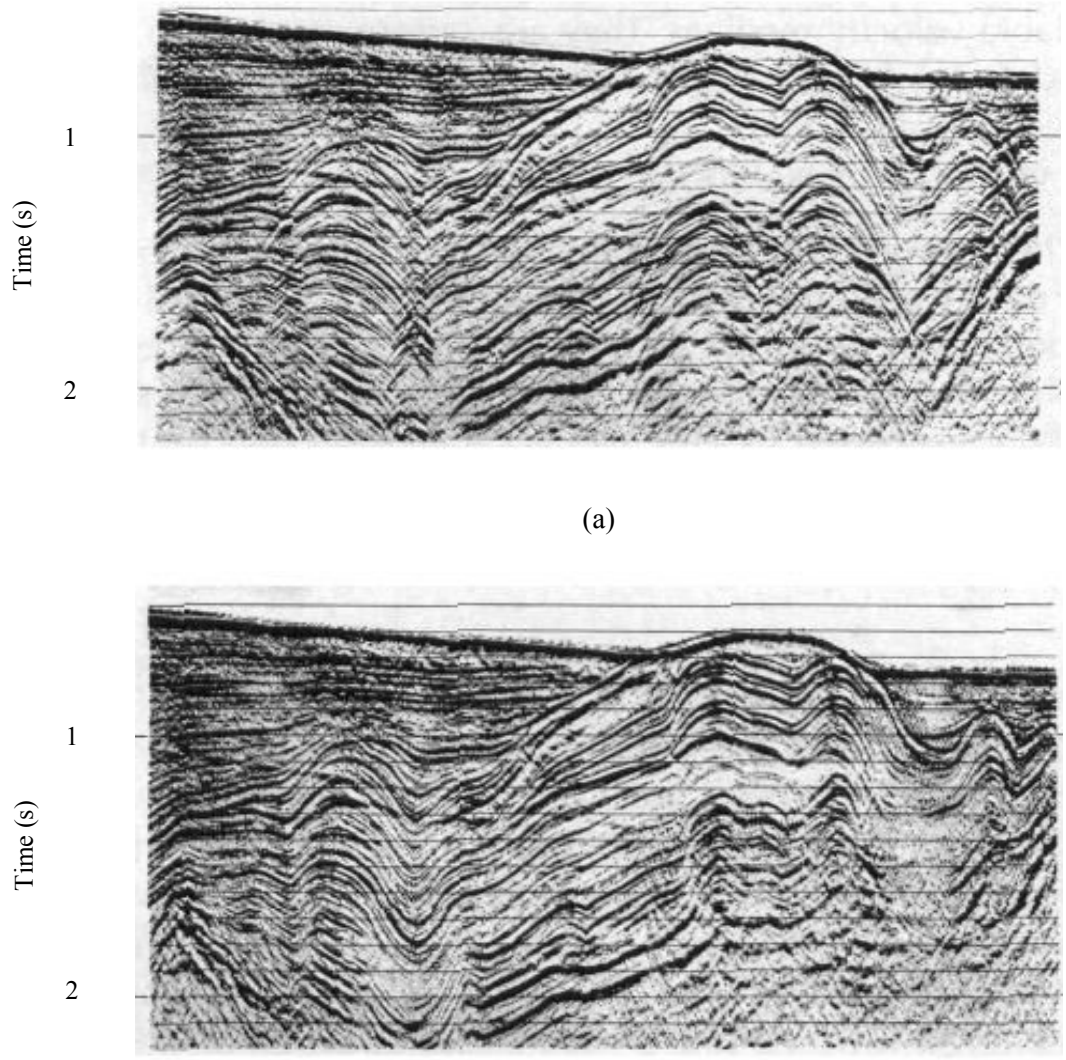

Figure 1.2 – Seismograph from the Santa Barbara Channel with (a) no data migration techniques applied and (b) migration techniques applied. The vertical ordinate denotes time in seconds. Figures from [46].

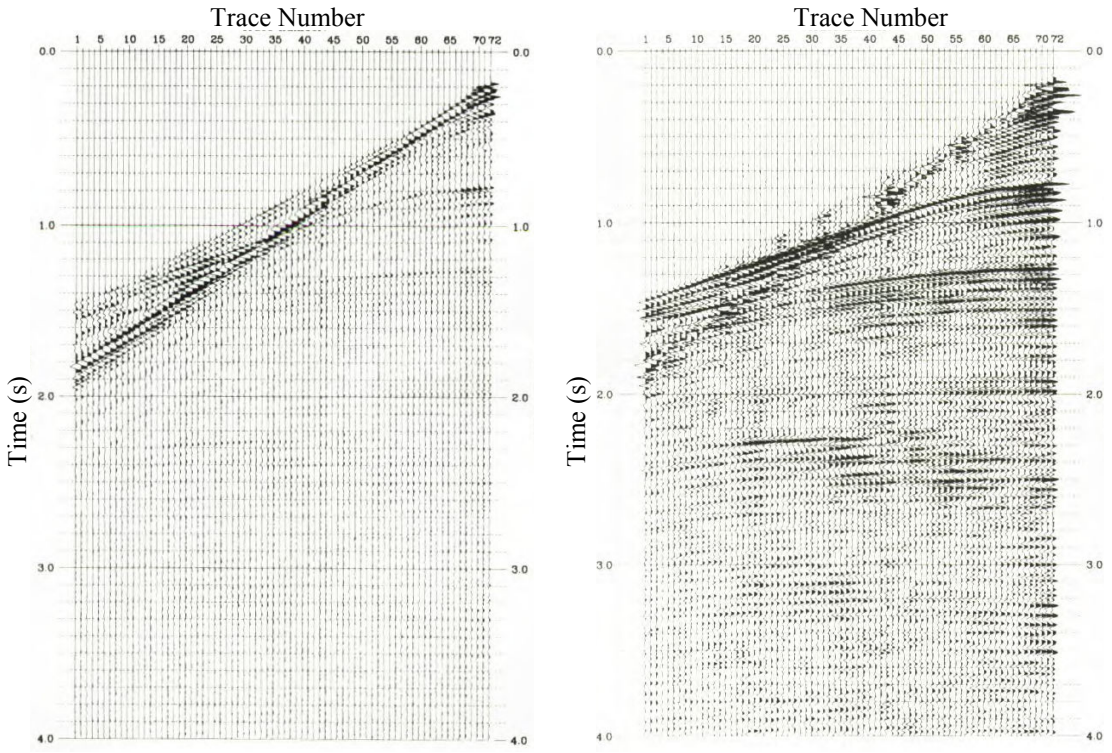

(a) (b)

Figure 1.3 - An example of velocity filtering. Figure 1.3 (a) shows data from a marine seismic reflection survey. The dominant straight line on the image corresponds to the propagation of waves through the water, with the curved line corresponding to reflections from the target being poorly visible. Figure 1.3 (b) shows the same data but with velocity filtering applied to remove the dominant water wave. The curved line corresponding to a subsurface is now more clearly visible. In both figures the vertical ordinate denotes time in seconds and the horizontal ordinate the trace number. From [54].

Figure 1.4 – Photograph of a source vehicle for a truck mounted vibrator. The base plate that transmits vibrations is located in the centre of the vehicle. From [113].

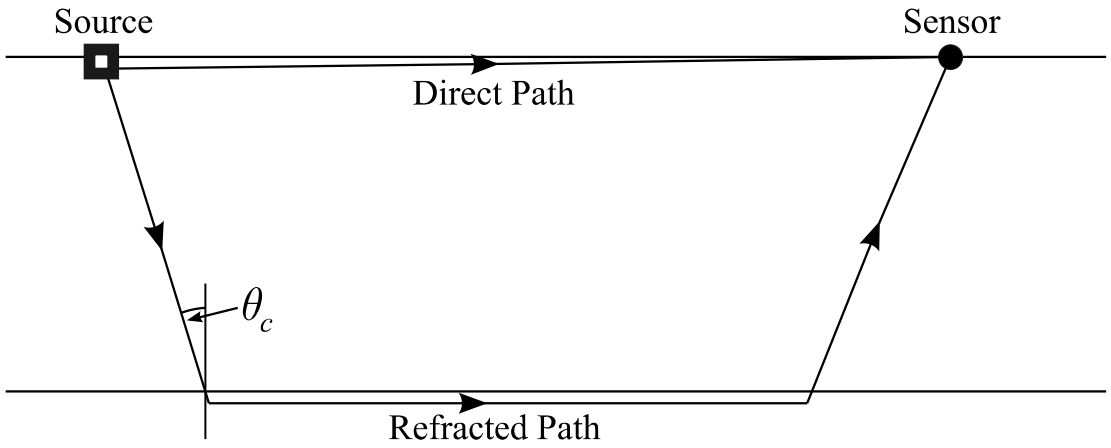

Figure 1.5 – Schematic of the propagation paths considered for the simplest seismic refraction survey. The critical angle required for the refraction path to propagate along the boundary is labelled θ_c. It is implicitly assumed here that the lower medium has a higher wavespeed than the upper medium.

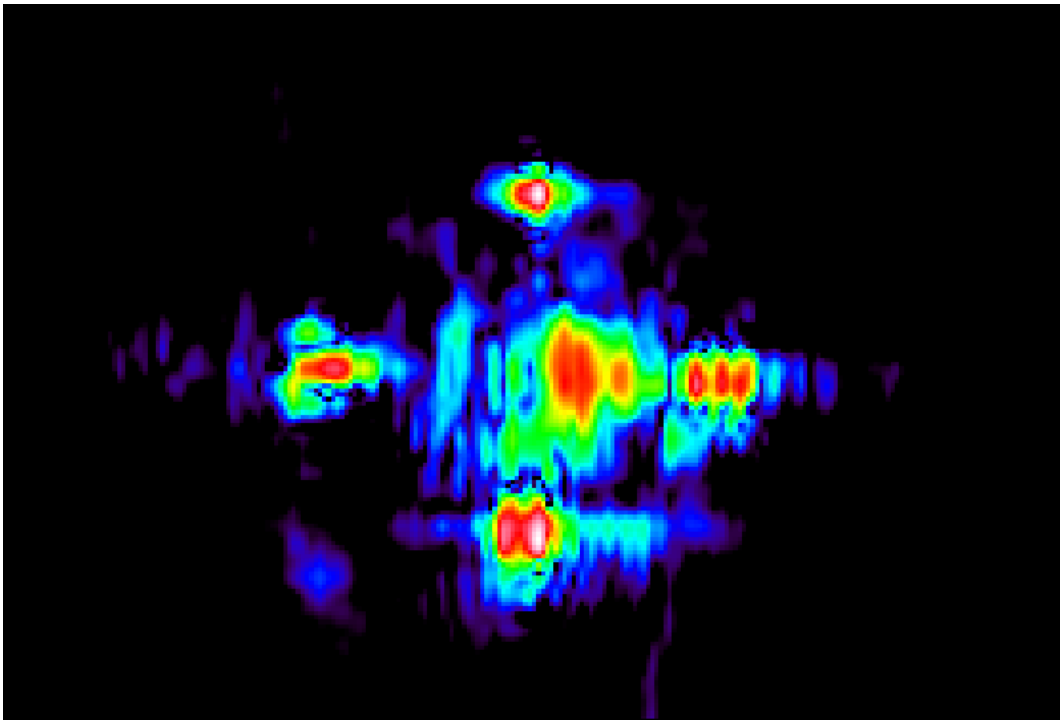

(a)

(b)

Figure 1.6 – (a) An example image produced by the target resonance detection method used in [76]. Black regions are of zero value, moving through blue, green, yellow, with red as the high value. The mines are clearly imaged by the method whereas the rocks are not. Images taken from [76]. Figure 1.6 (b) Photograph of the experimental targets used to obtain Figure 1.6 (a). The central target is an anti-tank mine. This is surrounded by four anti-personal mines and four rocks.

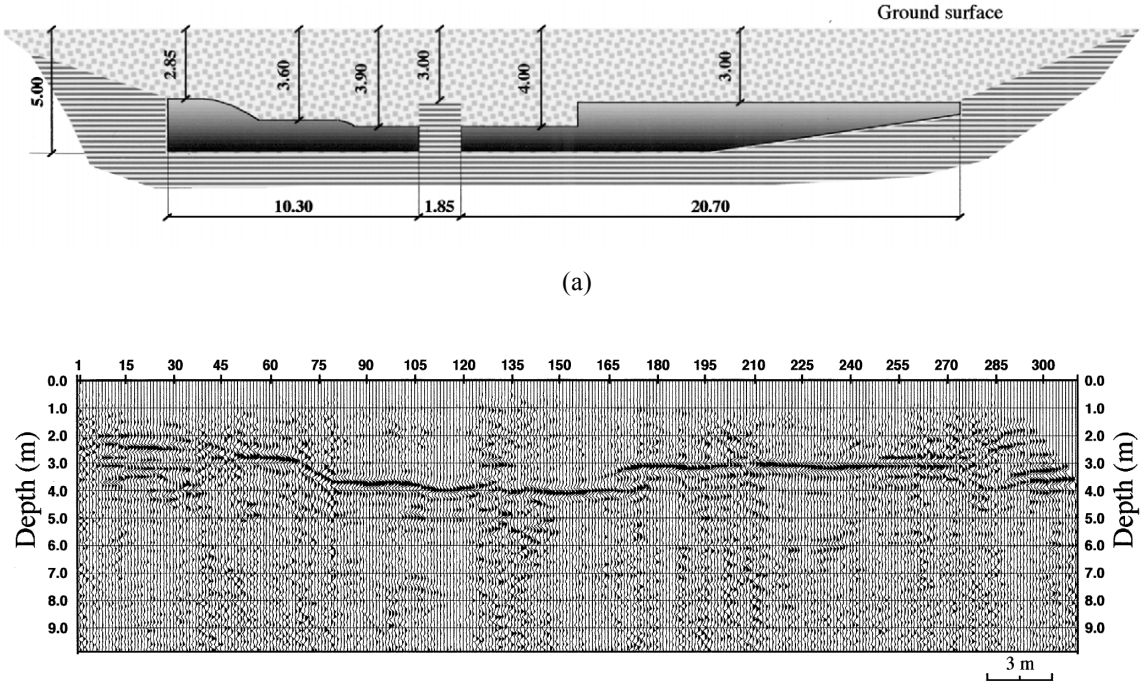

Figure 1.7 – (a) Cross-sectional diagram of the buried concrete object used by Deidda & Belia in [103]. The black fading to white block represents the concrete, the horizontal lined section the undisturbed ground, and the spotted area the back filled soil. All dimensions are in metres. The structure had a constant cross-section and was approximately 5 m wide. Figure 1.7 (b) shows the CDP stack of the buried concrete object. The numbering system of the horizontal ordinate denotes the individual trace obtained by the basic CDP stack method. Further details of the processing required to form the image can be found in Deidda & Belia [103]. Figures from [103].

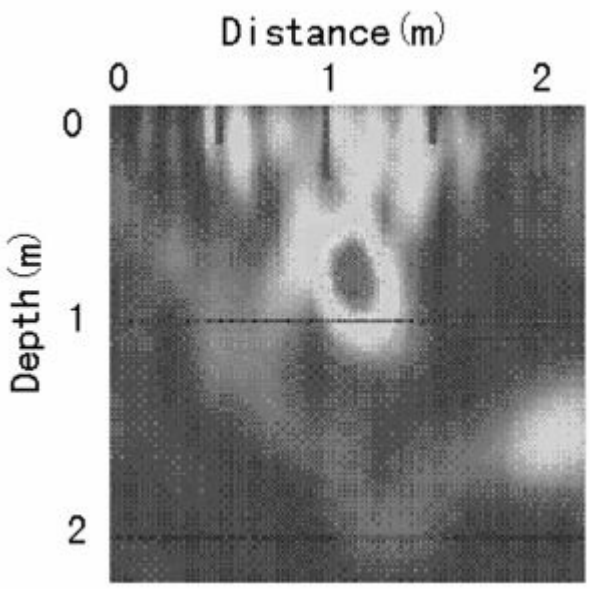

Figure 1.8 – Results of the imaging method applied by Sugimoto et al. The target object is a pipe and the survey undertaken across a section of the pipe. The circular outline of the pipe is visible in the centre of image and at a depth of a little less than 1 m. From [114].

2. Mathematical Modelling

Chapter 2

Mathematical Modelling

2.1 Introduction

The preceding chapter gave the aims of this thesis and examined their position relative to the existing work in the field. This chapter serves two purposes. The first of these is to gain familiarity with the various wave types that may exist, as well as their individual properties. This is important prior to using elastic waves in soil as it enables understanding and meaningful interpretation of the resulting analysis. Consideration of general wave propagation in idealised models of the ground is given in Section 2.2. This covers shear, compressional and Rayleigh waves.

The second aim of this chapter is to investigate the generation of these propagating waves by surface sources. To this end, Section 2.3 seeks to obtain the relative amounts of energy in each propagating wave type and the variation of these quantities with respect to soil properties. The source of interest in this thesis; a point source moving parallel to the surface of the ground, is discussed in Section 2.3.3, with previously developed techniques applied to obtain the relative amounts of energy in each propagating wave type. The results from this section are used in Chapter 5 when designing the source used in imaging experiments. Graphical representations of the derived source properties are described in Section 2.4. Limitations of the analysis presented here are outlined in Section 2.5. Finally, conclusions are drawn in Section 2.6.

2.2 Basic Wave Types in an Elastic Space

The simplest system supporting three-dimensional elastic waves is an infinite elastic space. This is considered in Section 2.2.1, with compressional and shear waves introduced and their key properties described. In Section 2.2.2 a free surface is introduced to the system to form a semi-infinite elastic half-space. This allows for the formation of surface Rayleigh waves and for the assignment of physically meaningful terminology to the two shear wave polarisations.

The basic theories of elasticity and elastic wave propagation are well established and documented. Consequently rigorous mathematical details are often omitted in this section. Such details are available in many of the textbooks on the subject [64, 115-117] and are referred to as appropriate.

2.2.1 Infinite Elastic Space

The system under consideration is that of an infinite elastic space. It is assumed that the medium is unbounded in all dimensions, linearly elastic, homogeneous and isotropic. A three-dimensional Cartesian coordinate system is imposed with arbitrary orientation, with component coordinates x, y and z, and the position vector $\mathbf{x}(x,y,z) = x\hat{\mathbf{x}} + y\hat{\mathbf{y}} + z\hat{\mathbf{z}}$, where the $(\hat{})$ superscript indicates a unit vector. Deformation displacement components of the elastic media are denoted by u_x, u_y and u_z, corresponding to the three Cartesian coordinates respectively. The deformation displacement vector at a given point in the medium is defined as $\mathbf{u}(x,y,z) = u_x\hat{\boldsymbol{x}} + u_y\hat{\boldsymbol{y}} + u_z\hat{\boldsymbol{z}}$, each component of which varies also as a function of time and space.

The general equation describing the system is given by [116]

$$(\lambda + \mu)\nabla(\nabla \bullet \mathbf{u}) + \mu\nabla^2\mathbf{u} = \rho\frac{\partial^2\mathbf{u}}{\partial t^2}, \tag{2.1}$$

where λ and μ are the Lamé constants, with the latter also referred to as the shear modulus, ρ is the density of the medium, $(\bullet)$ is the scalar (or dot) product, ∇ is the del operator; defined in Cartesian coordinates as

$$\nabla = \frac{\partial}{\partial x}\hat{\mathbf{x}} + \frac{\partial}{\partial y}\hat{\mathbf{y}} + \frac{\partial}{\partial z}\hat{\mathbf{z}}, \tag{2.2}$$

and ∇^2 is the Laplacian, which is equal to the divergence of the gradient of the del operator. Attention now moves to the different types of wave propagation possible in a system described by Equation (2.1). Taking the divergence of Equation (2.1) gives

$$\nabla^2\Phi = \frac{1}{c_p^2}\frac{\partial^2\Phi}{\partial t^2}, \tag{2.3}$$

where

$$c_p = \sqrt{\frac{\lambda + 2\mu}{\rho}}, \tag{2.4}$$

and

$$\Phi = \nabla \bullet \mathbf{u}. \tag{2.5}$$

Physically, the divergence of the displacement vector corresponds to dilation within the medium. As Equation (2.3) is a wave equation, it can be concluded that an infinite elastic space supports propagation of waves of dilation with a non-dispersive wavespeed c_p. These waves are referred to as compressional waves in accordance with the majority of relevant literature, and the wavespeed c_p as the compressional wavespeed.

Taking the curl of Equation (2.1) and using the fact that the curl of a gradient is always zero gives

$$\nabla^2\mathbf{h} = \frac{1}{c_s^2}\frac{\partial^2\mathbf{h}}{\partial t^2}, \tag{2.6}$$

where

$$c_s = \sqrt{\frac{\mu}{\rho}}, \tag{2.7}$$

and

$$\mathbf{h} = \nabla \times \mathbf{u}. \tag{2.8}$$

where $(\times)$ is the vector (cross) product. Physically the curl of the displacement vector corresponds to rotation within the medium. As Equation (2.6) is a wave equation, it can be concluded that an infinite elastic space supports propagation of waves of rotation with a non-dispersive wavespeed c_s. These waves are referred to as shear waves in accordance with the majority of relevant literature, and the wavespeed c_s as the shear wavespeed.

The ratio of the shear and compressional waves, defined as σ, is expressible solely as a function of the Poisson's ratio [64]:

$$\sigma = \frac{c_s}{c_p} = \sqrt{\frac{\mu}{\lambda + 2\mu}} = \sqrt{\frac{1 - 2v}{2(1 - v)}}. \tag{2.9}$$

where v denotes the Poisson's ratio. The dependence of σ with Poisson's ratio is shown in Figure 2.1 (a). Consideration of the direction of motion of the propagating waves [64] shows that for compressional waves the particle motion is parallel to the direction of propagation. A compressional wave is thus a longitudinal wave, and is analogous in its propagation to idealised acoustic or water body waves. For the shear waves the particle motion is perpendicular to the direction of propagation, and the wave is thus transverse. This condition permits two independent polarisations of shear waves to propagate with their particle motions perpendicular to both each other and the direction of propagation. In an infinite elastic space the two polarisations have no distinguishing physical significance due to the symmetry of the system.

2.2.2 Semi-Infinite Elastic Space and Rayleigh Waves

Whilst the infinite elastic space examined in Section 2.2.1 is useful for gaining an understanding of the basic types of wave propagating in an extended three-dimensional elastic medium, further development is necessary to include other relevant types of propagating wave. To solve Equation (2.1) in a more relevant system, a free surface is introduced, as this allows for the propagation of surface Rayleigh waves. Only a brief outline of the mathematical derivation is presented here. The main motivation for providing details of the derivation is to introduce the concept of elastic wave field potentials.

For convenience the free boundary is defined to lie in the *x*-*y* plane with the origin of the *z* axis defined at this boundary, and with a positive *z* direction corresponding to increasing distance from the

free surface. The equations describing the infinite elastic space are given by Equation (2.1). The displacement vector **u** is commonly split into two potentials

$$\mathbf{u} = \nabla\Phi + \nabla \times \mathbf{h} \quad ; \quad \nabla \bullet \mathbf{h} = 0\,, \tag{2.10}$$

where Φ is a scalar potential and **h** a vector potential. Although decomposition into potentials is assumed by a general mathematical theorem [118], the potentials have particular physical significance in this application. These two potentials correspond to the compressional and rotational parts of the motion respectively. Equation (2.10) can thus be viewed as a statement that the motion of the medium is the superposition of compressional and rotational motions. Substitution of the potential form of the displacement into the equation of motion of the system given by Equation (2.1) gives

$$\nabla\left[\left(\lambda + 2\mu\right)\nabla^2\Phi - \rho\frac{\partial^2\Phi}{\partial t^2}\right] + \nabla \times \left[\mu\nabla^2\mathbf{h} - \rho\frac{\partial^2\mathbf{h}}{\partial t^2}\right] = 0\,. \tag{2.11}$$

As the terms in square brackets must equal zero, two wave equations can be obtained, one for each potential:

$$\nabla^2\Phi = \frac{1}{c_p}\frac{\partial^2\Phi}{\partial t^2} \quad ; \quad \nabla^2\mathbf{h} = \frac{1}{c_s}\frac{\partial^2\mathbf{h}}{\partial t^2}\,. \tag{2.12}$$

These have wavespeeds corresponding to the compressional and shear waves, which is unsurprising considering these potentials correspond to these separate components of the motion. Equations (2.12) must be solved subject to the free boundary conditions at the surface. These are that all stresses must reduce to zero on the free surface, or mathematically,

$$\tau_{zx} = \tau_{zz} = \tau_{zy} = 0\,, \tag{2.13}$$

where τ_{ij} denotes a stress, with the first subscript coordinate describing the plane on which the stress is acting, and the second the direction in which it acts. Details of the implementation of the boundary conditions of Equation (2.13) to the general solutions to the equations of the potentials given in Equations (2.12) are omitted. Crucially, the Rayleigh wavenumbers are found to be the solutions of the equation

$$\left(2k_R^2 - k_S^2\right)^2 - 4k_R^2\sqrt{k_R^2 - k_p^2}\sqrt{k_R^2 - k_s^2} = 0\,, \tag{2.14}$$

where k_p, k_s and k_R denote the compressional, shear and Rayleigh wavenumbers respectively. These are defined as

$$k_p = \frac{\omega}{c_p}, \tag{2.15}$$

and

$$k_s = \frac{\omega}{c_s}, \tag{2.16}$$

and

$$k_R = \frac{\omega}{c_R}, \tag{2.17}$$

where c_R is the Rayleigh wavespeed. Equation (2.14) is termed the 'Rayleigh equation' in accordance with the literature [119]. The function on the left hand side of Equation (2.14) is used extensively in Section 2.3, and is thus defined as

$$F(\xi) = \left(2\xi^2 - k_s^2\right)^2 - 4\xi^2\sqrt{\xi^2 - k_p^2}\sqrt{\xi^2 - k_s^2}\,, \tag{2.18}$$

for later convenience, where ξ denotes a wavenumber variable. Substituting the angular frequency and wavespeeds for wavenumbers into Equation (2.14), defining

$$\chi = \frac{c_R}{c_s}, \tag{2.19}$$

and simplifying, gives an expression for the Rayleigh wavespeed as [64]

$$\chi^2\left[\chi^6 - 8\chi^4 + 8\left(3 - 2\sigma^2\right)\chi^2 - 16\left(1 - \sigma^2\right)\right] = 0\,. \tag{2.20}$$

Although Equation (2.20) has no simple analytical solution, if the Poisson's ratio, and hence σ, is known then numerical calculation of the roots is straightforward. Figure 2.1 (b) shows the ratio of the

Rayleigh to shear wavespeeds as a function of the Poisson's ratio. Over the possible range of values for the Poisson's ratio the ratio of the wavespeeds varies between about 0.88 and 0.96. The Rayleigh wave is thus constrained to propagate at a speed slightly less than the shear wavespeed.

Equation (2.20) has three non-trivial solutions and therefore three values of the Rayleigh wavespeed. A full account of these multiple solutions is given in a paper by Schroder and Scott [119]. The key conclusion is that one of the roots is always real and corresponds to a propagating wave, and it is this root that is used to obtain the Rayleigh wavespeed.

The nature of the other two roots of the equation varies with the Poisson's ratio. For lower values of the Poisson's ratio these roots correspond to complete mode conversion at the boundary. Mode conversion is the phenomenon whereby an incident wave type is reflected as a different wave type, and complete mode conversion is where a single wave type is incident on the free boundary and the entire reflected wave is of a different wave type. This mode conversion occurs only for specific angles of incidence. For higher values of the Poisson's ratio these roots correspond to non-physical waves whose motion is unbounded with respect to increasing depth.

To gain a better understanding of the behaviour of Rayleigh wave propagation it is instructive to examine the Rayleigh wave displacement components. These are obtained by assuming that the potentials of Equation (2.10) possess harmonic variation in the x direction and allowing for arbitrary behaviour in the z direction. This leads to displacement component expressions of [116]

$$u_x \propto k_R \left[e^{-z\sqrt{k_R^2 - k_p^2}} - \frac{2\sqrt{k_R^2 - k_p^2}\sqrt{k_R^2 - k_s^2}}{2k_R^2 - k_s^2} e^{-z\sqrt{k_R^2 - k_s^2}} \right] e^{-j(k_R x - \omega t)}, \qquad (2.21)$$

and

$$u_z \propto j\sqrt{k_R^2 - k_p^2} \left[e^{-z\sqrt{k_R^2 - k_p^2}} - \frac{2k_R^2}{2k_R^2 - k_s^2} e^{-z\sqrt{k_R^2 - k_s^2}} \right] e^{-j(k_R x - \omega t)}, \qquad (2.22)$$

where $j = \sqrt{-1}$, and the assumption that the displacement is bounded with depth has been made. Non-dimensionalisation of Equations (2.21) and (2.22) and normalising them by their respective surface values gives

$$\frac{u_x\left(\frac{z}{\Lambda}\right)}{u_x(0)} = \left[e^{-2\pi\frac{z}{\Lambda}\sqrt{1-\sigma^2\chi^2}} - \frac{2\sqrt{1-\chi^2}\sqrt{1-\sigma^2\chi^2}}{2-\chi^2} e^{-2\pi\frac{z}{\Lambda}\sqrt{1-\chi^2}} \right]\left[1 - \frac{2\sqrt{1-\chi^2}\sqrt{1-\sigma^2\chi^2}}{2-\chi^2} \right]^{-1}, \quad (2.23)$$

and

$$\frac{u_z\left(\frac{z}{\Lambda}\right)}{u_z(0)} = \left[e^{-2\pi\frac{z}{\Lambda}\sqrt{1-\sigma^2\chi^2}} - \frac{2}{2-\chi^2} e^{-2\pi\frac{z}{\Lambda}\sqrt{1-\chi^2}} \right]\left[1 - \frac{2}{2-\chi^2} \right]^{-1}, \quad (2.24)$$

where Λ denotes the wavelength of the Rayleigh waves. These expressions vary only as a function of the Poisson's ratio, and are plotted in Figure 2.3 for the specific case of the Poisson's ratio being 0.25. Both displacement amplitudes fall away rapidly with depth, and crucially the rate of this fall off increases with frequency. Significant displacement is confined to a depth of only one or two wavelengths.

The displacement components in Equations (2.21) and (2.22) vary by a factor of j and the motion is thus retrograde in nature. Figure 2.3 shows that horizontal displacement component becomes negative at a relatively shallow depth, indicating that motion of the Rayleigh waves changes from retrograde to prograde.

In addition to surface wave behaviour, the introduction of a free surface also allows for meaningful distinction between the two polarisations of shear wave. Shear wave motion perpendicular to the plane of the free surface is known as shear vertical (SV) wave propagation, whilst shear wave motion parallel to the plane of the free surface is known as shear horizontal (SH) wave propagation. For consistency with the literature on the subject, the compressional wave is referred to as the P wave. These three wave types are collectively known as body waves to distinguish them from the surface (Rayleigh) wave.

2.3 Surface Excitation

In the previous sections the types of wave propagation possible within an elastic space have been discussed. However, no consideration has been given to the actual method of generation of these waves. This is the aim of this section. It begins with an analysis of the simplest seismic source; that of an infinite SH line source, and progresses through the established point vertical source to the point SH

source. For both cases the displacement functions are calculated in a subsection, and the partition of energy between the generated wave types are given in the subsequent subsection.

Throughout this section a cylindrical coordinate system is used for surface waves and a spherical coordinate system is used for body waves. These are defined in Figure 2.2 (b) and 2.2 (c) respectively. It should be noted that *r* refers to the radius in cylindrical coordinates, and *R* to the radius in spherical coordinates.

2.3.1 Infinite SH Line Source

The simplest seismic source on an elastic half space is a line source of infinite length vibrating on a free surface, with the direction of vibration parallel to the length of the source. It is assumed that the source is time harmonic. The response to non-harmonic motion could be calculated by superposition of harmonic responses if desired. Although the procedure for the derivation is available in the literature [64], it is given here in some detail, as it has much in common with the derivations required for other source configurations considered in this chapter.

The free surface is again chosen to coincide with a plane defined by the origin of the *z* coordinate. The problem is greatly simplified by noting that, for a source acting in the $\hat{\mathbf{y}}$ direction, all motion will necessarily be in that direction. This is a consequence of the decoupling of the equations of motion of the system between the potentials describing SH waves and those describing P and SV waves [64]. Furthermore, due to the symmetry of the problem, variation in the $\hat{\mathbf{y}}$ direction is necessarily zero. The first of these conditions immediately reduces $\mathbf{u}$ to $\mathbf{u}\left(0,u_y,0\right)=u_y\hat{\mathbf{y}}$, and their application simultaneously causes the divergence of the displacement component vector to be zero. The fundamental equation of motion of system, given in Equation (2.1), reduces to

$$\nabla^2 u_y\left(x,z,t\right)=\frac{1}{c_s^2}\frac{\partial^2 u_y\left(x,z,t\right)}{\partial t^2}. \tag{2.25}$$

This is subject to the free surface boundary conditions with a harmonic horizontal stress of angular frequency ω and peak value τ_0 applied in the appropriate orientation

$$\tau_{yz}\left(x,z,t\right)\big|_{z=0}=\tau_0\delta\left(x\right)\mathrm{e}^{\mathrm{j}\omega t},\quad \tau_{zz}=\tau_{zx}=0, \tag{2.26}$$

with $\delta(x)$ denoting the Dirac Delta function, which is used so that the source has an infinitely small width. As the system is assumed to be linear, all consequent displacements and stresses are also harmonic with the same angular frequency as the input stress. Time dependence is therefore suppressed and is only reintroduced in the final result. This reduces Equation (2.25) to the Helmholtz equation:

$$\nabla^2 u_y(x,z) - k_s^2 u_y(x,z) = 0\,. \tag{2.27}$$

The expressions for the stress can be found from the constitutive stress-strain relationship. Stress and strain expressions are given here using standard summation convention notation for brevity (see, for example, Graff [64] for details),

$$\tau_{ij} = \lambda \gamma_{kk} \delta_{ij} + 2\mu \gamma_{ij}\,, \tag{2.28}$$

where δ_{ij} is the Kronecker delta and the strains are found from

$$\gamma_{ij} = \frac{1}{2}\left(u_{i,j} + u_{j,i}\right). \tag{2.29}$$

The non-zero stress of Equation (2.26) can be expressed in terms of the displacements by

$$\tau_{yz} = \mu \frac{\partial u_y(x,z)}{\partial z}\,, \tag{2.30}$$

where variation with respect to the y axis is zero due to symmetry. In order to proceed with the solution it is necessary to remove one spatial variable by Fourier transforming both the equation of motion in Equation (2.27) and the boundary conditions in Equation (2.26). The Fourier transform is applied to the x coordinate variable and is defined as

$$\overline{f}(\xi) = \frac{1}{\sqrt{2\pi}} \int_{-\infty}^{\infty} f(x)\, \mathrm{e}^{-\mathrm{j}\xi x}\, \mathrm{d}x\,, \tag{2.31}$$

and its inverse as

$$f(x) = \frac{1}{\sqrt{2\pi}} \int_{-\infty}^{\infty} \overline{f}(\xi) e^{j\xi x} d\xi , \tag{2.32}$$

where a bar over a quantity indicates that it has been Fourier transformed. The transform variable, ξ, represents a wavenumber variable. The transformed equation of motion is

$$\frac{\partial^2 \overline{u}_y(\xi, z)}{\partial z^2} - \left(\xi^2 - k_s^2\right) \overline{u}_y(\xi, z) = 0 , \tag{2.33}$$

which has the general solution

$$\overline{u}_y(\xi, z) = A e^{-z\sqrt{\xi^2 - k_s^2}} + B e^{z\sqrt{\xi^2 - k_s^2}} . \tag{2.34}$$

In order to prevent unbounded solutions to Equation (2.34) the condition that the real part of the z coordinate coefficient must be positive is imposed, enabling the second term to be set to zero.

The transformed expression for the stress in Equation (2.30) is

$$\overline{\tau}_{yz}(\xi, z) = \mu \frac{\partial \overline{u}_y(\xi, z)}{\partial z} . \tag{2.35}$$

The transform applied to the non-trivial stress of Equation (2.26) is

$$\overline{\tau}_{yz}(\xi, z) = \frac{1}{\sqrt{2\pi}} \int_{-\infty}^{+\infty} \tau_0 \delta(x) e^{jx\xi} dx = \frac{\tau_0}{\sqrt{2\pi}} . \tag{2.36}$$

Applying the transformed boundary condition of Equation (2.35) to the general solution given in Equation (2.34) and substituting the transformed applied stress of Equation (2.36) gives the final integral equation to be solved in order to obtain the displacement of the half-space to be

$$u_y(x, z) = -\frac{\tau_0}{2\pi\mu} \int_{-\infty}^{+\infty} \frac{e^{-z\sqrt{\xi^2 - k_s^2}} e^{jx\xi}}{\sqrt{\xi^2 - k_s^2}} d\xi \tag{2.37}$$

Solution of this equation is non-trivial, particularly as there is a square root in the denominator of the integrand. This causes the integrand to be a multi-valued function of the integration variable. Further complications arise due to infinite limits of the integration.

Two methods are available for the solution of this integral; one exact, and the other asymptotic. The exact solution is obtainable [64] by first considering the branch cuts resulting from the multi-valued properties on the integrand in Equation (2.37), then applying changes of variable, and finally applying standard integral results to obtain a solution in terms of Hankel functions. The asymptotic solution, although only valid in the far-field, uses the more general method of steepest descent. Whilst the exact solution may be preferable in this section, the method of steepest descent is introduced here as it is used in subsequent sections. The method is described in detail in Appendix A. A brief overview of the method is however justified, as it suffers from additional complexities that require modification in the more advanced applications in later sections.

The method of steepest descent is a method for the approximation of certain types of integral in the limit of a large value of a parameter within the integrand. In all the applications of the method within this thesis the large parameter is a radial distance from the source. Thus this method produces approximations to integrals that are valid in the far-field only. For the general consideration of the method, the integrals must be of the form

$$I = \int_C \mathrm{e}^{Rf(\xi)} g(\xi)\,\mathrm{d}\xi\,, \tag{2.38}$$

where ξ represents the integration variable, which may be complex, (the notation of the wavenumber variable is used for consistency with the featured applications), R the real parameter that takes a large value, $f(\xi)$ and $g(\xi)$ arbitrary functions, C the closed contour on the complex plane over which the integration is to be performed and I is the value of the integration. For example, in the case of Equation (2.37) the integration contour is along the entire real axis. This can be made into a closed contour by the addition of a semicircular contour of infinite radius in the upper half plane whose contribution can be made negligible by the application of Jordan's lemma.

As the argument of the exponential is complex the integrand will have both oscillatory and exponential behaviour, the latter of which must be decaying in order for the integral to remain bounded. The aim of the method of steepest descent is to deform the contour of integration so that it passes through a point which dominates the contribution to the integral. It is shown that this occurs at a saddle point within the function. The contour passes through this point so that it takes the steepest approach and descent from the point, thus ensuring that the main contribution to the integral comes

from the point itself. As the contour of integration can only be deformed through analytic regions of the complex function [120] without changing its value, singularities and branch points caused by multi-valued terms in the integrand must be accounted for. These are of particular significance when considering Rayleigh wave generation.

Application of the method of steepest descent to Equation (2.37) (see Appendix B for details) gives the resultant displacement function to be

$$u_y\left(R,t\right)=\frac{\tau_0}{\mu\sqrt{2\pi k_s R}}\mathrm{e}^{-\mathrm{j}\left(k_s R-\frac{3\pi}{4}\right)}\mathrm{e}^{\mathrm{j}\omega t}, \tag{2.39}$$

where the problem has been converted to spherical coordinates.

Several properties of the wave are evident. Firstly, the generated wave exhibits the properties of a shear wave, travelling with the shear wavespeed. The energy decay is proportional to the inverse of the radius, rather than the usual inverse square for the body wave. This is simply a consequence of the source being infinite in length [121]. Significantly, the displacement expression in Equation (2.39) is invariant with respect to the polar angle. The infinite SH source therefore produces horizontally polarised shear waves uniformly across the considered space.

As mentioned at the beginning of the solution of Equation (2.37), both the approximate method of steepest descent and a more specific exact solution are possible. The latter was chosen for its generality and applicability to later, more complicated, problems where no exact solution may be possible. For completeness the exact solution is [64]

$$u_y\left(R,t\right)=-\frac{\mathrm{j}\tau_0}{2\mu}\mathrm{H}_0^{(1)}\left(k_s R\right)\mathrm{e}^{\mathrm{j}\omega t}, \tag{2.40}$$

where $\mathrm{H}_0^{(1)}$ is a zeroth order Hankel function of the first kind. Using the asymptotic approximation of Hankel functions [122] that, for large generic variable κ,

$$\mathrm{H}_m^{(1)}\left(\kappa\right)\approx\sqrt{\frac{2}{\pi\kappa}}\mathrm{e}^{\mathrm{j}\left(\kappa-\frac{1}{4}\pi-\frac{1}{2}m\pi\right)}\left\{1-\frac{4m^2-1^2}{1!\left(8\mathrm{j}\kappa\right)}+\frac{\left(4m^2-1^2\right)\left(4m^2-3^2\right)}{2!\left(8\mathrm{j}\kappa\right)}-\ldots\right\}, \tag{2.41}$$

where m is the order of the Hankel function. Taking the far-field limit and therefore assuming first order small in the reciprocal of κ, Equation (2.40) becomes equal to the result of Equation (2.39), after minor rearrangement.

2.3.2 Point Vertical Source

The ultimate goal of this section on surface excitation of an elastic half space is the derivation and calculation of displacement functions and energy partition for a point shear horizontal source. To achieve this it is useful to first consider these quantities when the surface excitation is a point vertical excitation. The reasoning for this is two-fold; firstly this system is well documented in the literature. The two papers by Miller & Pursey [123, 124] are particularly useful, and their work lays the foundation for many others in the field. The second advantage of examination of a point vertical surface excitation is that due to the cylindrical symmetry of the problem the complexity of the derivation and the result are reduced, as there is necessarily no variation in the azimuthal surface coordinate. This is a simpler problem than the point SH case. In Section 2.3.2.1 the displacement components are given, along with a sketch of their derivation. Section 2.3.2.2 details the method for the acquisition of the ratios of energy partition from these displacements.

2.3.2.1 Displacement Components

Full details of the derivation are not given here, but can be obtained from case (c) of the first of Miller & Pursey's papers [123]. A vertically oscillating harmonic rigid source of radius a is located at the origin of the coordinate system and acts in the $\hat{\mathbf{z}}$ direction. The equations of motion are considered in terms of the wave potentials given in Equation (2.10) and expressed in the natural coordinate system from the problem: i.e. that of cylindrical polar coordinates. Hence, the displacement components are $\mathbf{u}\left(r,\theta,z\right)=u_r\hat{\mathbf{r}}+u_\theta\hat{\boldsymbol{\theta}}+u_z\hat{\mathbf{z}}$. Boundary conditions are provided by stipulating the normal and shear stresses at the surface. These are null stress everywhere (the free surface condition), except for the source location, where a vertical harmonic stress τ_0 is applied. As before, time dependency is suppressed and only reintroduced in the final expressions.

An integral solution is obtained by applying the Hankel transform to both the equations of motion and the boundary conditions in order to replace a spatial variable with a wavenumber variable, ξ. Solving the transformed equations with the transformed boundary conditions and applying the associated inverse transform gives the displacements to be

$$u_z = \frac{a\tau_0}{\mu}\int_0^\infty \frac{\mathrm{J}_1(\xi a)\sqrt{\xi^2 - k_p^2}}{F(\xi)}\left\{2\xi^2 \mathrm{e}^{-z\sqrt{\xi^2-k_s^2}} + \left(k_s^2 - 2\xi^2\right)\mathrm{e}^{-z\sqrt{\xi^2-k_p^2}}\right\}\mathrm{J}_0(\xi r)\,\mathrm{d}\xi\,, \qquad (2.42)$$

and

$$u_r = \frac{a\tau_0}{\mu}\int_0^\infty \frac{\mathrm{J}_1(\xi a)\xi}{F(\xi)}\left\{2\sqrt{\xi^2 - k_p^2}\sqrt{\xi^2 - k_s^2}\,\mathrm{e}^{-z\sqrt{\xi^2-k_s^2}} + \left(k_s^2 - 2\xi^2\right)\mathrm{e}^{-z\sqrt{\xi^2-k_p^2}}\right\}\mathrm{J}_1(\xi r)\,\mathrm{d}\xi\,, \qquad (2.43)$$

where the standard notation of J_m denoting an m$^{\text{th}}$ order Bessel function is used, and $F(\xi)$ is defined in Equation (2.18).

Comparing the displacement component integrals of Equations (2.42) and (2.43) with that of the infinite SH line source, given in Equation (2.37), it is apparent that some additional complexity has been introduced. Of interest is the presence of the function $F(\xi)$, which is associated with Rayleigh wave propagation. As this appears in the denominator of the integrand, singularities in the function will occur at wavenumber values equal to those for Rayleigh wave propagation.

As only point sources are of interest, rather than extended circular discs in Miller and Pursey's paper, the assumption of small source radius, a, compared to a wavelength is made. Application of the Taylor theorem, which states that a general function, $K(\kappa)$, can be approximated about a point, κ_0, as

$$K(\kappa)\big|_{\kappa\approx\kappa_0} = K(\kappa_0) + K'(\kappa_0)(\kappa - \kappa_0) + \frac{1}{2!}K''(\kappa_0)(\kappa - \kappa_0)^2 + \ldots \qquad (2.44)$$

where the single and double primes denote derivative and double derivate of the function with respect to the variable respectively, to a first order Bessel function for small argument ξa gives the approximation

$$\mathrm{J}_1(\xi a)\big|_{\xi a\approx 0} = \mathrm{J}_1(0) + \xi a\left.\frac{\mathrm{dJ}_1(\xi a)}{\mathrm{d}(\xi a)}\right|_{\xi a=0} + \ldots. \qquad (2.45)$$

Using the standard result [122]

$$\frac{\mathrm{dJ}_1(\xi a)}{\mathrm{d}(\xi a)} = \frac{1}{2}\left(\mathrm{J}_0(\xi a) - \mathrm{J}_2(\xi a)\right), \tag{2.46}$$

and the fact that for a null argument all Bessel functions equal zero, with the exception of zeroth ordered Bessel functions, which equal unity, Equation (2.45) reduces to

$$\mathrm{J}_1(\xi a)\big|_{\xi a \approx 0} \approx \frac{1}{2}\xi a\,. \tag{2.47}$$

In addition to this approximation, all wavenumbers are normalised with respect to the compressional wavenumber, k_p, to allow for direct comparison with the relevant literature. The ratio of the compressional to shear waves is defined as ε, where $\varepsilon = \sigma^{-1}$. Equations (2.42) and (2.43) thus become

$$u_z = \frac{a^2\tau_0}{2\mu}\int_0^\infty \frac{\xi\sqrt{\xi^2 - 1}}{F_0(\xi)}\left\{2\xi^2 \mathrm{e}^{-z\sqrt{\xi^2-\varepsilon^2}} + \left(\varepsilon^2 - 2\xi^2\right)\mathrm{e}^{-z\sqrt{\xi^2-1}}\right\}\mathrm{J}_0(\xi r)\,\mathrm{d}\xi\,, \tag{2.48}$$

and

$$u_r = \frac{a^2\tau_0}{2\mu}\int_0^\infty \frac{\xi^2}{F_0(\xi)}\left\{2\sqrt{\xi^2 - 1}\sqrt{\xi^2 - \varepsilon^2}\,\mathrm{e}^{-z\sqrt{\xi^2-\varepsilon^2}} + \left(k_2^2 - 2\xi^2\right)\mathrm{e}^{-z\sqrt{\xi^2-1}}\right\}\mathrm{J}_1(\xi r)\,\mathrm{d}\xi\,, \tag{2.49}$$

where

$$F_0(\xi) = \left(2\xi^2 - \varepsilon^2\right)^2 - 4\xi^2\sqrt{\xi^2 - 1}\sqrt{\xi^2 - \varepsilon^2}\,. \tag{2.50}$$

Equation (2.50) demonstrates the reason for the normalisation of the wavenumbers with respect to the compressional wavenumber, as now the modified Rayleigh equation, $F_0(\xi)$, is expressed in terms of ε and the argument variable, ξ, only. This is for later convenience in plotting expressions as a function of the Poisson's ratio only, and also for non-dimensionalising integration variables.

The branch points, caused by the occurrence of the radicals, are located at $\xi = \pm\varepsilon$ and $\xi = \pm 1$. It is necessary to prohibit the contour of integration from encircling the branch points; else discontinuities will be introduced into the integration. An appropriate choice of branch cuts is used in preference to

consideration of the multi-valued function as a composite of several Riemann sheets. Whilst the latter option does offer some additional physical insight [119], the concepts and details of mathematics involved [125] make the former option preferable in this circumstance.

The branch cuts are moved from the real axis by consideration of a damping term. This damping term can be removed by letting the damping tend to zero. The details of the branch cuts are not described in detail here as their contribution to the integral proves negligible in the asymptotic limit [123].

Solutions to the integral equations again proceeds via the method of steepest descent, and the results are accordingly valid in the far-field only. The method of steepest descent has been outlined in Appendix A and implemented in Appendix B for the case of the infinite SH source. A full application of the method for the point vertical source is not given here, as its application is similar to that for the infinite SH source, and is furthermore covered in detail in the literature [64, 123]. The main difference in the application is the presence of the singularity in the integrand caused by the zeros of the $F_0(\xi)$ function. This is discussed later in this section.

The two terms of each of the integrals of Equations (2.48) and (2.49) are considered separately and are expressed in the required form of Equation (2.38). Applying the method of steepest descent and for now ignoring the singularity, the body wave displacement components are found to be [123]

$$u_R = -\frac{a^2\tau_0}{2\mu}\frac{e^{-jk_pR}}{R}\frac{\cos\theta\left(\varepsilon^2 - 2\sin^2\theta\right)}{F_0\left(\sin\theta\right)}e^{j\omega t}, \tag{2.51}$$

and

$$u_\theta = -\frac{ja^2\tau_0\varepsilon^3}{2\mu}\frac{e^{-jk_sR}}{R}\frac{\sin 2\theta\sqrt{\varepsilon^2\sin^2\theta - 1}}{F_0\left(\varepsilon\sin\theta\right)}e^{j\omega t} \tag{2.52}$$

where the previously suppressed time dependence has been reintroduced, as this is the final form of the displacement expressions, and the coordinate system has been converted to spherical polar coordinates, with the usual notation of R denoting the radius and θ denoting the angle from the vertical ordinate. The azimuthal coordinate, φ, does not feature in either displacement component equation due to the symmetry of the vertical source about this axis.

Equations (2.51) and (2.52) represent the compressional and shear vertical waves generated by the source respectively. This is apparent from the longitudinal and transverse nature of the wave types.

The amplitude of the displacement is inversely proportional to the propagation distance. This is to be expected to maintain conservation of energy despite geometric attenuation. There is also complicated angular dependency, particularly as the function F_0 has an angular argument. The directivity patterns are considered in detail in Section 2.3.2.2.

Discussion now returns to the consequences of the singularity in the integrand of the exact displacement expressions to the application of the method of steepest descent. Both the saddle point, through which the contour must be deformed to pass through, and the singularity, occur on the real axis. Consideration of their respective locations [123] indicates that the contour will have to pass through the singularity if

$$\theta > \text{cosec}^{-1}\left(\xi_p\right), \tag{2.53}$$

or

$$\theta > \text{cosec}^{-1}\left(\frac{\xi_p}{\varepsilon}\right) \tag{2.54}$$

where ξ_p is the real root of the Rayleigh equation, and the choice of Equations (2.53) or Equations (2.54) depends on which term of the integrals of Equations (2.51) and (2.52) is being considered. Arbitrary deformation of an integration contour is permitted, provided that the contour does not self-intersect and only passes through analytic regions. This illustrated in Figures 2.4 (a) and (b). This shows the case of the deformation of an arbitrary contour, C, to C`, in the presence of a singularity. As a singularity is not analytic it is necessary to add a loop around the singularity. Provided the paths connecting the loop to the rest of the contour become arbitrarily close, their contributions to the integral will cancel and the integration loop can be treated in isolation to the deformed curve. Its contribution will be given by $2\pi j$ multiplied by the residue of the singularity. The problem thus reduces to the calculation of the residues of the integrands of Equations (2.48) and (2.49) [123].

The residues are straightforward to calculate as the evaluation is about a simple pole. Although the Rayleigh equation given does not factorise neatly, to demonstrate the fact that the pole is a simple one, it is noted that the third order equation produces three different roots. As no root is repeated, each of the associated poles must be simple. Calculating the residues of the singularities the integrals of the Equations (2.48) and (2.49), converting units of length back to un-normalised form, and using the asymptotic limit of the Bessel functions:

$$\mathrm{J}_m\left(\xi r\right) \to \sqrt{\frac{2}{\pi\xi r}}\mathrm{e}^{\mathrm{j}\left(\xi r-\frac{\pi}{4}-\frac{m\pi}{2}\right)}, \tag{2.55}$$

where m is the order of the Bessel function, the Rayleigh wave displacement components are found to be

$$u_z = \frac{a^2\tau_0\mathrm{e}^{-\mathrm{j}\frac{\pi}{4}}}{\mu F_0'\left(\xi_p\right)}\sqrt{\frac{\xi_p k_p\left(\xi_p^2-1\right)}{2\pi r}}\left\{2\xi_p^2 p\left(\xi_p\right)-\left(2\xi_p^2-\varepsilon^2\right)q\left(\xi_p\right)\right\}\mathrm{e}^{\mathrm{j}\left(\omega t-\xi_p k_p r\right)}, \tag{2.56}$$

and

$$u_r = \frac{-\mathrm{j}a^2\tau_0\mathrm{e}^{-\mathrm{j}\frac{\pi}{4}}}{\mu F_0'\left(\xi_p\right)}\sqrt{\frac{\xi_p^3}{2\pi r}}\left\{2\sqrt{\xi_p^2-1}\sqrt{\xi_p^2-\varepsilon^2}\,p\left(\xi_p\right)+\left(2\xi_p^2-\varepsilon^2\right)q\left(\xi_p\right)\right\}\mathrm{e}^{\mathrm{j}\left(\omega t-\xi_p k_s r\right)}, \tag{2.57}$$

where

$$p\left(\xi\right) = \mathrm{e}^{-k_p z\sqrt{\xi^2-\varepsilon^2}}, \tag{2.58}$$

and

$$q\left(\xi\right) = \mathrm{e}^{-k_p z\sqrt{\xi^2-1}} \tag{2.59}$$

Here the functions F_0', p and q are evaluated at $\xi = \xi_p$. As previously stated, the contribution from deforming the contour of integration around the branch points is negligible in the asymptotic limit, and is thus not considered here.

Whilst these displacement components have complicated dependency on the wavenumber, some important conclusions can still be drawn. Both Equations (2.56) and (2.57) represent propagating waves travelling away from the source and decaying by a factor $r^{-0.5}$. This corresponds to an energy reduction inversely proportional to the propagation distance. This is to be anticipated for surface wave propagation due to conservation of energy. The surface nature of the wave is further confirmed by noting that both displacement components of the wave decay exponentially with respect to the depth coordinate, and that this effect increases for increasing wavenumber.

2.3.2.2 Energy Partition

When considering seismic sources it is desirable to evaluate the relative efficiency of the sources at producing different wave types. Consideration therefore moves to calculation of the different amounts of the total energy supplied to the system by each wave type. The derivation from the literature is outlined here, and the results given in preparation for application to other source types.

The intensities for the compressional, shear, and surface waves are given respectively as [124]

$$\Psi_P = -\frac{1}{2}\frac{\partial u_R}{\partial t}\tau^*_{RR}, \tag{2.60}$$

$$\Psi_{SV} = -\frac{1}{2}\frac{\partial u_\theta}{\partial t}\tau^*_{R\theta}, \tag{2.61}$$

$$\Psi_{RAY} = -\frac{1}{2}\frac{\partial u_z}{\partial t}\tau^*_{zr} - \frac{1}{2}\frac{\partial u_r}{\partial t}\tau^*_{rr}. \tag{2.62}$$

where asterisks denotes complex conjugation and P, SV and RAY denotes quantities associated with compressional, shear vertical and Rayleigh waves respectively. Using Equations (2.28) and (2.29) to obtain expressions for the stress components from the displacements of Equations (2.51), (2.52), (2.56) and (2.57) the intensities are found to be

$$\Psi_P = \frac{\omega^2 a^4 \varepsilon^4 \tau_0^2}{8\rho c_p^3 R^2}\left|\frac{\cos\theta\left(\varepsilon^2 - 2\sin^2\theta\right)}{F_0\left(\sin\theta\right)}\right|^2, \tag{2.63}$$

$$\Psi_{SV} = \frac{\omega^2 a^4 \varepsilon^9 \tau_0^2}{8\rho c_p^3 R^2}\left|\frac{\sin 2\theta\sqrt{\varepsilon^2\sin^2\theta - 1}}{F_0\left(\varepsilon\sin\theta\right)}\right|^2, \tag{2.64}$$

$$\Psi_{RAY} = \frac{\omega^2 a^4 \varepsilon^2 \tau_0^2}{2\rho c_p^3 r} X\left(k_p z\right), \tag{2.65}$$

where

$$X\left(k_p z\right)=\frac{\pi\left(2\xi_p^2-\varepsilon^2\right)}{4\left(F_0^{'}\left(\xi_p\right)\right)^2}\Big[4\xi_p^2\left(\xi_p^2-1\right)\left\{2\xi_p^2 p\left(\xi_p\right)-\left(2\xi_p^2-\varepsilon^2\right)q\left(\xi_p\right)\right\}\left(p\left(\xi_p\right)-q\left(\xi_p\right)\right)$$
$$+\left(2\xi_p^2-\varepsilon^2\right)\left\{\left(2\xi_p^2-\varepsilon^2\right)p\left(\xi_p\right)-2\xi_p^2 q\left(\xi_p\right)\right\} \tag{2.66}$$
$$\times\left\{\left(2\xi_p^2-\varepsilon^2\right)p\left(\xi_p\right)-\left(2\xi_p^2+\varepsilon^2-2\right)q\left(\xi_p\right)\right\}\Big],$$

These terms contain the non-dimensional variable $k_p z$ that determines the value of the function for a given Poisson's ratio. Only the terms which dominate in the far-field have been used in this derivation; all terms which decay faster than the inverse of the radius are discarded. Whilst the function $X\left(k_p z\right)$ is complicated, it is composed of various multiples of decaying exponentials and its numerical calculation is thus straightforward.

The expressions for the power radiated in each of these wave types can be found by integrating the appropriate intensity expression. For the compressional and shear waves this integration will be over a spherical shell, and for the Rayleigh wave it will be over a cylindrical shell. In both systems there is no azimuthal angular dependence, and the radial factor of the integration volume element cancels with the radial dependency of the intensity. This is in accordance with energy propagation in a system without damping – regardless of the propagation distance; the total energy remains the same. Using the same subscripts as before, denoting radiated power by W, and with area element $R^2\sin\theta d\theta d\varphi$ in the spherical coordinate systems, the radiated body wave powers are found to be

$$W_P=\frac{\pi\omega^2 a^4\tau_0^2}{2\rho c_p^3}\int_0^{\frac{\pi}{2}}\left|\frac{\cos\theta\left(\varepsilon^2-2\sin^2\theta\right)}{F_0\left(\sin\theta\right)}\right|^2\varepsilon^4\sin\theta\,\mathrm{d}\theta\,, \tag{2.67}$$

and

$$W_{SV}=\frac{\pi\omega^2 a^4\tau_0^2}{2\rho c_p^3}\int_0^{\frac{\pi}{2}}\left|\frac{\sin2\theta\sqrt{\varepsilon^2\sin^2\theta-1}}{F_0\left(\varepsilon\sin\theta\right)}\right|^2\varepsilon^9\sin\theta\,\mathrm{d}\theta\,. \tag{2.68}$$

Numerical evaluation of these integrals is simple to achieve using sufficient discretisation of the angular variable to allow for convergence of the integral. The surface wave case is slightly more complicated, and, by integrating over a cylindrical shell with area element $r^2 dz d\varphi$, is given by

$$W_{RAY} = \frac{\pi\omega^2 a^4 \tau_0^2}{2\rho c_P^3} \int_0^\infty 2\varepsilon^2 X\left(k_p z\right) \mathrm{d}\left(k_p z\right), \tag{2.69}$$

where the compressional wavenumber has been included within the integration variable so that the integration produces a non-dimensional constant. Difficulty in obtaining a solution to this integral arises from the numerical calculation of the real root of the denominator, ξ_p. A simple search algorithm is used, and the value of the derivative of the Rayleigh equation at this point calculated from the formula

$$F_0'\left(\xi_p\right) = 8\xi_p \left\{ \left(2\xi_p^2 - \varepsilon^2\right) - \frac{\left(2\xi_p^2 - \varepsilon^2\right)^2}{4\xi_p^2} - \frac{2\xi_p^4\left(2\xi_p^2 - \varepsilon^2 - 1\right)}{\left(2\xi_p^2 - \varepsilon^2\right)^2} \right\}. \tag{2.70}$$

Expanding the function $X\left(k_p z\right)$ and integrating gives

$$\begin{aligned} \int_0^\infty 2\varepsilon^2 X\left(k_p z\right) \mathrm{d}\left(k_p z\right) = \frac{\pi\varepsilon^2\left(2\xi_p^2 - \varepsilon^2\right)}{2\left|F_0'\left(\xi_p\right)\right|^2} \Bigg\{ & \frac{8\xi_p^4\left(\xi_p^2 - 1\right) + \left(2\xi_p^2 - \varepsilon^2\right)^3}{2\sqrt{\xi_p^2 - \varepsilon^2}} \\ & + \frac{4\xi_p^2\left(\xi_p^2 - 1\right) + 2\xi_p^2\left(2\xi_p^2 - \varepsilon^2\right)^3\left(2\xi_p^2 + \varepsilon^2 - 2\right)}{2\sqrt{\xi_p^2 - 1}} \\ & + \frac{4\xi_p^2\left(\xi_p^2 - 1\right)\left(4\xi_p^2 - \varepsilon^2\right) + \left(2\xi_p^2 - \varepsilon^2\right)^2\left(4\xi_p^2 + \varepsilon^2 - 2\right)}{\sqrt{\xi_p^2 - \varepsilon^2} + \sqrt{\xi_p^2 - 1}} \Bigg\}. \end{aligned} \tag{2.71}$$

Whilst Equation (2.71) is not small, it is a function of the Poisson's ratio only.

A Poisson's ratio of $\nu = 0.25$ is assumed for the purpose of comparison with Miller & Pursey's paper. Equations (2.67-69) then give

$$W_P = 0.333 \frac{\pi\omega^2 a^4 \tau_0^2}{\rho c_P^3}, \tag{2.72}$$

$$W_{SV} = 1.246 \frac{\pi\omega^2 a^4 \tau_0^2}{\rho c_P^3}, \tag{2.73}$$

$$W_{RAY} = 3.258 \frac{\pi \omega^2 a^4 \tau_0^2}{\rho c_p^3}. \qquad (2.74)$$

Thus the division of the total power radiated between the differing wave types is 67% into the Rayleigh wave, 26% into the shear wave and 7% into the compressional wave. This is in accordance with the well referenced results for a point vertical source [126].

In addition to the results presented for a single value of the Poisson's ratio, it is informative to consider these percentages as a function of the material properties. This was not performed in Miller & Pursey's papers [123], presumably because of the computational limitations when it was written. Note that in all following figures where expressions are plotted as a function of the Poisson's ratio, the highest Poisson's ratio shown is $\nu = 0.45$. This is because some of the expressions become infinite as the Poisson's ratio approaches its maximum value of one half. This behaviour is discussed below.

Figure 2.5 shows a plot of the percentage division of the total power radiated between the different wave types over a range of Poisson's ratio values. With increasing Poisson's ratio the amount of energy in the shear wave component of the motion increases relative to the compressional and Rayleigh wave components. The variation of the energy division with respect to the Poisson's ratio is substantial, with the ratio of the energy in the Rayleigh wave to that in the shear wave changing from 4.1 to 1.4 over the range of Poisson's ratio considered.

Figure 2.6 shows the variation of Equations (2.72-74) with respect to the Poisson's ratio, normalised by their common coefficient. The shear and Rayleigh wave coefficients increase in an unbounded manner with the Poisson's ratio, whilst the compressional wave coefficient falls with increasing Poisson's ratio. The increasing energy in the shear and Rayleigh waves is caused by the dependency of the displacements associated with their behaviour on the quantity ε. This is the ratio of the shear to compressional wavenumbers, which is equal to the ratio of the compressional to shear wavespeeds. Compressional wavespeeds become infinite as the Poisson's ratio approaches its maximum value of one half. This is because for this value of the Poisson's ratio the material is incompressible, and thus any compressional disturbance is propagated instantly through the medium. The unbounded behaviour observed in Figure 2.6 is a result of this.

As ε becomes large, there will be more oscillations of the angular displacement per unit distance than the compressional, with this ratio becoming infinite. The expressions for the stresses, which are necessary for the calculation of the radiated power, include the derivative of the displacements with

respect to the radial variable. Due to the more rapid spatial oscillations this further increases the energy in the shear wave relative to that in the compressional wave.

These observations explain the relative increase in the shear wave energy relative to the compressional wave energy. The Rayleigh wave displacements have been given in Equations (2.56) and (2.57). The Rayleigh wave is a composite of both shear and compressional motion, and can therefore be expected to also increase in an unbounded manner. This is observed, albeit with a slower increase in the energy coefficient in Figure 2.6 compared to the shear wave case; hence the decrease of the Rayleigh wave energy relative to the shear wave energy.

The directivity of the source is also considered. The polar dependence of the body waves is complicated, and varies with the Poisson's ratio of the material. Polar plots of the directivity are obtained by numerical calculation of Equations (2.63) and (2.64) as a function of the polar angle. The resultant plots are shown in Figures 2.7 (a) and (b) for the P and SV waves respectively.

Both body waves have zero amplitude both on the surface and directly below the source. The lack of body wave propagation over the surface is a consequence of the far-field limit that has been assumed, as body waves decay faster over the surface than when propagating through the ground [121, 126]. Physically this can be attributed to the coupling of coupling of the P and SV wave types at the free surface. Waves propagating along the free surface suffer from mode conversion, with the new wave type radiated back down into the medium [127].

2.3.3 Point SH Source

Attention is now focused on the application of the methods of the previous section to the problem of a point SH source on the surface of the ground. The result can be anticipated to vary substantially from the case of the infinite SH line source presented in Section 2.3.1, as the displacement functions now vary in the azimuthal direction. The structure of this section is analogous to that for the point vertical source, with Section 2.3.3.1 dealing with the displacement components generated by the source and Section 2.3.3.2 with the resultant energy partition between the various wave types produced by the source. The expressions for the displacement components are taken from the literature, whilst the energy partition is derived from stated formulae.

2.3.3.1 Displacement Components

The integral equations for the displacement components for the point SH source are stated in this section, with readers referred to the literature [127, 128] for full details. Due to the relaxation on the

symmetry of the problem there are three displacement components. In a cylindrical coordinate system, with the source excitation parallel to the surface in the direction of $\varphi = 0$, these are given by the integrals

$$\begin{aligned} u_r\left(r,\varphi,z\right) = \frac{a\tau_0}{\mu}\cos\varphi\Bigg\{ & -\int_0^\infty \frac{2\xi\sqrt{\xi^2 - k_s^2}}{F\left(\xi\right)}\sin\left(\xi a\right)\frac{\partial}{\partial r}\left[\mathrm{J}_1\left(\xi r\right)\right]\mathrm{e}^{-z\sqrt{\xi^2-k_p^2}}\,\mathrm{d}\xi \\ & + \int_0^\infty \frac{\sin\left(\xi a\right)}{r\xi\sqrt{\xi^2 - k_s^2}}\mathrm{J}_1\left(\xi r\right)\mathrm{e}^{-z\sqrt{\xi^2-k_s^2}}\,\mathrm{d}\xi \\ & + \int_0^\infty \frac{\sqrt{\xi^2 - k_s^2}\left(2\xi - k_s^2\right)}{\xi F\left(\xi\right)}\sin\left(\xi a\right)\frac{\partial}{\partial r}\left[\mathrm{J}_1\left(\xi r\right)\right]\mathrm{e}^{-z\sqrt{\xi^2-k_s^2}}\,\mathrm{d}\xi\Bigg\}, \end{aligned} \tag{2.75}$$

$$\begin{aligned} u_\varphi\left(r,\varphi,z\right) = \frac{a\tau_0}{\mu}\cos\varphi\Bigg\{ & -\int_0^\infty \frac{2\xi\sqrt{\xi^2 - k_s^2}}{F\left(\xi\right)}\sin\left(\xi a\right)\frac{\mathrm{J}_1\left(\xi r\right)}{r}\mathrm{e}^{-z\sqrt{\xi^2-k_p^2}}\,\mathrm{d}\xi \\ & + \int_0^\infty \frac{\sin\left(\xi a\right)}{\xi\sqrt{\xi^2 - k_s^2}}\frac{\partial}{\partial r}\left[\mathrm{J}_1\left(\xi r\right)\right]\mathrm{e}^{-z\sqrt{\xi^2-k_s^2}}\,\mathrm{d}\xi \\ & + \int_0^\infty \frac{\sqrt{\xi^2 - k_s^2}\left(2\xi - k_s^2\right)}{\xi F\left(\xi\right)}\sin\left(\xi a\right)\frac{\mathrm{J}_1\left(\xi r\right)}{r}\mathrm{e}^{-z\sqrt{\xi^2-k_s^2}}\,\mathrm{d}\xi\Bigg\}, \end{aligned} \tag{2.76}$$

and

$$\begin{aligned} u_z\left(r,\varphi,z\right) = \frac{a\tau_0}{\mu}\sin\varphi\Bigg\{ & \int_0^\infty \frac{2\xi\sqrt{\xi^2 - k_s^2}}{F\left(\xi\right)}\sin\left(\xi a\right)\mathrm{J}_1\left(\xi r\right)e^{-z\sqrt{\xi^2-k_s^2}}\,\mathrm{d}\xi \\ & - \int_0^\infty \frac{\xi\left(2\xi - k_s^2\right)}{F\left(\xi\right)}\sin\left(\xi a\right)\mathrm{J}_1\left(\xi r\right)e^{-z\sqrt{\xi^2-k_s^2}}\,\mathrm{d}\xi\Bigg\}. \end{aligned} \tag{2.77}$$

It can be seen that whilst the equations are more complex than the equivalent equations for the point vertical source, their form is similar. The method of steepest descent can be applied as before in order to obtain the displacement components for the body wave motion. This gives the far-field body wave displacements components to be [127]

$$u_R = \frac{a^2\tau_0}{\mu}k_p^4\frac{\sqrt{\varepsilon^2 - \sin^2\theta}}{F\left(-k_p\sin\theta\right)}\sin 2\theta\frac{\mathrm{e}^{-\mathrm{j}\left(k_p R - \omega t\right)}}{R}\sin\varphi\,, \tag{2.78}$$

$$u_\theta = \frac{a^2\tau_0}{\mu} k_s^4 \frac{\cos\theta\cos 2\theta}{F\left(-k_s\sin\theta\right)} \frac{\mathrm{e}^{-\mathrm{j}\left(k_s R-\omega t\right)}}{R}\sin\varphi\,, \tag{2.79}$$

$$u_\varphi = \frac{a^2\tau_0}{\mu} \frac{\mathrm{e}^{-\mathrm{j}\left(k_s R-\omega t\right)}}{R}\cos\varphi\,. \tag{2.80}$$

where, as in the point vertical case, the conversion to spherical coordinates has been made as this is the natural coordinate system in which to consider body wave propagation. The wave amplitudes are inversely proportional to the distance because of energy conservation. The displacement components also represent propagating waves with wavespeeds of compressional (Equation (2.78)) and shear (Equations (2.79) and (2.80)) respectively.

When considering the Rayleigh wave displacements, the singular contribution to the integrals in Equations (2.75-77) comes from the $F\left(\xi\right)$ function. This is identical to that from the point vertical excitation, and is not surprising considering this function has already been associated with Rayleigh wave propagation. As for point vertical excitation, Rayleigh wave displacements can be found by evaluation of the residue of the pole associated with the real root of the Rayleigh equation in the denominator. For consistency with the preceding work, the Rayleigh pole is derived from the normalised Rayleigh equation, $F_0\left(\xi\right)$, so that that the resulting root ξ_p is a non-dimensional constant. This poses no problem provided the factors of k_p are reintroduced correctly. Equations (2.41) and (2.46) can also be used in conjunction to first find the derivative of the Bessel function that appears some of the integrals, and then the asymptotic limit of this derivative.

Considering only the dominant far-field terms and applying the normalisations and Bessel function limits as described, the Rayleigh wave displacement components are found to be

$$u_r = -\mathrm{j}\frac{a^2\tau_0}{\mu F_0^{'}\left(-\xi_p\right)} \mathrm{e}^{-\mathrm{j}\frac{\pi}{4}} \sin\varphi\sqrt{\frac{2\xi_p k_p}{\pi r}}\sqrt{\xi_p^2-\varepsilon^2}\left(2\xi_p^2 q\left(\xi_p\right) - \left(2\xi_p^2-\varepsilon^2\right)p\left(\xi_p\right)\right)\mathrm{e}^{-\mathrm{j}\left(k_p\xi_p r-\omega t\right)}\,, \tag{2.81}$$

and

$$u_z = -\frac{a^2\tau_0}{\mu F_0^{'}\left(\xi_p\right)} \mathrm{e}^{-\mathrm{j}\frac{\pi}{4}} \sin\varphi\sqrt{\frac{2\xi_p k_p}{\pi r}}\xi_p\left(2\sqrt{\xi_p^2-1}\sqrt{\xi_p^2-\varepsilon^2}\,q\left(\xi_p\right) - \left(2\xi_p^2-\varepsilon^2\right)p\left(\xi_p\right)\right)\mathrm{e}^{-\mathrm{j}\left(k_p\xi_p r-\omega t\right)}\,. \tag{2.82}$$

2.3.3.2 Energy Partition

The expressions for the energy remain unchanged from the Equations (2.60-62), with the exception that an additional energy calculation is now required for the energy propagating in the SH wave. Consideration of the motion of a spherical SH wave implies that the intensity is given by

$$\Psi_{SH} = -\frac{1}{2}\frac{\partial u_{\varphi}}{\partial t}\tau^{*}_{R\varphi}\,. \tag{2.83}$$

Substitution of the body wave displacements from Equation (2.78-80) into the intensity expressions of Equations (2.60), (2.61) and (2.83) gives the intensities as

$$\Psi_{P} = \frac{a^4\tau_0^2\omega^2\varepsilon}{2c_s^3\rho}\sin^2\varphi\frac{\sin^2 2\theta\left(\varepsilon^2 - \sin^2\theta\right)}{R^2\left|F_0\left(\sin\theta\right)\right|^2}, \tag{2.84}$$

$$\Psi_{SV} = \frac{a^4\tau_0^2\omega^2}{2c_s^3\rho}\sin^2\varphi\frac{\cos^2\theta\cos^2 2\theta}{R^2\left|F_0\left(\varepsilon\sin\theta\right)\right|^2}, \tag{2.85}$$

$$\Psi_{SH} = \frac{a^4\tau_0^2\omega^2}{2c_s^3\rho}\frac{\cos^2\varphi}{R^2}\,. \tag{2.86}$$

To obtain the power radiated from the source the intensity expressions are again integrated over a semi-spherical shell. Prior to this integration though, it is informative to note the directivity patterns of the wave types. Both the shear vertical and compressional waves have identical dependence with respect to the azimuth, as may be expected from the close association between the two waves in terms of their origins in the equations of motion; specifically in the decoupling of the potentials. The intensity of these wave types is maximal in the direction parallel to the movement of the source, and zero perpendicular to the movement of the source. This is physically intuitive.

The shear horizontal wave type shows the opposite azimuthal behaviour to the compressional and shear vertical waves, with the shear horizontal wave intensity at a maximum perpendicular to the direction of the motion of the source, and progressively reducing to zero parallel to the source. The directivity is also independent of the angle to the vertical. This is consistent with the result of the infinite SH line source given in Equation (2.39), and this consistency is to be expected given the similarity of the problem in this plane.

The azimuthal dependence presents no problem when integrating to find the radiated powers. The dependence on the polar angle to the vertical, whilst complicated, is easily integrated numerically. The resulting expressions for the power radiated are given by

$$W_P = \frac{a^4 \tau_0^2 \omega^2 \pi}{c_s^3 \rho} \int_0^{\frac{\pi}{2}} \varepsilon \frac{\sin^2 2\theta \left(\varepsilon^2 - \sin^2 \theta\right) \sin\theta}{\left|F_0\left(\sin\theta\right)\right|^2} \mathrm{d}\theta, \tag{2.87}$$

$$W_{SV} = \frac{a^4 \tau_0^2 \omega^2 \pi}{c_s^3 \rho} \int_0^{\frac{\pi}{2}} \frac{\cos^2 \theta \cos^2 2\theta}{\left|F_0\left(\varepsilon \sin\theta\right)\right|^2} \sin\theta \mathrm{d}\theta, \tag{2.88}$$

$$W_{SH} = \frac{a^4 \tau_0^2 \omega^2 \pi}{c_s^3 \rho}. \tag{2.89}$$

The polar directivity of the P and SV waves are shown in Figure 2.8. The P wave directivity is similar to the point vertical source case, except that now the directivity is zero directly below the source. The SV wave is directional, with the energy concentrated in a narrow angular range. Confidence in the polar dependency is obtained by comparison with the case of an infinite line stress applied tangentially to the surface and the axis of the source. This case was also considered in Miller & Pursey [123], with both the radial and polar displacements (and thus P and SV intensities) having identical polar directivity patterns to those given in Equation (2.87) and (2.88). This is to be expected, as for a zero azimuthal angle (i.e. in the direction of source excitation) these source distributions become indistinguishable in terms of the polar variable.

Consideration is now given to the case of the surface Rayleigh waves. The procedure for calculation is as the point vertical case. Using the expressions for the Rayleigh wave intensity from Equation (2.62) gives

$$\Upsilon_{RAY} = \frac{a^4 \tau_0^2 \omega^2}{c_s^3 \rho} \frac{k_p}{2\pi r} \sin^2 \varphi \frac{\xi_p^2}{\left|F_0'\left(\xi_p\right)\right|^2} \left[\alpha_1 q\left(\xi_p\right)^2 + \alpha_2 p\left(\xi_p\right)^2 + \alpha_3 q\left(\xi_p\right) p\left(\xi_p\right)\right], \tag{2.90}$$

where

$$\alpha_1 = 2\xi_p^2 \left(\varepsilon^2 - 2\right)\left(\xi_p^2 - \varepsilon^2\right)\left(2\xi_p^2\left(\varepsilon^2 - 1\right) + 2\right) + 2\sqrt{\xi_p^2 - 1}\sqrt{\xi_p^2 - \varepsilon^2}\left(2\xi_p^2 - \varepsilon^2\right)^2,$$

$$\alpha_2 = \left(2\xi_p^2 - \varepsilon^2\right)^2 \left[\left(\varepsilon^2 - 1\right)\left(\varepsilon^2 - 2\right)\left(\xi_p^2 - \varepsilon^2\right) + \left(2\xi_p^2 - \varepsilon^2\right)\right],$$

$$\begin{aligned}\alpha_3 = \left(2\xi_p^2 - \varepsilon^2\right)^2 \Big[& 2\xi_p^2\left(\varepsilon^2 - 1\right)\left(\varepsilon^2 - 2\right)\left(\xi_p^2 - \varepsilon^2\right) + \left(2\xi_p^2\left(\varepsilon^2 - 1\right) + 2\right)\left(\varepsilon^2 - 2\right) \\ & + 2\sqrt{\xi_p^2 - 1}\sqrt{\xi_p^2 - \varepsilon^2}\left(2\xi_p^2 - \varepsilon^2\right) + \left(2\xi_p^2 - \varepsilon^2\right)\Big]\end{aligned}. \qquad (2.91)$$

Integrating over a cylindrical shell to obtain the radiated power leads to the final result

$$W_{RAY} = \frac{a^4 \tau_0^2 \omega^2 \pi}{c_s^3 \rho} \frac{\xi_p^2}{\pi \left|F_0'\left(\xi_p\right)\right|^2} \left[\frac{\alpha_1}{2\sqrt{\xi_p^2 - 1}} + \frac{\alpha_2}{2\sqrt{\xi_p^2 - \varepsilon^2}} + \frac{\alpha_3}{\sqrt{\xi_p^2 - 1} + \sqrt{\xi_p^2 - \varepsilon^2}}\right]. \qquad (2.92)$$

For comparison with previous work the specific case of $\nu = 0.25$ is considered, and the ratio of the radiated power in each of the propagating wave types is calculated. The shear horizontal wave dominates with 81% of the emitted energy, the shear vertical wave 13%, the compressional 5% and the Rayleigh only 1%. This can, as in the case of the point vertical source, be plotted as a function of the Poisson's ratio. This is shown in Figure 2.9. The energy partition between the different wave types shows some variation with respect to the Poisson's ratio, however the SH wave dominates at all Poisson's ratio values. As the Poisson's ratio increases the increase in the shear vertical motion at the expense of the compressional motion is apparent, as in the case of the point vertical source. As before, this is due to the material becoming incompressible and thus vertical compressions increasingly causing lateral motion which produces shear vertical waves.

2.4 Graphical Representation of the Source Properties

Properties of the generated wave types including wavespeeds, relative amplitudes, geometric attenuations and directivities, can be illustrated in an informative manner on a single diagram. Such a diagram has been constructed by Woods [126] for the point vertical source. A recreation of his figure is shown in Figure 2.10.

The three propagating wave types; Rayleigh, shear vertical and compressional, are shown, with a separation determined by their relative wavespeed. Hence the compressional wave front is significantly further from the source than either the shear or Rayleigh waves, whose wave fronts are at a similar distance from the source. The vertical and horizontal components of the Rayleigh wave are shown on the left and right hand side of the source respectively.

In all cases the thick line shows the location of the wave front. For the compressional and shear vertical waves, the thinner line associated the wave fronts shows the directivity of that wave type. As the Rayleigh wave has no polar directivity, the thinner lines instead show the shape of the variation of the amplitude of the Rayleigh wave displacement with depth. The phase of the shear vertical wave is reversed at certain angles and the horizontal component of the Rayleigh wave motion after a certain depth, with positive and negative signs labelling this.

Although the compressional and shear vertical waves have no surface component in the radiated power expressions of Equations (2.67) and (2.68), these expressions are only valid in the far-field. In the derivation of these expressions terms whose geometric attenuation was greater than the reciprocal of the radial distance from the source were neglected. For the illustrative purposes of Figure 2.10 a non-zero displacement is shown at the surface for both body waves. This is justified both to be in accordance with the aforementioned reference to original version of this figure by Woods, and also as the experimental work used in this thesis will be close enough to the source for non-far-field terms to be measurable.

It should be stressed that Figure 2.10 has, as was the original figure by Woods [126], been constructed to give a clear illustration of the relative properties of generated wave types. Accurate mathematical quantities should be taken from the derived expressions.

Similar diagrams are constructed for the point shear horizontal source. Multiple diagrams are required, however, due to the dependence of the propagating wave types on the azimuthal coordinate. Figures 2.11 and 2.12 show these for $\varphi=0$ and $\varphi=\pi/2$ respectively. For the first of these the same wave types as for the point vertical case are present; P, SV and Rayleigh waves. As these are the same types of wave propagation their geometric attenuations and relative wavespeeds are unchanged. Their directivities and relative amplitudes do however differ. This information has been stated previously in this section, and these figures are presented only to summarise the information in a clear way. For the case of the null azimuthal angle in Figure 2.12, the only wave type present is the SH wave, resulting in a simple figure. Of note is the geometric decay for the SH wave along the free surface; as the SH wave does not couple with other wave types there is no radiation of waves generated by mode conversion back into the medium. The SH wave therefore maintains its r^{-1} geometric attenuation along the surface.

For intermediate azimuthal angles all four wave types are present, with their relative amplitudes given by the trigonometric dependence on the azimuth. For example, at $\varphi=\pi/4$ the equivalent figure to

that shown in Figures 2.10 - 2.12 would simply be the overlay of Figures 2.11 and 2.12 scaled by $\sin(\pi/4) = \cos(\pi/4) = 1/\sqrt{2}$.

2.5 Limitations of the Theoretical Analysis

The theoretical work described in this chapter has several limitations. These stem both from the assumptions used in defining the mathematical model, and those used in the process of obtaining solutions. The consequences of the relaxation of these assumptions to an experimental environment are examined in this section.

The assumption that the medium is homogeneous and isotropic has been made throughout this analysis. In practice, however, the earth can exhibit a large degree of heterogeneity, on varying scales. The consequences of the large scale layering of the earth's structure has long been observed in global seismic data [129, 130] as the presence of an additional propagating wave type. This wave is referred to as a Love wave, and is a dispersive surface wave whose particle motion is SH in nature. The wave is a consequence of SH waves becoming trapped within the upper surface layers. Near surface heterogeneity is also present due to the sedimentary soil layering, unconsolidated media overlying a harder substrate, or the presence of a water table. This has been experimental observed to result in substantial variations in propagation wavespeeds in the near surface [101]. For the depths considered in the shallow near-surface work undertaken in this project it has been demonstrated by others authors that Love wave propagation is minimal and does not interfere with SH studies [131].

Heterogeneity within the media can also influence the wave types already described in this chapter. As both the compressional and shear wavespeeds are non-dispersive, and Equation (2.15) does not have any dependence on frequency, Rayleigh wave propagation in a semi-infinite homogenous elastic half space is also non-dispersive. In general, however, a real section of soil exhibits a layered sedimentary structure. The stiffness of these layers is likely to increase with increasing depth. As Rayleigh surface waves with longer wavelengths penetrate deeper into the ground they will propagate, on average, in stiffer media, and because of this propagate faster. This behaviour will be prominent once the wavelength becomes of the same order as the distance between geological layers, and so may not necessarily be evident in experimentation within the shallow top layer. This behaviour is experimentally observed and is the basis of methods such as the spectral analysis of surface waves (SASW) method [132, 133].

Throughout this chapter terms whose radial dependence decays rapidly have been assumed negligible to keep the mathematics tractable and enable solutions to be obtained. Consequently, the displacement

components, directivities and energy partitions are valid only in the idealised far-field limit. More specifically, the far-field limit is assumed with respect to two different parameters. The first of these is the wavelength of the generated waves and the second the dimensions of the source. The latter of these has been examined both theoretically and experimentally [134], and shown to only produce significant effects when the product of the wavenumber of the generated waves and the source dimensions are greater than unity. Whilst this is exceeded for the higher frequencies used later in the thesis, the effect is actually to increase the directivity of the source in a manner helpful to the desired application. The former of these parameters could only be relaxed by attempting numerical solutions to the Equations of the system.

As the experimental work in this thesis concerns relatively small propagation distances there is liable to be discrepancies between the theoretical and experimental results. For example, in certain circumstances it has been experimental observed that there is near-field coupling between the body waves [135], producing an additional wave type.

2.6 Conclusions

This chapter has given an analysis of an idealised mathematical model of the ground. The analysis is broadly split between a review of the basic types of wave propagation in the system under consideration in Section 2.2, and the examination of surface sources in Section 2.3.

Initially, the review of basic wave types considers an infinite elastic space so that the differential equation of motion of the system can be introduced and solved to describe compressional and shear wave propagation. A free surface is then introduced to model the surface of the ground and enable the additional surface (Rayleigh) wave propagation to be derived.

The analysis of surface sources in Section 2.3 begins with the simplest case; that of an infinite SH line source. This enables the introduction of the method of steepest descent for a simple problem. The case of a point vertical source is next considered, with expressions for the displacements of the different wave components used to obtain the relative amounts of energy in each generated wave type. Of interest in this thesis is the case of a point source moving parallel to the surface of the ground. Expressions for the displacement are taken, and from these the relative of amount of energy in each generated wave type derived.

In Section 2.4 the results for both the vertical and parallel source are displayed in the graphically concise manner used in the literature.

Finally, the limitations of the mathematical analysis are outlined. Provided the results of this chapter are used to build an understanding of the general system, rather than for accurate quantitative comparison with experimental data, these assumptions are not sufficiently detracted from reality to render the mathematical analysis irrelevant.

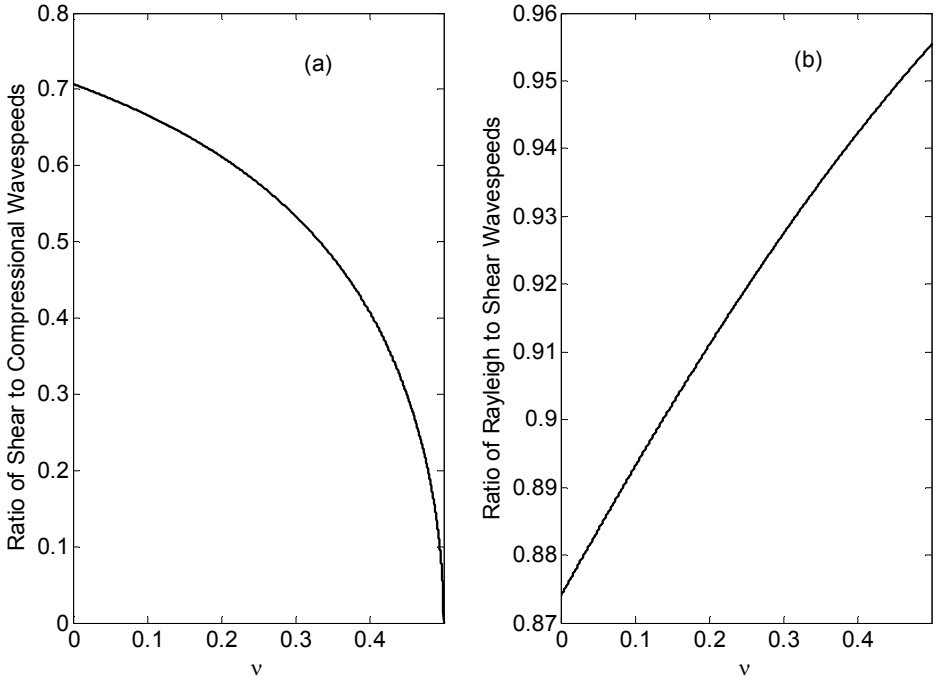

Figure 2.1 – (a) Plot of the ratio of the shear to compressional wavespeeds over the possible ranges of the Poisson's ratio and (b) plot of the Rayleigh to shear wavespeeds over the possible ranges of the Poisson's ratio.

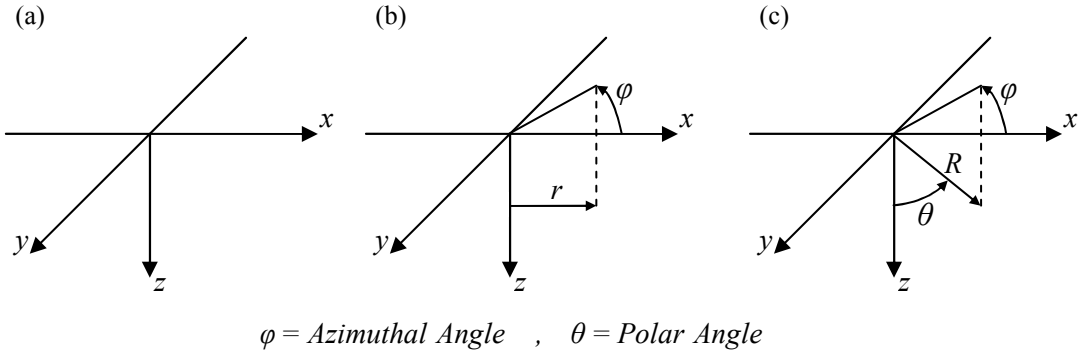

Figure 2.2 – Definitions of the three coordinate systems used in this chapter: (a) Cartesian ; (b) cylindrical polar; (c) spherical polar.

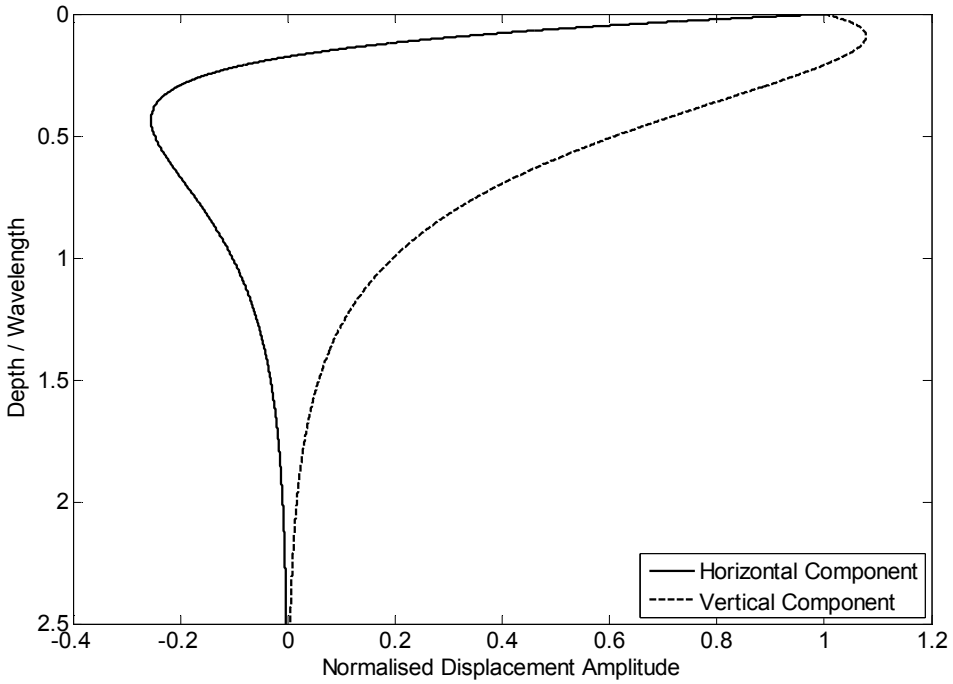

Figure 2.3 - Plot of the horizontal and vertical displacement components of a Rayleigh wave as a function of the depth to wavelength ratio, with $\nu = 0.25$. Both displacements are normalised to their respective surface values.

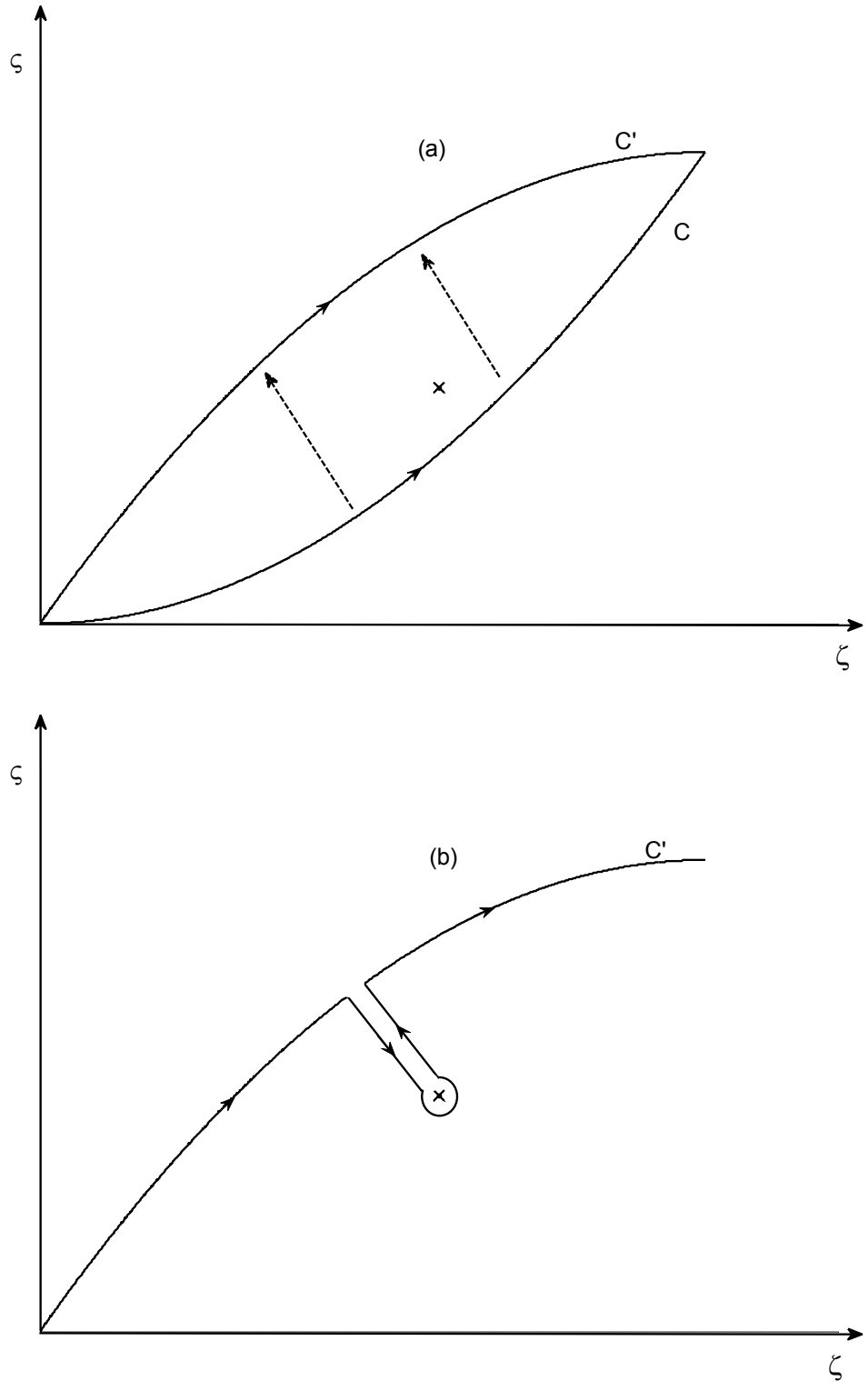

Figure 2.4 – (a) shows the deformation of a contour C to contour C`, passing through the singularity marked by the cross. (b) shows how the singularity can be encircled by the deformed contour such that the contour does not pass through non-analytic regions of the complex plane.

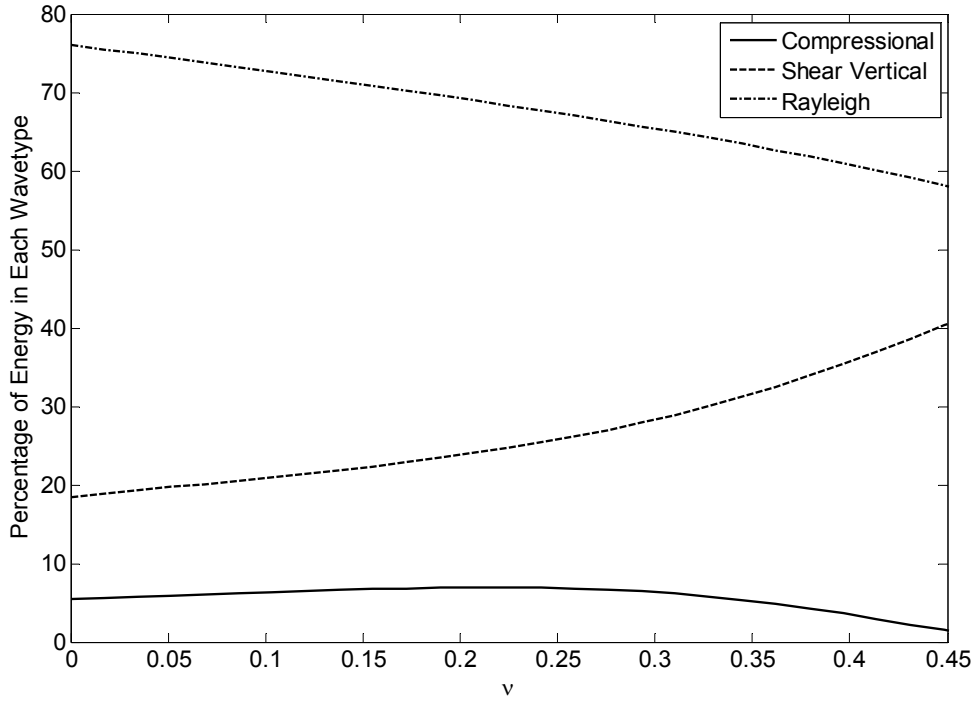

Figure 2.5 – Plot of the percentage division of the energy inputted by a point vertical source between the different wave types produced as a function of the Poisson's ratio of the material.

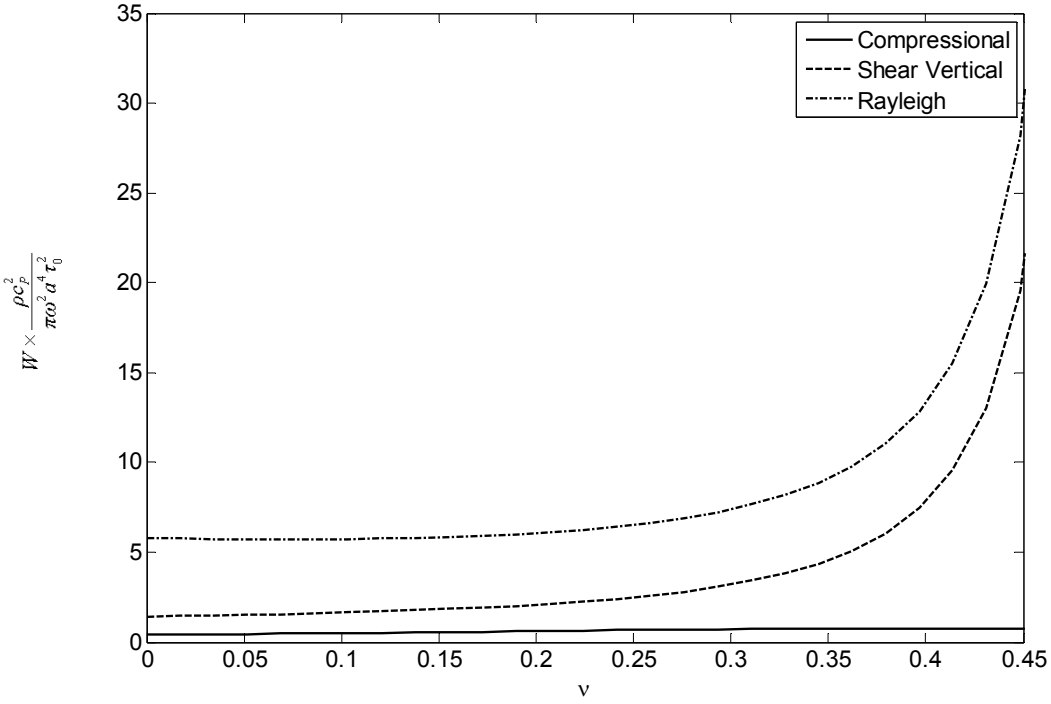

Figure 2.6 – Plot of the power emitted scaled by their common coefficient for the different wave types produced by a point vertical source as a function of the Poisson's ratio of the material. It is the ratio of these coefficients that is used to calculate the percentage of energy in each wave type in Figure 2.5.

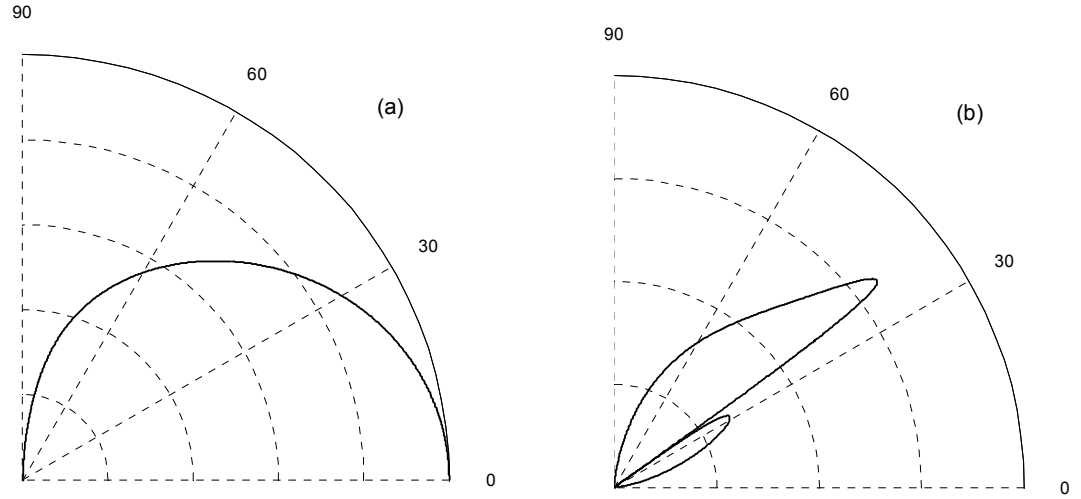

Figure 2.7 – Polar plots of the directivity of the radiated power of the (a) P and (b) SV wave energy intensities for the point vertical case for a Poisson's ratio of $\nu = 1/3$.

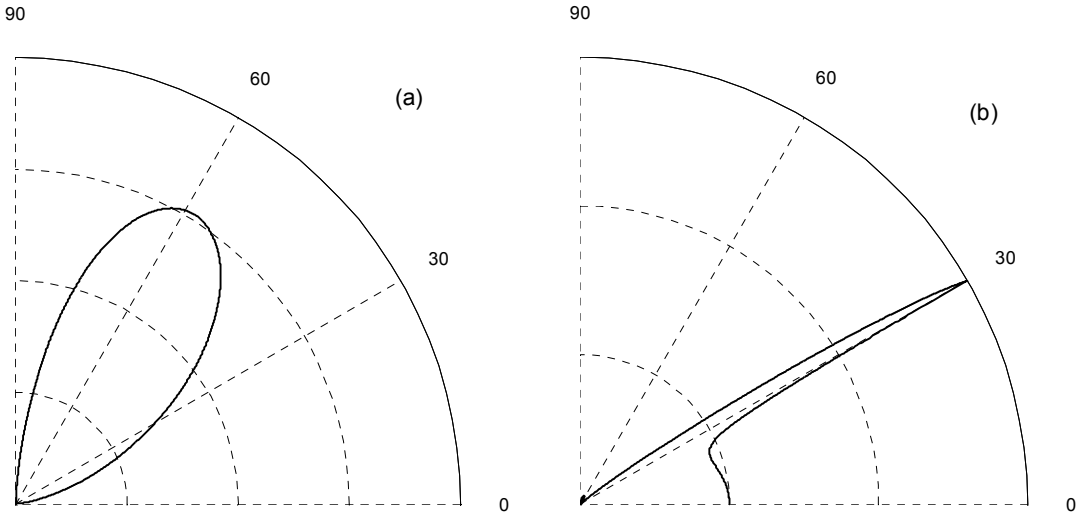

Figure 2.8 – Polar plots of the directivity of the radiated power of the (a) P and (b) SV wave energy intensities for the point source moving parallel to the surface for a Poisson's ratio of $\nu = 1/3$.

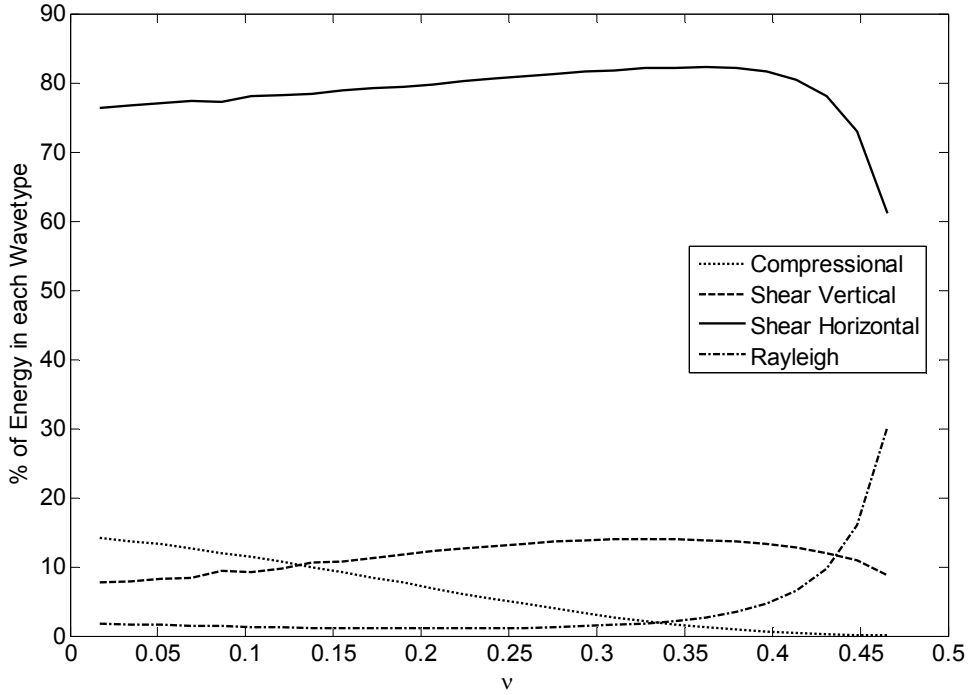

Figure 2.9 – Plot of the of the percentage division of the energy inputted by a point source moving parallel to the surface as a function of the Poisson's ratio of the material.

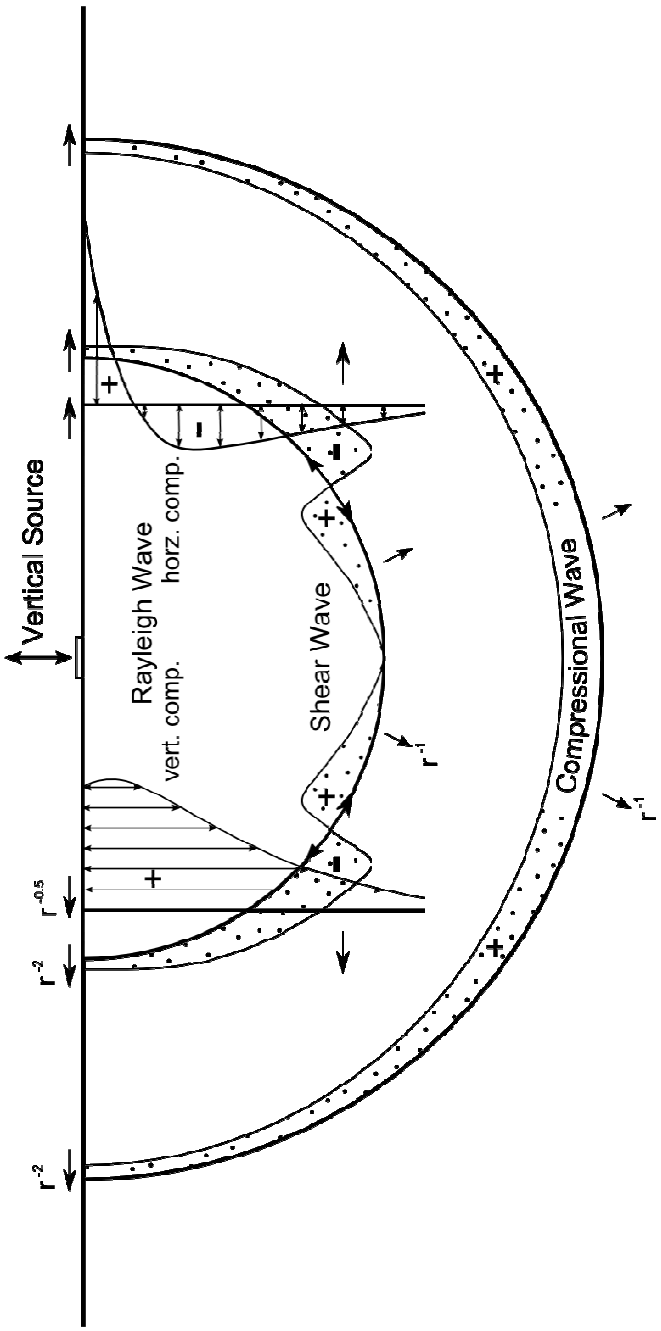

Figure 2.10 - Illustrative diagram of the wave types and their relative properties produced by a point vertical source. The thick black lines denote the location of the wave fronts, with their locations governed by their relative wavespeeds. For the compressional and shear vertical waves, the thin black line shows the directivity, with the distance between the thick and thin lines giving an indication of the relative amplitude of the displacements. The Rayleigh wave is broken into its vertical and horizontal components, shown on the left and right of the source respectively. Here the thin black lines show the variation of the wave amplitude with depth. The phase of the waves is shown by the positive and negative signs. The geometric attenuation values are labelled both in for propagation in the ground and over the surface. This example assumed $\nu = 0.25$ to correspond to the figure produced by Woods [126].

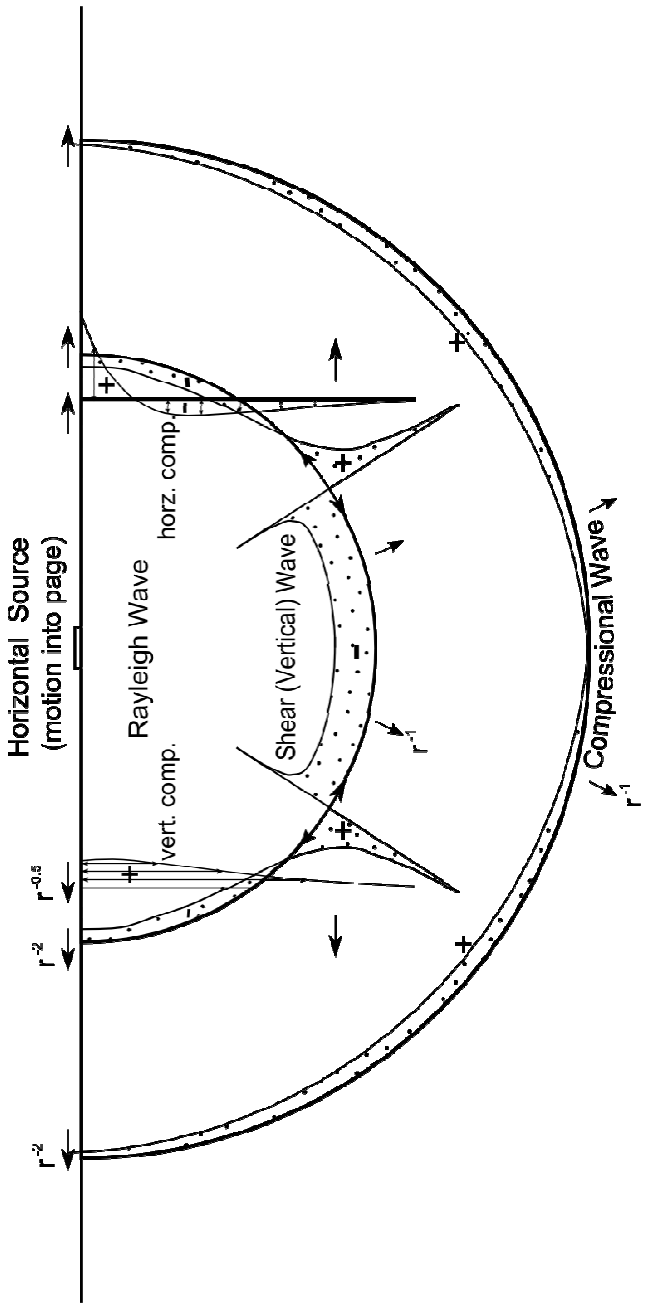

Figure 2.11 - Illustrative diagram of the wave types and their relative properties produced by a point SH source, with the source orientated parallel to the displayed plane ($\varphi = 0$). The motion of the source is into the page. The thick black lines denote the location of the wavefronts, with their locations governed by their relative wavespeeds. For the compressional and shear vertical waves, the thin black line shows the directivity, with the distance between the thick and thin lines giving an indication of the relative amplitude of the displacements. The Rayleigh wave is broken into its vertical and horizontal components, shown on the left and right of the source respectively. Here the thin black lines show the variation of the wave amplitude with depth. The phase of the waves is shown by the positive and negative signs. The geometric attenuation values are labelled both in for propagation in the ground and over the surface. This example assumed $\nu = 0.25$ to correspond to Figure 2.10.

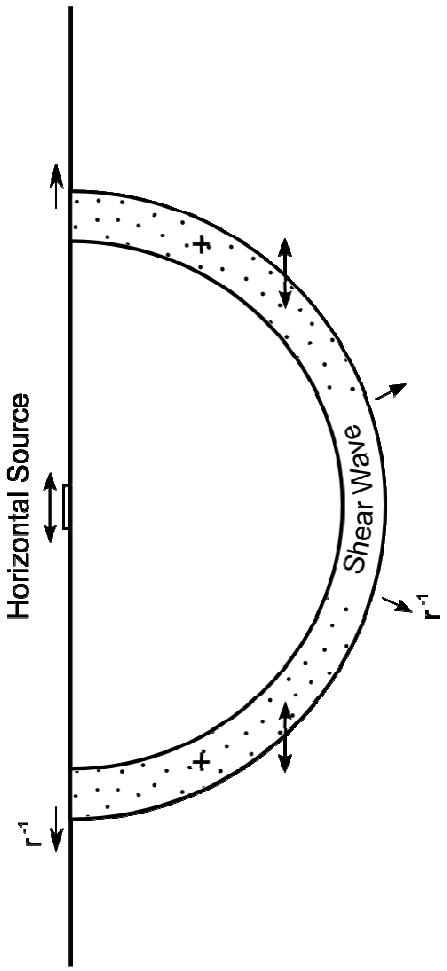

Figure 2.12 - Illustrative diagram of the SH wave and its properties produced by a point SH source, with the source is orientated perpendicular to the displayed plane ($\varphi = \pi/2$). The thick black line denotes the location of the wave front. The geometric attenuation values are labelled both in for propagation in the ground and over the surface. This example assumed $\nu = 0.25$ to correspond to Figure 2.11.

3. Imaging Methodology

Chapter 3

Imaging Methodology

3.1 Introduction

The aim of this chapter is to describe the concept and implementation of the imaging method used in this thesis. The imaging method has many similarities with the some of the methods used for imaging and target detection in the other applications reviewed in Chapter 1. Details of the method are discussed in Section 3.2 for the limited case of impulsive excitation. Here the basic experimental outline and post-processing are described, as well as justification for the selection the wave type used for investigation. The method is then expanded by the replacement of impulsive excitation with time-extended signals in Section 3.3. This is shown to mandate alterations to the basic methodology, such as the inclusion of cross-correlation functions. In Section 3.4 additional signal processing techniques used in the imaging method are detailed. These additional techniques are used to counter specific problems that occur from practical application of the imaging method, such as limited bandwidth of received signals and oscillations in the cross-correlation functions. Finally, conclusions are drawn in Section 3.5.

3.2 Overview of the Method

This section begins with an explanation of the experimental arrangement and post-processing used in the imaging method. For simplicity the imaging method is described using impulsive waveforms as excitation signals. The excitation signal is generalised in Section 3.3. This section also contains justification for the use of SH waves in the imaging method.

3.2.1 Imaging Method Using Impulses

The aim of the imaging method is to form a cross-sectional image through the ground in a plane perpendicular to the surface, with regions of high value on the image corresponding to the location of buried objects. The experimental setup used in the method is shown in Figure 3.1. It consists of an array of geophones, which define the image plane, and a vibrating source. All equipment is located on the surface. Similar experimental setups are used in seismic measurements aiming to detect both deeply buried hydrocarbon reserves [42] and shallow buried targets [103, 114]. Often an impulsive excitation is used; typically from a hammer strike. For the following discussion it is assumed that this is the case. Geophones measure the resulting vibrations which are digitised and stored for post-processing.

To form an image the distances from the source to sensor locations via each pixel on the image plane are first calculated. These are related to times of flight by the speed of the wave which is assumed to reflect from the target and propagate to the sensors. This wavespeed is estimated in-situ due to large variability of soil conditions between and within test sites.

Using the assumed wavespeed the geophone recordings at times corresponding to the calculated delay times are then summed at each pixel location to form an image. If the image pixel corresponds to a reflector then the contribution from each geophone should be larger and thus produce a peak in the image. If the image pixel does not correspond to location of a reflector then, whilst the contribution from an individual geophone may be maximal, the combined contribution of all geophones will not.

It should be noted that this method assumes a point-like target at the pixel location. Referring to Figure 3.1, the time interval, τ_i, for propagation between the source and *i*-th geophone via a pixel at (x,z) is

$$\tau_i = \frac{1}{c}\left\{\sqrt{(x - x_s)^2 + z^2} + \sqrt{(x - x_{g,i})^2 + z^2}\right\} \qquad (3.1)$$

where c denotes the assumed wavespeed, x_s the distance of the source from the origin and $x_{g,i}$ the distance of the *i*-th geophone from the origin.

To improve the quality of the image the location of the source can be moved and the measurement procedure repeated. The resultant images from the individual source locations are then summed to form a final image. This additional summing both increases the signal to noise ratio and reduces the

influence of anomalous dead spots in propagation caused by ground heterogeneities, although it obviously also increases the time taken to perform measurements.

It should be noted that for the practical implementation used in this thesis, far fewer sensors are used than in the techniques described in Sections 1.4 and 1.5.3. These methods rely on dense sensor arrays that are sufficiently closely spaced relative to the wavelengths of interest that spatial aliasing does not occur [53]. The algorithms used in these methods both combine the data prior to formation of the imaging and utilise spatial Fourier transforms to remove data from the measured signals. In both these circumstances geophone spacing must exceed the familiar Nyquist limit. In the method described in this thesis the array is arranged such that it is under sampled. This is not problematic as the data is only combined when images have already been formed, and spatial Fourier transforms are applied only to the final image and not measured signals.

3.2.2 Selection of Imaging Method Wave Type

The imaging method only allows for one type of wave propagation in the ground. In practice there will potentially be at least three waves propagating: shear, compressional and Rayleigh waves. Additional types of wave propagation, such as Biot waves [85], may occur, but as these depend on the soil type they are excluded from the current analysis. The amplitude of the Rayleigh wave decreases exponentially with depth, with the rate of fall-off increasing with frequency, and is thus not suitable for subsurface investigation. The choice of wave to be used is therefore between the shear and compressional waves.

Ideally the excitation mechanism should maximise energy in waves that will propagate into the ground. In practice, however, it is to be expected that there will be surface wave propagations on a path directly between the source and sensors. The nature and relative amplitude of these waves will vary with the exact seismic source used, but it can be anticipated that they will be larger in amplitude due to their shorter propagation paths and hence both reduced hysteretic and geometric attenuation.

To decrease the effects of the surface waves on the imaging method it is necessary to maximise the time difference between the arrival of the surface wave and wave reflected from the object. Chapter 2.2 showed that the shear and Rayleigh wavespeeds are approximately the same, whilst the compressional wavespeed is, in general, much higher. For the short horizontal measurement distances used in this experimental setup the relatively large difference between the surface and reflected path lengths means that the time difference is maximised by the use of shear waves.

This can be demonstrated by considering a source and sensor of variable separation on a surface with a target of arbitrary location, as shown in Figure 3.2 (a). It is assumed that the surface wave is a Rayleigh wave. If it is instead a shear surface wave, the similarity in shear and Rayleigh wavespeeds means that the argument is not significantly altered. A surface compressional wave is unlikely to dominate, as when generating compressional waves the subsequent Rayliegh wave amplitude is usually much larger. $\delta_s^{Threshold}$ is defined as the source sensor separation required for the compressional, rather than shear wave, to give a larger time difference between Rayleigh and reflected wave arrival. Figure 3.2 (b) shows $\delta_s^{Threshold}$ as a function of target depth and for several source target separations. For $\delta_s < \delta_s^{Threshold}$ the use of a shear wave is preferable for target detection, thus the regions of the graph below the lines on the plot indicate values of δ_s and z_t for which shear wave generation is preferable. For depths of around 1 m and source sensor separations with a maximum of around 2 m shear waves are preferable.

A major advantage of using shear waves, and specifically shear horizontal waves, is that they can be generated by a source configuration that produces only small quantities of other wave types. This is shown mathematically in Chapter 2. The generation of a single wave type is desirable to ensure that only one reflection from the target occurs, as target reflections propagating at different wavespeeds are not interpreted correctly by the imaging algorithm.

A further advantage of using shear over compressional waves for investigation is that due to their lower wavespeed they have, for a given frequency, a smaller wavelength than the compressional wave. This lowers diffraction around targets and increases the ability of the method to detect smaller buried objects.

3.3 Time Extended Signals

The imaging method described in the previous section is constrained to use impulsive excitation. In this section the imaging method is modified to include time extended signals. It begins by describing the motivation for this. This is followed by details on the practical implementation and the modifications to the imaging method's post-processing.

3.3.1 Advantages of Time Extended Signals

Impulsive signals can be generated by either a strike, for example using a hammer, or by using a transducer. Impulsive strikes are commonly used by those working in the field of work, but suffer

from a lack of control of the frequency content of the input. In shallow seismic work the frequencies of interest are higher than those in deeper work for the reasons given in Section 1.5.3. Whilst it is possible to influence the inputted frequency content when using impulsive strikes, for example by minimising the duration of the impact [104], this influence is limited in its scope.

The use of transducers to generate impulses can overcome this problem. Impulses of arbitrary frequency content can be produced, limited only by the properties of the transducer itself. A further consideration, however, that applies when using both impulsive strikes and impulsive signals generated by transducers, is that with impulsive excitation the inputted energy is transferred to the ground in a very short period of time. This constrains the energy supply to the system if it is to remain linear. This problem is overcome by using a time extended signal. The energy is thus supplied to the ground over a sufficient period of time such that linearity is maintained.

3.3.2 Practical Implementation of the Source

Time extended signals are implemented using an electromagnetic transducer coupled to the ground. As discussed in Section 3.2.2, it is desirable for the source to preferentially produce shear waves. An inertial electromagnetic shaker is used so the source needs only to be coupled to the structure at a single point. Section 2.3.2 shows that although using a point vertical source does generate some shear waves, these do not form the dominant generated wave type. Instead it is preferable for the orientation of the excitation to be parallel to the surface of the ground. The inertia shaker is thus coupled to the ground via a platform which is inserted into the ground. The coupling platform used in this thesis is discussed in detail in Chapter 5.

The main property of interest when selecting an excitation waveform is the range of its frequency content. Both chirps and random excitation are suitable: the former can be set to sweep over the frequency range of interest, whilst the latter can be defined and then bandpass filtered to produce a signal with the correct frequency content.

3.3.3 Modifications to Imaging Method

The time-domain approach described in Section 3.2.1 is not directly applicable to cases where non-impulsive excitation is used. This is because the method described in Section 3.2.1 assumes that the time domain signals being used only have notable magnitude at time values the time between emission and reception of the signal. For time extended signals the magnitude of the signal will be high for large ranges of time. It is necessary to modify the image method to account for this.

This is achieved by summing cross-correlation functions, rather than the time domain signals directly. This method is applied in the Vibroesis techniques used in geophysical exploration [136]. To calculate cross-correlation functions a reference signal must be used to define the time of signal emission. Several options are available: the signal outputted from the signal generator, the output of an accelerometer located in the shaker or a reference geophone located as close as possible to the source. The aim is to choose the signal that offers the maximum level of correlation with the reflected signal. Consequently the option of the reference geophone is used in the measurements in this thesis. This is because both alternatives fail to account for the phase and magnitude variations introduced by the shaker and the transmission of the signal into the ground.

An estimate of the cross-correlation function, $R_{1i}(\tau)$, between the signal measured by the reference geophone close to the source, $s_1(t)$, and the signal measured by the *i*-th geophone, $s_i(t)$, is given by [110]

$$R_{1i}(\tau) = \frac{1}{T}\int_0^T s_1(t)\, s_i(t+\tau)\,\mathrm{d}t \tag{3.2}$$

where τ denotes a time lag variable and T is the length of the time histories. If one signal is a delayed replica of the other then cross-correlation function is maximal at that delay. If the signals have no correlation then the positive and negative contributions to the integral in Equation (3.2) cancel, resulting in a null value of the cross correlation function. The cross-correlation function will thus have notable magnitude at time values equal to the time between emission and reception of the signal, as required.

An alternative form of the cross-correlation function useful for practical implementation is given by [137]

$$R_{1i}(\tau) = \int_{-\infty}^{\infty} S_{1i}(f)\, \mathrm{e}^{2\pi \mathrm{j} f t}\,\mathrm{d}f \tag{3.3}$$

where $S_{1i}(f)$ is the cross-spectral density between the reference and the *i*-th geophone, and f is frequency. Equation (3.3) is a statement that the cross-correlation function is equal to the inverse Fourier transform of the cross-spectral density. Numerical implementation of the cross-correlation functions uses the relation of Equation (3.3) to exploit the computational efficiency of the fast Fourier

transform. This also allows for generalisations to the cross-correlation function that are discussed in the next section.

3.4 Signal Processing

In the previous two sections the basic imaging method using time-extended excitation signals has been described. This section details several signal processing additions to the imaging method. These are applied to overcome specific difficulties arising in the practical implementation of the method.

3.4.1 Generalised Cross-Correlation Functions

It is desirable to minimise the width of peaks in the cross-correlation functions prior to application of the imaging algorithm. The reason for this is two-fold. Firstly, if the cross-correlation peaks are too wide then multiple peaks in the cross-correlation domain, due for example, to the propagation of multiple wave types, may coalesce. Secondly, if the peaks are very wide, then a cross-correlation function with a single peak will produce an image where all regions have a high value with only a relatively minor peak at the target location, making target detection more difficult.

There is, however, a limit on the desirability of the minimisation of the width of the cross-correlation functions. If these peaks sufficiently small that when they are converted to distances and projected onto the image their width is smaller than the pixel size they may be completely overlooked by the image. This problem is easily overcome by reducing the pixel size used in the image formation. Very narrow cross-correlation peaks can also make the formation of a single image peak difficult as, for reasons of accuracy, the hyperbola on the image do not necessarily exactly overlap at the location of the target. Due to high levels of attenuation in the ground, problems associated with cross-correlation peaks are not an issue in experimental application of the method.

Limitations on the bandwidth of time domain signals results in an increase in the width of these peaks [112]. Due to the high attenuation of waves propagating in the ground there are unavoidable bandwidth limitations in the measured data. The effects of this limited bandwidth are reduced by the use of generalised cross-correlation functions (GCCs). These involve the incorporation of a frequency dependent weighting function [138], $\psi(f)$, to Equation (3.3) to give

$$R_{1i}(\tau) = \int_{-\infty}^{\infty} \psi(f) S_{1i}(f) \mathrm{e}^{2\pi \mathrm{j} f t} \mathrm{d}f \,. \tag{3.4}$$

There are several different weighting functions [139]. The phase transform (PHAT) is one such weighting function and is defined by

$$\psi_{PHAT}(f) = \left|S_{1i}(f)\right|^{-1}. \tag{3.5}$$

The PHAT has the effect of 'pre-whitening' the signal by setting the magnitude of the cross-spectral density to unity whilst preserving the phase information. This is effective because the estimation of the time delay requires only knowledge of the phase, and the attenuated magnitude information serves only to broaden the cross-correlation peaks. A drawback of the PHAT is that it takes no account of the coherence of the signal and therefore increases the magnitude of regions of the cross-spectral densities that correspond only to noise. This reduces the accuracy of the time delay estimate.

Another weighting function is the smoothed coherence transform (SCOT) [140]. This is similar to the PHAT, but in addition to pre-whitening, the cross-spectral density is also weighted by the coherence function. The coherence function is an indication of the strength of linear relation between two signals [110]. Frequency regions of the received signal unrelated to the input thus have an appropriately reduced contribution to the calculation of the cross-correlation function. Mathematically the weighting function is

$$\psi_{\mathrm{SCOT}}(f) = \frac{\gamma_{1i}(f)}{\left|S_{1i}(f)\right|}, \tag{3.6}$$

where γ_{1i} denotes the coherence function between the reference signal and the signal measured at the *i*-th geophone. The coherence function is defined as

$$\gamma_{1i}^2(f) = \frac{\left|S_{1i}(f)\right|^2}{S_{11}(f)\,S_{ii}(f)} \tag{3.7}$$

where S_{1i} denotes the cross-spectral density between the reference geophone and the *i*-th measurement geophone, and S_{11} and S_{ii} denote the auto-spectral density functions of the reference geophone and the *i*-th measurement geophone respectively [110]. Substitution of Equation (3.7) into Equation (3.6) gives

$$\psi_{\mathrm{SCOT}}(f) = \frac{1}{\sqrt{S_{11}(f)S_{ii}(f)}}. \tag{3.8}$$

Prior to application of ensemble averaging it is necessary to consider the length of time of the anticipated target reflections relative to the length of time of each segment used for the ensemble averaging. If the time length of a segment is comparable to the time delays in the measured signals then the reflected signal is not in the same segment as the reference signal, resulting in low coherence function values at the frequencies corresponding to the reflection. This is obviously undesirable. As the time delays involved in shallow seismic reflections are small (of order of tens of milliseconds) this does not pose a serious constraint on the estimation of the cross-correlation functions in this thesis.

3.4.2 Hilbert Transform Envelopes

It has been noted by authors using the imaging method with impulsive excitation [114] that enveloping the time histories results in improvement in the quality of the image. This is because the residual oscillations of the impulse in the time histories cause cancellation when they are summed, resulting in distinct oscillatory behaviour in the final image. This observation applies equally to cross-correlation functions. This because of the oscillatory behaviour in the cross-correlation functions around peak values due to limitations in the bandwidth of measured signals. These oscillations result in degradation of the final image for the same reasons as the impulsive excitation case.

Enveloping is achieved via the use of the Hilbert transform. The Hilbert transform of the *i*-th calculated cross-correlation function is defined as [110]

$$\tilde{R}_{1i}(\tau) = R_{1i}(\tau) \otimes \frac{1}{\pi\tau}, \tag{3.9}$$

where $\otimes$ denotes convolution and a superscript $(\sim)$ the Hilbert transform of a function. The sum of the original function with its Hilbert transform multiplied by j is defined as the analytic signal. As this is a complex quantity it can be expressed in terms of separate magnitude and phase functions. It can be shown [141] that the magnitude of the analytic signal is the envelope of the original signal:

$$Env\left(R_{1i}(\tau)\right) = \sqrt{R_{1i}(\tau)^2 + \tilde{R}_{1i}(\tau)^2}, \tag{3.10}$$

where *Env* denotes the envelope of the signal.

The use of the Hilbert transforms for calculating the envelopes of the cross-correlation functions is preferable to interpolation techniques because it naturally includes negative values of the cross-correlation functions. Negative values of correlation occur when the two signals being correlated are out of phase with each other. Phase changes in the signals may occur through propagation, or, of particular relevance, upon reflection from an object, and their inclusion is thus significant.

A consequence of using Hilbert transforms to calculate envelopes, and the flip-side of the above argument, is that phase information is destroyed. This information is used by other methods (such as the CDP described in Section 1.4) to provide cancellation of the data in the construction of the images, enabling the removal of spurious signals. This approach is not taken in shallow seismic work (see, for example, [114]) because of the high level of oscillations of the cross-correlation functions in the central peak caused by the use of higher frequency inputs [112]. It is demonstrated in Chapter 6 that enveloping is essential for the method to be able to provide useable images.

3.4.3 Spatial Filtering

To improve the quality of imaging method, spatial filtering is applied to the final image. Spatial filtering [142] is a standard technique applied in a wide range of fields (see also MacDougall [143] for an excellent introduction). Spatial filters perform two-dimensional Fourier transforms and then remove undesired spatial frequencies. Many of the standard digital filtering techniques [110], such as windowing, are applicable. Once undesired frequencies have been removed, the data is inverse Fourier transformed to obtain a filtered image.

High pass filtering is applied to exclude the lowest spatial frequencies. This process introduces no new information but instead serves to make the location of any objects detected by the method more visible. The lowest spatial frequencies, corresponding to large regions of high image value, are caused by the repeated summation of the contributions from the different source-sensor arrangements. These can obscure the image of the object.

Implementation of spatial filtering in this thesis is via existing functions in MATLAB®, with a FIR (finite impulse response) high pass filter described by 50 coefficients used in conjunction with a standard image filtering function. Filtering is set to remove spatial frequencies over 5 m^{-1}.

3.5 Conclusions

In this section an imaging methodology has been detailed. This method was initially described using impulsive excitation signals to provide a conceptually simple introduction. The justification of the use

of shear waves in the method is given. This is based on maximising the time difference between the arrival of waves that propagate directly between the source and the sensor and those that are reflected from the target, and also because shear waves are easier to generate in isolation from other wave types.

The motivation for the introduction of time-extended signals was then introduced, with details of the practical implementation discussed. To accommodate time-extended signals, rather than impulses, the post-processing of the imaging method was modified to include cross-correlation functions.

Several additions to the post-processing method are required to overcome specific problems that occur during implementation. These include high attenuation causing a broadening of cross-correlation peaks, which can be partially countered using generalised cross-correlation functions, and large regions of high image value obscuring the imaging of target objects, which can be improved using spatial filtering.

The imaging methodology described in this chapter is numerically simulated in Chapter 4 and experimentally applied in Chapter 6.

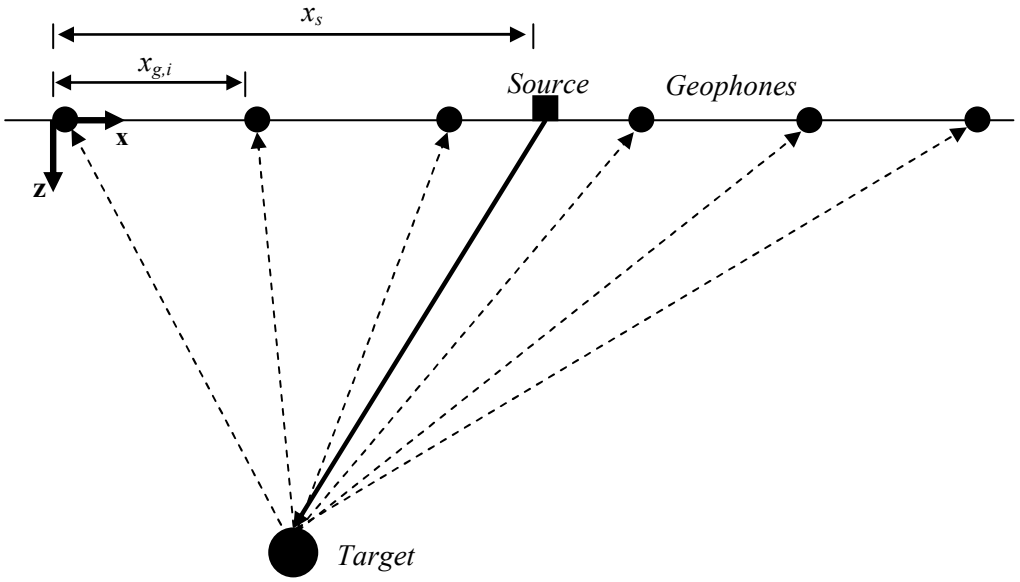

Figure 3.1 - Diagram of the experimental setup used for the imaging method with relevant dimensions labelled. The circles on the surface denote geophones and the square on the surface the source.

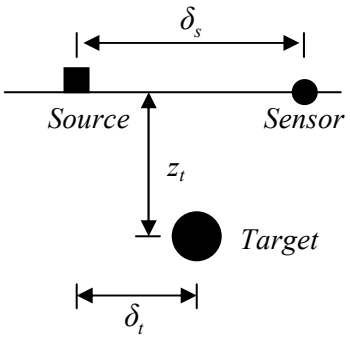

(a)

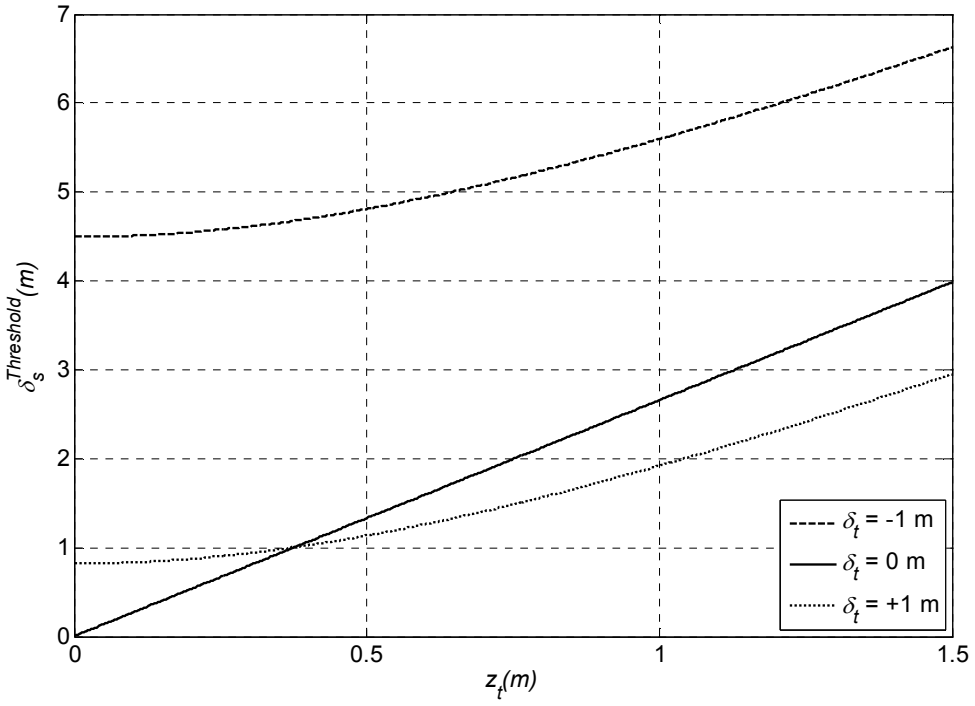

(b)

Figure 3.2 - (a) an experimental setup to illustrate the advantages of using shear waves, with the circles on the surface denoting geophones and the square on the surface the seismic source; (b) plot of the variation of $\delta_s^{Threshold}$, the value of δ_s at which the time difference between the compressional and Rayleigh wave arrival times exceeds that between the shear and Rayleigh waves, with respect to the depth of the target. The Rayleigh wavespeed is taken to be 75 ms^{-1} and the Poisson's ratio of $\nu = 0.45$, with other wavespeeds calculated via relations given in Chapter 2.

4. Numerical Simulations

Chapter 4

Numerical Simulations of the Imaging Method

4.1 Introduction

The aim of this chapter is to evaluate the experimental methodology described in Chapter 3 by way of numerical simulations. Whilst the aim of this thesis is an experimentally validated method, the lack of control over environmental and soil conditions that arises in field experimentation means that it is useful to undertake numerical simulations. This is both to confirm the methodology and the post-processing algorithms.

This chapter begins by describing the implementation of the numerical simulations as well as the limitations that are a consequence of this method of implementation. An important parameter for the imaging methodology described in Chapter 3 is the estimated speed of the reflected seismic wave. The effects of error in the wavespeed measurement on the resultant image are given specific attention in Section 4.3, as it is subject to large site-to-site variability and can be difficult to measure accurately. In Section 4.4 the assumption of heterogeneity in the medium is relaxed in some specific situations. Section 4.5 gives brief consideration to the consequences of target reflectors lying outside the measurement plane. Finally, some conclusions are drawn in Section 4.6.

4.2 Description of the Numerical Simulations

This section begins by describing the numerical simulations and their practical implementation in Section 4.2.1. The focus is on creating a basic a framework which can then be modified to evaluate the effects of more realistic experimental considerations. The limitations of the basic numerical

simulation are discussed in Section 4.2.4. The aim of the numerical simulations is to produce time histories to which the imaging method of the previous chapter can be applied. Of the possible types of propagating waves only SH waves are included in these numerical simulations. This is justified by the analysis in Chapter 2 of the wave motion generated by a source moving parallel to the surface of the ground. The numerical simulations are, however, constructed such that the properties of wave propagation over the surface could differ from those through the ground. This allows for the possibility of simulating circumstances where Rayleigh waves are propagating in addition to SH waves.

4.2.1 Simulation of Single Propagation Path Time History

The method for constructing the simulated time history of a single source-to-sensor path is first considered. This is followed by extension of this method to the experimental setup used for the imaging method. Numerical simulations are constructed in the frequency domain and signals are subsequently converted back to the time domain to form the final simulated time histories. This is more computationally efficient than simulating the time domain signals directly, especially because time domain signals would have to be converted to the frequency domain and back to implement hysteretic attenuation (see later in this section). The frequency domain representation of the time histories is referred to throughout the following description as the frequency signal.

The first stage is to define the bandwidth of the Fourier transform of the signal that is used as the system input i.e. that emitted by the source. The Fourier transform of the signal is given unit magnitude over the desired bandwidth. If the Fourier transform of the signal is defined with only a real part in the frequency domain it will have zero phase over the whole frequency range and is thus approximately equivalent to an impulse response in the time domain (the exact form will be that of a sinc function). Whilst an impulsive signal may contain the desired frequencies, it is not desirable for the numerical simulations in this thesis. This is because the imaging method uses time extended, not impulsive, signals. The reasons for this were given in Chapter 3; i.e., the difficulty in controlling the frequency content of the input using impulsive sources, and the desire to keep the input small to prevent non-linearity. These do not apply in the context of numerical simulations, but it is desirable to use the same post-processing techniques on the experimental and simulated time histories to maintain confidence in the numerical validation.

The experimental post-processing techniques use generalised cross-correlation functions, including the smoothed coherence transform (SCOT). This weights the cross-spectral density by the square of the coherence function (see Section 3.3.1). Calculation of the coherence function requires the use of ensemble averaging, which is not valid for a non-statistically stationary signal such as an impulse.

Consequently, it is important that the input signal has stationary statistical values such that it can be segmented and ensemble averaged. This is achieved by giving the Fourier transform of the signal a random phase. Thus when the Fourier transform of the signal is inverse transformed to obtain a time history a 'white noise' signal is produced.

The Fourier transform of the signal inputted to the system has been defined and is now modified to simulate the effects of propagation through the ground. Modifications to the magnitude and phase information of the Fourier transform of the signal are performed separately. For a given propagation distance and propagation wavespeed the time delay, τ, is known. Assuming non-dispersive propagation, the phase will vary linearly as a function of angular frequency, ω, with the gradient of the phase variation equal to the value of the time delay. Thus the phase, γ, is given by

$$\gamma(\omega) = \omega\tau . \tag{4.1}$$

The magnitude of the Fourier transform of the signal is calculated by varying the unit amplitude bandwidth of the excitation signal to attempt to replicate attenuation in the ground. Both hysteretic and geometric attenuation are considered. Hysteretic damping is applied to simulate the loss of energy due to friction in propagation through the medium. The fractional change in the amplitude of the magnitude of the Fourier transform of the signal over a propagation distance d is

$$A_\eta = \mathrm{e}^{-\eta\omega d/c}, \tag{4.2}$$

where η is the loss factor of the ground and c is the speed of wave propagation. Geometric attenuation is accounted for by using an inverse power law such that the fractional change in the amplitude of the magnitude of the Fourier transform of the signal is

$$A_g = \left(\frac{d}{d_{\mathrm{ref}}}\right)^{-n}, \tag{4.3}$$

where d_{ref} is the distance from the source to which the amplitude reduction applies, and n is the geometric power attenuation constant. This reference distance from the source must be non-zero for application to the simulations and is set a small distance from the source. The distance is physically the distance at which the energy is considered inputted into the system, and thus the approximate extent of the source. A distance of 10 cm was chosen on the basis of the source design described in Chapter 5. The geometric power attenuation constant will vary between wave types, and its theoretical

values for the system considered in this thesis are given in Chapter 2. From Equations (4.1-3) the Fourier transform of a single attenuated propagating wave, denoted β, with time delay τ is

$$\beta(\omega) = \mathrm{e}^{-\eta\omega d/c}\left(\frac{d}{d_{\mathrm{ref}}}\right)^{-n}\mathrm{e}^{\mathrm{j}\omega\tau}. \tag{4.4}$$

To illustrate the process used for the construction of the Fourier transform of the signals that are inverse transformed to give the simulated time histories, the magnitude of the Fourier transform of the input signal is shown in Figure 4.1 (a), with the magnitude of the Fourier transform of a measurement geophone signal shown in Figure 4.1 (b). There are three effects that have modified the magnitude: hysteric damping, which reduces higher frequencies in an exponentially increasing manner; geometric damping, which reduces the amplitude of all frequencies equally; and comb-filtering, resulting in the visible undulations. This is a result of constructive and destructive interference from the presence of two propagation paths.

4.2.2 Simulation of Imaging Method Time Histories

The basic time histories for the setup used for the imaging experiments are now simulated, with this section restricted to the case of point reflectors. There are two propagation paths between the source and sensor; that directly along the surface and that from the source to the sensor via a reflection at a point target. These two paths are referred to as the direct and reflected paths, and quantities associated with these propagation paths (such as distance, propagation speed etc.) are labelled with subscripts D or Rl respectively.

Due to the assumed linearity of the system and the linear property of the Fourier transform, the final response at each geophone is taken to be the inverse Fourier transform of the sum of the Fourier transform of the signals representing the direct and reflected waves. The types of direct and reflected propagating waves are, for the purpose of generality, left undefined, and can vary depending on the source used and arrangement of the sensors relative to the source. The distance for the surface propagation from the source to the i-th sensor is given by

$$d_{D,i} = \left| x_s - x_{g,i} \right|. \tag{4.5}$$

This can be substituted into Equation (4.4) with the wavespeed of the direct wave to give the Fourier transform of the signal for this wave at each geophone. The propagation distance from the source to a sensor via the point target at (x_t, z_t) is

$$d_{Rl,i} = \sqrt{(x_t - x_s)^2 + z_t^2} + \sqrt{(x_t - x_{g,i})^2 + z_t^2} \,. \tag{4.6}$$

Substitution of this distance into Equation (4.4) with the appropriate wavespeed allows calculation of the Fourier transform of the signal for the reflected wave at each geophone.

Including both propagation paths gives the transfer function between the source and the *i*-th sensor as

$$\beta_i(\omega) = \mathrm{e}^{-\eta_D \omega d_{D,i} / c_D} \left(\frac{d_{D,i}}{d_{ref}} \right)^{-n_D} \mathrm{e}^{\mathrm{j}\omega\tau_{D,i}} + \mathrm{e}^{-\eta_{Rl} \omega d_{Rl,i} / c_{Rl}} \left(\frac{d_{Rl1,i} d_{Rl2,i}}{d_{\mathrm{ref}}^2} \right)^{-n_{Rl}} \mathrm{e}^{\mathrm{j}\omega\tau_{Rl,i}} \,. \tag{4.7}$$

4.2.3 Application to Non-Point Reflectors

Extension of the method of numerical simulation to the case of targets of finite size is achieved by discretisation of the target into point targets. Due to the linearity of the process, the Fourier transform of the signals from each of the points that compose the target can be summed and then inverse Fourier transformed to create a simulated time history. The target is discretised so that its elements coincide with image pixels. The level of discretisation of the target therefore depends on both the dimensions of the target reflector and the chosen pixel size. Alternative methods, such as those relying on Kirchoff migration techniques [46], are possible. These have not been applied due to the additional complexity they introduce into these basic simulations.

When using spatially extended targets complications arise in scaling the reflected wave in relation to the direct surface wave. As stated above, the reflected signal for an extended object is formed by summing its constituent point reflectors. The surface sensor, however, is assumed to be a point receiver. Compensation must thus be made for the discretisation of the space. If it were not then a target object composed of, say, 20 individual point reflectors would, after summation, have a Fourier transform of the signal with an amplitude 20 times greater than a point receiver. If the discretisation were to be increased such that the same target object was now composed of 40 individual point reflectors, then the amplitude of the Fourier transform of the signal relative to a point receiver would have doubled, despite no physical increase in the size of the target object. To compensate for this arbitrary behaviour the amplitude of the Fourier transform of the signal representing the reflected

wave is divided by the total number of constituent point reflectors, making the reflection amplitude independent of the discretisation of the space.

An additional factor must be included to account for the increase in the amplitude of the reflected signal from a larger target. This is not meant to account for diffraction or other frequency dependent effects, but rather the portion of the seismic energy emitted by the source that will reach a target of a given size. Here the term energy refers to the energy propagating in the elastic waves emitted by the source. For example, ignoring attenuation, a large target closer to the source will receive and thus reflect a larger amplitude signal than a small target far from the source would. To include an indication of the relative proportion of the emitted energy that reaches the reflector, the angular extent of the reflector in the half space is calculated. The ratio of this to the maximum value (π) is then used to scale the signal amplitude. For example, for the linear horizontal target shown in Figure 4.2 the multiplication factor, defined as Γ, is the angle subtended by the target, θ_e, divided by π. The implicit assumption that the source radiates omnidirectionally is justified for an SH source by the analysis in Chapter 2.

It is important that a similar division of the radiated energy is applied to the surface sensors. If it is not then the surface sensors are implicitly assumed to have received radiated energy from the whole half space, as failure to implement any division of radiated energy is equivalent to setting $\Gamma = 1$. As the ratio of the direct and reflected waves is vital for the assessing the ability of the imaging method to detect targets, it is important that this is not overlooked. The assumption thus far that the sensors are point-like causes difficulties in the implementation, as the angular extent is technically zero, and therefore $\Gamma = 0$. Defining the surface sensor as the size of a single pixel to approximate a point source and then calculating the angular extent is arbitrary, as it will vary with the discretisation of the space.

It is necessary to define the sensors as non-point-like to overcome these problems. They can then be assigned a meaningful value of the proportion of the emitted seismic energy. The geophones used in the experimental application of the imaging method extended 7.5 cm into the ground, and this distance is taken to define their size. This depth value, in addition to their distance from the source, enables an estimate of their angular extent.

These complications are a direct consequence of the unphysical assumptions of point source and sensor. These problems can be avoided through the use of the more complicated methods, such as the Kirchoff migration described discussed in Section 1.4.2.2.

Using the index *k* to sum over all N elements of the extended object gives the Fourier transform of the signal at the *i*-th geophone to be

$$\beta_i(\omega) = \mathrm{e}^{-\eta_D \omega d_{D,i} / c_D} \left(\frac{d_{D,i}}{d_{ref}} \right)^{-n_D} \mathrm{e}^{\mathrm{j}\omega\tau_{D,i}} + \frac{\alpha\Gamma}{N_i} \sum_{k}^{N_i} \mathrm{e}^{-\eta_{Rl} \omega d_{Rl,i,k} / c_{Rl}} \left(\frac{d_{Rl,i,k}}{d_{\mathrm{ref}}} \right)^{-n_{Rl}} \mathrm{e}^{\mathrm{j}\omega\tau_{Rl,i,k}} \qquad (4.8)$$

where α represents the ratio of the reflected wave amplitude to the direct wave amplitude. If multiple wave types are propagating along the same propagation path, for example if both compressional and shear waves were propagating via the target, then additional terms could be added to Equation (4.8), with the same form as Equation (4.8) but with differing propagation parameters.

Prior to inverse Fourier transforming to obtain the simulated time histories at the geophones the spectrum of the signal must be made two-sided. This is achieved by extending the signal to negative frequencies symmetrically about the origin and taking the complex conjugate of the signal at negative frequencies. This is necessary to ensure that the resultant signal is real [110]. Finally random noise is added to the signal. This is to better replicate experimental data, which will always be contaminated by some random noise.

In accordance with the experimental procedure described in Chapter 3 the measurements are repeated with an identical sensor arrangement but with the source moved. This is both to increase the signal-to-noise ratio and to ensure full illumination of the target with the incident seismic waves. As in the experimental work (see Chapter 6) the simulations are repeated with the source located equidistant between each pair of adjacent sensors. A final image is obtained by summing the images produced from the measurements runs.

A summary of the method for forming the time history outputs of the numerical simulations is given in the flowchart of Figure 4.3. For the application of the post-processing required for the imaging method it is necessary to calculate cross-correlation functions between the simulated time histories and a reference signal representing the signal generated by the source. This reference time history is simply taken as the original, unmodified random signal that was generated at the beginning of the simulation procedure.

An example experimental setup with parameters given in Table 4.1 is used in the simulations of imaging method. Source, sensor and the target location are chosen to coincide with experimental work in Chapter 6. The wavespeeds and attenuation values are chosen to be representative of those measured in experiments, both those presented in Chapter 6 and those presented by other authors [77,

101, 144]. For the calculation of the coherence function the SCOT GCC is used with a 10 second simulated time history which is segmented into 20 equal sections with a hamming window applied to each. The spatial filtering described in Section 3.4.3 is applied.

The image produced using this set of parameters is shown in Figure 4.4. Surface sensors are denoted by circles, surface sources by squares, and the target location by the black line. The imaging method produces high value in the vicinity of the target and low value elsewhere, and makes the target location clearly visible.

It is anticipated that the image quality will reduce when the target is moved away from the centre of the measurement line because of a reduction in the amplitude of the target's image peak. This is due to the total propagation distance from the source to the sensor via the target being higher for the targets located away from the centre of the measurement line. This reduces the amplitude of the reflected signal relative to the surface signal due to increased attenuation. To illustrate this effect the target has been shifted 0.5 m leftwards in the image. The resultant image is shown in Figure 4.5. The target is still clearly visible, although the quality of the image is reduced.

4.2.4 Limitations of the Numerical Simulations

The numerical simulations described in the previous section suffer from various limitations and omissions. Here, these are discussed in turn, with their implications for the accuracy and relevance of the evaluated simulated time histories.

Target reflection coefficients have not been included in the numerical simulation, and thus perfect reflection from the target has been assumed. This means that it is assumed that the target is rigid, i.e., that vibrations do not occur within the target when it is subject to an incident wave from the vibration source. Information on the target geometry could be used to include detailed reflection effects. For example, for a cylindrical target the reflection coefficient could be obtained by mathematical analysis, producing a result which is a function of frequency and directivity [145]. Derivation of these results frequently makes far-field approximations, i.e. that the assumption that the derived results are valid at distances much greater than the wavelength of the seismic waves. Care must be taken, however, as the simulations consider circumstances in which far-field approximations are not valid. This mandates a more in depth analysis of the reflection coefficients which, as this thesis is concerned with testing the basic principle of the imaging method to shallow buried targets, lies outside scope of this work.

It has been assumed throughout the implementation of the numerical simulations that only SH waves are propagating. This has been justified from the mathematical analysis performed in Chapter 2,

which was in turn subject to various assumptions that will not be met in field experimentation. Factors such as components of source motion not parallel to surface and near-field effects could lead to the generation of other wave types. The presence of near-field waves or coupling between wave types during propagation [135] is not considered. As the focus of the numerical simulations is not on sources where SV and compressional waves are generated in large quantities, their interaction in the form of wave coupling at the target is assumed small. For a more detailed numerical simulation that could include the effects of wave coupling, both during propagation or upon interaction with a reflector, or near-field effects, alternate simulation structures could be considered. For example, finite difference time domain methods have been used successfully by several authors for elastic wave propagation problems [146].

The numerical simulation detailed in this chapter does, however, have an important advantage over finite difference time domain methods and finite element models in that the described method gives a much greater control over the types of wave propagating and their relative properties. For example, it is possible to completely remove one wavetype from the simulations (for example eliminating the surface wave) or to scale wavetypes arbitrarily. The latter of these is particularly useful for examining the relative amplitude of the reflected wave relative to the surface wave required to enable detection.

The concept of a homogeneous medium used in forming the numerical simulations is clearly an idealisation. In reality the structure of soil is subject to both anomalous heterogeneity, for example caused by objects other than the desired target, and more ordered heterogeneity caused by particular soil structures, particularly layering of soil properties. For the first of these the anomalous nature of the heterogeneity removes utility from considering specific examples. For useful analysis of such anomalies large sets of data would be required to perform a statistical analysis of their impact. This approach is not examined within this thesis due to the likelihood of large variations in anomalous heterogeneity between experimental sites. For the second type of heterogeneity; that caused by soil structure, it is practical to remove the assumption from the numerical simulations for a few specific cases. This is considered in Section 4.4.

A limitation fundamental to the imaging method, and previously discussed in Chapter 3, is that all seismic reflections measured at the surface sensors are assumed to originate from objects within the vertical plane defined by the measurement line. This limitation is a consequence of the use of a one dimensional array of surface sensors, and could be lifted by using a two dimensional array of surface sensors. As this limitation remains in the experimental part of this thesis the consequences of reflections from targets outside the measurement plane are examined using the numerical simulations in Section 4.5.

The consequences of some of the limitations and omissions given in this section are now evaluated in the rest of this chapter by modifying the previous numerical simulations.

4.3 Effects of Wavespeed Measurement Error

A crucial parameter within the imaging algorithm is the speed of the reflected wave from the target. It is likely that in-situ measurement of the wavespeed will suffer from notable inaccuracy. This is because of the variation in the soil properties with location and weather conditions, as well as the presence of ground heterogeneity over the region of ground of a single experiment. It is therefore important to assess the effects of error in the wavespeed used in the imaging algorithm. The numerical simulations enable this evaluation to be performed in a controlled manner.

Other than the assumed wavespeed used in the post-processing of the simulated time histories all other parameters remain unchanged from that used in forming the image of Figure 4.4. A wavespeed measurement error ranging from a 20% underestimate to a 25% overestimate of the true wavespeed is used in calculating the simulated time histories. Post-processing proceeds as before.

The image for a wavespeed error of 10% overestimate of a true wavespeed of 100 ms^{-1} is shown in Figure 4.6. The main image peak is still clearly visible, although it is shifted from the correct location. The use of too large a wavespeed value causes the individual geophone image hyperbolas that form the final image to be shifted away from the source. Provided this shift is small, the width of the cross-correlation functions calculated during imaging method's post-processing will ensure that the individual geophone image hyperbolas still intersect to form a target image.

Of use in Chapter 6 is the behaviour of the image values very near to the surface. These areas of high image value are observed in Figures 4.4 and 4.5 at the surface, and are an imaging artefact caused by the interpretation of the wave that propagates directly from the source to the sensor over the surface. The imaging method assumes that all measured waves come from reflections. The only reflector location that can correspond to the direct wave is one very close to the surface, such that the reflected path effectively becomes the direct surface path. In Figure 4.6 these direct wave artefacts have been shifted away from the surface into the ground due to the incorrect wavespeed. This observation is put to use in Chapter 6, where the presence of the direct wave artefacts away from the surface indicates that an inaccurate wavespeed has been used in the imaging method.

To show the effect of wavespeed measurement error in the imaging method, the difference between the peak image location and the target location is measured as a function of the wavespeed error. The

resultant plot is shown in Figure 4.7 for a true wavespeed of 100 ms^{-1}. This wavespeed value was chosen because it is representative of values typically obtained from the field experiments performed for this thesis. In this figure negative values of the distance correspond to the image peak being deeper than the actual target location. Whilst the value of the wavespeed does have some effect on imaging method, principally due to the variation of hysteretic damping with wavespeed, as shown in Equation 4.4, the difference in the image is small provided the wavespeed remains of the same order of magnitude.

Referring to Figure 4.7, the minimum image peak error is when the wavespeed measurement error is zero. The error increases in a roughly linear manner as the wavespeed measurement error increases. For a sufficiently large wavespeed measurement error the hyperbolas fail to intersect, and the image does not contain a coherent target peak. An example is shown in Figure 4.8, when a 30% overestimate of the wavespeed is used. General rules for failure of the image hyperbolas to intersect are difficult to construct as the gradual deterioration of the image depends on many image parameters, such as damping levels and target location.

Although a general rule is not possible, it is concluded that provided the estimated wavespeed is within about 10% of the true value then an image can be successfully formed, even if there is a small shift in the peak location.

4.4 Variation of Wavespeed with Depth

The assumption of homogeneity leading to a constant wavespeed in the medium has been discussed in Section 4.2.4. It was stated that this assumption is likely to be violated in experiment, particularly with regard to variation of the wavespeed with depth. The effects of the variation of wavespeed as a function of depth can be assessed using numerical simulations in a controlled manner which is very difficult to achieve by experiment. The purpose of this section is to relax this assumption by allowing for variation of the speed of the reflected wave as a function of depth. Only the parts of the numerical simulation dealing with reflected waves require modification; surface wave propagation is not affected. For surface shear or compressional waves the propagation is assumed to occur only over the surface, and as there is no lateral variation in the wavespeed this will remain unchanged. For surface Rayleigh waves, where there is penetration of wave into the medium, variation of wavespeed with depth will result in dispersive propagation (see Section 2.2.2). This is beyond the scope of these numerical simulations and is not included.

Both continuous and step variation in the wavespeed are considered. The first of these is covered in Section 4.4.1, which details implementation of a continuously changing wavespeed with depth, the

simplifications required for this implementation, and finally gives several examples to show the effects on the performance of the imaging method. The effects of step changes caused by a discontinuity in material properties are illustrated in Section 4.4.2, with two practical situations considered - the effect of a top soil layer and the effects of a rigid boundary.

4.4.1 Continuous Variation of Wavespeed with Depth

In this section the propagation speed of the wave that propagates to and reflects from the target is allowed to vary in a continuous manner. This variation is with respect to depth only, with the aim of replicating the general increase in propagation velocity with depth caused by the increasing over-burden pressure [147]. Variation with respect to lateral position is assumed to be caused by anomalous heterogeneity and is therefore not included. Implementation is kept as simple as possible by assuming that, whilst the time taken for the wave to propagate will alter with the variation in the wavespeed, the path it takes and its amplitude will not.

In addition to this, refraction of the waves also causes deviation of their path from the assumed direct lines of propagation. This is not considered for continuous variation implemented in this section, and it is instead assumed that the propagation paths are unchanged from the constant wavespeed case. This is a valid assumption provided that the variation remains relatively small over the propagation depths considered, as the curvature of the path can be neglected relative to the length of the propagation path. Deviations in propagation path are discussed and implemented in the following section relating to step variations in the wavespeeds.

The wavespeed, c_{Rl}, is allowed to vary as a function of the depth element z_k, where k is the index over the discretised depth. The time of propagation over an increment of depth, Δz, is

$$\Delta\tau_k = \frac{1}{c_{Rl}(z_k)}\sqrt{\Delta x_k^2 + \Delta z_k^2}\,, \tag{4.10}$$

where the incremental horizontal distance travelled during propagation over the depth increment is Δx. Summing over an entire reflection path gives the total propagation time to the i-th geophone, τ_i, as

$$\tau_i = \left[\sqrt{z_t + \left(x_t - x_{g,i}\right)^2} + \sqrt{z_t + \left(x_t - x_s\right)^2}\right]\left(\sum_{k=1}^{k=N_e}\frac{1}{c_{Rl}(z_k)N_e}\right). \tag{4.11}$$

where N_e is the total number of elements in the summation, and will depend of the discretisation considered space and the depth of the target. Comparison with Equation (4.6), which gives the propagation distance in the case of constant propagation speed, shows that the only difference is the addition of averaging of the wavespeed. This is simple to implement in the numerical simulations.

A greater problem occurs in creating realistic velocity-depth profiles. This profile will vary substantially between soil types and environmental conditions, and accurate measurements at such shallow depths are not available in sufficient quantity for generalisations to be drawn. The observed trend varies in the literature from no measurable variation in the first few metres [45] to a doubling within a few propagation wavelengths [101]. The variation of the wavespeed with depth will, furthermore, differ depending on wave type.

An example is the saturation of otherwise porous soil with the level of saturation increasing with depth. This may have different effects on the shear and compressional wavespeeds. The compressional wave can propagate through the water, and will do so with a greater speed than in soil. The shear wave, however, cannot propagate in water as shear motion is not supported and is instead constrained to the skeletal structure of the porous medium. This is mass loaded by the presence of water, thus causing a reduction in the wavespeed. The effects are complicated by the increased stiffness of the skeletal structure due to the mass loading by the heavier material above [147].

Complications such as these mean that the velocity-depth profiles used are not chosen to correspond to measured data - rather they give an indication of the effects of a general increase in the propagation wavespeed with depth on the quality of the images produced by the method described in this thesis. Two profiles are illustrated: one with slight linear dependence with depth, and one that varies more severely as the square root of the depth. The latter of these is expected to replicate more accurately the general trend in velocity increase in unconsolidated sediments [77]. The wavespeed used in the post-processing of the imaging method where velocity varies as a function of depth is that at the surface. This is because in experimentation this is the wavespeed that can be most readily measured.

The linear depth profile is shown in Figure 4.9 and the resultant image in Figure 4.10. Whilst the image peak is no longer in the correct location, the image still forms a coherent peak that is shifted by only a reasonably small amount. Whilst this is not accurate, in experimentation it would be sufficient to indicate that there is a reflective target present. Both the exact location and size of the target are, however, unclear.

The second depth profile considered is that which increases proportionally to the square root of the depth, and is shown in Figure 4.11. This profile also has considerably greater variation with depth, such that at the target the wavespeed is 40% higher than at the surface. Figure 4.12 shows the resultant image. The distortion to the image is too severe for the formation of an image peak and instead the imaging method fails to detect the target. The reason for this is that if the contributing hyperbolas from each image are sufficiently shifted they fail to intersect to form an image peak.

In conclusion, the imaging method is capable of forming an image even in the presence of a continually varying wavespeed as a function of depth, provided that this variation is not too large. Reasonably small variation leads to a shift in the location of the target, but still allows for the targets detection. Large variation totally obscures the presence of the target and renders the imaging method ineffective.

4.4.2 Step Variation of a Wavespeed with Depth

The second type of variation of wavespeed with depth is a step change. The purpose of this section is to examine the consequences of having stratified heterogeneity within the medium, typically caused by a layer of top soil overlaying a stiffer foundation. This section begins by examining the implementation of the step variation before moving to some specific examples.

4.4.2.1 Implementation of the Step Variation

Unlike in Section 4.4.1, where it was assumed that the variation in wavespeed was sufficiently small to allow for propagation paths to be assumed linear, in this section variation in the propagation path is permitted. This variation is caused by refraction of the seismic wave as it enters the underlying medium. Only SH wave propagation is considered here. As SH waves, unlike P and SV waves, do not experience mode conversion upon interaction with a boundary, implementation is straightforward.

Two situations are implemented separately; the case where target is in the upper medium and the case where the target is in the lower medium. The situations are shown in Figure 4.13 and 4.14 respectively. The density and shear wavespeed in the upper medium are ρ and c respectively, with the equivalent quantities in the lower medium ρ' and c'. In both cases there is a direct reflection from the layer which creates a propagation path independent of the target object. The angles of incidence and reflection are equal and are denoted θ_r. The calculation of reflection and transmission coefficients between two elastic media for SH waves is straightforward, with the expressions given by [148]

$$R = \frac{\cos\theta_i - Z_R \cos\theta_t}{\cos\theta_i + Z_R \cos\theta_t}, \tag{4.12}$$

$$T = \frac{2\cos\theta_i}{\cos\theta_i + Z_R \cos\theta_t}, \tag{4.13}$$

where Z_R is the ratio of the wave impedance of the two materials, given by

$$Z_R = \frac{\rho' c'}{\rho c}. \tag{4.14}$$

If the target is in the upper medium the reflection from the target occurs independently of the change in material properties. If the target is in the lower medium then the propagation path will suffer from variation both propagating to the target and propagating to the sensor after reflection. The angles of incidence and transmission when propagating to the target are denoted by θ_i and θ_t respectively, with θ_i' and θ_t' used for the propagation from the target to the sensor.

The relationship between the angles that determine the variation of the propagation path at the boundary between the medium is described by Snell's law. This states that

$$c'\sin\theta_i = c\sin\theta_t. \tag{4.15}$$

In the cases considered in this section, the propagation velocity in the lower medium is higher than in the upper medium, and thus with reference to Figure 4.14 $c' > c$. This means that upon entering the medium with the faster propagation velocity, the path of the wave will bend away from the line normal to the boundary, as indicated in the figure.

Once wavespeeds, source, sensor and target locations have been specified it is necessary to calculate the path. The aim is to be able to calculate the propagation path length in each medium so that Equation (4.8) can be successfully implemented. The angle of incidence is found by searching through all values, starting from zero, and for each value calculating the horizontal propagation distance at the target depth. This is continued whilst the horizontal distance is less than the known horizontal separation. This condition, expressed mathematically for the propagation from the source to the target is

$$z_l \tan\theta_i + \left(z_t - z_l\right)\tan\left[\arcsin\left(\frac{c_2' \sin\theta_i}{c_2}\right)\right] < \left|x_t - x_s\right|, \qquad (4.16)$$

where the depth of the discontinuity in the material properties is z_l. For sufficiently small discretisation in the increment of the angle of incidence this will produce a result whose error is less than the spatial discretisation of the considered space. A similar process is used to determine the angles θ_i' and θ_t', with the exception that the geophone positions are used rather the source positions, and the wave speeds are reversed as the incident wave now originates from the lower medium.

Once the angles of incidence and transmission are known the propagation distance, and hence time, can be calculated from simple geometry. In addition, Equation (4.8) must also be scaled by the transmission coefficients for both propagation directions, calculable from Equation (4.13).

The assumption of linearity allows for the inclusion of the additional propagation paths by simple addition of the calculated frequency domain functions. Extended targets are, as before, composed from individual point targets with the same procedures outlined in Section 4.2.3.

The following two sections detail the application of the described additions to the simulations in two specific circumstances of particular interest.

4.4.2.2 Effect of Top Soil Layer

It is common for a layer of top soil to overlie harder substrates. Typical values have been taken from the literature [149] for soft saturated clay (a density of 2000 kgm^{-3} and shear wavespeed of 180 ms^{-1}) and stiff clay (density 2300 kgm^{-3} and shear wavespeed of 300 ms^{-1}). For consistency with the other simulated data in this chapter the wavespeed in the upper medium is set to be 100 ms^{-1}. The wavespeed in the lower medium is scaled appropriately to be 167 ms^{-1}. Although this is different from the data from the literature, only their ratio is important for calculation of both the transmission and reflection coefficients and refraction angles at the boundary. The impedance ratio, Z_R, is approximately 1.9.

The depth of the boundary between the two media must also be set. The target depth remains unchanged at 0.7 m. It is expected to be significant which side of the boundary the target lays; below the boundary will mean that the reflected wave will be subject to a reduction in amplitude when both entering and leaving the lower medium. Using the above parameters with a boundary depth of $z_l = 1$

m produces the image shown in Figure 4.15. The boundary is indicated by the dashed line. The target object is still clearly visible, although there are some high image values at the boundary depth.

The case of a boundary depth of 0.4 m is shown in Figure 4.16. As expected, the reduction in the amplitude of the reflected signal from the target due to transmission coefficients and the decreased attenuation of the wave reflected from the boundary means that the imaging method fails to detect the target.

4.4.2.3 Effect of Rigid Boundary

The limiting case of a rigid boundary in next considered. For this the impedance of the lower layer is set many orders of magnitude higher than the upper medium. This could model approximately a situation where there is a hard layer of bedrock or, for shear wave propagation, a water table. The wavespeed is the upper medium is again assumed to be 100 ms^{-1}. No other material properties are required: the absence of propagation in the lower medium means that the wavespeed in the lower medium is irrelevant, and the densities are only needed for the calculation of the impedance ratio which is simply set to a large value in the simulations. As there is no transmission into the lower medium, if the target is located in the lower medium it will not be detected.

Of more interest is the case where the rigid boundary is located below the target. This is shown in Figure 4.17 for a boundary depth of 1 m. As expected, the boundary is more clearly visible than in the equivalent case for the top soil boundary. This is because the reflection coefficient of the boundary will be maximal. The target is, however, still visible, although with greatly reduced amplitude. It should be stressed that the chosen values represent a limiting case, and therefore that, provided the target lays above the boundary, the imaging method remains viable.

4.5 Targets Off Measurement Line

A fundamental assumption of the imaging method used in this thesis is that the problem can be reduced to a two-dimensional cross-section through the ground. Whilst this assumption enables the use of a linear array of sensors, it is unlikely to be met in reality. In practice heterogeneity within the medium will result in reflections from outside the considered measurement plane. Furthermore, the exact plane of location of the target object is often not precisely known, and it is plausible that it may not be directly under the measurement line. As described previously, the consideration of specific cases of heterogeneity is often of little utility - generally by its anomalous nature a statistical analysis of many cases would be more appropriate. The specific case of the target object being outside of the measurement plane is, however, considered.

Implementation is particularly simple. The only modification required is the inclusion of an additional distance, y_t, into Equation (4.6) to allow for out of plane motion to and from the target. This then becomes

$$d_{R,i} = \frac{1}{c_{Rl}}\left[\sqrt{\left(x_t - x_s\right)^2 + y_t^2 + z_t^2} + \sqrt{\left(x_t - x_{g,i}\right)^2 + y_t^2 + z_t^2}\right]. \qquad (4.17)$$

An example error of 0.25 m in the location of the measurement plane in relation to the target is considered. All the other parameters, including the source and sensor positions and the location of the target object in the measurement plane, are left unchanged from Section 4.2. The output of the imaging method is shown in Figure 4.18. The image peak is no longer in correct location, but rather is shifted to a slightly greater depth. This is to be expected, as the extra propagation distance is interpreted by the algorithm as meaning that the target is located deeper. The change in peak location is, however, small. The imaging method can therefore be said to be reasonably robust to target location outside of the measurement plane. The exact location could be found by using multiple parallel measurements lines, with the correct location under the measurement line where the image peak has a minimal depth.

4.6 Conclusions

This chapter has detailed the concept, structure and implementation of a frequency domain based numerical simulation capable of producing time histories suitable for use with the imaging method described in Chapter 3. A basic form of the numerical simulations has been described, from which modifications have been made so that the implications of some limitations and omissions from the imaging method can be examined. Numerical simulation is more appropriate for these investigations, as it allows for a level of control of soil and wave parameters not possible in the field.

Error in the estimated wavespeed used in the post-processing has been evaluated. It has been shown that provided the error is not more than approximately 10% the imaging method is capable of forming an image of the target, although there may be some moderate inaccuracy in the location of the image peak. For higher levels of wavespeed measurement error the imaging method will produce increasingly poor images, and will eventually fail to detect a target.

Two types of variation in the wavespeed as functions of depth have been considered; continuous variation and step variation. The former of these attempted to replicate the increase in wavespeed with depth caused by over-burden pressure. For small increase the imaging method is sufficiently robust to

enable an image of the target to be formed. For high levels of variation, in the example given 40% increase from the surface value at the target, the imaging method fails to detect the target.

Consideration of step variation in the material properties shows that if the target object lies below a discontinuity in the material properties then the reflection from the boundary is sufficient to obscure the target. This is true even for moderate increases in the impedance (a factor 1.9 in the given example). The imaging method is capable of detecting the target if the material lies in the upper medium. This is true even in the limiting case of a rigid boundary.

Finally the effects of the target object lying outside the measurement plane are examined by simple modifications to the numerical simulations. The imaging method is found to be robust to out of plane distances plausible in experimental measurement.

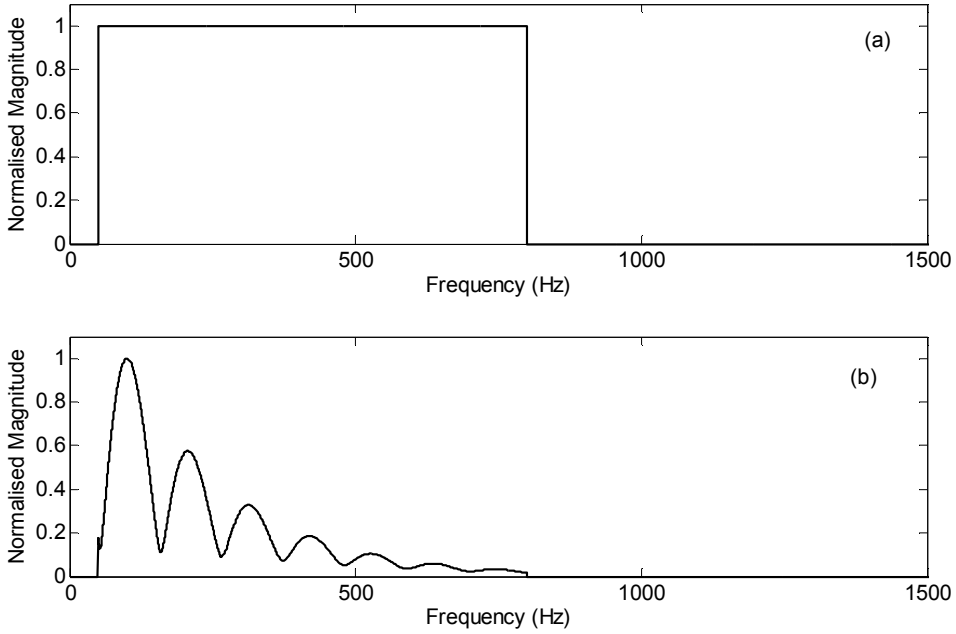

Figure 4.1 - Plot of the magnitude of the Fourier transform of (a) the reference signal, and (b) an example measurement geophone signal.

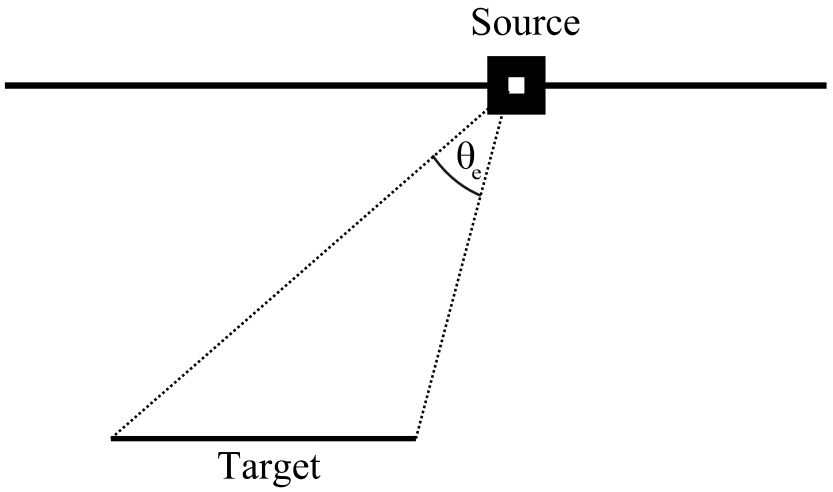

Figure 4.2 – Diagram showing the angle used for calculation of the portion of the energy of the source that is considered to reach the target object, in this case an arbitrarily located linear horizontal target. θ_e is the angle subtended by the target.

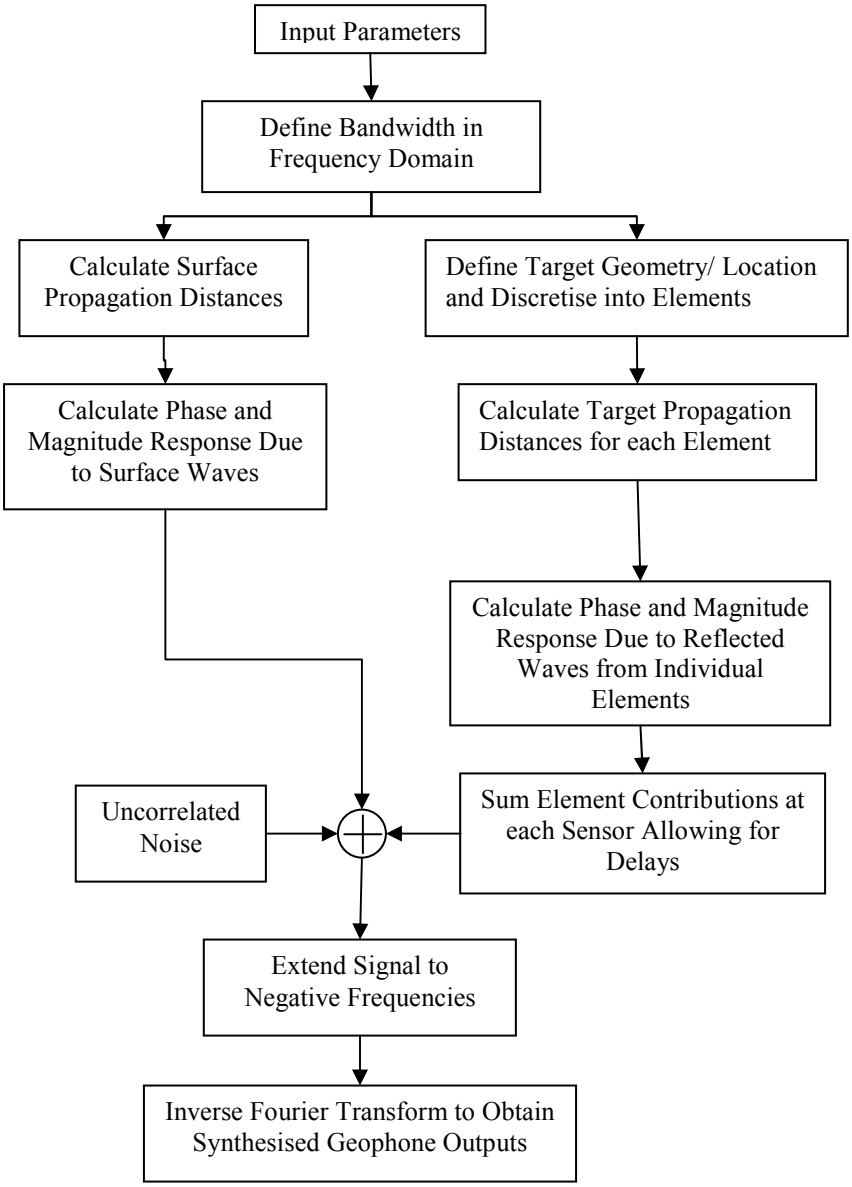

Figure 4.3 – Flow chart of the steps used in constructing the basic simulations.

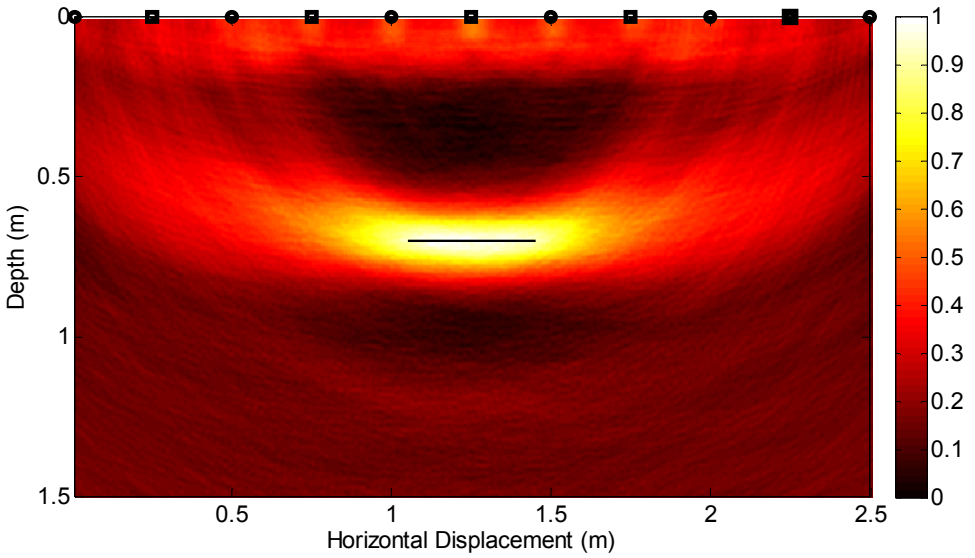

Figure 4.4 - Cross-sectional image through the ground produced by the imaging method using simulated time histories. The surface sensors are denoted by circles, the surface source locations by squares, and the location of the target by the black line. The scale is normalised to the peak image value. The image was formed using the parameters shown in Table 4.1.

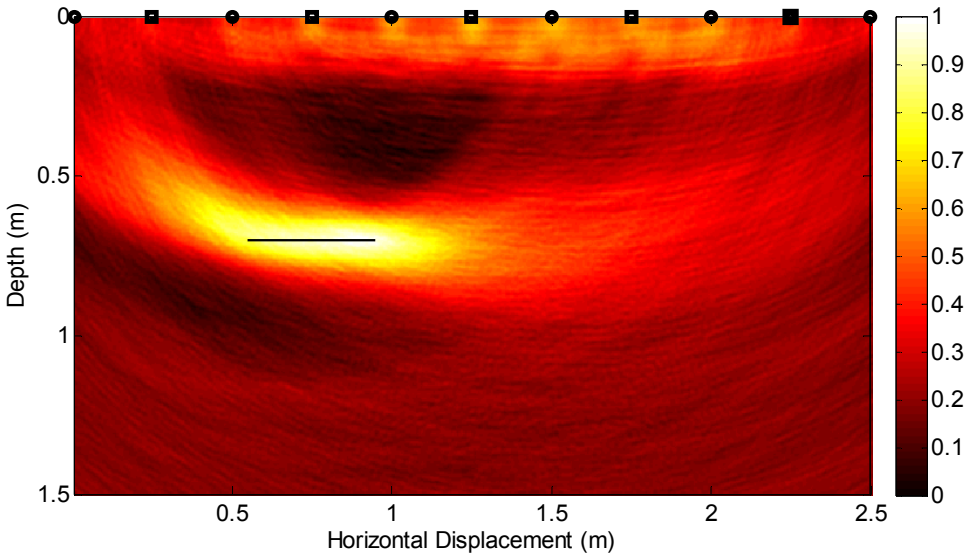

Figure 4.5 - As figure 4.4 but with the target shifted 0.5 m to the left.

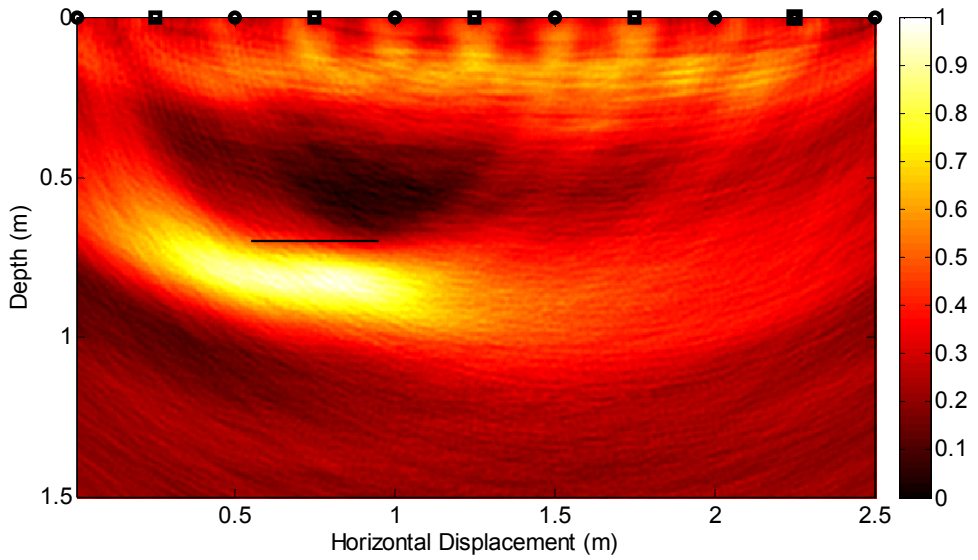

Figure 4.6 - Cross-sectional image through the ground produced by the imaging method using simulated time histories. The surface sensors are denoted by circles, the surface source locations by squares, and the location of the target by the black line. The scale is normalised to the peak image value. The image was formed using the parameters shown in Table 4.1 and the post-processing was applied with a wavespeed of 110 ms^{-1}, corresponding to a 10% overestimate.

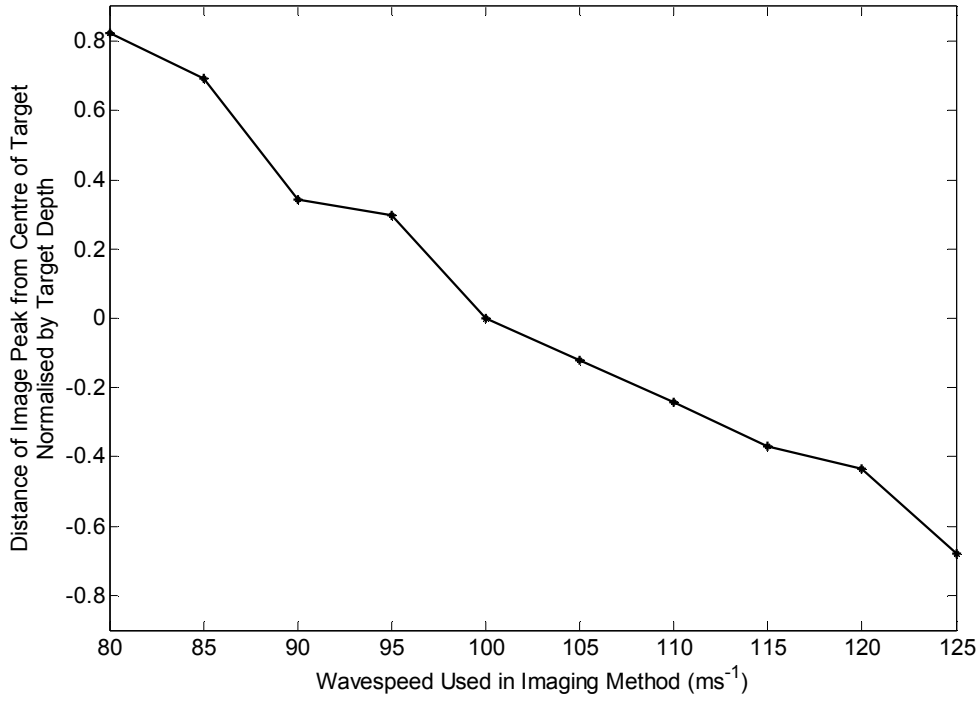

Figure 4.7 - Plot of the variation of the distance between the image peak and the centre of the actual target location, normalised to the depth of the target, as a function of the wavespeed used in the post-processing of the imaging method. The actual target depth is 0.7 m. The wavespeed used in calculation of the simulated time histories was 100 ms^{-1}. Negative values of the distance correspond to the image peak being deeper than the actual target location.

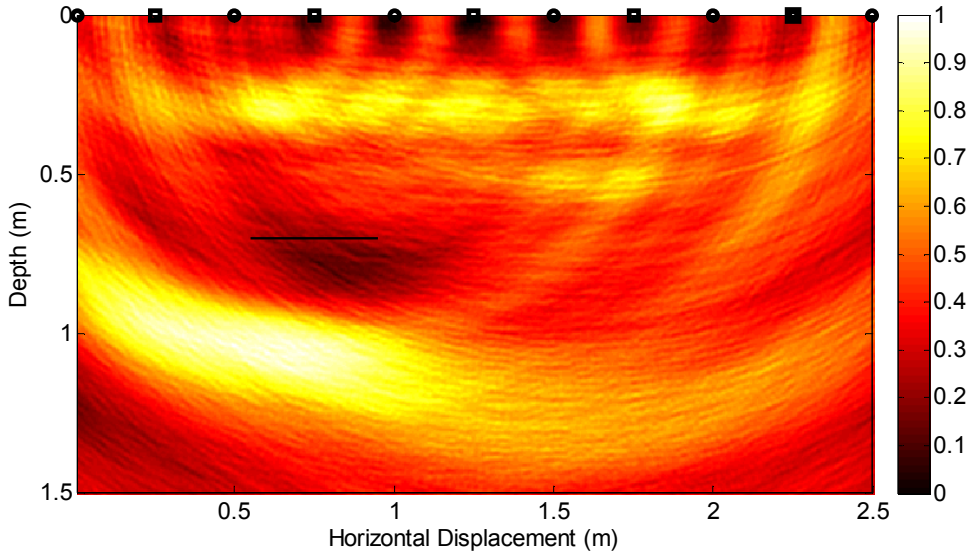

Figure 4.8 - Cross-sectional image through the ground produced by the imaging method using simulated time histories. The surface sensors are denoted by circles, the surface source locations by squares, and the location of the target by the black line. The scale is normalised to the peak image value. The image was formed using the parameters shown in Table 4.1 and the post-processing was applied with a wavespeed with of 130 ms^{-1}, giving a 30% overestimate.

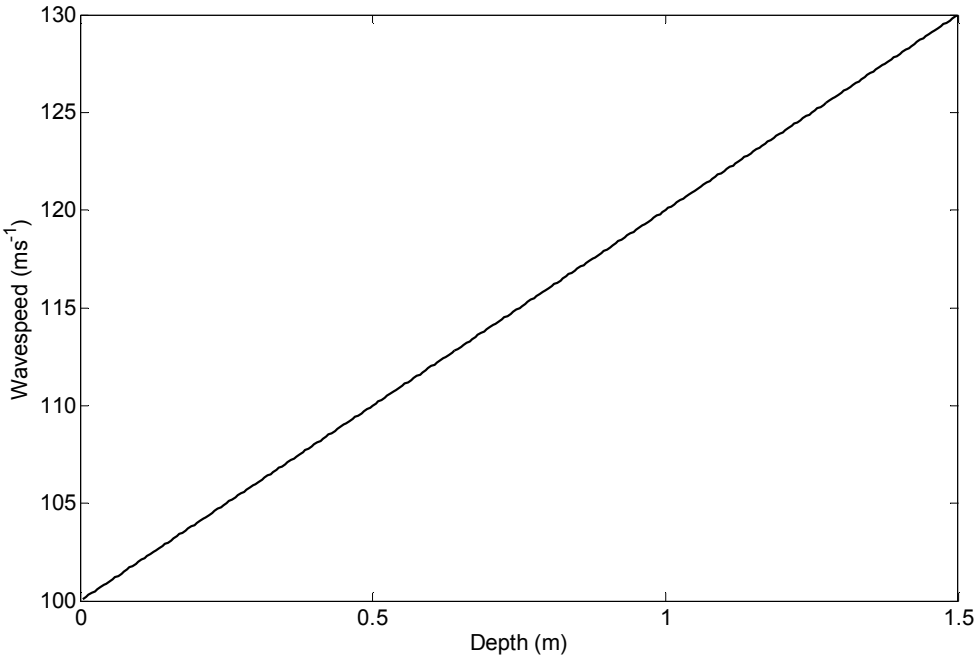

Figure 4.9 – Linear depth-velocity profile used in the numerical simulation that produces Figure 4.10.

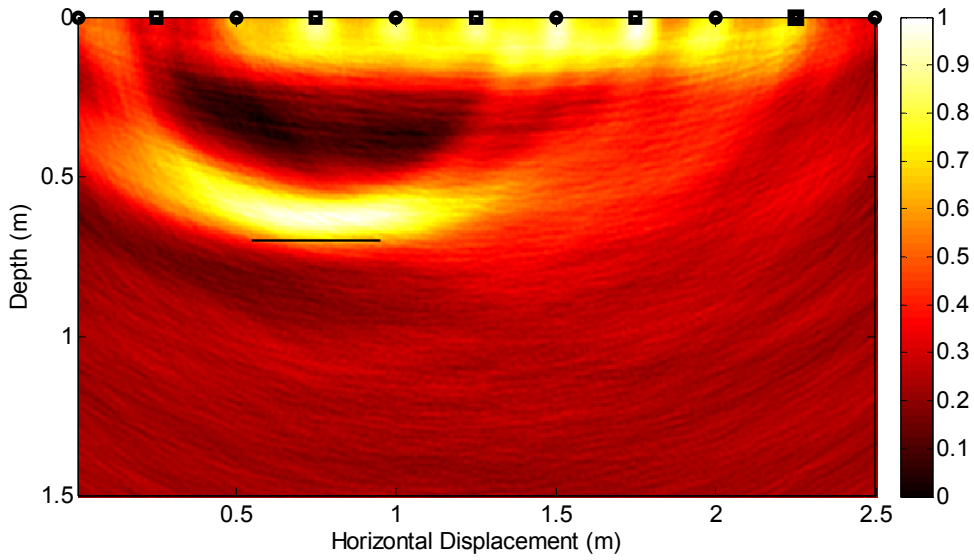

Figure 4.10 - Cross-sectional image through the ground produced by the imaging method using simulated time histories. The surface sensors are denoted by circles, the surface source locations by squares, and the location of the target by the black line. The scale is normalised to the peak image value. The image was formed using the parameters shown in Table 4.1 and the linear velocity depth profile shown in Figure 4.9.

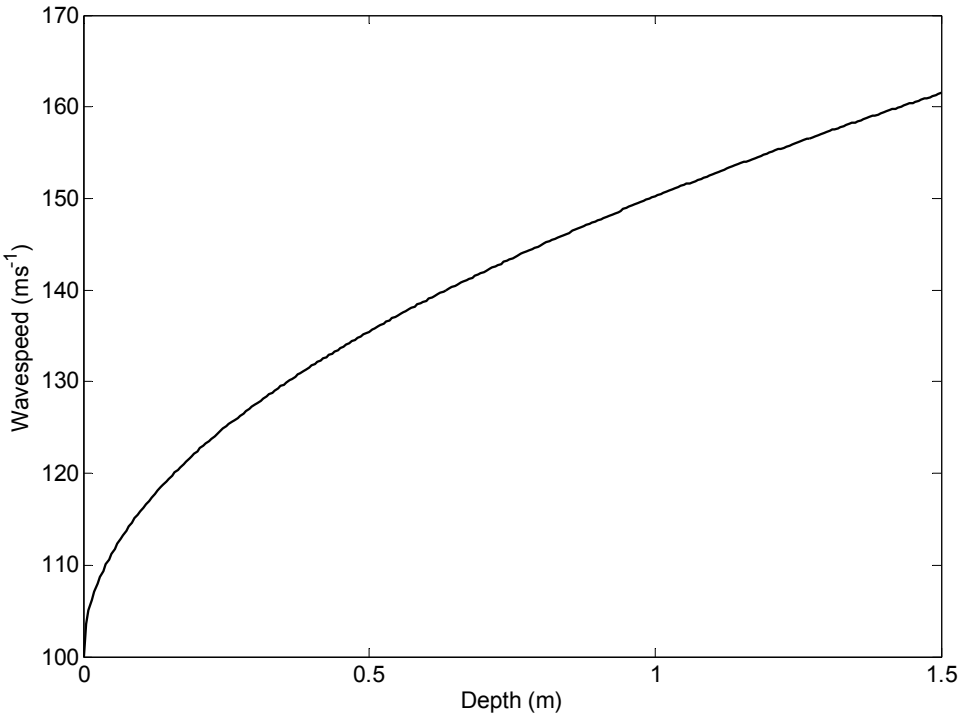

Figure 4.11 – Depth-velocity profile used in the numerical simulation that produces Figure 4.12.

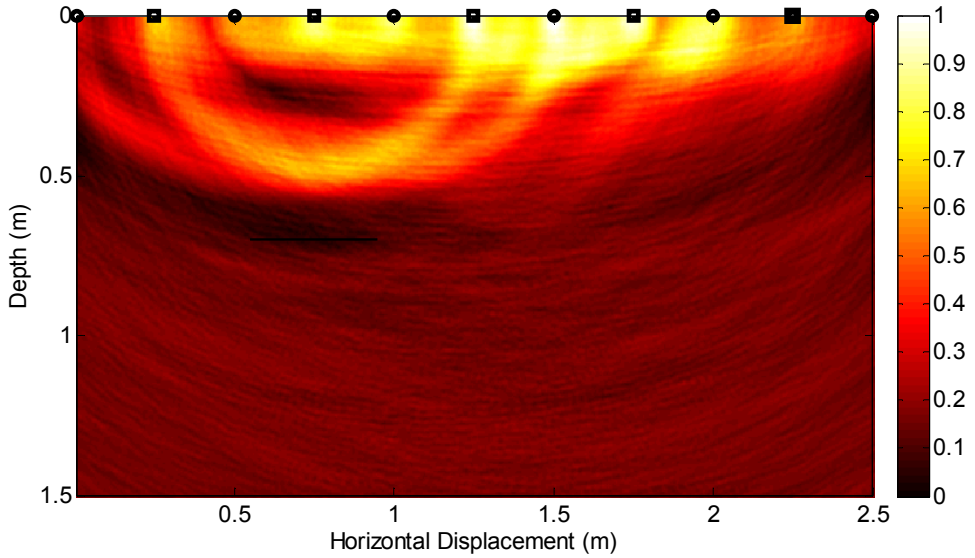

Figure 4.12 - Cross-sectional image through the ground produced by the imaging method using simulated time histories. The surface sensors are denoted by circles, the surface source locations by squares, and the location of the target by the black line. The scale is normalised to the peak image value. The image was formed using the parameters shown in Table 4.1 and the velocity depth profile shown in Figure 4.11.

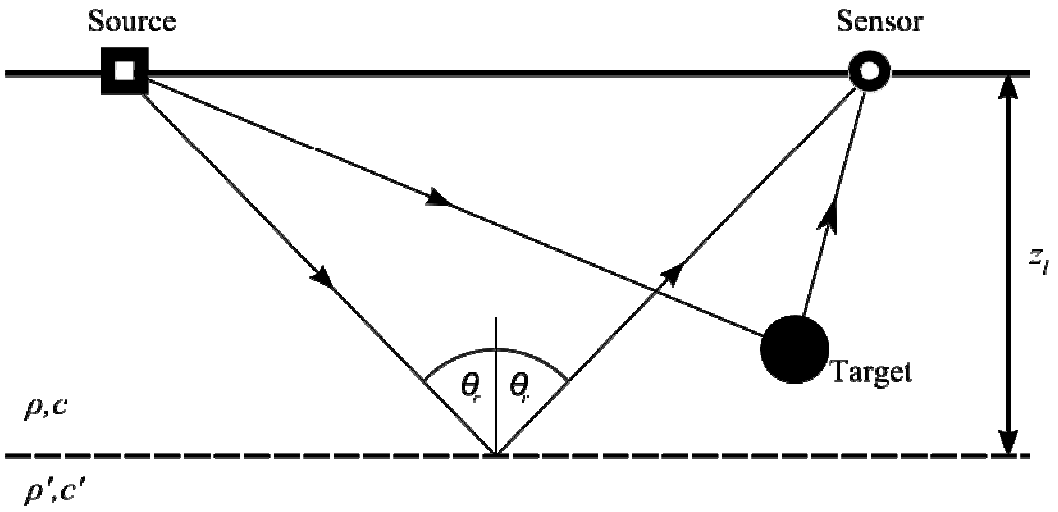

Figure 4.13 - Diagram of the propagation paths considered when the target is in the upper medium of a system with a discrete change in the material properties, from density ρ and wavespeed c in the upper medium to a density ρ' and wavespeed c' in the lower medium.

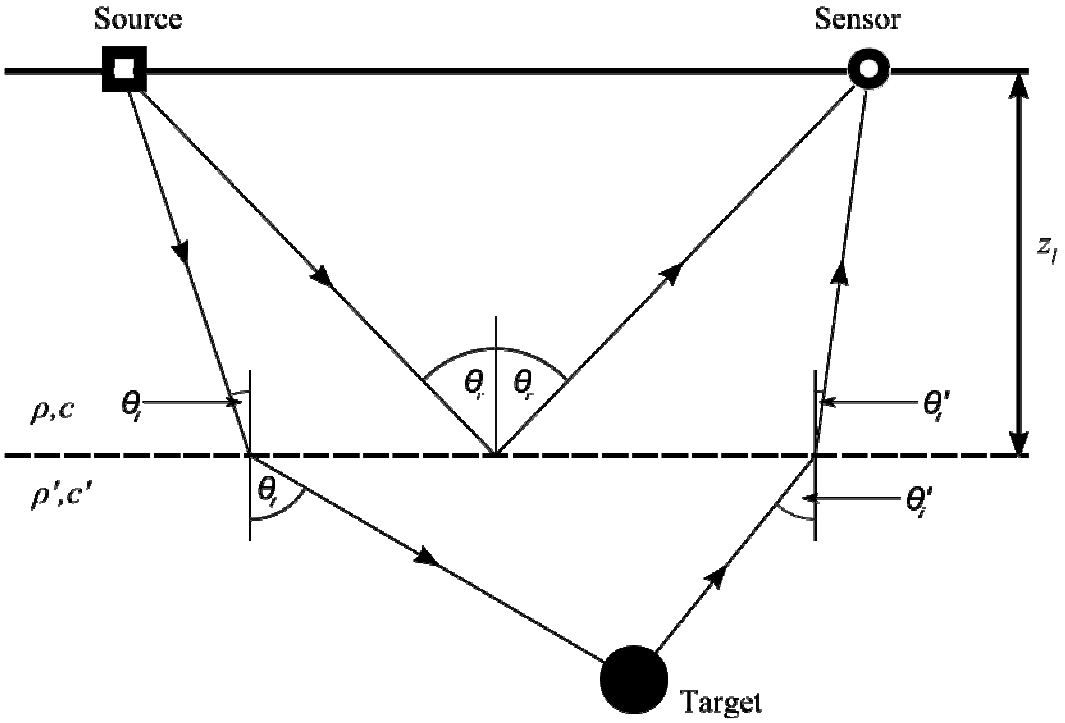

Figure 4.14 - Diagram of the propagation paths considered when the target is in the lower medium of a system with a discrete change in the material properties, from density ρ and wavespeed c in the upper medium to a density ρ' and wavespeed c' in the lower medium. The assumption is made that $c' > c$ so that the propagation paths bend away from the normal at the boundary.

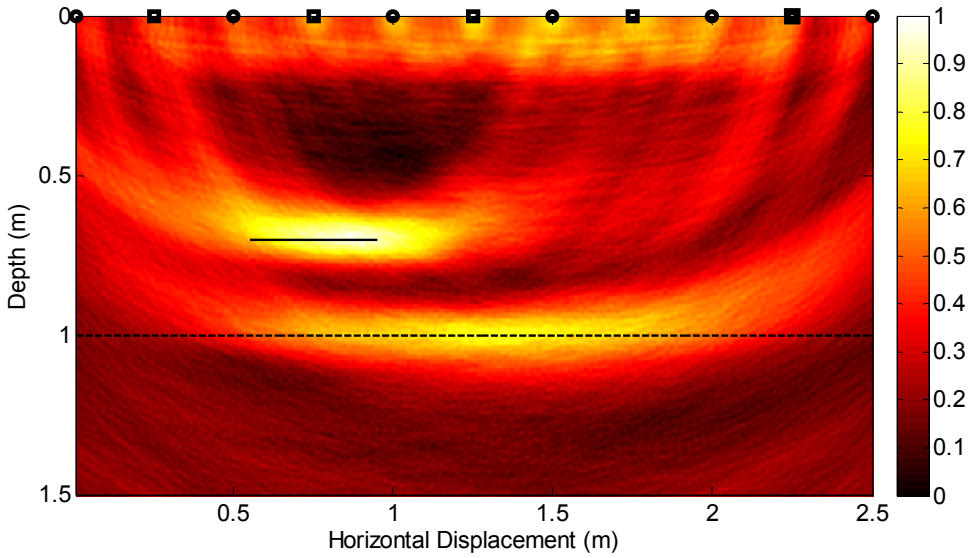

Figure 4.15 - Cross-sectional image through the ground produced by the imaging method using simulated time histories. The surface sensors are denoted by circles, the surface source locations by squares, and the location of the target by the black line. The scale is normalised to the peak image value. The image was formed using the parameters shown in Table 4.1. The density in the upper and lower layers was taken to be 2000 kgm^{-3} and 2300 kgm^{-3} respectively, and the propagation speed of the reflected wave 100 ms^{-1} in the upper medium and 167 ms^{-1} in the lower medium. The boundary between the two media is at 1 m and is shown by the dashed line.

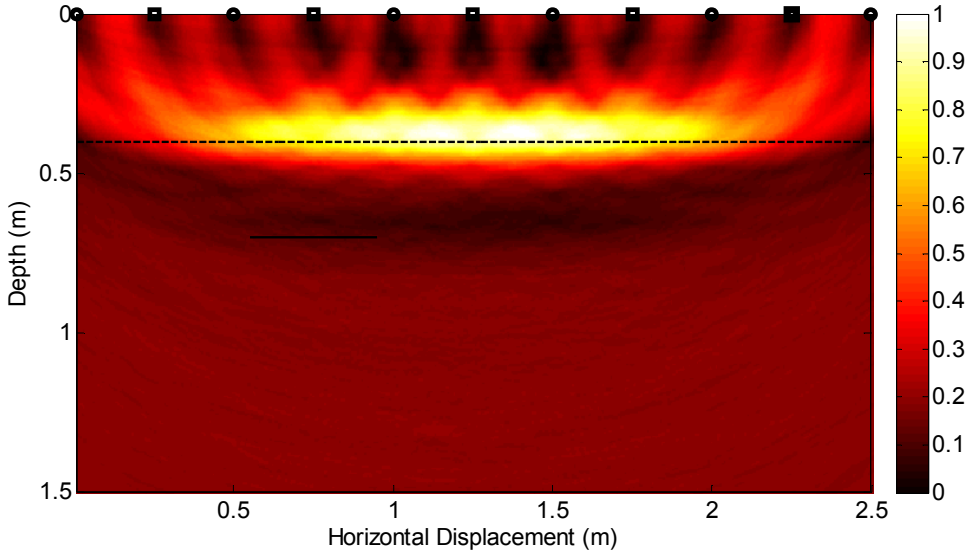

Figure 4.16 - Cross-sectional image through the ground produced by the imaging method using simulated time histories. The surface sensors are denoted by circles, the surface source locations by squares, and the location of the target by the black line. The scale is normalised to the peak image value. The image was formed using the parameters shown in Table 4.1. The density in the upper and lower layers was taken to be 2000 kgm^{-3} and 2300 kgm^{-3} respectively, and the propagation speed of the reflected wave 100 ms^{-1} in the upper medium and 167 ms^{-1} in the lower medium. The boundary between the two media is at 0.4 m and is shown by the dashed line.

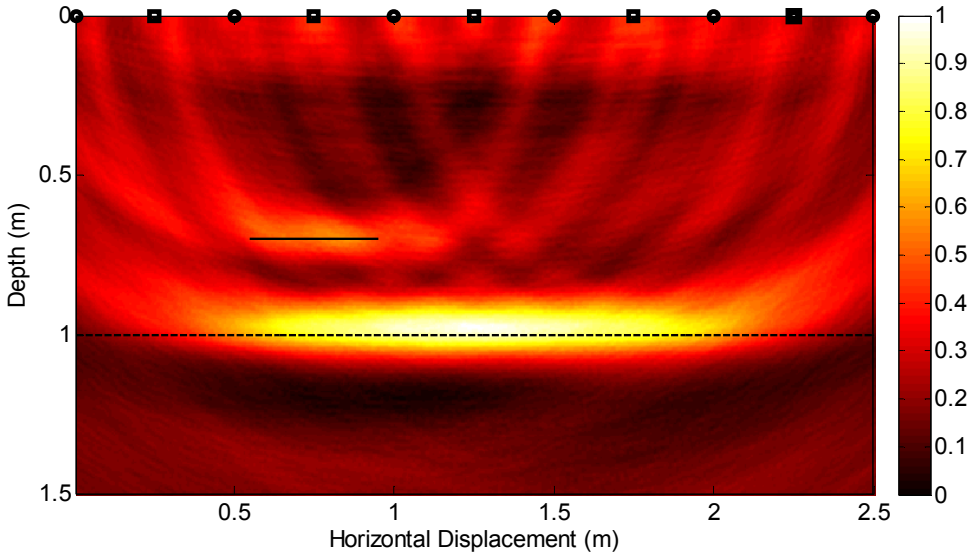

Figure 4.17 - Cross-sectional image through the ground produced by the imaging method using simulated time histories. The surface sensors are denoted by circles, the surface source locations by squares, and the location of the target by the black line. The scale is normalised to the peak image value. The image was formed using the parameters shown in Table 4.1. The propagation speed of the reflected wave 100 ms^{-1} in the upper medium. The lower medium has a large impedance to replicate a rigid boundary. The boundary between the two media is at 1 m and is shown by the dashed line.

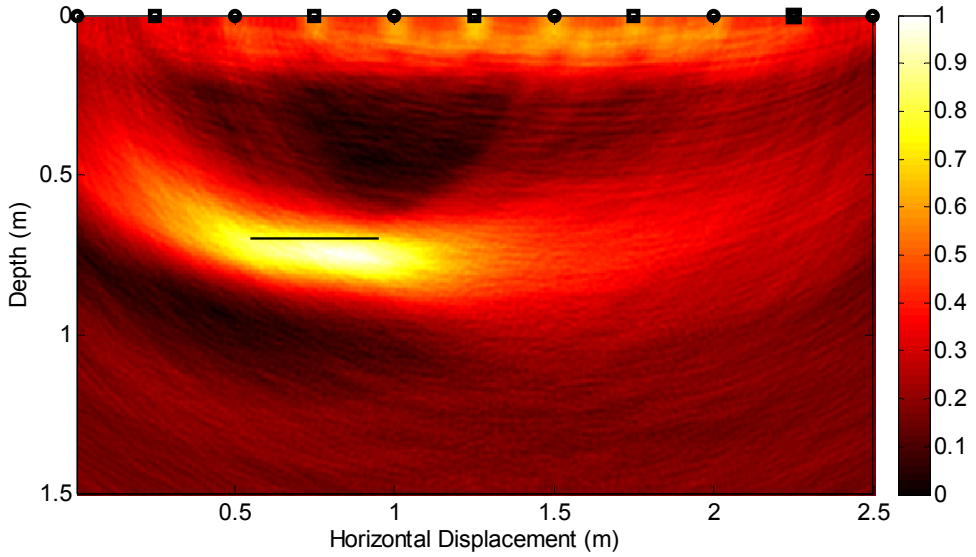

Figure 4.18 - Cross-sectional image through the ground produced by the imaging method using simulated time histories. The surface sensors are denoted by circles, the surface source locations by squares, and the location of the target by the black line. The scale is normalised to the peak image value. The image was formed using the parameters shown in Table 4.1. The target has been shifted by 0.25 m from the measurement plane.

TABLE I. Parameters used in the imaging algorithm simulation.

Parameter	**Value**	**Symbol**
Spatial Discretisation	5 mm^2	N/A
Reflected Wavespeed	100 ms^{-1}	c_{Rl}
Direct Wavespeed	100 ms^{-1}	c_D
Surface Wave Amplitude (Relative to Body Wave Amplitude)	1	α
Uncorrelated Noise Level (Relative to Body Wave Amplitude)	0.1	N/A
Body Wave Hysteretic Damping Coefficient	0.1	η_{Rl}
Surface Wave Hysteretic Damping Coefficient	0.1	η_D
Reference Distance for Geometric Attenuation	0.1 m	d_{ref}
Reflected Wave Geometric Attenuation Power	1	n_{Rl}
Direct Wave Geometric Attenuation Power	1	n_D
Spatial Filtering	On	N/A
Input Frequency Range	50Hz – 1 kHz	N/A

5. Source Design and Characterisation

Chapter 5

Source Design and Characterisation

5.1 Introduction

In an imaging method where seismic reflections are used to locate a buried object it is preferable to input only one wave type into the ground to prevent multiple reflections being measured at the surface from a single buried reflector. The advantages of using shear waves for the imaging method were shown in Chapter 3, with the work of Chapter 4 demonstrating the method using numerical simulations. The aim, in this chapter, is to design and experimentally verify the source to be used in the imaging experiments. The chapter begins by describing the design of the sources under evaluation. Section 5.3 compares the performance of two possible shear sources. Sections 5.4 and 5.5 detail further experimentation on the chosen shear source, with a vertical source used for comparison. Surface and buried sensors are used in these sections respectively. Finally conclusions are drawn in Section 5.6.

5.2 Source Design

At the heart of the vibration source was a Wilcoxen Research F4 inertial shaker. As it is an inertial shaker it requires only a single attachment to the structure to be excited. Whilst the shaker could be placed directly onto the ground and excited to produce seismic vibrations, coupling platforms were used. This was to improve the coupling of the shaker to the ground and enable horizontal excitation. Two such platforms were evaluated experimentally.

The first coupling platform designed was chosen for the purpose of flexibility in the initial feasibility stages of the project. The shaker could be coupled to this platform such that its motion was either perpendicular or parallel to the surface of the ground. The platform was constructed of aluminium with steel prongs attached to couple the platform to the ground. A schematic of the platform is given in Figure 5.1, and it is shown on the right of the photograph of Figure 5.2. This coupling platform has an approximately square base, and is henceforth referred to as the low aspect ratio coupling platform.

Whilst this coupling platform was useful for initial experimentation, once the use of shear waves was decided upon a second coupling platform was constructed that could only be orientated such that vibration was parallel to the ground's surface. This consisted of an aluminium block to which the shaker could be attached, with the block bolted to a single line of prongs for insertion into the ground. Reinforcing struts were added to stiffen the structure. A schematic of the platform is given in Figure 5.3, and it is shown on the left of the photograph of Figure 5.2. This coupling platform is henceforth referred to as the high aspect ratio coupling platform.

The relative merits of these two designs are assessed in Section 5.3.

5.3 Comparison of Shear Sources

The aim of the coupling platforms is to preferentially generate shear waves. The relative performances of the two coupling platforms at this task were compared by measuring the amplitude of motion of ground's surface close to the seismic sources during an excitation. The signal generation and measurement equipment are shown schematically in Figure 5.4. A laptop computer was used to generate excitation signals and was connected to a shaker amplifier produced by Wilcoxen Research specifically for the inertial shaker used. The geophones were input/output SM-9's, which were attached directly into an eight channel Prosig P-8000 data acquisition unit. The laptop was connected to the acquisition unit trigger channel to ensure triggering operated reliably and was repeatable.

The experimental arrangement is shown in Figure 5.5. Two sets of three mutually orthogonally orientated geophones were located 0.5 m from the source. One set was located in the direction of the motion of the source, with the other set perpendicular to this. For the measurements the source was set to produce a chirp ranging between 50 Hz and 1 kHz and lasting 10 seconds. Evaluation of the two sources was performed at the same test site, although not on the same day. Consequently, amplitudes are only compared between measurements made during the same day.

The RMS amplitudes of the surface velocity are shown in Figures 5.6 and Figure 5.7 for the low and high aspect ratio coupling platforms respectively. The geophone numbers correspond to the

numbering in Figure 5.5. As the purpose of the source is to generate shear waves, in preference to the exclusion of all other wave types, it is desired that either geophone number 1 or number 6 should dominant the measured response. This is not observed for the low aspect ratio coupling platform. Instead geophone 4, orientated horizontally and in line with the direction of excitation of the shaker, measured the largest signal. This is because of the approximately square base of the coupling platform, which means that in the direction of excitation there is a large part of the platform in contact with the ground. This seems to cause large amounts of surface compressional waves or Rayleigh waves, with the presence of a relatively large vertical component of motion (as indicated by the relatively high output of the number 5 geophone) supporting this interpretation.

The second coupling platform has a much smaller surface in contact with the ground in the direction of excitation. This can thus be expected to reduce the amount of energy that goes into exciting waves in this direction. This is observed in Figure 5.7, where the RMS amplitude of geophone number 1 now dominates, as desired. This coupling platform thus seems to preferentially generate shear waves in the direction perpendicular to its long axis, and is therefore used for all further shear wave generation.

The results of this section can be compared with the theoretical results of Chapter 2. For a point horizontal source it is predicted that shear wave motion should dominate in a direction perpendicular to the direction of excitation and reduce to zero parallel to the direction of the excitation. The directivity of the Rayleigh, compressional and shear vertical waves are predicted to be opposite to this. These directivities are broadly observed. Problems arise in comparison with the theoretical work when attempting to calculate the effects of the Differences between the theory and experiment occur due to both assumptions made in the theoretical work that are violated in experiment, such as near-field and linear assumptions (see Section 2.5), and experimental inaccuracy. Experimental inaccuracies include factors such as cross-sensitivity of the geophones, small misalignment of sources and sensors, and variability in the coupling of the sensors with the ground. Note that direct comparison with numerical values calculated from Chapter 2 is not possible due to the frequency dependence of the Rayleigh wave propagation. This means that numerical evaluation requires additional mathematics and, moreover, considerably more detailed information on coupling of the source to the ground if any meaningful comparison between analytical and theoretical values is to be made.

5.4 Wave Propagation with Surface Sensors

Further analysis of the high aspect ratio coupling platform was undertaken to confirm the generation of shear waves from the source. This section utilises phase information, rather than the amplitude information used previously. The aim was to compare the measured speeds of propagation from the

high aspect ratio coupling platform with those from a vertical source. The vertical source should primarily generate Rayleigh waves over the surface (See Section 2.3). As the shear wavespeed and the Rayleigh wavespeed are closely related, the wavespeeds measured from the high aspect coupling platform and the vertical source should be similar. As the low aspect ratio coupling platform allowed for vertical shaker excitation this coupling platform was used for the vertical source. Although the shaker could have simply been placed directly onto to the ground to create a vertical source, the use of the coupling platform was found to increase the transmission into the ground.

Propagation wave speeds were calculated by measuring the time of flight between a reference geophone and surface measurement geophones. The input signal used was a broadband random excitation between 50 Hz and 1 kHz. The time of flight was estimated using generalised cross-correlation functions, as outlined in Section 3.4.1. Specifically, the SCOT was used with the data broken into 20 equal length segments and averaged to allow for calculation of the coherence function. Enveloping was achieved using the Hilbert transform method described in Section 3.4.2. The signal generation and measurement is the same as that shown in Figure 5.4.

A direct method for calculating the propagation wavespeeds would be to simply divide the propagation times of the main peaks of the generalised cross-correlation functions by the propagation distances to obtain a value for the wavespeed at the sensor, and then repeat this sensor by sensor. A preferable method is to plot the propagation times as a function of the propagation distance. For ideal propagation at a constant wavespeed this should yield a linear relation, with the reciprocal of the gradient giving an estimate of the wavespeed.

This gradient method has several important advantages over the estimation of the wavespeed on a sensor by sensor basis. In the sensor by sensor method as each wavespeed value is an average wavespeed from the reference sensor to the measurement sensor, abnormal regions of the ground will affect the results of all sensors past these locations on the measurement line. Calculation of the gradient on a time-distance plot, however, provides an average of the wavespeeds of the speed of propagation between surface measurement sensors, rather than from the reference sensor. The cumulative contribution of errors from abnormalities is thus reduced. Furthermore, gradient estimation of the linear plots is numerically simple and naturally includes averaging in a way that is insensitive to anomalous results.

The orientation of the sensors used for measurement was chosen to be those for which the sensor response was the largest. The orientation of the sensors with relation to the source is shown in Figure 5.8. Other orientations produced weak responses at the sensors. The measurement line in both cases consisted of ten geophones spaced one metre apart, as well as a reference geophone located as close

as possible to the source. As the number of available geophones was insufficient to allow for this measurement to be performed in one run, the measurement distance was split into two separate equal length measurements. These used identical input signals and measurements were taken immediately after one another. Each measurement run had a separate reference geophone from which the cross-correlation functions are calculated.

With the vertical coupling platform attached, measurements were taken using both vertical sensors and horizontal sensors orientated parallel to the measurement line. Figure 5.9 shows an example generalised cross-correlation function, in this case that between the reference geophone and the furthest horizontal measurement geophone, 10 m away. There is a clear maximum at approximately 100 ms. There is also notable correlation at delay times less of that of the main peak.

Plotting the time delays corresponding to the largest peak in the cross-correlation functions as a function of the propagation distance gives the approximately linear plot shown in Figure 5.10. The linear fit to the data is shown by the dashed line, and produces a gradient of 9.3 ms m^{-1}. This equates to an average wavespeed of (107±3) ms^{-1}, with wavespeed errors calculated from the best fit by standard data analysis methods [150]. Repeating the process for the vertically orientated source but with the horizontal geophones gives the peak time to propagation distance plot of Figure 5.11. The gradient of the linear fit to this data is 10.6 ms m^{-1}, implying a wavespeed of (95±2) ms^{-1}.

It is to be expected that when the motion of the source is orientated vertically the results of Section 2.3.2 should be observed. The result of interest is that for point vertical excitation, the Rayleigh wave should dominate the response. The point like assumption, whilst not fulfilled, is adequate as for the measured wavespeeds of around 100 ms^{-1} the wavelength should exceed the source dimensions until approximately 500 Hz.

As Rayleigh wave motion is composed of both vertical and horizontal motion, with the latter orientated in the direction parallel to that of propagation, the sensors considered should be dominated by the Rayleigh wave. They should therefore have the same dominant wavespeed. Whilst this is not precisely observed, their wavespeeds are sufficiently consistent to assume that a Rayleigh wave is dominating. There are also notable correlation values at delay values less than the main peak. These may correspond to compressional surface waves. Whilst there is theoretically no surface compressional wave in the far-field limit, surface compressional motion can be anticipated when the far-field assumption is relaxed (see Figure 2.10). An alternative explanation may be that early refractions from a subsurface layer are being observed [40]. Confirmation of the cause of these correlation peaks could be obtained by extending the measurement line further.

When using the high aspect ratio coupling platform only horizontal measurement geophones were used, as shown in Figure 5.8. An example of the cross-correlation function between the reference geophone and the furthest measurement geophone is shown in Figure 5.12. Here the main peak is clearly visible, with fewer regions of high correlation value around the main peak than in the correlation function of the vertical source and sensors shown in Figure 5.9. This is to be expected from the results of Section 2.3.3, which showed that for a source oriented parallel to the ground the shear horizontal wave will dominate the response completely in the direction perpendicular to the source motion. The corresponding peak time to propagation distance graph is given in Figure 5.13. The gradient of the linear fit is 9.4 ms m^{-1}, implying a wavespeed of (105±5) ms^{-1}.

All three of the measured wavespeeds are similar. This is to be expected as the shear and Rayleigh waves propagate with approximately the same speed (see Figure 2.1). It is concluded that both of the sources were producing waves with surface speeds and directions of motion consistent with those anticipated from the mathematical analysis in Chapter 2. In addition to these measurements reinforcing the experimental evidence that the high aspect ratio coupling platform is predominately producing shear waves, the measurement of the surface wavespeeds are later useful for the imaging experiments of Chapter 6.

It was stated in Chapter 2 that, whilst the Rayleigh wave is in theory non-dispersive, in practice it may exhibit dispersive behaviour if there is sufficient variation with depth of the soil properties near the surface. This is because the Rayleigh wave is a surface wave that only exists within a few wavelengths of the surface. Thus, if the material properties change with depth such that the wavespeed is significantly altered, it is to be expected that the wave would propagate in a dispersive manner. This effect is documented, and is the basis for the spectral analysis of surface waves (SASW) method [132, 133].

In general, wave propagation speeds in the ground increase with depth [101]. For the line of sensors used in the presented measurements low frequencies will increasingly dominate with increasing propagation distance due to the high attenuation. Consequently, for substantial variation of the wavespeed with depth, the Rayleigh wave will exhibit increasing wavespeed with propagation distance, causing the graphs plotted in Figure 5.10 and 5.11 to curve upwards at higher propagation distances. This is not observed. It can thus be concluded that, whilst there may be some variation of the wavespeed with depth, it is limited. Given that the lowest frequency inputted to the system is 50 Hz, corresponding to a wavelength of about 2 m for the wavespeeds measured, it can be concluded that the variation of the soil properties was not large in the first few metres of the ground.

5.5 Buried Sensor Experiments

Thus far when evaluating the source only surface sensors have been considered. Wave propagation through the ground does, however, vary from that over the surface. One obvious difference is in the motion due to Rayleigh waves. These will be less prominent at a given depth for higher frequencies due to the reduced penetration of the Rayleigh waves. Body waves can also be expected to behave differently when interacting with the surface rather than propagating through ground. It is necessary to measure the vibrations of the source directly through the ground in order to determine these effects.

Measurements were made with three cylindrical tri-axial sensors located at shallow depths. These were approximately 20 cm in length and buried at depths of 0.3 m, 0.6 m, and 0.9 m. A borehole driller was used to dig the holes for these sensors to minimise the disturbance to the surrounding soil. The sensors were left for several months before experiments were conducted to allow for the soil to settle. A schematic of the experimental setup is shown in Figure 5.14. The buried sensors were orientated such that there was a vertical element, a horizontal element parallel to the main axis of the sensor, and a horizontal sensor perpendicular to main axis of the sensor. Measurements were performed by placing both the low aspect ratio coupling platform acting as a vertical excitation source and the high aspect ratio coupling platform acting as a horizontal source, in turn, directly above the sensors. A broadband random excitation was then generated between 50 Hz and 1 kHz and the three sensor outputs recorded. Details of the signal generation and measurement equipment are identical to those in the previous section and shown schematically in Figure 5.4.

To examine the relative amplitude of the displacements the RMS value of the signals were again calculated. The results for the vertically orientated source are shown in Figure 5.15. The response of the vertically oriented sensor is larger than the two horizontal sensors, with the horizontal sensors giving reasonably similar responses. This corresponds with the work of Section 2.3.2 for the vertically orientated source. The similar responses of the horizontal sensors were expected from the axisymmetric nature of the problem.

The response of the sensors with the horizontal source is shown in Figure 5.16. The horizontal component parallel to the orientation of the source gives the largest displacement. The horizontal sensor orientated perpendicular to the excitation produces a relatively small output. These results are physically intuitive. The vertical component, which should in theory (as described in Chapter 2) be zero, instead has substantial amplitude. The exact cause of this vertical motion is unknown, but may be due to the platform rocking about its central axis during oscillation, creating a component of motion perpendicular to the surface of the ground.

It is not possible to measure accurate attenuation values over the range of depths considered. This is because the measurements were made with the sensors buried at different locations. Variability in soil properties and source coupling could interfere with the accuracy of any estimated values. Numerical comparison of amplitude is therefore constrained to the relative values measured at each sensor location. A qualitative comparison of the amplitudes from the data indicates that, for the vertically orientated source, the compressional wave measured by the vertical sensor suffers from much greater attenuation with depth than the measurements made with the horizontally orientated geophones. For the horizontally orientated source the attenuations of the measured signals with depth are approximately the same for all three sensors.

Note that it is not possible to provide meaningful numerical values from the theoretical analysis of Chapter 2 to compare with the results of the buried sensor experiments. This is because of the difficulties in calculating the value of the contribution from the Rayleigh wave in the experiments, relative to the other wavetypes. The amplitude of the Rayleigh wave at a given depth varies strongly with wavelength, meaning that the amplitude of a broadband signal at depth must be found by integrating over the frequency range of interest. Whilst this is theoretically possible, any meaningful numerical value needs to account for material damping of the Rayleigh wave and the coupling between the source and the ground. This information is highly localised, and its estimation is not possible from the experiments in this thesis.

The effects of geometric attenuation could be removed by scaling the data with reference to Equation (4.3). This however, suffers from the same problem: that simply scaling by Equation (4.3) would assume that the Rayleigh component is suffering from the same type of geometric attenuation. From the analysis of Chapter 2, this is not the case, and compensating for geometric attenuation by simple scaling would incorrectly amplify the frequency dependant Rayleigh component of the measured displacement.

The results using buried sensors confirm that the high aspect ratio coupling platform is preferentially generating shear horizontal waves, but also that these are propagating through the ground as well as along the surface. The results of this section also again confirm the work of theoretical chapter for both types of source.

5.6 Conclusions

For the generation of shear waves from a shaker it is necessary to couple the shaker to the ground using a platform. Two platforms were constructed and simple surface measurements undertaken to assess their relative performance. A coupling platform with a high aspect ratio was found to generate

shear waves well. This coupling platform was compared to a vertically orientated source, with both surface wavespeeds and through ground wave amplitudes measured. These were found to reinforce the previous conclusion that the high aspect ratio coupling platform was producing waves of shear and also to be in broad agreement with the theoretical results of Chapter 2. Wavespeeds were measured using surface sensors. They were determined by calculating the cross-correlation function with reference to a geophone located close to the source and finding the gradient of the approximately linear relationship between the propagation distance and the delay time of the main correlation peak. Cross-correlation functions for the shear source generally contained only one clear peak, confirming the theoretical prediction that shear horizontal wave generation should be pure in a direction perpendicular to the direction of the source excitation. Amplitude information from buried sensors was consistent with expectations, although the vertical component of motion with the shear source was higher than anticipated. This may be due to rocking of the source during its oscillations.

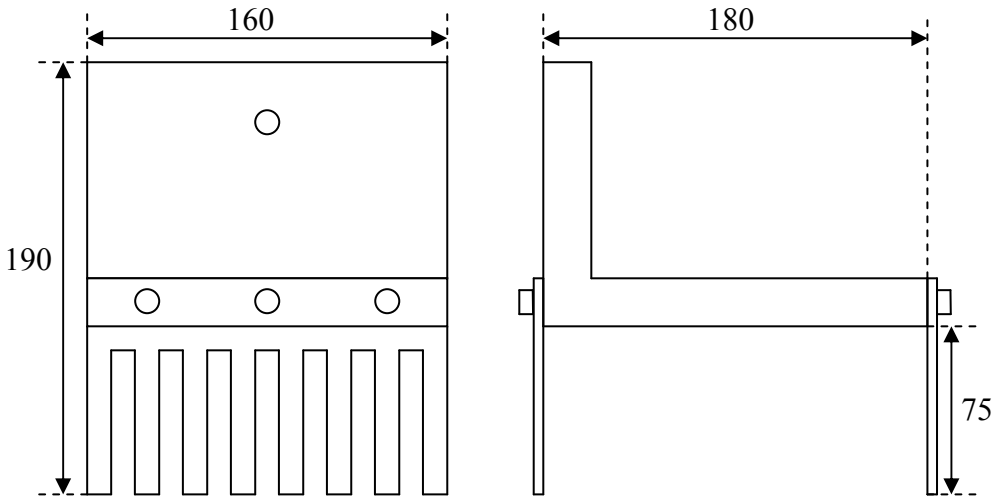

Figure 5.1 – Schematic of the low aspect ratio coupling platform. Dimensions are given in millimetres. The main platform structure was made of aluminium with the prongs made of steel.

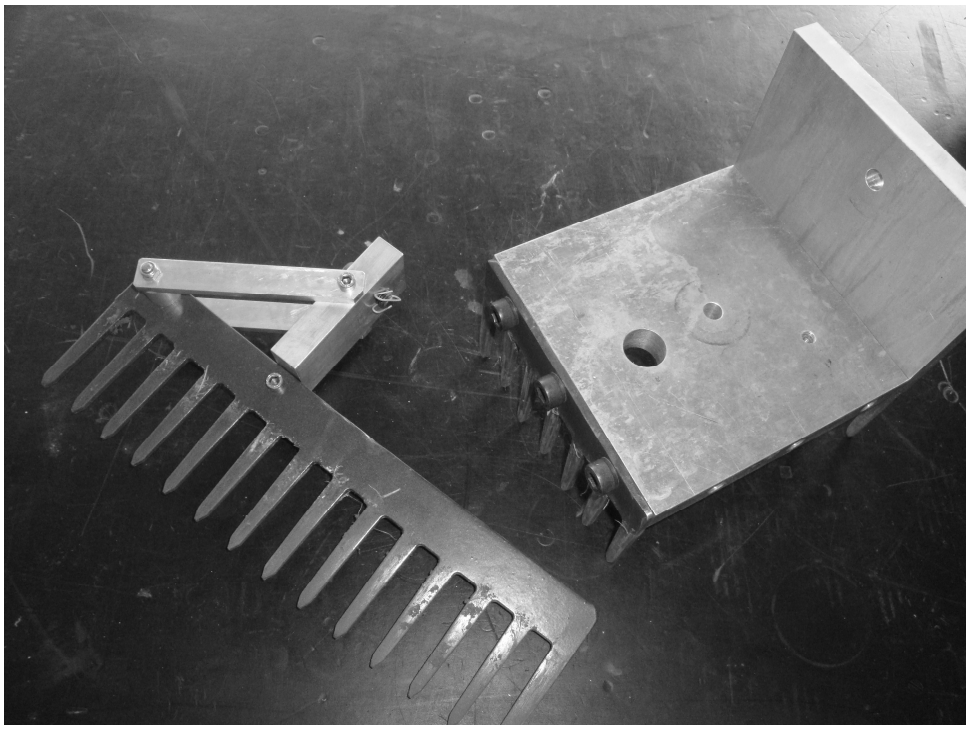

Figure 5.2 – Photograph of the low (left) and high aspect ratio coupling platform (right).

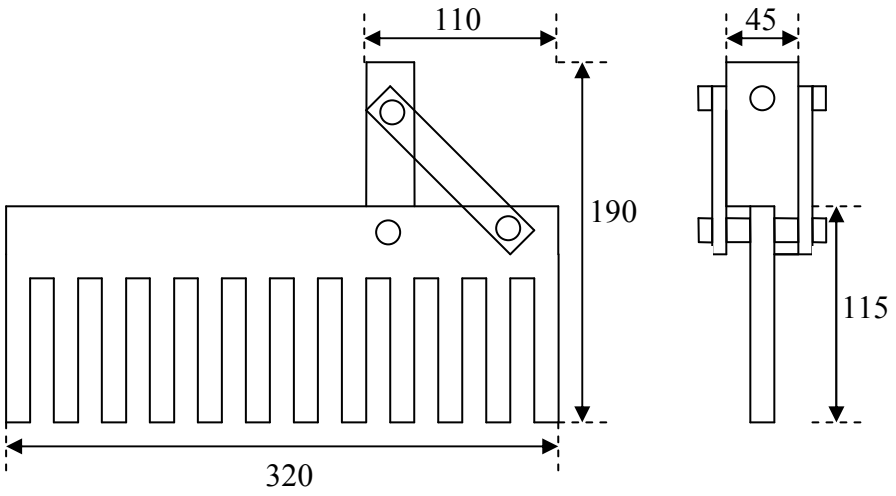

Figure 5.3 – Schematic of the high aspect ratio coupling platform, used for horizontal excitation. Dimensions are given in millimetres. The top platform structure was made of aluminium with the prongs made of steel.

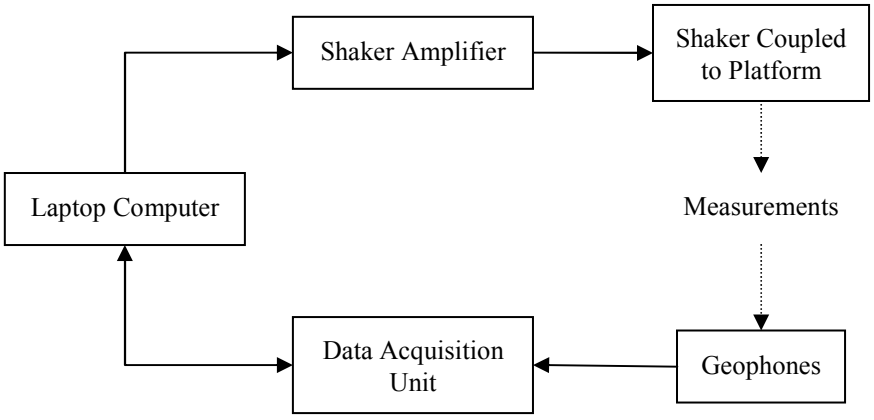

Figure 5.4 – Diagram of the equipment setup used for the generation of seismic waves and their measurement. The source and geophone arrangement are described in the text, and vary between specific experiments. The laptop computer was used to generate signals, to run the acquisition unit and to trigger the acquisition unit to begin measurement.

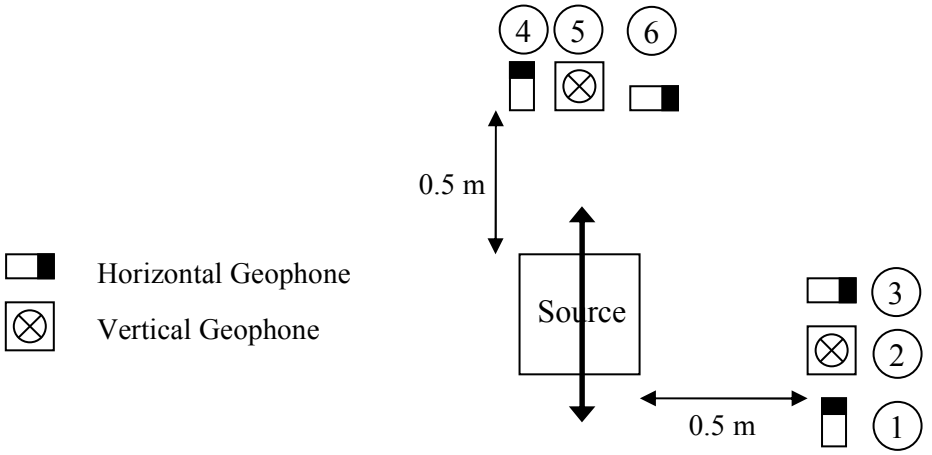

Figure 5.5 – Diagram of the experimental setup used for the evaluation of the directivity of the sources in terms of their amplitude. Both types of shear source platform are evaluated using this setup, with the direction of excitation of the shaker in both cases shown by the arrow over the source. The geophone numbers correspond to those in Figures 5.6 and 5.7 and are used when comparing the RMS amplitudes of the measured signals. The horizontal geophones are sensitive along their longer axis. Not to scale.

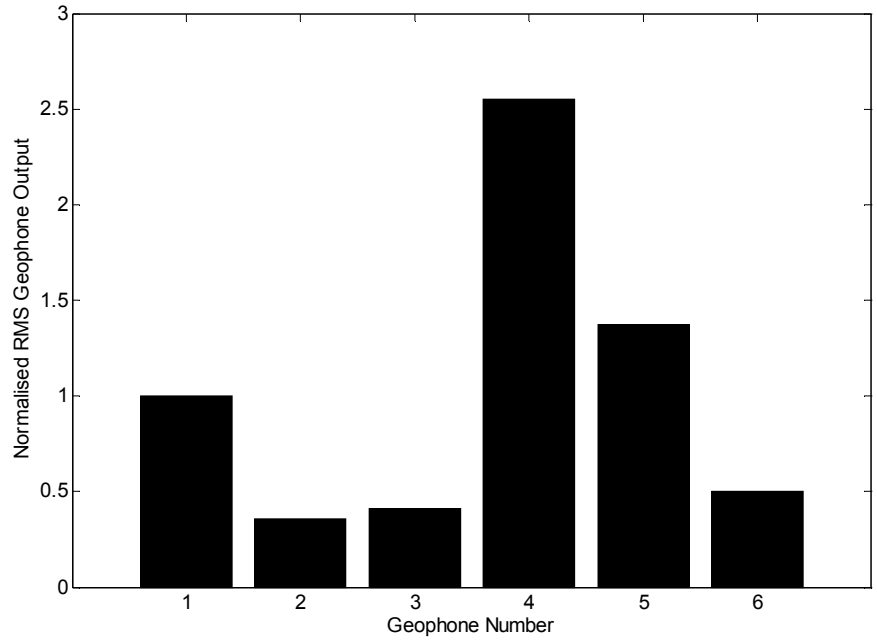

Figure 5.6 – Bar plot of the RMS output values of the geophones used in the experimental setup described in Figure 5.5 with the low aspect ratio coupling platform used as excitation. All values are normalised to the RMS value of geophone 1.

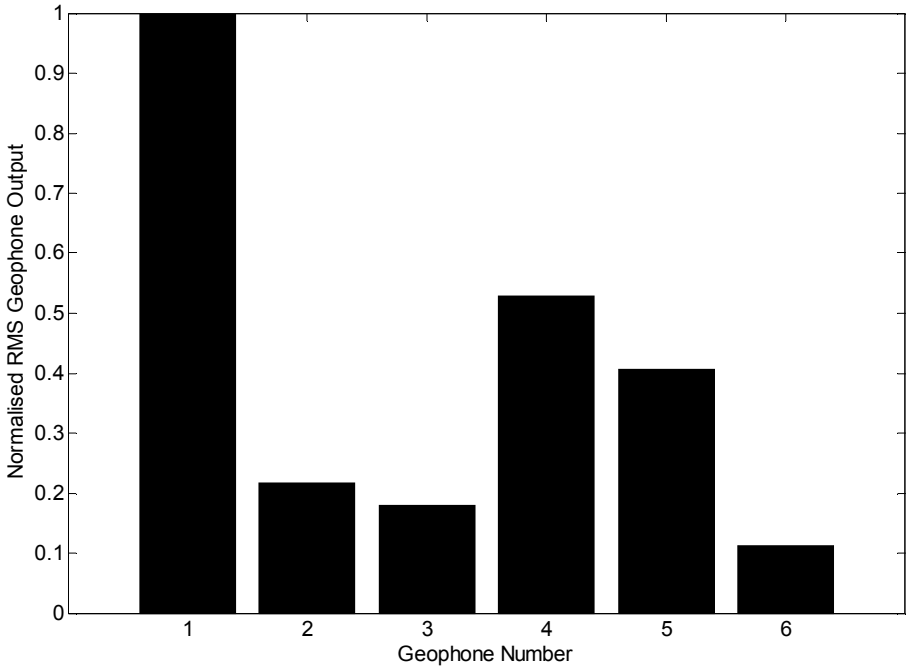

Figure 5.7 – Bar plot of the RMS output values of the geophones used in the experimental setup described in Figure 5.5 with the high aspect ratio coupling platform used as excitation. All values are normalised to the RMS value of geophone 1.

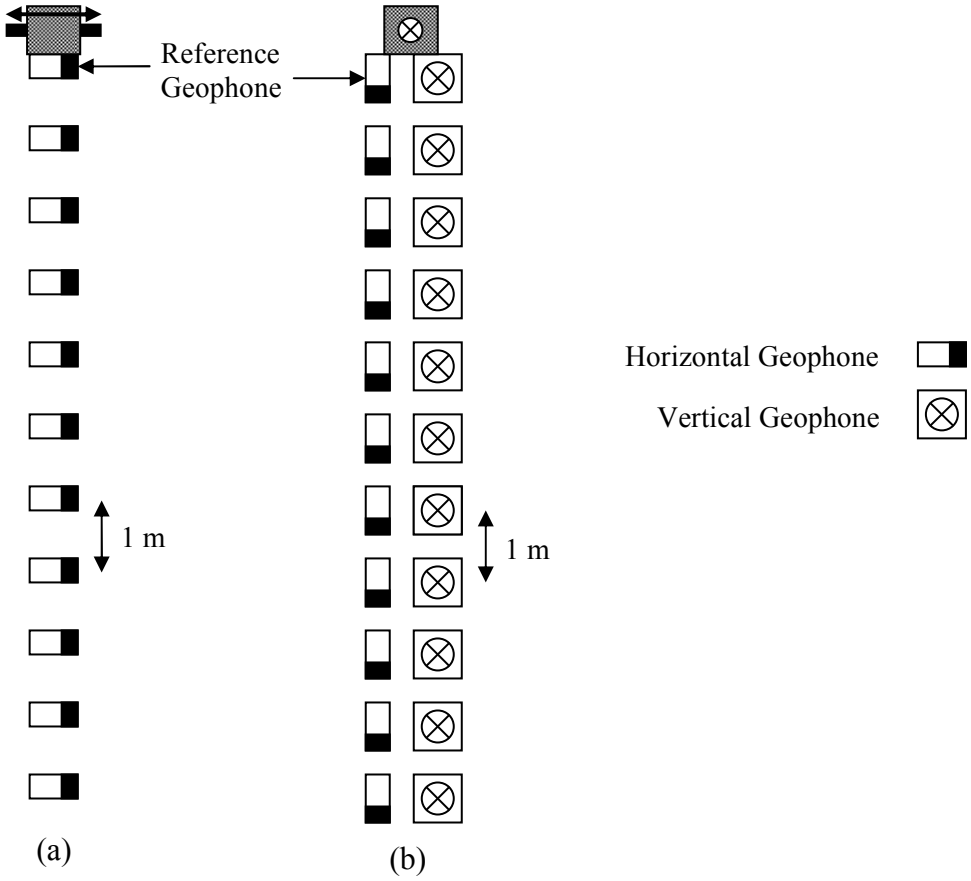

Figure 5.8 – Diagram of the experimental setup of the source and sensors for the surface experiments for the source characterisation experiments. (a) High aspect coupling platform acting as a horizontal excitation source; (b) low aspect ratio coupling platform acting as a vertical excitation source. The horizontal geophones are sensitive along their longer axis. Not to scale.

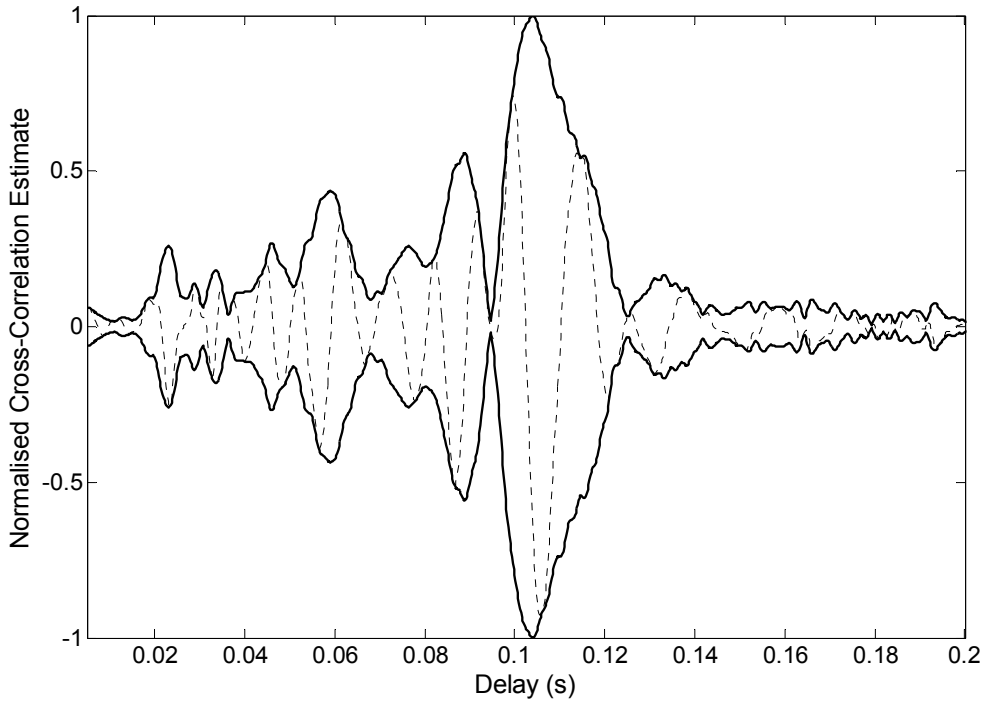

Figure 5.9 - Cross-correlation function between the horizontally orientated reference geophone and the furthest (10 m) measurement geophone. The low aspect ratio coupling platform with a vertically orientated excitation was used as a source. The cross-correlation function is normalisation to its peak (envelope) value.

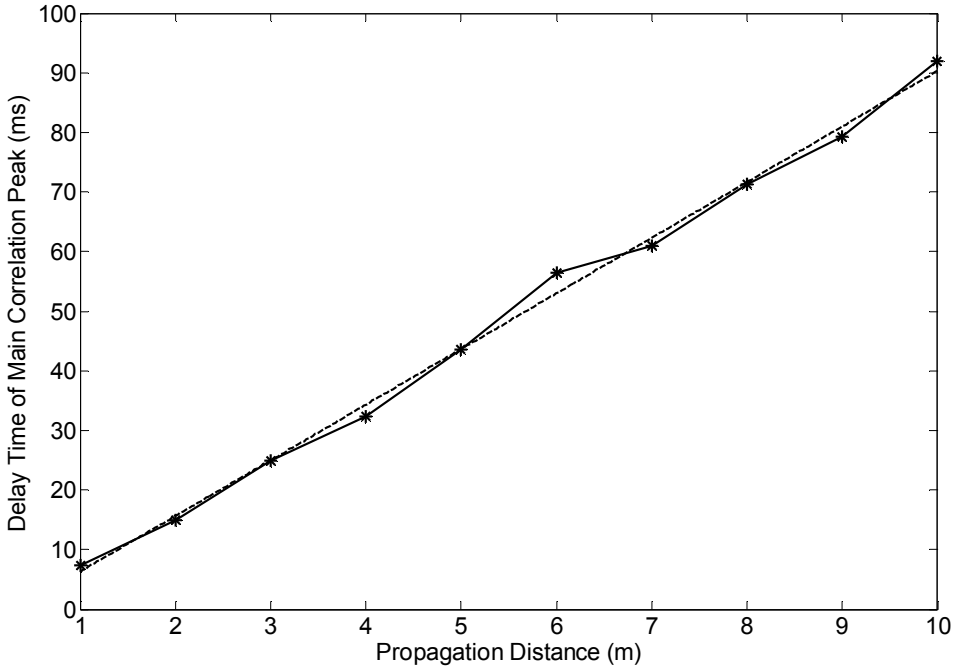

Figure 5.10 - Plot of the delay times of the main correlation peak as a function of the propagation distance for the vertically orientated geophones and the low aspect ratio coupling platform with a vertically orientated excitation as a source. The dashed line indicates the linear fit to the data.

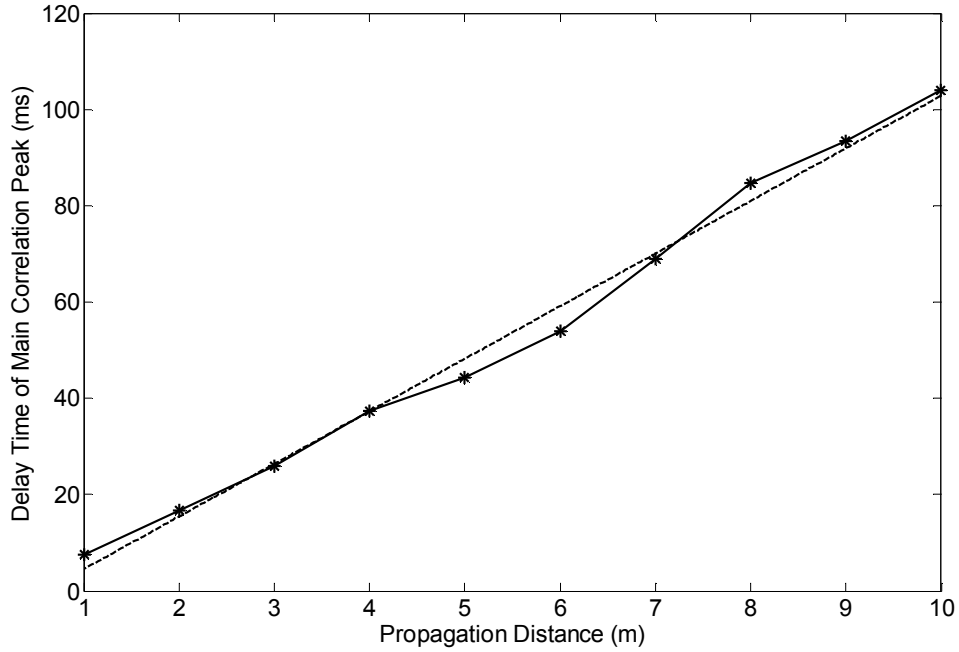

Figure 5.11 - Plot of the delay times of the main correlation peak as a function of the propagation distance for the horizontally orientated geophones and the low aspect ratio coupling platform with a vertically orientated excitation as a source. The dashed line indicates the linear fit to the data.

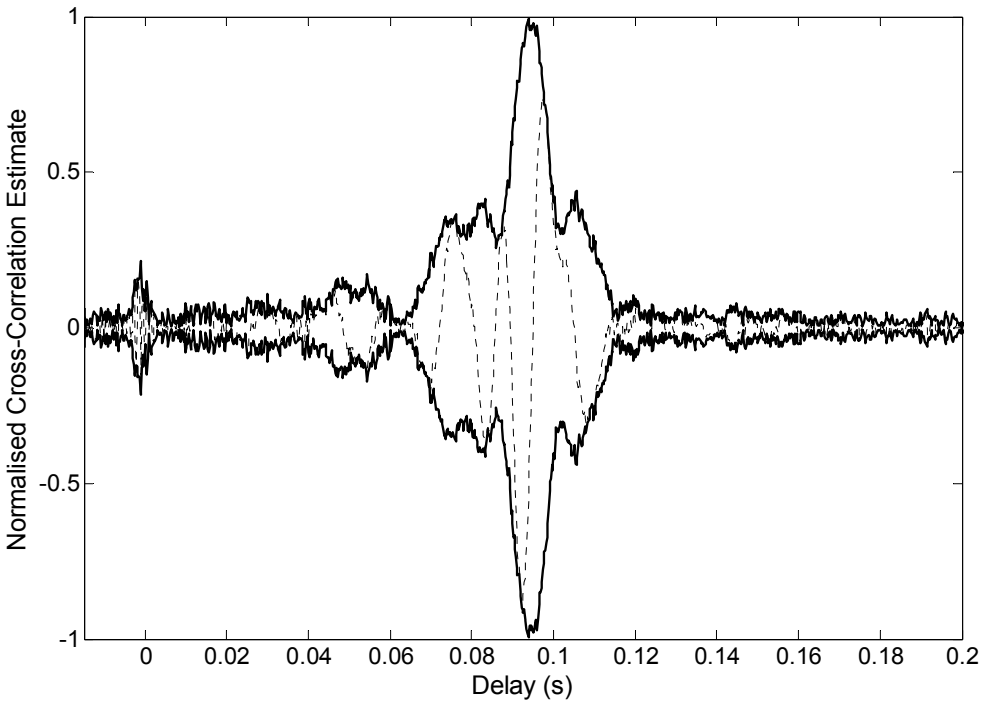

Figure 5.12 - Cross-correlation function between the reference geophone and the furthest (10 m) measurement geophone. The high aspect ratio coupling platform was used as the source. The cross-correlation function is normalisation to its peak (envelope) value.

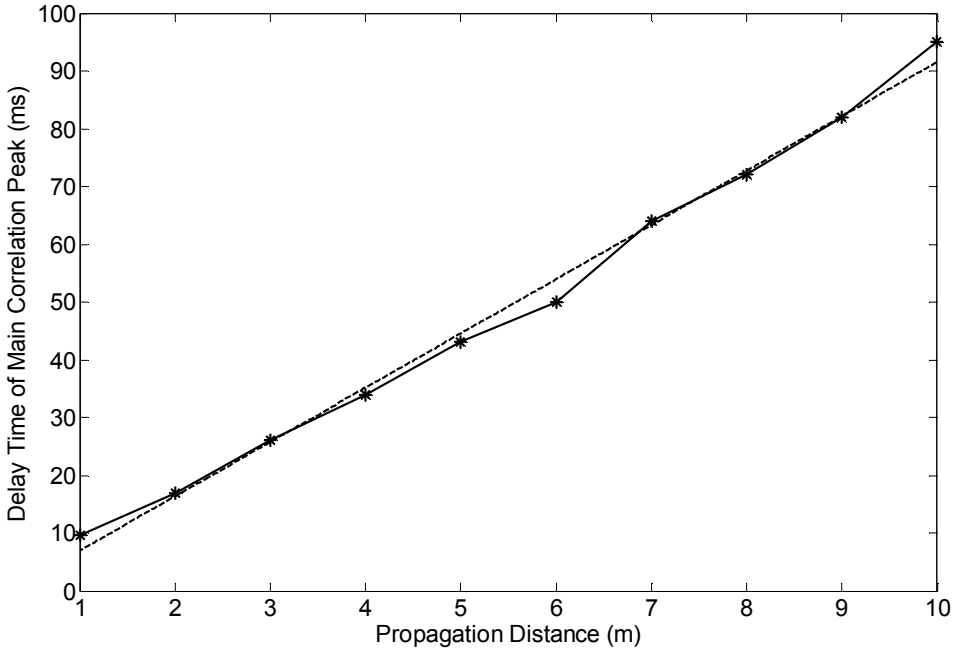

Figure 5.13 - Plot of the delay times of the main correlation peak as a function of the propagation distance for the high aspect ratio coupling platform. The dashed line indicates the linear fit to the data.

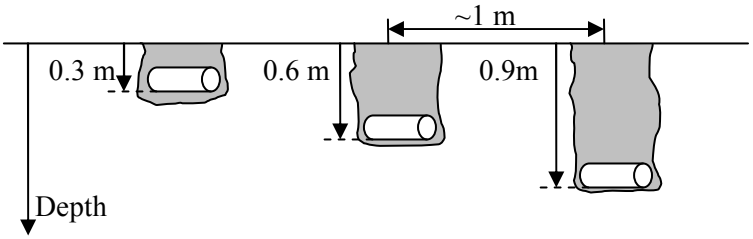

Figure 5.14 – Diagram of the experimental setup of the buried tri-axial sensors. The cylinders denote the sensors and the grey regions indicate the disturbed soil. Not to scale.

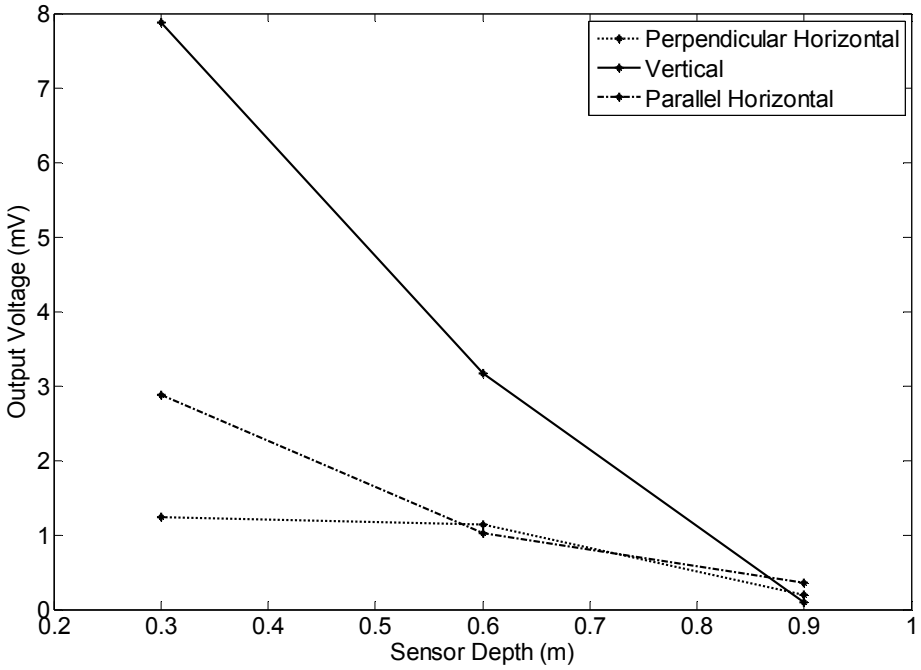

Figure 5.15 – Plot of the RMS of the sensor outputs as a function of depth for the three orthogonally orientated sensors using the low aspect ratio coupling platform with a vertically orientated excitation as a source. The three lines correspond to the three buried sensor orientations. As the source is vertical the distinction between the two horizontal orientations is arbitrary and is chosen only to coincide with the labelling of orientations for the horizontal source.

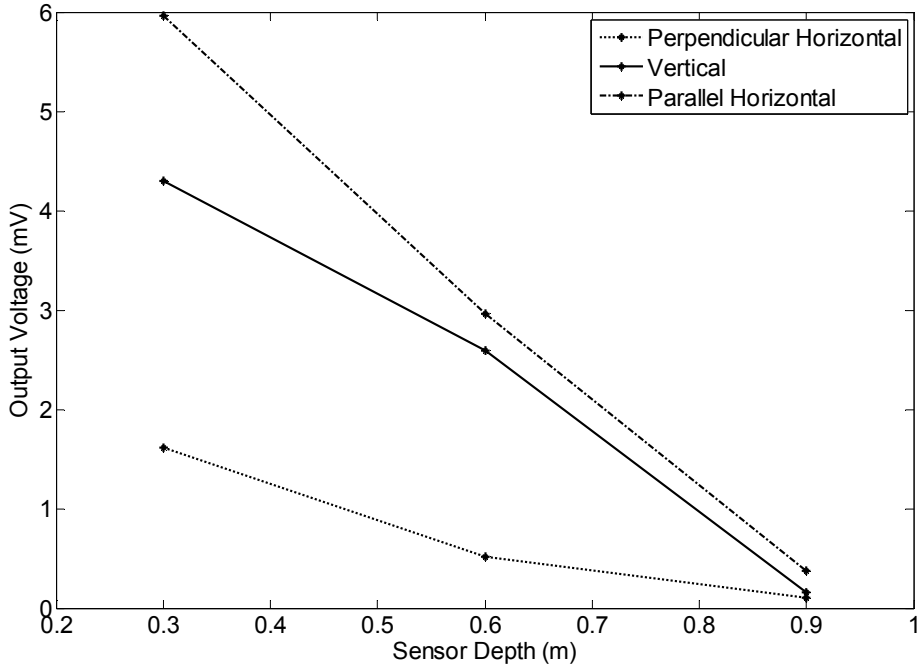

Figure 5.16 – Plot of the RMS of the sensor outputs as a function of depth for the three orthogonally orientated sensors using the high aspect ratio coupling platform as a source. The horizontal sensors are labelled in relation to their orientation with respect to the direction of the source excitation.

6. Imaging Experiments

Chapter 6

Imaging Experiments

6.1 Introduction

The purpose of this chapter is to attempt to experimentally validate the imaging method described in Chapter 3 and simulated in Chapter 4, using the experimental source validated in Chapter 5. Experiments were performed at several sites with the aim of imaging targets buried at known depths and locations. The first set of imaging experiments were performed in Kent, and are described in Section 6.2. Further experiments at a site in Dorset and a site in Japan are described in Sections 6.3 and 6.4. Conclusions are then drawn in Section 6.5.

6.2 Experimentation at the Kent Site

6.2.1 Site Description

Measurements were performed at a site in Kent. The target objects were concrete pipes approximately 0.6 m in diameter buried at a depth of 1 m. No borehole measurements were performed, but shallow digging indicated that the soil type was clay. For this experiment both surface sensors and a sensor attached to the inside of the pipes were used. The measurements at the Kent site were the first experimental application of the imaging method. As this was before the construction of the high aspect ratio coupling platform, the low aspect ratio coupling platform, described in Chapter 5, was used throughout in a shear orientation.

6.2.2 Wavespeed Measurements

Measurements were made both over the surface and through the ground to the pipe sensor. The sensor inside the pipe was a B&K accelerometer coupled with epoxy to the roof of the pipe. All measurements were made using the same equipment as in Chapter 5, with a diagram of the setup shown in Figure 5.4. The geophones were horizontally orientated (parallel to the direction of the shaker motion) input/output SM-9's, which were attached directly into an eight channel Prosig P-8000 data acquisition unit. The laptop was connected to the acquisition unit trigger channel to ensure triggering operated reliably and was repeatable. The excitation signal used was a linear chirp of length one second. The frequency range of the input was varied from 50 Hz, the minimum frequency for the shaker, to 2 kHz, after which attenuation in the ground was such that the wave propagation distance was negligible. Signals were measured with a sample rate of 5 kHz, and with low pass filter built into the acquisition unit filtering above 2 kHz to prevent aliasing.

The cross-correlation function between the reference and a surface geophone located 1 m away is shown in Figure 6.1. The cross-correlation function was calculated using the PHAT, as the SCOT could not be applied to non-statistically stationary signals for reasons given in Section 3.4. There is a clear peak at approximately 17 ms, giving a wavespeed of approximately 60 ms^{-1}. Figure 6.2 shows the cross-correlation function between an accelerometer built into the shaker and the pipe transducer. An acceleration signal from the shaker was used so that two acceleration signals could be directly compared. There is a clear peak at a time delay of 4.4 ms, corresponding to a wavespeed of about 225 ms^{-1} for the assumed pipe depth.

The value of the wavespeed measured through the ground is considerably higher than that along its surface. Whilst it is expected that there will be an increase in the wavespeed with depth, a nearly four fold increase within a metre is considered severe. An alternative explanation is that the wave propagating to the target is a compressional wave. The measured wavespeeds are consistent with this. In theory, the ratio of the wavespeeds depends only the Poisson's ratio (see Section 2.2). Using the measured wavespeeds, an estimated Poisson ratio of 0.45 is obtained from Figure 2.1. This is consistent with values from the literature for clay [151]. Imaging measurements were therefore performed with the expectation of reflected compressional waves.

6.2.3 Imaging Experiments

The imaging method was applied using a linear array of six geophones spaced 0.5 m apart. The excitation signal was, as for the wavespeed measurements, a linear chirp with a frequency content between 50 Hz and 2 kHz. The source was located, in turn, equidistantly between each adjacent pair

of measurement geophones, giving 5 source locations. A wavespeed of 225 ms^{-1} was used during application of the imaging algorithm.

The results obtained were generally poor, and failed to detect the target. This is attributed to the poor functioning of the seismic source at generating the desired wave type. Shear waves have already been demonstrated preferable in Section 3.2.2, and the source used here is generating behaviour consistent with compressional waves at the target object.

One source location did provide a positive result. This may have been because of better coupling at this location, or a fortunate absence of heterogeneities or debris between the source and target at that location. The result of the imaging method at this source location is shown in Figure 6.3. The expected target location is denoted by the large black circle. A target peak at the top of pipe is clearly visible. It is expected that the strongest reflection comes from the top of the pipe as this reflections from this location will have suffered from less attenuation.

6.2.4 Conclusion of the Kent Experiments

Experiments were performed at a site in Kent with the aim of detecting a large buried concrete pipe. The low aspect ratio platform was used, as these experiments were undertaken before the high aspect ratio platform has been constructed. This experiment used both sensors on the surface and a sensor located inside the pipe. This enabled the signal at the pipe to be measured and a through ground wavespeed to be estimated. The measured wavespeed was considerably higher than that measured over the surface of the ground. It is concluded that this is because compressional waves are reaching the target. Imaging experiments using the measured through ground wavespeed were generally poor. The exception was an image formed from a single source location, which was capable of detecting the top of the target pipe. The poor performance is attributed to inadequacies in the source design. This provided motivation for the construction of the high aspect ratio coupling platform and its experimental validation, as described in Chapter 5. The use of horizontally, rather than vertically, orientated geophones also reduced the proportion of the reflected wave relative to the surface wave, thus reducing the likelihood of successful imaging. This was because the geophones have poor sensitivity in the anticipated direction of the compressional motion.

6.3 Experimentation at Dorset Site

6.3.1 Site Description

Several sets of experiments were performed at a site in Dorset. The site consisted of a field with a river running adjacent. It was owned by an academic member of The University of Southampton, and

consequently it was possible to bury a target of choice. The target object used was a square concrete paving slab with sides approximately 40 cm in length and a thickness of approximately 3 cm. This paving slab had several Analogue Devices ADXL330 tri-axial accelerometers attached. The slab was buried using the soil excavated from the hole in which it was placed, with any large rocks or debris removed. Once buried, the paving slab was left for several months to allow the ground to settle. Unfortunately, during this period the attached tri-axial accelerometers were water damaged and failed to operate throughout the experiments.

6.3.2 First Set of Experiments

Results from the first set of experiments performed in Dorset, during August 2009, are presented in this section. For these experiments the excitation signal used was 10 seconds of white noise, band limited in the region of 50 Hz to 1 kHz. Six horizontal geophones were used, equally spaced by a distance of 0.5 m in a line, giving a total measurement length of 2.5 m. The centre of the line was located over the location of the paving slab. Five source locations were used: each source location being equidistant between two adjacent geophones. In accordance with the previous work of Chapter 5, the high aspect ratio horizontal source was used, operating with its excitation perpendicular to the measurement line, and all measurements made using the horizontal geophones orientated parallel to the direction of source excitation. The reference signal for the measurement of the cross-correlation functions was a reference geophone located very close to the source. All measurements were made using the equipment shown diagrammatically in Figure 5.4 and used previously in Section 6.2.

Prior to application of the imaging method, measurement of an in-situ wavespeed is required. Unfortunately surface results give anomalous but consistently low wavespeeds of around 35 ms^{-1}. This wavespeed is considerably lower than those measured on other occasions at the same site. The cause of this is not known. A possibility is soil cracking on the surface of the ground due to the hot weather at the time. Regardless of the cause, application of the imaging method with this implausibly low wavespeed consistently fails to produce not only images of the target, but any image with significant value below very shallow depths (~10 cm).

The imaging method was therefore tried with a variety of values of the wavespeed parameter that are closer to those found in other experiments performed at the site. The application of the imaging method with a wavespeed value of 80 ms^{-1} is found to produce a high image value at the correct location. This is shown in Figure 6.4, with the expected location of the target shown by the black line. This image is generated from cross-correlation functions estimated using the SCOT weighting and formed from divided the signal in to 20 equal segments to perform ensemble averaging. These are then enveloped using the Hilbert transform method and normalised to their peak value. The time

histories from the two measurement geophones (as opposed to the reference geophone) adjacent to the source are excluded. This is because they were found to be dominated by the direct source to sensor wave, and therefore contained negligible information of reflections from the target object. Although the wavespeed used is consistent with other wavespeed estimates from the site, it is not supported by in situ wavespeed measurements taken that day.

To try and give additional support for the use of this wavespeed the consequence of an observation made in Chapter 4 regarding the numerical simulations is discussed. It was noted that the cross-correlation values relating to waves propagating directly from the source to the sensors along the surface of the ground are interpreted by the imaging method as reflectors located very close to the surface. It has been stated that the time histories from the two measurement geophones adjacent to the seismic source are excluded from each measurement run. An image produced in an identical manner to that in Figure 6.4, with the exception that the time histories from the two measurement geophones adjacent to the seismic source are included, is shown in Figure 6.5. The target object is still detected, although with a significant reduction in the image value compared to the image value of the near-surface regions. Comparison between Figures 6.4 and 6.5 clearly show the introduction of this near surface activity in the latter, caused by the aforementioned interpretation of the direct source-sensor signal by the imagining algorithm.

The consequence of this observation is (as stated in Chapter 4) that if the wavespeed estimate is approximately correct then this near-surface activity should occur and be just below the surface. The presence of this near-surface activity in Figure 6.5 indicates that the wavespeed chosen is likely to be approximately correct. There is thus confidence that the image shown in Figure 6.4 is genuinely locating the paving slab.

To illustrate the necessity of using the post processing additions described in Section 3.4 identical processing is applied to that to use Figure 6.4 but using basic, rather than generalised, cross-correlation functions. The result is shown in Figure 6.6. The quality of the image is clearly degraded, although the image peak is still in approximately the correct location. Figure 6.7 shows the image created without the application of enveloping. Here, the oscillations in the cross-correlation functions cause cancellation upon their summation when forming the image. This prevents the imaging method from successfully detecting the target object.

6.3.3 Second Set Experiments

In October of 2009 additional imaging experiments were performed at the Dorset site. The aim of the experiments was to obtain a wavespeed estimate that could be used in the imaging method and to

recreate the previously obtained imaging results. The experimental setup of the imaging experiments was consequently unchanged, with an array of six horizontal geophones spaced by a distance of 0.5 m. The excitation signal used throughout was white noise band limited in the region of 50 Hz to 1 kHz.

Wavespeed measurements were made by placing the source 5 m from the line of measurement sensors, as shown in Figure 6.8. The measurement line was over the location of the target, but the distance from the source to the target means that reflections from the target should be negligible and not interfere with wavespeed estimation. This experimental setup was used as it was quick to setup in experiments and allowed several different measurements at approximately the same source-sensor separation for averaging of the resultant estimates.

Cross-correlation functions between the reference geophone, located as close to the source as possible, and measurement geophones, are obtained using the SCOT weighting and formed from dividing the signal in 20 equal segments to perform ensemble averaging. These are then enveloped using the Hilbert transform method and normalised to their peak value. The estimated cross-correlation functions are shown in Figure 6.9. The cross-correlation functions are broadly similar to each other with all, with the exception of Figure 6.9 (c), having two discernible peaks. This indicates that substantial wave propagation from the source to the sensor is either occurring via two types of propagating wave or by one type of wave with two propagation paths, such as in the case of refraction along a discontinuity in the medium (see Section 1.5.1).

Assuming these peaks correspond to direct propagation paths, then wavespeeds of (162 ± 16) ms^{-1} and (75± 2) ms^{-1}. Although the faster of these wavespeeds has a relatively high uncertainty, the lower wavespeed is consistently measured. The wavespeed values are consistent with observed values of the propagation speed of shear and compressional waves; although from both the mathematical analysis of Chapter 2 and the previous experimental work of Chapter 5 the compressional wave generated by the source from the arrangement shown in Figure 6.8 should be small. It is not possible to confirm or deny if a refracted path is causing a peak in the cross-correlation functions. This is because of an absence of measurements over a range of source-sensor separations, which is required for refraction measurements, as described in Section 1.5.1.

The slower and more consistent of the two wavespeeds is assumed to be the shear wavespeed. This is both because of its low standard deviation, as expected from the dominantly produced and measured wave from the given source-senor arrangement, and because of its comparable value with other experimentally obtained values of the shear wavespeed at the Dorset site.

The result of the imaging method, whose constituent cross-correlation functions are estimated using the same parameters as in the estimation of the wavespeed value, and with an assumed wavespeed of 75 ms^{-1}, is shown in Figure 6.10. Although there is a high image value at the location of the target, the result cannot be taken as positive as there is another area of high image value nearby. As this high image value is at the same horizontal location as the target but at a shallower depth, it is unlikely to correspond to a reflector, as this region was backfilled after the burial of the paving slab and did not contain any large rocks or debris. It is therefore likely to either be an anomalously slow surface wave or correlation from the propagation of an additional wave type.

To confirm that the measured wavespeed is appropriate the imaging process was repeated with the time histories from the two geophones adjacent to the source at each location included. This is shown in Figure 6.11. The contribution introduced to the image is, as expected, dominated by the direct wave propagating from the source to the sensor. This effect is, as required for an approximately correct estimate of the wavespeed, located near to the surface. Of note is the low amplitude of the peak near to the expected target location relative to the direct wave peaks, indicating that the amplitude of the reflection from the target is very low. The cause of the lowering of the reflection amplitude relative to the surface wave, when compared with the relative values in the previous experiments at the Dorset site, is unknown. It is possibly caused by variation in the ground properties that affect the damping attenuation values.

6.3.4 Conclusions of the Dorset Experiments

Multiple measurements were performed at a site in Dorset, with a concrete paving slab buried at a depth of 0.7 m used as a target. The first set of measurements undertaken at the site was unable to obtain a value of the wavespeed consistent with other experimental work performed by the author and those found in the literature. Application of a more plausible wavespeed was able to produce an image where the target object is clearly identified. The use of a wavespeed different to that measured on the day is justified not only by consistency with other results but also by an examination of the location of artefacts in the imaging process, caused by the presence of surface waves that propagate directly from the source to the sensors.

A second set of measurements at the site were able to obtain a consistent wavespeed value by using multiple sensors at a fixed distance. A shear wavespeed was identifiable in addition to a faster signal, either caused by an additional wave propagation or a refracted wave path. It was not possible to verify which of these two scenarios was physically occurring due to limitations of the experimental setup. Application of the imaging method was unsuccessful. Although an image peak at the location of the target is present, other peaks of near equal magnitude prevent the clear identification of the presence

and location of the target. The inability of the imaging method to successfully detect the target is due to the amplitude of the wave reflected from the target being too small relative to the surface wave.

6.4 Experimentation at the Japanese Site

6.4.1 Description of the Test Site and Available Equipment

Experimentation was performed at a site in Tokai, Japan, in January 2010, in collaboration with Professor Sugimoto of the Toin University. This collaboration was possible due to a grant from the Daiwa Anglo-Japanese Foundation. This site has been used by Professor Sugimoto for some time, with the ground therefore well settled, and has a variety of objects buried at different depths. The experimental site consists of a field surrounded by irrigation ditches, with the surrounding area used for growing rice. The experiments were performed in the winter and the area was relatively dry, with no standing water. The targets studied were cylindrical terracotta pots, approximately 30 cm in length and 10 cm in diameter. Three identical pots were buried at depths of 30 cm, 50 cm and 70 cm. Measurements were performed over all three.

The constraints of transporting the experimental equipment from the UK to Japan mandated the use of Professor Sugimoto's equipment. The only piece of equipment that was taken was the PROSIG data acquisition unit. A sample rate of 5 kHz was used. The low pass filter built into the data acquisition unit was set to filter above 2 kHz. The geophones, signal generator, electromagnetic shaker and coupling platform used were those belonging to Professor Sugimoto. This imposed additional limitations on the experimental procedure that required some modifications. The signal generator used was a Tektronix AFG 3022B and was only capable of generating relatively short chirp signals. For the experiments performed a practical limit of one second was imposed. Consequently one second chirps were used throughout the experiments.

The shaker and coupling platform used were of an unusual design which is worthy of some discussion. The electromagnetic shaker was a magnetostriction vibrator, specifically a Moritex AA140J013-MS1. This is coupled to an aluminium platform that is fixed to both ends of the shaker, with the platform inserted into the ground with metal prongs. A photograph of the shaker attached to the platform and inserted into the ground is shown in Figure 6.12. A diagram of the experimental equipment used to generate signals and take measurements is shown in Figure 6.13.

Although this platform was designed to primarily generate waves of shear, the manner in which the shaker is coupled to the platform makes this far from ideal. A diagram illustrating the likely directions of motion of the shaker and the platform is given in Figure 6.14. Figure 6.14 (a) shows the result for the shaker platform used in Chapter 5. The force generated by the inertial shaker acts on the

supporting strut and forces motion of the platform parallel to the ground. Previous experiments showed that this seismic source predominantly results in motion that is in the anticipated direction.

The anticipated motion of the source and platform used by the Japanese researchers is shown in Figure 6.14 (b). As the shaker is not an inertial shaker, it must be fixed at the end that is not intended to move. If it was fixed to the platform in Figure 6.14 (a) then the majority of the generated force would be used to move the shaker relative to the platform, not the platform relative to the ground. Consequently, the shaker used by the Japanese researchers has been fixed to the platform at both of its ends. It is anticipated that the motion that this produces is not perpendicular to the surface, but that rather it will cause a bending motion in the platform leading to the platform effectively generating input surface moments (shown in Figure 6.14 (b)), rather than the desired surface traction parallel to the ground. This type of source is unusual, and has not been considered mathematically in Chapter 2. The use of the seismic source was therefore not ideal, but necessary as it was the only equipment available.

6.4.2 Phase Reversal

A procedure that has been used by many researchers, including Professor Sugimoto, is to perform all measurements twice with the phase of the excitation signal reversed for the second measurement. It is frequently stated that shear components of the motion will be reversed in phase whilst compressional components will not. Thus by subtracting the signals any compressional waves can be eliminated from the signal whilst the shear components are reinforced. As this process was strongly personally recommended by the Japanese researchers at this site, a comparison between measured data of the two phases is made.

A comparison of two complete chirps is shown in Figures 6.15 (a) and (b), where the phase of the input signal has been reversed between measurements. This measurement was made using a geophone located very close to the seismic source (~5 cm), adjacent to the centre of the long axis of the coupling platform, and with the geophone orientated parallel to the direction of excitation of the shaker. Assuming linearity, and because the input signal is a chirp, the time scale of these corresponds roughly to the frequency of the input signal. The signal was started 0.2 s through the measurement, with a frequency increase of approximately 100 Hz per 0.1 s. The two signals, viewed from this scale, are virtually identical, as expected.

To examine the phase of the two measured signals they are overlaid on the same graph. Along the length of the signal the two signals changes between being predominately in and out of phase. Examples of in phase and out of phase behaviour are shown in Figures 6.16 and 6.17 respectively

which show the data on expanded time-axes. The variation between the phase of the two measured signals over the frequency range is likely to be caused by either variation in the type of wave that the platform is generating over that frequency range, or the presence of resonant modes within the structure itself. As the platform is not available for further examination back in UK it is not possible to draw a definite conclusion. The effect of the variation in the phase of the signals on the performance of the imaging method is evaluated in Section 6.4.4.

6.4.3 Wavespeed Measurements

Calculation of wavespeeds is by the same method used in elsewhere in this thesis when data from multiple source-sensor separations is available: the main peak of the cross-correlation functions are calculated between each member of an array of measurement geophones and a reference geophone is plotted as a function of the distance between the two geophones. The inverse of the gradient of a linear best fit then gives an estimate of the wavespeed. As a single chirp was used as the excitation signal it was not possible to use the SCOT, as the ensemble averaging required for calculating an estimate of the coherence function is not valid. Consequently, the PHAT is used. The data is bandpass filtered in the region of 100Hz - 600Hz prior to application of the PHAT. If this filtering is not performed then the PHAT boosts regions outside the frequency range of the excitation signal that can only correspond to noise, not to the signal, resulting in a degradation of the cross-correlation functions.

Initially, calculations are performed only on the data measured with one phase of the excitation signal. Consideration to measurements with the opposite phase is given later in this section. The cross-correlations calculated are more complicated than those found in Section 5.3. In Section 5.4, which used the high aspect ratio designed for this thesis, it was noted that the shear seismic source produced very ‘clean’ cross-correlation functions, which contained a single dominant peak. This was indicative of a source producing one wave type in preference to others, as desired in this circumstance. For comparison, the cross-correlation function calculated from the Japan data are shown in Figure 6.18. Whilst some exhibit a relatively dominant single peak, such as Figure 6.18 (c), others are far from the ideal. Figure 6.18 (a), for example, shows the cross-correlation function between the reference geophone and the closest measurement geophone. The function is complicated, with adjacent peaks of near equal magnitude. The cross-correlation function with the next closest measurement geophone, shown in Figure 6.18 (b), shows two distinct peaks. This indicates that the source is not predominately producing a single wave type, as might be hoped for. This is, however, not unexpected given the discussion of the source motion in Section 6.4.2.

For wavespeed estimation the time delay of the largest cross-correlation peak was taken and plotted as a function of the separation between the reference and measurement geophones, with the resultant data plotted as the solid line in Figure 6.19. The linear best fit, shown as the dashed line, has a gradient of 13.8 ms m^{-1}, giving a wavespeed estimate of (73±4) ms^{-1}.

To evaluate the validity of subtracting signals measured at sensors with the excitation phase reversed, the cross-correlation functions of Figure 6.18 are computed using the difference between the two signals measured with opposite phases of excitation. All processing parameters are unchanged. The cross-correlation functions are shown in Figure 6.20. They are very similar to the case of a single excitation phase, with the time delays to the peak correlation function values suffering little (of order of a few tenths of a millisecond) or no change. Repeating the method for the estimation of the wavespeed from these cross-correlations gives a result of (71±4) ms^{-1}. The difference in estimated wavespeeds is within the margins of error for these results, and therefore not significant.

Thus the unusual source used in the experiments in Japan produces motion that is, at least in part, independent of the phase of the input, as seen from Figure 6.16. Despite this the procedure of subtracting signals measured with opposite excitation phase does not have a significant effect on the calculated cross-correlation functions. The purpose of this subtraction is to remove compressional waves whilst preserving the measurement of shear waves. For the measurements undertaken in Japan, there is no indication that this is removing compressional motion. Either there is insufficient compressional motion to produce any difference in the cross-correlation functions or the phase of the compressional wave is also reversed. As the cross-correlation functions are the basis of the imaging method it can therefore be concluded that there is no utility in the applying the phase reversal procedure for these measurements.

6.4.4 Imaging Experiments

The imaging method post-processing does not require modification prior to its application to data from the Japanese site. A linear array of six geophones spaced 0.5 m apart is used, with the centre of the array over the anticipated target location. The orientation of the measurement line was perpendicular to the long axis of the buried pots. The calculation of the estimated cross-correlation functions is as described in Section 6.4.3. The method is applied for source locations mid-way between the geophone locations, as in previous imaging measurements. As in the experiments at the Dorset site all cross-correlation functions are enveloped using the Hilbert transform and normalised to their (envelope) peak value. The time histories from the two measurement geophones closest to the seismic source on each measurement run are again excluded from processing, as they are dominated by the direct surface wave.

The result of the imaging method over the 50 cm terracotta pot is shown in Figure 6.21, with the expected location of the target object shown by the black line. The wavespeed used for this method used was 72 ms^{-1}, in accordance with the results of Section 6.4.3. It can be seen that the imaging method fail to detect the target.

In anticipation of the generally observed increase in the propagation wavespeed with depth, and allowing for error and variability in the measurement of the wavespeed, other, higher values of the wavespeed are used for the imaging method. It is found that a speed of 85 ms^{-1} allows for the formation of a single image peak, and that this image peak is in approximately the correct location. The resulting image is shown in Figure 6.22. It is therefore suggested that either inaccuracy in the measurement of the wavespeed, a difference in the value of the wavespeed between the area of ground where it was measured and where the target was buried, or an increase in the value of the wavespeed with depth causes a higher value of the wavespeed than that measured in Section 6.4.3 to be successful in producing an image.

As final confirmation that the reversal of the phase of the excitation signal does not influence the image produced by the method, an image produced in an identical manner to Figure 6.22 is shown in Figure 6.23 with the exception that the difference between the two signals measured when the phase of the excitation signal is reversed. Differences between the two images are small, and not significant for the imaging method.

In addition to the measurements performed over the pot buried at a depth of 50 cm, measurements were also performed over the identical targets at depths of 30 cm and 70 cm. An identical processing method was applied to this data as to obtain a comparable set of images. The 30 cm target image is shown in Figure 6.24. The imaging method fails to detect the target. A justification for the use of a wavespeed higher than that measured on the surface was that there may be an increase in the wavespeed with depth. The image in Figure 6.24 is therefore repeated with the original measured wavespeed, with the result shown in Figure 6.25. Here the spatial filtering of the image has been removed to illustrate that the surface wave influence is reaching to similar depths, and thus obscuring a possible reflected image.

The image for the measurements with the target at a depth of 70 cm, shown in Figure 6.26, does produce a small high region of image value, but this is not the largest peak in the image. The reduction in the amplitude of the target peak in the image is likely to be the result of the increased attenuation of the reflected wave from the target relative to the direct surface wave and reflected waves from anomalous heterogeneities.

6.4.5 Conclusions of the Japanese Experiments

Experimentation was performed at a site in Japan with the aim of finding several identical targets; terracotta pots approximately 30 cm in length, buried at several different depths. An estimate of the wavespeed was obtained using an array of sensors. In processing, it is found that a slightly higher wavespeed than that measured is capable of producing images at the middle depth of 50 cm. This is plausible given the generally observed increase in propagation speeds with depth. Experiments with the deepest target, buried at 70 cm, are unable to conclusively find the target. Whilst a weak image peak at the approximate target location is observed, it is not the largest peak in the image and so the target could not be identified without prior knowledge of its location. The shallowest target, which was buried at 30 cm, could not be detected at all. This is because it is too close to the surface to be separated from the surface wave artefacts in the image, and is consequently obscured by them and then removed with the application of spatial filtering.

An interesting complication with the experimentation performed at the Japanese site was the use of a seismic source designed by the researchers in Japan. The design of the source is not ideal for the generation of shear waves, and resulted in complicated wave generation by the source. Efforts to utilise the subtraction of two signals measured with opposite excitation phase are shown to be ineffective with this type of excitation, despite their suggested use by many in this area of research.

6.5 Conclusions

Experiments have been undertaken with the aim of validating the imaging method. These were performed at three sites; in Kent and Dorset in the UK, and at one in Japan. The Kent experiment produced inconsistent imaging of the target object due to the predominance of a compressional, rather than shear wave, reaching the target. This was verified by using a sensor on the buried target. To improve the seismic source, the high aspect ratio source described in Chapter 5 was designed and constructed.

Two sets of measurements from the Dorset site are presented. The first of these was able to successfully detect the target object buried at a depth of 0.7 m. Difficulties arose in the measurement of the propagation wavespeed, which was anomalous. Confidence was obtained in the validity of the final image by comparison with other measurements at the site and by examining the appearance of surface wave artefacts in the image. The second set of measurements in Dorset were able to produce a reliable estimate of the wavespeed. The amplitude of the reflected wave relative to the surface wave was, however, too low to enable a positive image of the target object.

The experiments performed in Japan suffered from complications arising from the unavoidable use of a source that did not predominantly produce shear waves. Investigations were made into the possibility of using phase reversal of the excitation signals to enable removal of unwanted wave types, but this was found to make no practical difference to either measurement of the wavespeed or application of the imaging method. Although cross-correlation functions were complex, it was possible to obtain a reliable estimate of the wavespeed. The imaging method was applied over three identical targets buried at different depths. The shallowest target, buried at 0.3 m, was found to be too near to the surface to be imaged correctly, and was instead obscured by the image artefacts of the direct surface waves. A clear image of the middle depth target, buried at 0.5 m, was obtained. The deepest target, buried at 0.7 m was, however, too deep to generate a sufficiently large reflected signal, relative to the surface wave, to enable clear detection.

It is concluded that the imaging method is capable of imaging buried targets, although many difficulties remain which affect the reliability of the method. Problems include the measurement of a wavespeed that is not only consistent, but indicative of the propagation speed at depth as well as on the surface, and achieving a sufficiently large reflected wave amplitude relative to the direct surface wave. This direct surface wave is also found to prevent measurement of targets at the shallowest depths.

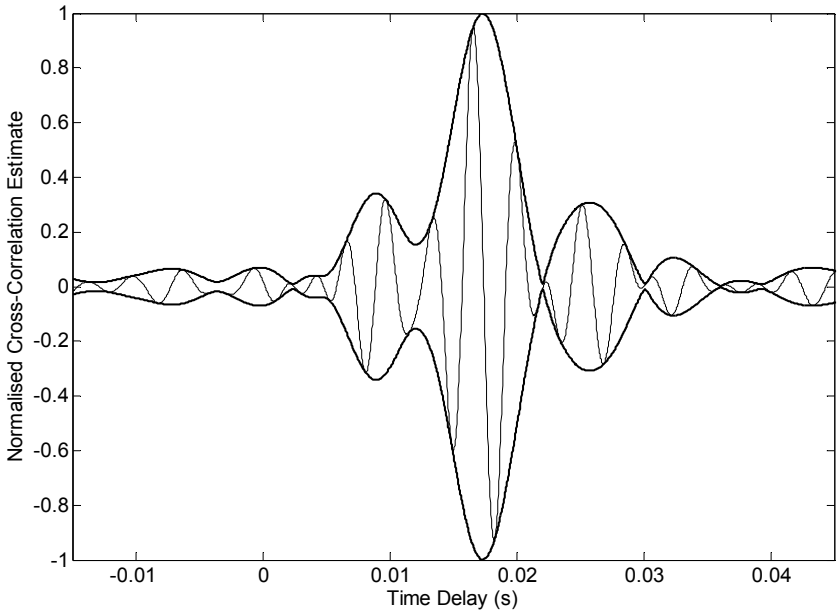

Figure 6.1 – Cross-correlation function estimate between a reference geophone, located close to the seismic source, and a measurement geophone 1 m away. Cross-correlation estimation is with the PHAT. The dashed line shows the cross-correlation function and the solid line its envelope calculated via the Hilbert transform. The cross-correlation function is normalised to its (envelope) peak values.

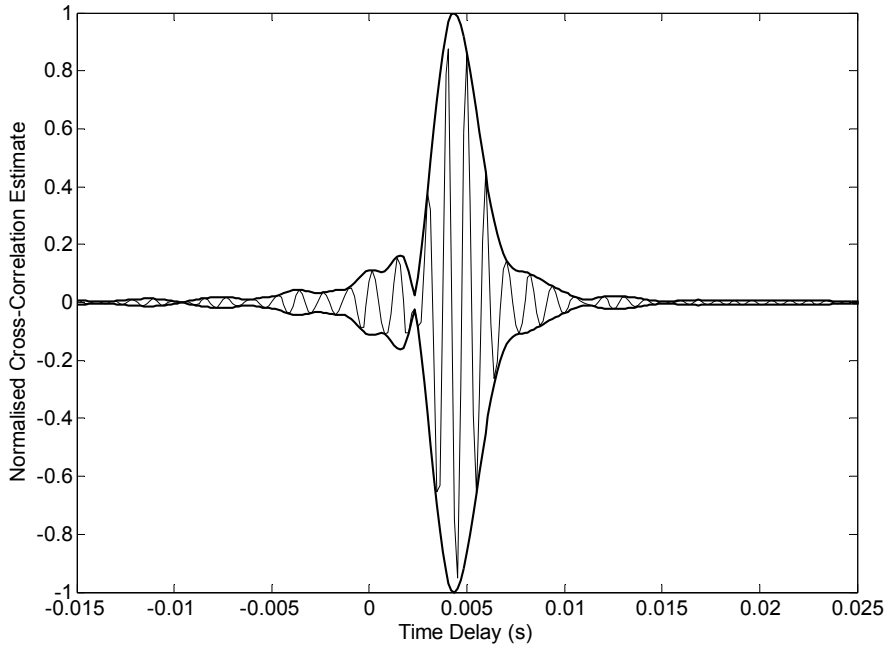

Figure 6.2 – Cross-correlation function estimate between the shaker acceleration and an accelerometer located inside the buried pipe. Cross-correlation estimation is with the PHAT. The dashed line shows the cross-correlation function and the solid line its envelope calculated via the Hilbert transform. The cross-correlation function is normalised to its (envelope) peak values.

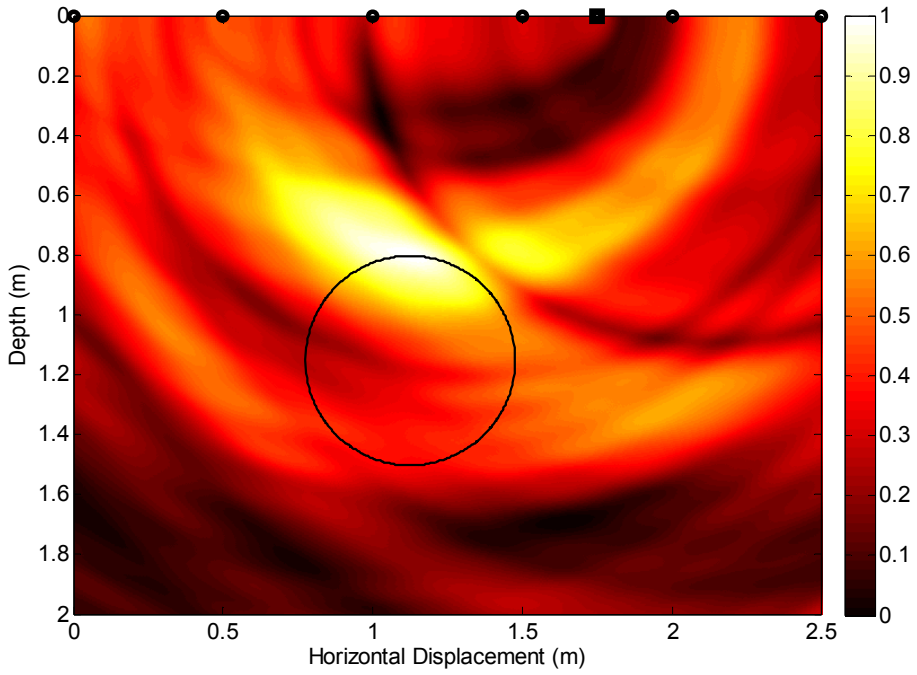

Figure 6.3 - Cross-sectional image through the ground produced by the imaging method using data measured from the Kent site. The surface sensors are denoted by circles, the surface source location by the square, and the anticipated location of the target by the large black circle. The image is scaled such that its minimum and maximum values correspond to zero and one respectively. The imaging wavespeed used was 225 ms^{-1}.

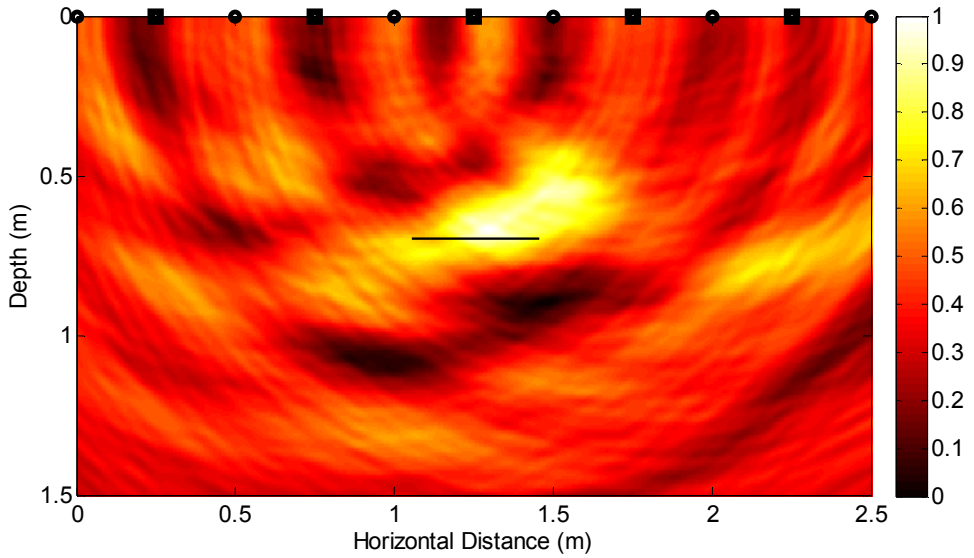

Figure 6.4 - Cross-sectional image through the ground produced by the imaging method using data measured from the Dorset site. The surface sensors are denoted by circles, the surface source locations by squares, and the anticipated location of the target by the black line. The image is scaled such that its minimum and maximum values correspond to zero and one respectively. The imaging wavespeed used was 80 ms^{-1}.

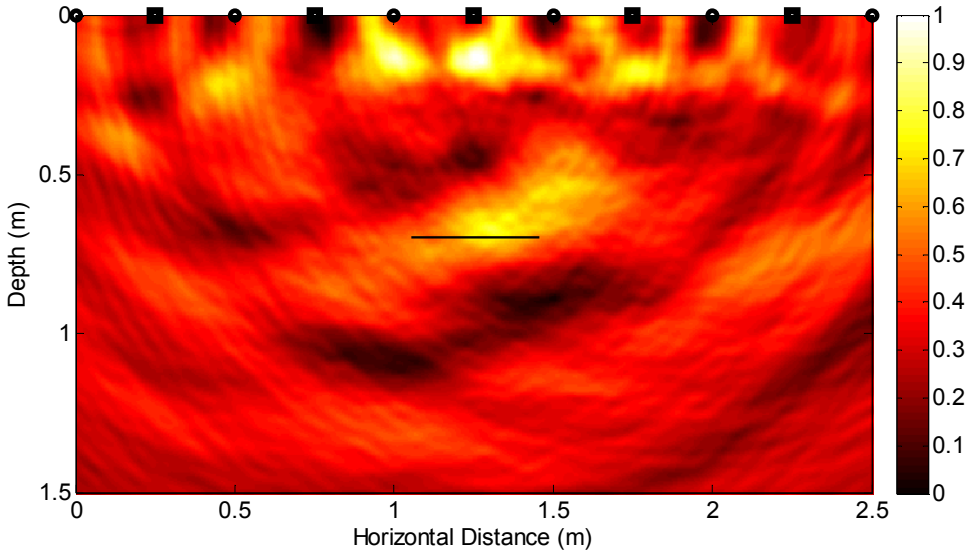

Figure 6.5 - Cross-sectional image through the ground produced by the imaging method using data measured from the Dorset site. The surface sensors are denoted by circles, the surface source locations by squares, and the anticipated location of the target by the black line. The image is scaled such that its minimum and maximum values correspond to zero and one respectively. Formation of the image is as Figure 6.4, with the exception that the data from the sensors closest to the geophone were included in the formation of the image.

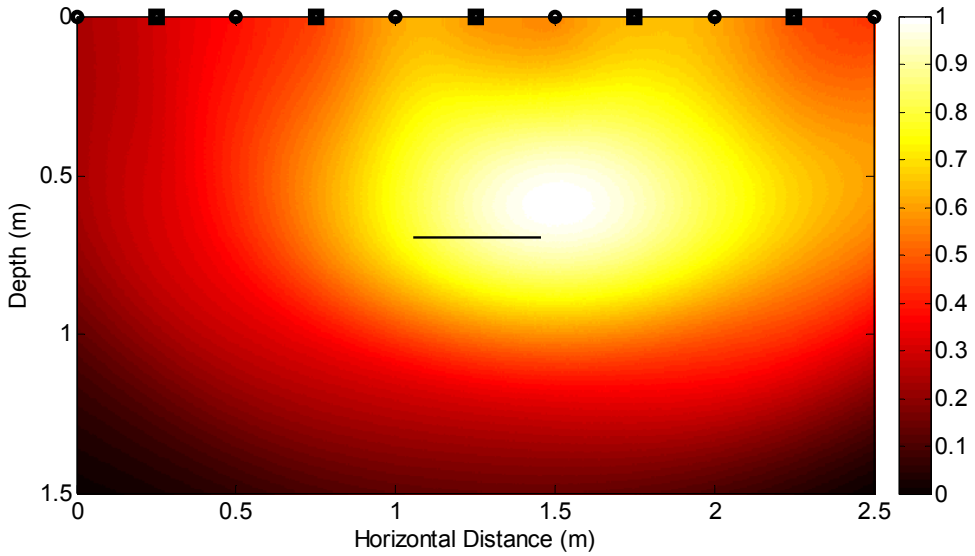

Figure 6.6 - Cross-sectional image through the ground produced by the imaging method using data measured from the Dorset site. The surface sensors are denoted by circles, the surface source locations by squares, and the anticipated location of the target by the black line. The image is scaled such that its minimum and maximum values correspond to zero and one respectively. Formation of the image is as Figure 6.4, with the exception that basic, rather than generalised, cross-correlation functions are used.

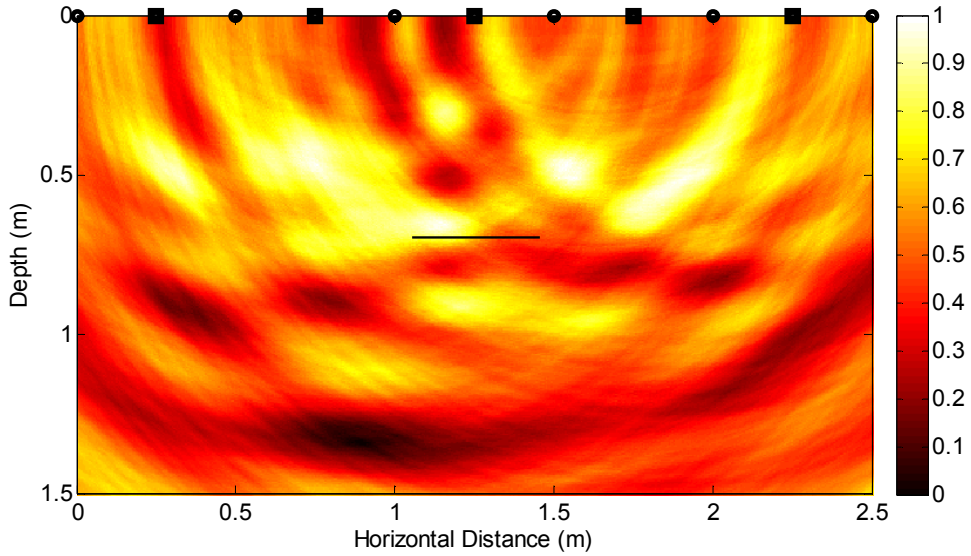

Figure 6.7 - Cross-sectional image through the ground produced by the imaging method using data measured from the Dorset site. The surface sensors are denoted by circles, the surface source locations by squares, and the anticipated location of the target by the black line. The image is scaled such that its minimum and maximum values correspond to zero and one respectively. Formation of the image is as Figure 6.4, with the exception that no enveloping is applied to the cross-correlation functions.

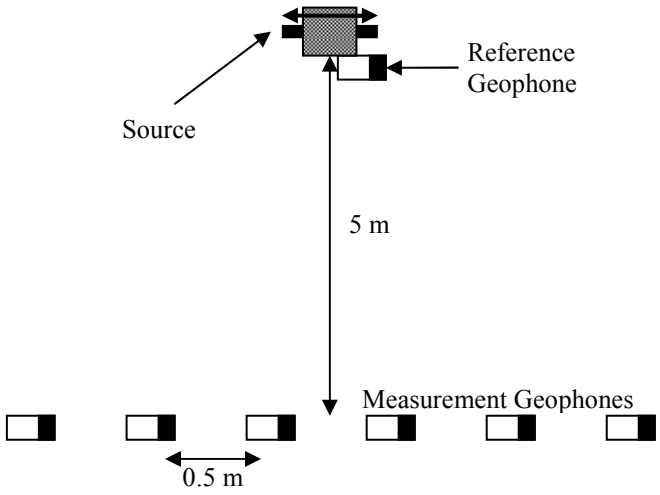

Figure 6.8 – Diagram of the experimental arrangement used in the measurement of the wavespeed during tests at the Dorset site. The source is denoted by the object at the top of the image, with its direction of oscillation shown. The geophones shown are horizontal geophones sensitive in the direction of their long axis. The geophones were orientated with their sensitive axis parallel to the direction of source excitation. They were arranged in a linear array with its centre 5 m from the source and its elements equally spaced by 0.5 m.

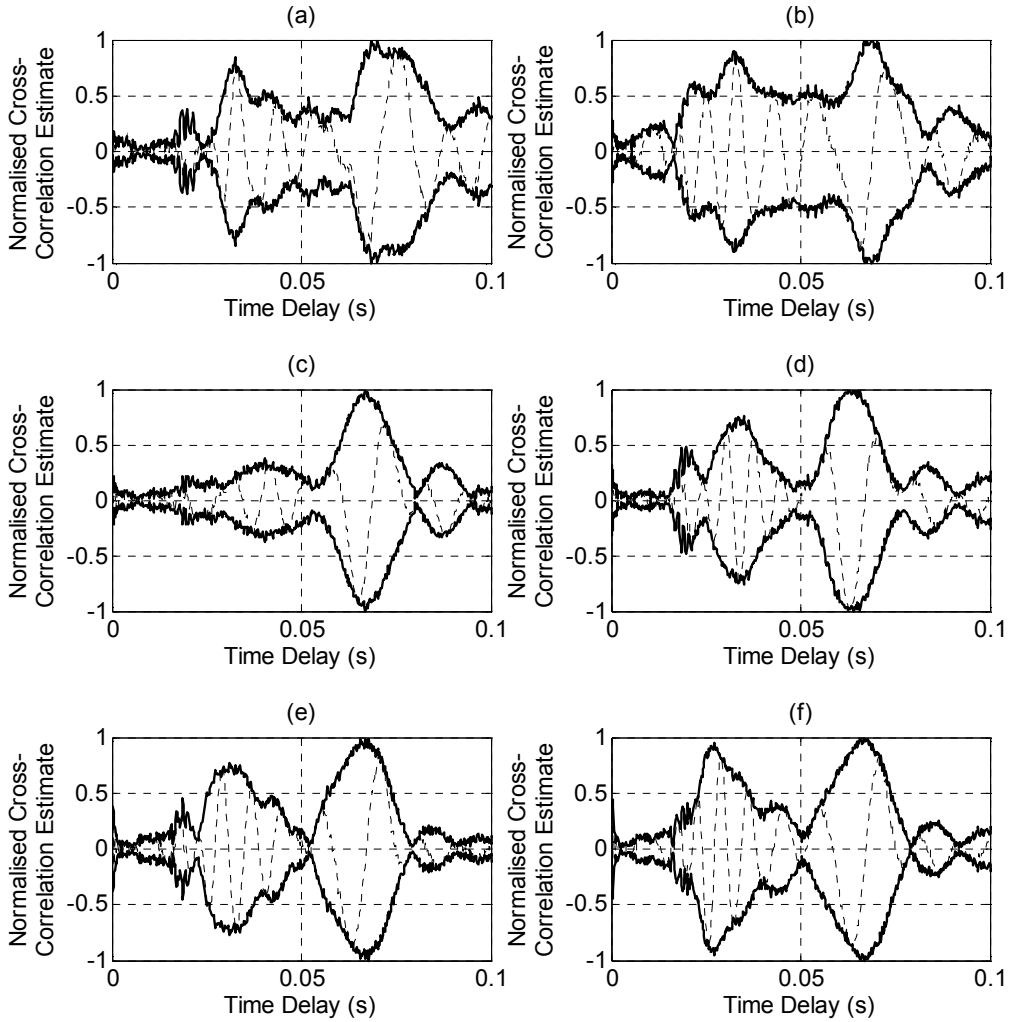

Figure 6.9 –Cross-correlation function estimates between a reference geophone, located close to the seismic source, and 6 measurement geophones which where spaced 0.5 m apart in the arrangement shown in Figure 6.8. Cross-correlation estimation is with the SCOT with 20 averages used for ensemble averaging. The dashed line shows the cross-correlation function and the solid line its envelope calculated via the Hilbert transform. All the cross-correlation functions are normalised to their (envelope) peak values.

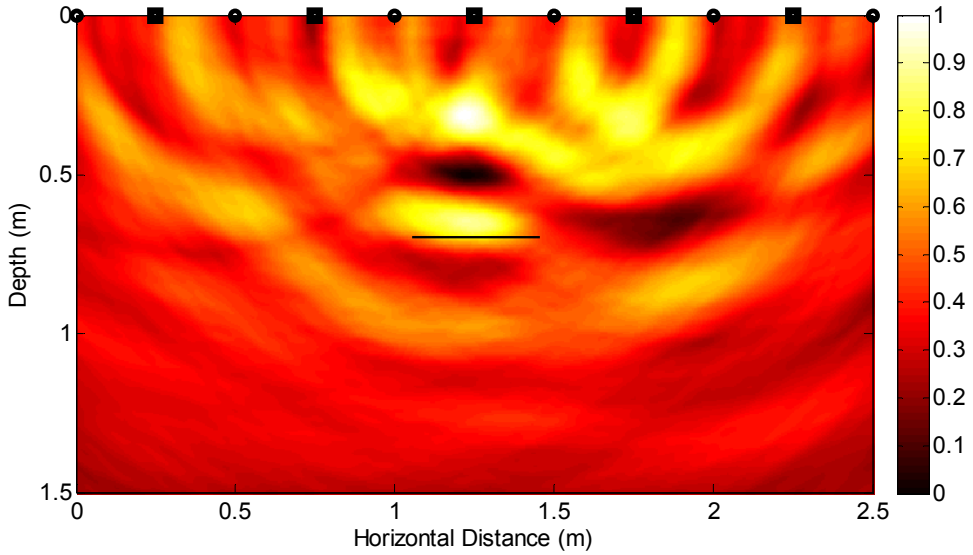

Figure 6.10 - Cross-sectional image through the ground produced by the imaging method using data measured from the Dorset site. The surface sensors are denoted by circles, the surface source locations by squares, and the anticipated location of the target by the black line. The image is scaled such that its minimum and maximum values correspond to zero and one respectively. The imaging wavespeed used was 75 ms^{-1}.

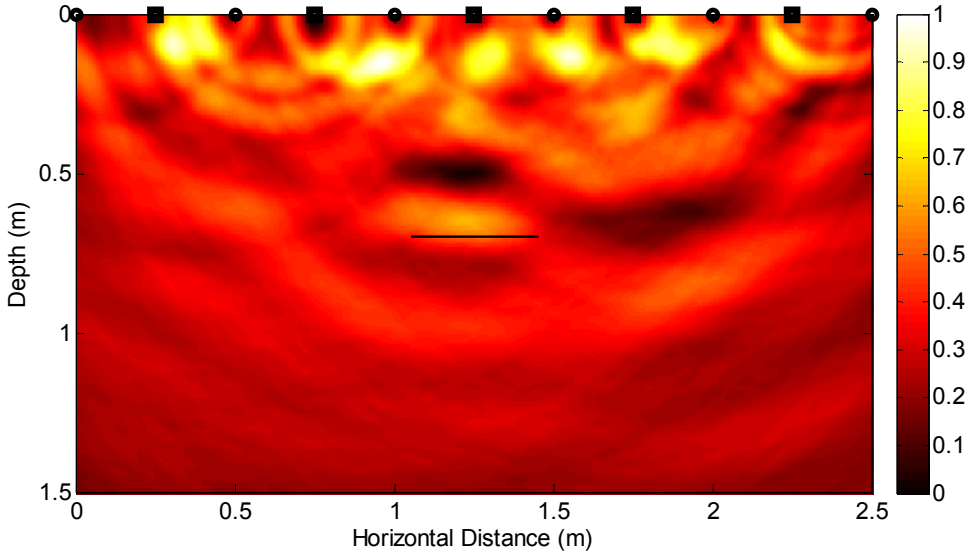

Figure 6.11 - Cross-sectional image through the ground produced by the imaging method using data measured from the Dorset site. The surface sensors are denoted by circles, the surface source locations by squares, and the anticipated location of the target by the black line. The image is scaled such that its minimum and maximum values correspond to zero and one respectively. Formation of the image is as Figure 6.10, with the exception that the data from the sensors closest to the geophone were included in the formation of the image.

Figure 6.12 – Photograph of the seismic source used at the experimental site in Japan.

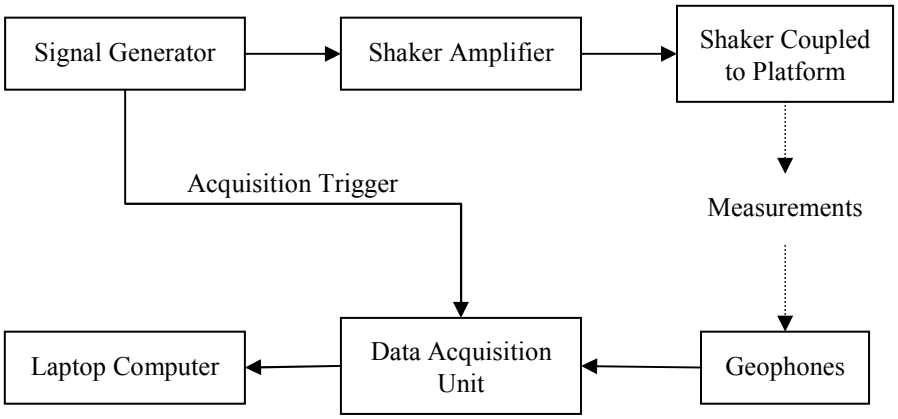

Figure 6.13 – Diagram of the equipment setup used for the generation of seismic waves and their measurement at the Japanese site. The source and geophone arrangement are described in the text, and vary between specific experiments.

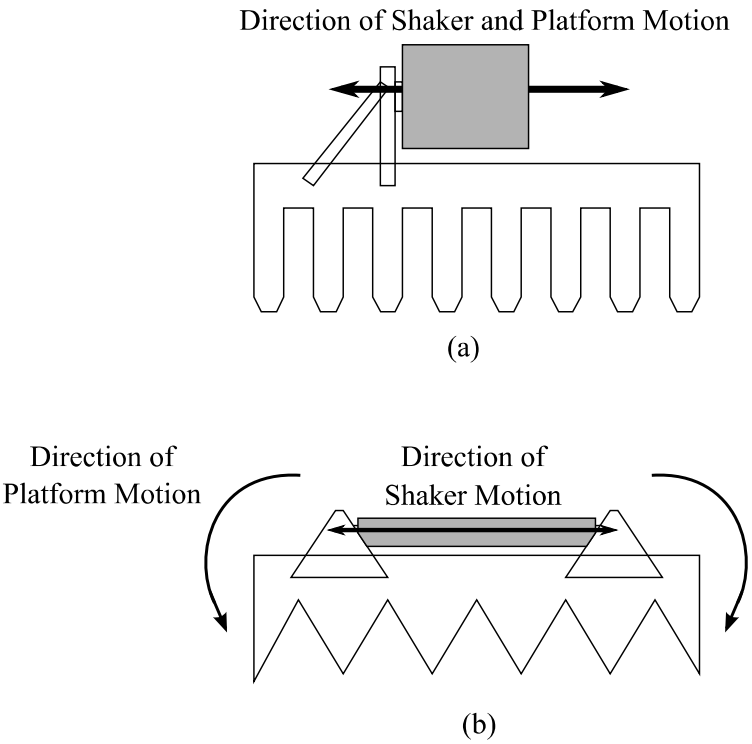

Figure 6.14 - Schematic of seismic sources used in (a) the UK and (b) Japan. The shakers are shown in grey, with the coupling platforms in white. In the UK an inertial shaker was used and in Japan a magnetostrictive shaker was used. The anticipated motions of the shakers and the platforms are labelled for a single direction of one oscillation.

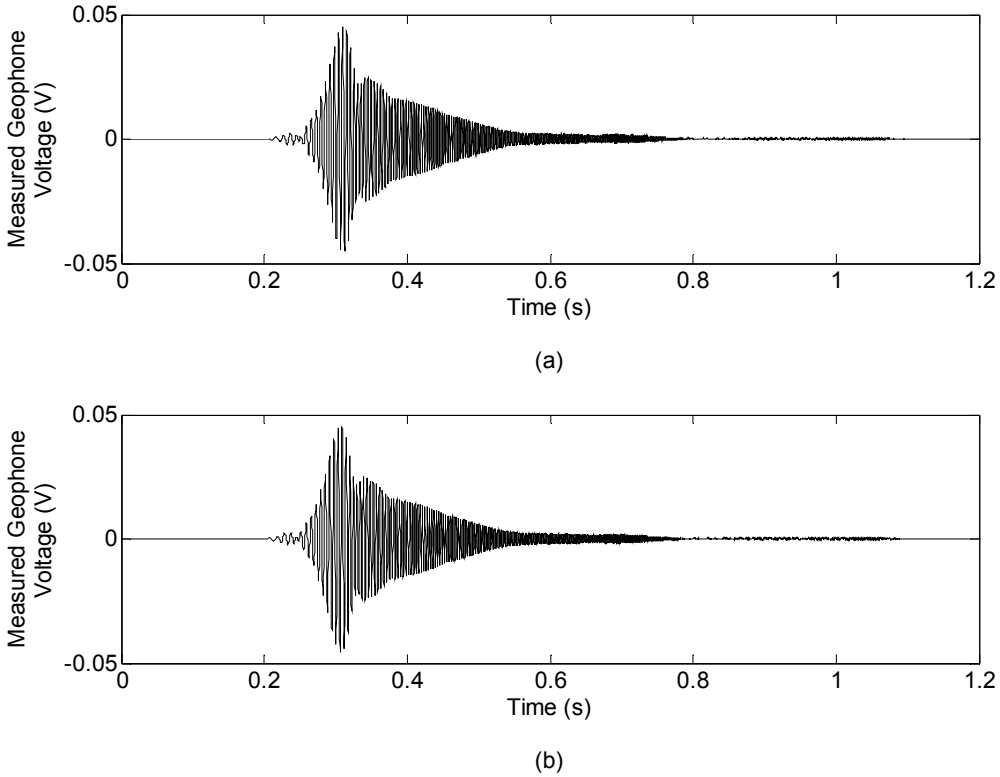

Figure 6.15 – Plots of the measured geophone signals from a geophone located very close (~5 cm) from the seismic source used in Japan. The geophone is located adjacent to the centre of the long axis of the source, with its sensitive orientation parallel to the excitation of the shaker. Figure 6.15 (a) and (b) show the signal for the two opposite phases of excitation.

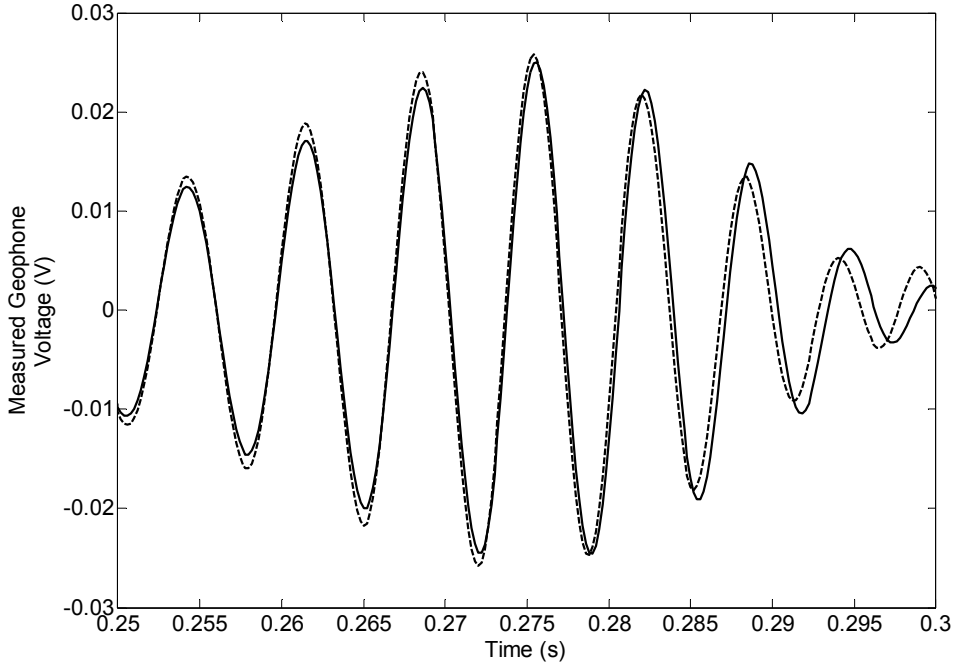

Figure 6.16 – Overlaid plot of the measured signals from the two different phases of excitation, with Figure 6.15 (a) shown by the solid line and Figure 6.15 (b) by the dashed line. In this portion of the signal input frequencies are approximately in region of 100 Hz -150 Hz.

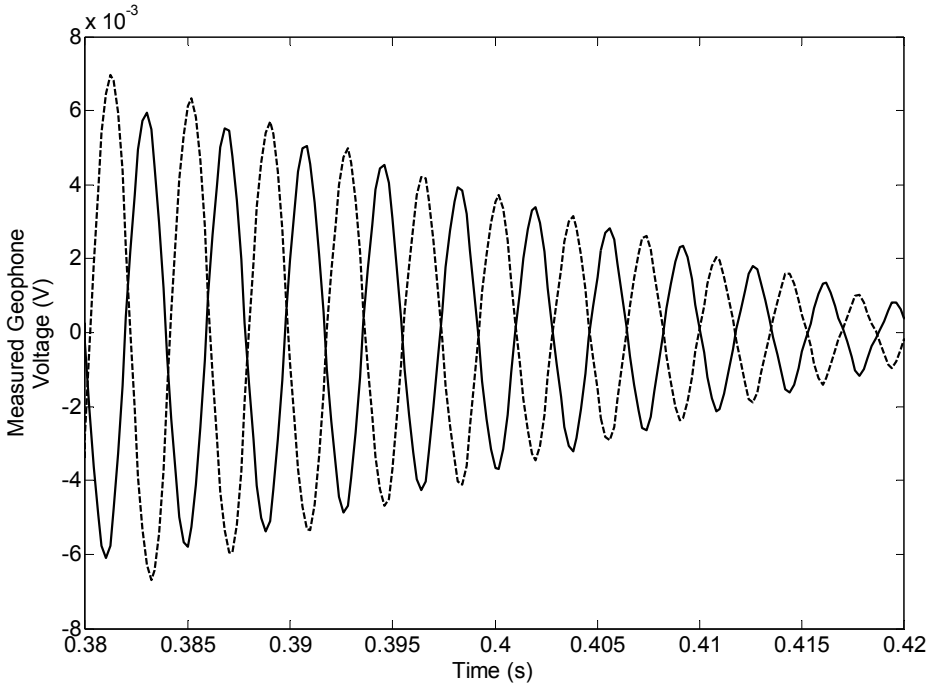

Figure 6.17 – Overlaid plot of the measured signals from the two different phases of excitation, with Figure 6.15 (a) shown by the solid line and Figure 6.15 (b) by the dashed line. In this portion of the signal input frequencies are approximately in region of 250 Hz -300 Hz.

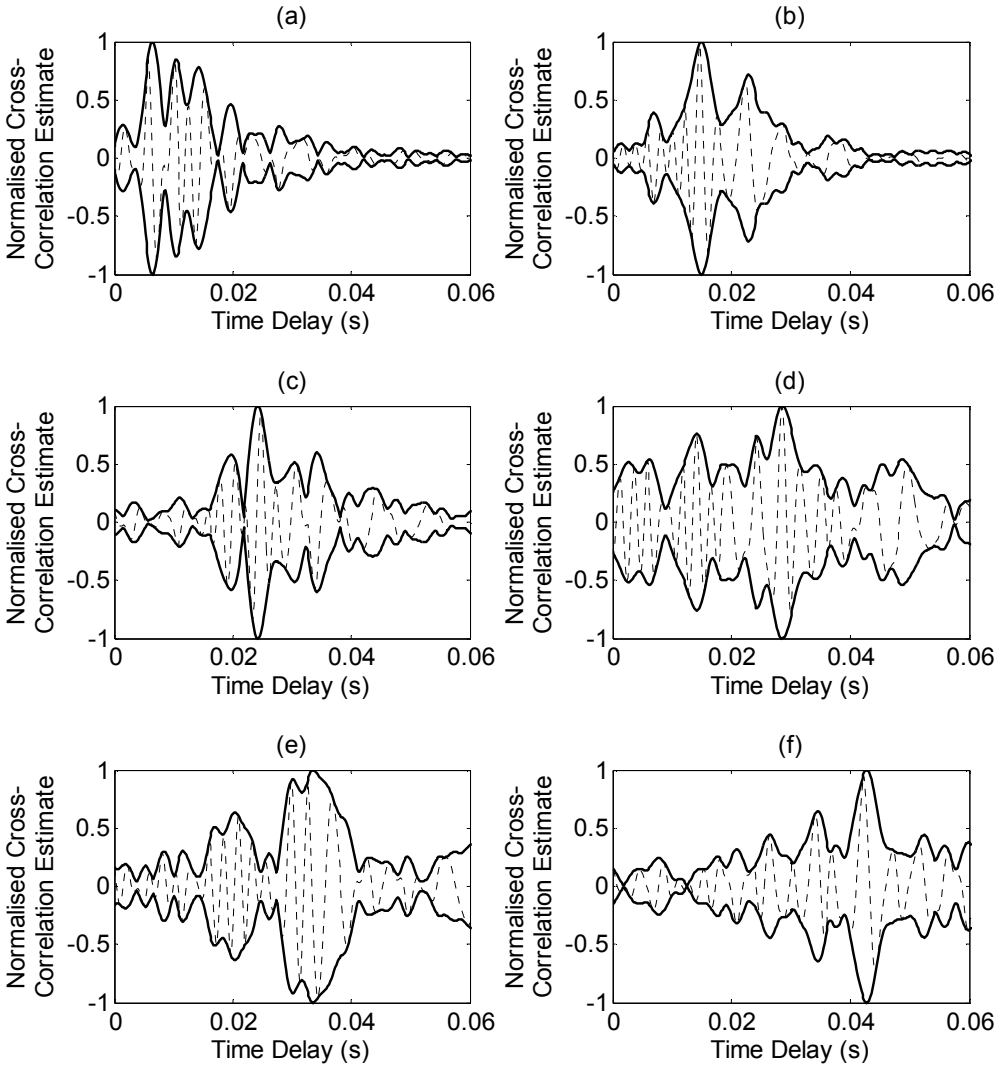

Figure 6.18 – Cross-correlation function estimates between the reference geophone, located close to the seismic source, and 6 measurement geophones which where spaced 0.5 m apart. The data used was from only one excitation phase of the measurements. Cross-correlation estimation is with the PHAT, with signals bandpass filtered in the region of 100 Hz – 600 Hz prior to the application of the PHAT. The dashed line shows the cross-correlation function and the solid line its envelope calculated via the Hilbert transform. All the cross-correlation functions are normalisation to their (envelope) peak values.

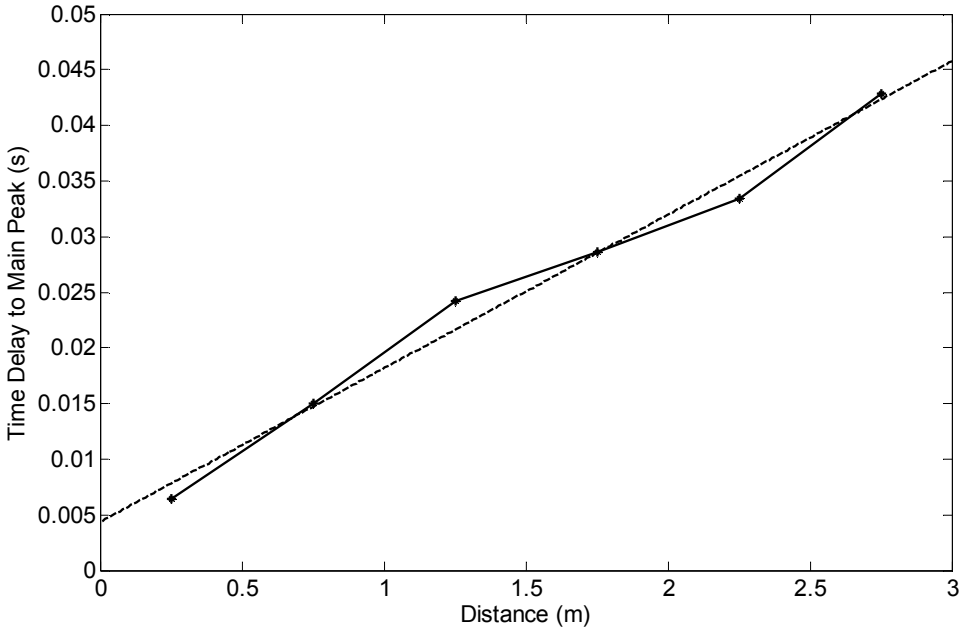

Figure 6.19 – The solid line shows the time delays at which the main peaks in the cross-correlation functions of Figure 6.18 occur as a function of the distance between the reference and measurement geophones. The dashed line is a linear best fit to the data.

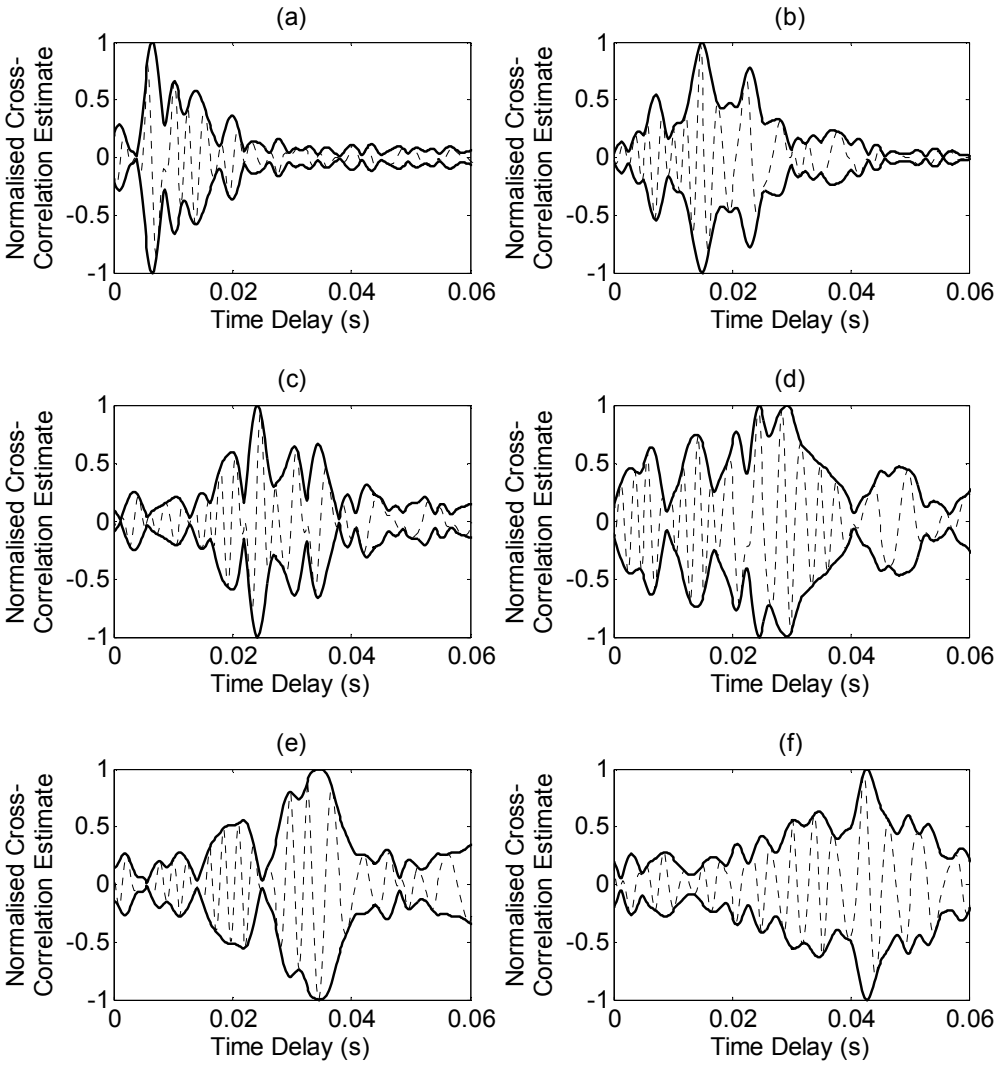

Figure 6.20 –Cross-correlation function estimates between the reference geophone, located close to the seismic source, and 6 measurement geophones which where spaced 0.5 m apart. The data used was the difference between the two phases of the excitation measured. Cross-correlation estimation is with the PHAT, with signals bandpass filtered in the region of 100 Hz – 600 Hz prior to the application of the PHAT. The dashed line shows the cross-correlation function and the solid line its envelope calculated via the Hilbert transform. All the cross-correlation functions are normalisation to their (envelope) peak values.

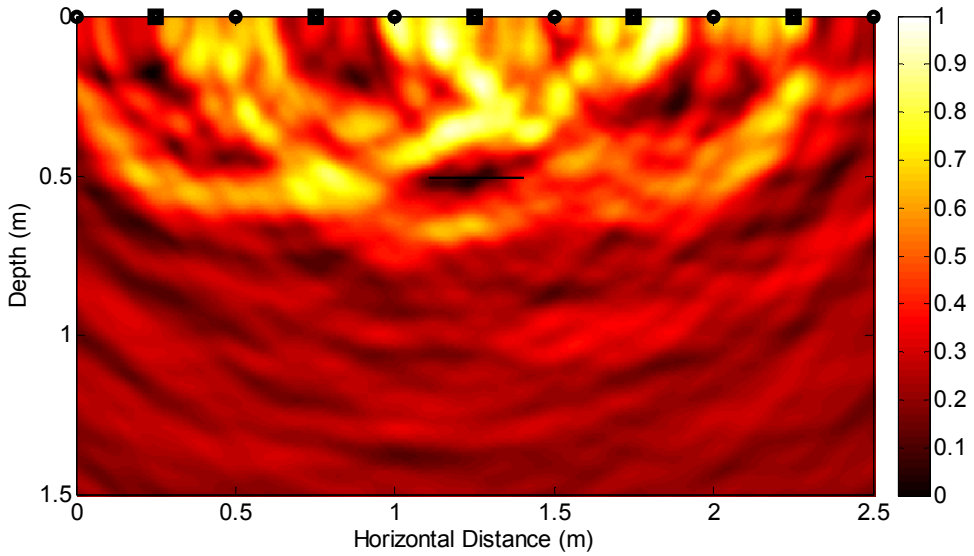

Figure 6.21 - Cross-sectional image through the ground produced by the imaging method using data from the Japanese experiments over the pot buried at 50 cm. The surface sensors are denoted by circles, the surface source locations by squares, and the anticipated location of the target by the black line. The imaging wavespeed used was 72 ms^{-1}. The image is scaled such that its minimum and maximum values correspond to zero and one respectively.

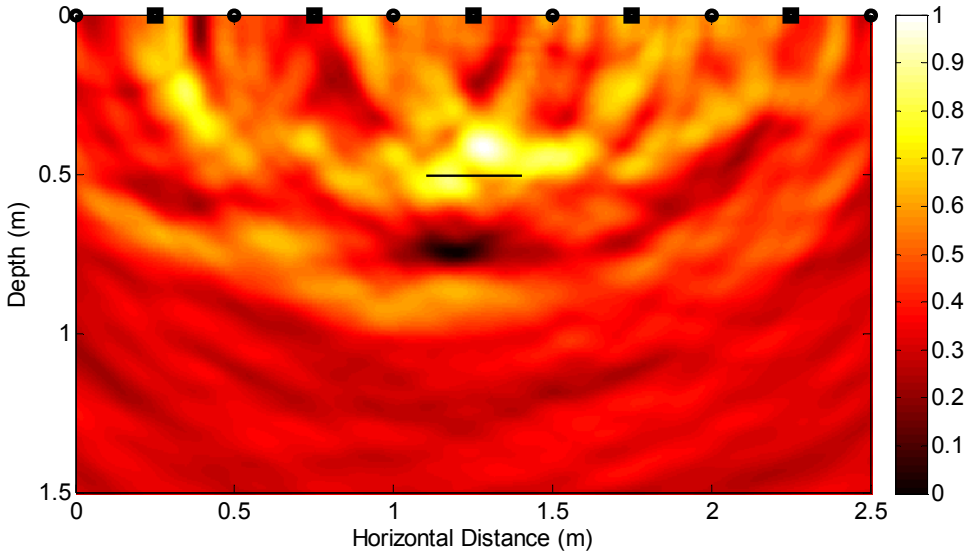

Figure 6.22 - Cross-sectional image through the ground produced by the imaging method using data from the Japanese experiments over the pot buried at 50 cm. The surface sensors are denoted by circles, the surface source locations by squares, and the anticipated location of the target by the black line. The imaging wavespeed used was 85 ms^{-1}. The image is scaled such that its minimum and maximum values correspond to zero and one respectively.

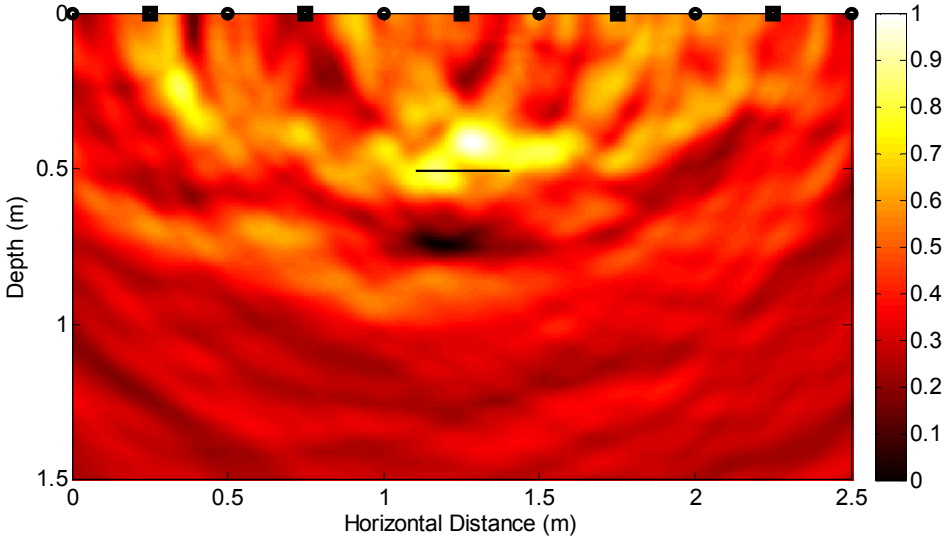

Figure 6.23 - Cross-sectional image through the ground produced by the imaging method using data from the Japanese experiments over the pot buried at 50 cm. The surface sensors are denoted by circles, the surface source locations by squares, and the anticipated location of the target by the black line. The imaging wavespeed used was 85 ms^{-1}. The difference between two signals measured when the phase of the excitation was reversed were used for processing. The image is scaled such that its minimum and maximum values correspond to zero and one respectively.

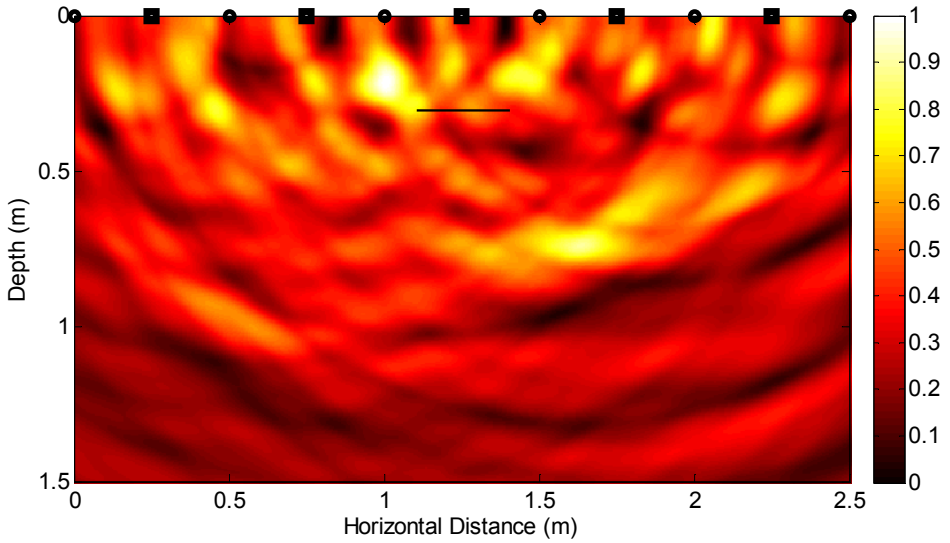

Figure 6.24 - Cross-sectional image through the ground produced by the imaging method using data from the Japanese experiments over the pot buried at 30 cm. The surface sensors are denoted by circles, the surface source locations by squares, and the anticipated location of the target by the black line. The imaging wavespeed used was 85 ms^{-1}. The image is scaled such that its minimum and maximum values correspond to zero and one respectively.

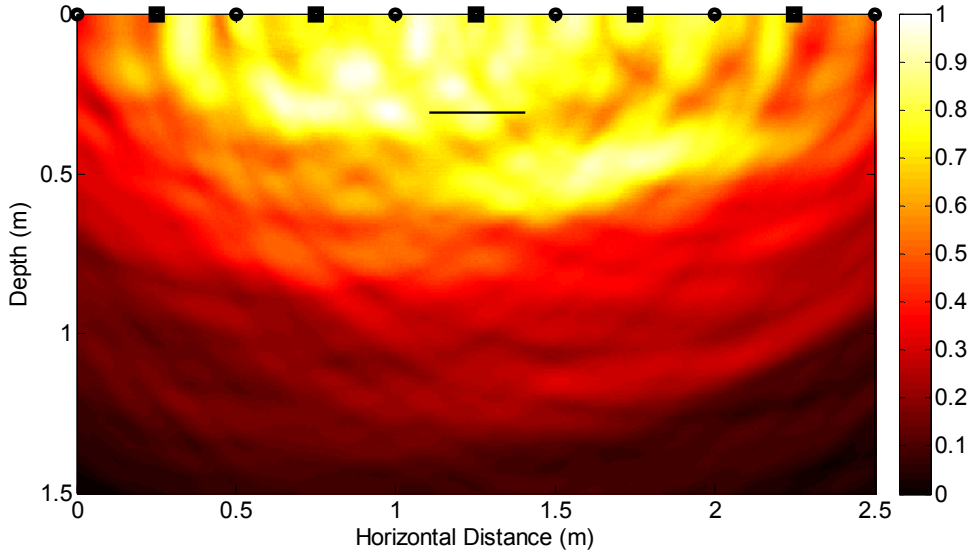

Figure 6.25 - Cross-sectional image through the ground produced by the imaging method using data from the Japanese experiments over the pot buried at 30 cm. The surface sensors are denoted by circles, the surface source locations by squares, and the anticipated location of the target by the black line. The imaging wavespeed used was 72 ms^{-1}. The image is scaled such that its minimum and maximum values correspond to zero and one respectively. Spatial filtering has not been applied in this image.

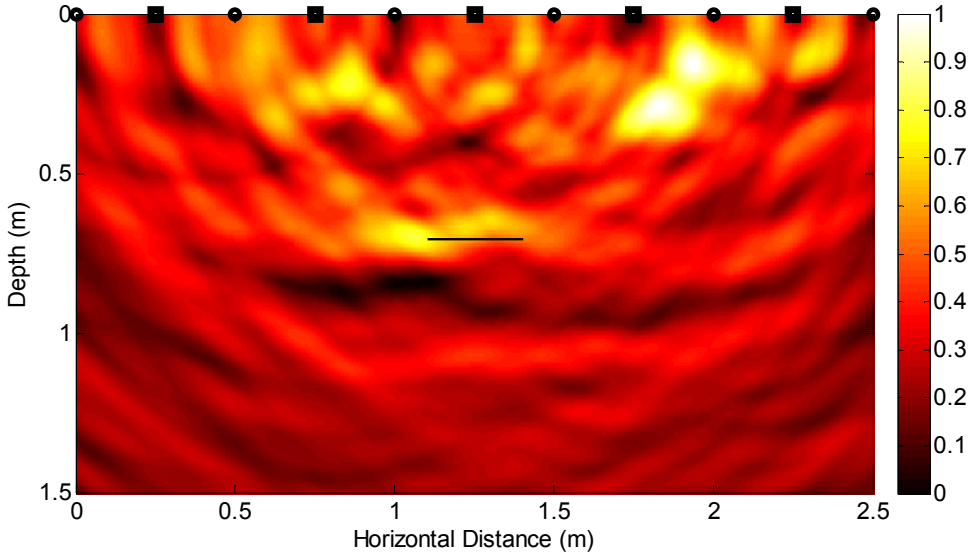

Figure 6.26 - Cross-sectional image through the ground produced by the imaging method using data from the Japanese experiments over the pot buried at 70 cm. The surface sensors are denoted by circles, the surface source locations by squares, and the anticipated location of the target by the black line. The imaging wavespeed used was 85 ms^{-1}. The image is scaled such that its minimum and maximum values correspond to zero and one respectively.

7. Conclusions and Future Work

Chapter 7

Conclusions and Future Work

This chapter gives a general overview of the content of the thesis in Section 7.1. The major conclusions resulting from this work are summarised in Section 7.2. Suggestions for further work are included in Section 7.3.

7.1 Overview of the Content of the Thesis

This thesis has been concerned with the detection of objects buried at shallow depths, of the order of less than 1 m, using seismic wave reflections.

A mathematical analysis of an idealised elastic space has been considered to establish the relevant types of propagating waves and their properties. An examination of sources on the surface of a semi-infinite elastic space was then made, with three types of surface source considered. The first was an infinite SH line source. This is the simplest source and was used to introduce the mathematical techniques required for the solution of more complex problems. A point vertical source was then examined, with expressions for the displacement components derived and from these the division of energy inputted into the system between the different wave types calculated. These derivations are already documented in the literature, and were repeated to establish a framework. The results on the division of energy were extended to include variation with the Poisson's ratio of the material. The final source considered was a point horizontal source, as this source configuration was used in the experimental application of the imaging method. Displacement components were taken from the

literature, and the partition of the inputted seismic energy between different wave types calculated as a function of the Poisson's ratio. Results for both the point vertical and point horizontal sources are shown in a graphically concise way.

An imaging methodology that is capable of forming two-dimensional images through the ground was described. It was initially described assuming that the source excitation is impulsive for conceptual simplicity. The use of a source producing time-extended signals was then considered, with the necessary modifications made to the imaging method detailed. The addition of several signal processing techniques completes the formulation of the imaging method.

Numerical simulations were constructed. This was to verify the imaging algorithms used in the method, and to enable an evaluation of the robustness of the method to work under non-ideal conditions. The numerical simulations were implemented by defining the signals in the frequency domain, and then modifying these signals to account for attenuation and propagation. The effect of an inaccurate wavespeed in the imaging method was assessed.

Both continuous and discontinuous variation in material properties as a function of depth were included in the numerical simulations. These scenarios were chosen to simulate the general increase in wavespeed with depth due to increasing overburden pressure and to simulate the step changes in soil properties due to the layering of material in the ground. Simulation of targets lying outside of the measurement plane was also considered. This was required as the imaging method contains the assumption that all reflectors lie in the image plane.

Prior to experimental application of the imaging method, experiments were undertaken to validate the seismic source used. Two seismic sources were compared, and the source best at producing shear waves chosen for further experimentation. To verify the wave types produced by the seismic source the wave speed over the surface was compared to that from a vertical source. Experiments were also performed using buried sensors to measure the relative amplitude of the wave types that propagate at depth.

Field experiments were undertaken at a number of sites to provide experimental validation of the imaging method. Results are presented from experiments at sites in Kent, Dorset and Japan. The experiments in Kent were the first to be performed, and used the low aspect ratio coupling platform described in Chapter 5. The target object was a large concrete pipe buried at a depth of 1 m. Wavespeed values were obtained using both surface sensors and a sensor inside the buried pipe. These produced wavespeed values consistent with compressional waves. The imaging method was therefore applied using a compressional wavespeed, with limited success.

Two sets of experiments were presented from the Dorset site, which used a paving slab at a depth of 70 cm as a target and the high aspect ratio coupling platform described in Chapter 5. The first of these experiments measured anomalously low surface wavespeeds. The imaging method was applied using wavespeeds consistent with those obtained at the site previously, with an examination of the surface wave artefacts in the resulting image providing verification of the chosen wavespeed. These experiments could successfully detect the object. The second set of experiments at the site, whilst giving successful wavespeed measurements, were not capable of positively imaging the target due to a small reflected wave amplitude relative to that from the direct source to sensor propagation path.

The experiments performed at the Japanese site featured three identical pots at depths of 30 cm, 60 cm, and 90 cm as targets. The experiments were complicated by the need to use a seismic source that was not ideal. Wavespeed measurements were successful but the imaging method could only positively image the pot buried at 50 cm. The imaging of the shallowest target was not possible because it was too close to the surface and the deepest target because of the attenuation of the reflected wave. A phase cancellation technique was investigated and shown ineffective for this source arrangement.

7.2 Major Conclusions of the Thesis

This section summarises the main conclusions of this thesis. These are as follows:

- A mathematical analysis of an idealised semi-infinite elastic space shows that for point excitation parallel to the surface of the ground, horizontally polarised shear waves dominate in the direction perpendicular to the excitation. Whilst other wave types are produced in the direction parallel to the excitation, the majority of the total energy inputted by the source is in the form of shear horizontal waves. The relative amount of energy in each wavetype varies with the value of the Poisson's ratio of the material.

- A method to form two-dimensional cross-sectional images through the ground can be constructed, and that for such an imaging method, used on the scales of relevance to this thesis, it is preferable to use shear wave excitation.

- Conceptually simple numerical simulations show that this imaging method can successfully image targets when there is some error in the wavespeed values used in the processing of the simulated data. Errors in the imaging method are measured by calculating the distance between the image peak and the true target location. For typical target depths (~ 0.5 m), errors

in the wavespeed of around 10 % still allow for the formation of an image with a single clear peak. The effect of wavespeed errors on the image reduces with increase depths.

- Numerical simulations indicate that continuous variations in the wavespeed with depth degrade the accuracy of the imaging method, and if these variations are sufficiently large successful imaging is not possible. If the variation in the wavespeed occurs discontinuously, then successful imaging of objects below the discontinuity is not possible even for moderate changes in material properties. Numerical simulations of objects above a discontinuity indicate that imaging may still be possible with the method.

- Experimental implementation of the imaging method shows that it is capable of detecting targets, but that this is not consistently achieved. Problems are caused by difficulty in obtaining representative wavespeed values and with the amplitude of the wave reflected from the buried object being too small relative to the direct wave between the source and sensors.

- The implementation of generalised cross-correlation functions, enveloping of these functions, and the application of spatial filtering to final images aid in successful imaging of buried objects.

- Imaging artefacts caused by the interpretation of surface waves by the imaging algorithm can indicate if a correct wavespeed estimate is being used in the data processing. These artefacts hinder the detection of targets very close to the surface.

7.3 Future Work

Although the imaging method described in this thesis has been demonstrated capable of successfully imaging buried targets, suggestions for further research into this imaging method are now given. These are:

- The use of three-dimensional arrays. A constraint of the presented imaging method is that it interprets all reflections as coming from the measurement plane. Modification to allow three-dimensional surveys is conceptually straightforward to implement.

- Investigations of more sophisticated processing algorithms. The imaging method uses a conceptually simple method. Whilst this is sufficient for this thesis, which was concerned with the development and validation of a complete experimental methodology, there are many

examples in the literature that have the potential to be modified for inclusion into the problem in this thesis.

- The application of non-contact sensors. Other methods utilising non-contact sensors, such as LDVs, have been described in Chapter 1. Application of non-contact sensors may remove problems with coupling the sensors to the ground, speed up the imaging process and/or enable a greater number of points on the surface at which measurements can be made.

- The use of more sophisticated numerical simulations. Finite difference models of elastic half spaces have been considered previously in the literature, and seem particularly suited to this system. The displacements at the surface in the presence of a target could be estimated to give the simulated time histories. This has the advantage of including complex effects such as near-field waves.

- Further experimentation on known buried objects, preferably with sensors attached to the target. Although this is clearly not how the technology would be used in practice, it is extremely helpful for analysing the potential effectiveness of any post-processing modifications. Without these measurements, it is not possible to know the amplitude and frequency content of the signal reaching the target.

- Use of SAWS or refraction surveys to obtain an estimated for the variation of wavespeed with depth, and modification of the imaging method to account for these wavespeed-depth profiles.

Appendix A - The Method of Steepest Descent

Development of the method of steepest descent is given in the most general terms. The method is outlined in many texts [64, 152]. The aim of the method of steepest descent is to approximate solutions to integrals of the form

$$I = \int_C \mathrm{e}^{Rf(\xi)} g(\xi)\,\mathrm{d}\xi \tag{A.1}$$

This integral occurs frequently in Fourier transforms. Consequently the contour of integration is assumed here to be along the entire real axis. The integration variable ξ is assumed complex and the constant R is real. The notation uses the wavenumber variable from the thesis as the complex variable to correspond to the application of the method in the thesis. The real and imaginary components of the complex integration variable are defined as $\xi = \zeta + \mathrm{j}\varsigma$.

In order to gain approximate solutions to the integral it is necessary to first qualitatively understand the behaviour of the integrand. The exponential function has a complex argument, and therefore will exhibit both oscillatory and exponential behaviour. The exponential argument is redefined in terms of its real and imaginary components as

$$f(\xi) = f_1(\xi) + \mathrm{j}f_2(\xi) \tag{A.2}$$

It is shown that the contribution to the integral can, for a suitably deformed contour, be dominated by the contribution of the real part of the exponential function from a small region about some point. For this to be valid the contribution from real part must decrease rapidly away from the extreme point. Furthermore if the value of $f_2(\xi)$ is not reasonably constant then the consequent rapid phase oscillations due to the imaginary part of the exponential will result in the desired maximal contributions from the real part of the exponential cancelling each other during integration. Approximation of the integral proceeds by the examination of the geometry of a function of a complex variable, $f(\xi)$. The aim is to understand the geometry so that the extreme point of $f_1(\xi)$, and the path of most rapid descent from it, can be found, as well as the locations where $f_2(\xi)$ is sufficiently invariant for phase oscillations not to invalidate the approximation.

It is essential throughout the analysis of that the complex function is analytic in the region of interest. It necessarily follows that the Cauchy-Riemann equations will hold. These stipulate that [120]

$$\frac{\partial f_1}{\partial \zeta} = \frac{\partial f_2}{\partial \varsigma} \quad , \quad \frac{\partial f_1}{\partial \varsigma} = -\frac{\partial f_2}{\partial \zeta} \tag{A.3}$$

These conditions are as a result of from the requirement that the function must be differentiable from any infinitesimally incremental change in location, regardless of the relative real and imaginary contributions of the change in location.

It is instructive when attempting to visualise the problem as thinking of the functions $f_1(\zeta,\varsigma)$ and $f_2(\zeta,\varsigma)$ as contour maps. The complex plane defines two of the axes, with the third being provided by the value of the functions at each value of the complex variable. The gradient of the real function, ∇f_1, is given by

$$\nabla f_1 = \frac{\partial f_1}{\partial \zeta}\hat{\boldsymbol{\xi}} + \frac{\partial f_1}{\partial \varsigma}\hat{\boldsymbol{\varsigma}}. \tag{A.4}$$

where $\hat{\boldsymbol{\xi}}$ and $\hat{\boldsymbol{\varsigma}}$ are the unit vectors on the complex plane. The gradient operator (as in the real case) represents the direction of the maximum variation of the function. A unit vector is defined in this direction;

$$\hat{\mathbf{n}}_1 = \frac{\nabla f_1}{|\nabla f_1|}. \tag{A.5}$$

The contour lines of the function will be, at each value of the complex plane, perpendicular to this vector. A unit vector defining the contour lines of the function is given by

$$\hat{\mathbf{s}}_1 = \frac{1}{|\nabla f_1|}\left(-\frac{\partial f_1}{\partial \varsigma}\hat{\boldsymbol{\xi}} + \frac{\partial f_1}{\partial \zeta}\hat{\boldsymbol{\varsigma}}\right). \tag{A.6}$$

Equations (A.5) and (A.6) can be confirmed to be normal by taking their inner product which gives a result of zero. The analogous equations for the imaginary function $f_2(\xi)$ are

$$\hat{\mathbf{n}}_2 = \frac{\nabla f_2}{|\nabla f_2|}, \tag{A.7}$$

$$\hat{\mathbf{s}}_2 = \frac{1}{|\nabla f_2|}\left(-\frac{\partial f_2}{\partial \varsigma}\hat{\boldsymbol{\zeta}} + \frac{\partial f_2}{\partial \zeta}\hat{\boldsymbol{\varsigma}} \right). \tag{A.8}$$

The inner product of the two unit vectors defining the contours of the real and imaginary component functions gives

$$\hat{\mathbf{s}}_1 \bullet \hat{\mathbf{s}}_2 = \hat{\mathbf{s}}_1 = \frac{1}{|\nabla f_1||\nabla f_2|}\left(\frac{\partial f_1}{\partial \varsigma}\frac{\partial f_2}{\partial \varsigma} + \frac{\partial f_1}{\partial \zeta}\frac{\partial f_2}{\partial \zeta} \right) = 0, \tag{A.8}$$

where the terms cancel due to imposition of the Cauchy-Riemann conditions. This means that real and imaginary components of the function $f(\xi)$ are orthogonal. Thus the direction of maximal gradient of the real component function will be equal to that of the contour lines (i.e. lines of no variation) of the imaginary component function. One of the specifying criteria has been met already; if the contour where the real component function undergoes maximum variation is selected then there will be a constant phase in the imaginary part of the complex exponential in Equation A.1, eliminating the problem of rapid oscillations causing cancellation of the desired contribution from real component of the function.

It is now necessary to find the location on the complex plane where movement along the deformed contour, in either direction, results in a maximal reduction in the value of the real component of the function $f(\xi)$. The implication from this is that the point will be extreme, and can therefore be found by setting the gradient of the real component function to zero;

$$\nabla f_1 = \frac{\partial f_1}{\partial \zeta}\hat{\boldsymbol{\zeta}} + \frac{\partial f_1}{\partial \varsigma}\hat{\boldsymbol{\varsigma}} = 0. \tag{A.9}$$

Using the analogous derivation for f_2 and the Cauchy-Riemann conditions, the gradient of the imaginary component function will also be zero at this location, and that the condition for the location of the extreme can be simplified to

$$\frac{\mathrm{d}f}{\mathrm{d}\xi} = 0. \tag{A.10}$$

The maximum modulus theorem is now invoked [153]. This is quoted without proof, and states that if a function of a complex variable cannot attain a local maximum or minimum value within a contour

C, it will attain the extreme values only on C. By this theorem the only way that the real component function can satisfy the requirement of Equation (A.10) is if the desired extreme point is a saddle point. The location of the saddle point on the complex plane is denoted by ξ_0.

To determine the geometry in the vicinity of this saddle point the function $f(\xi)$ is expanded around this saddle point.

$$f(\xi)\big|_{\xi=\xi_0} = f(\xi_0) + f'(\xi_0)(\xi-\xi_0) + \frac{1}{2}f''(\xi_0)(\xi-\xi_0)^2 + \ldots \qquad \text{(A.11)}$$

where the single and double primes denote derivative and double derivate of the function with respect to the variable respectively. By Equation (A.10), it can be seen that the second term of this expansion can be set to zero. A simplifying assumption is that the second derivative cannot be zero at the saddle point. This assumption could be removed, if required, at the expense of some additional complexity. A polar coordinate system is defined on the complex plane with its origin at the saddle point:

$$\xi - \xi_0 = r\mathrm{e}^{\mathrm{j}\theta}. \qquad \text{(A.12)}$$

The value of the second derivative at the saddle point is a constant, and is defined in polar terms as

$$\frac{1}{2}f''(\xi_0) = b_2\mathrm{e}^{\mathrm{j}\beta_2}. \qquad \text{(A.13)}$$

Substitution of these terms into Equation (A.11) and truncating the expansion at the second derivative

$$f(\xi)\big|_{\xi=\xi_0} \approx f(\xi_0) + b_2 r^2 \mathrm{e}^{\mathrm{j}(2\theta+\beta_2)}. \qquad \text{(A.14)}$$

Taking the real part of Equation (A.14) the expansion of the real component function is

$$f_1(\xi)\big|_{\xi=\xi_0} \approx \Re\{f(\xi_0)\} + b_2 r^2 \cos(2\theta+\beta_2) \qquad \text{(A.15)}$$

The first term of this equation is constant, whilst the second varies with the location on the complex plane away. It can be seen that this variation increases with distance, with its value depending on the polar angle. There are two angles of both maximal additive and subtractive contributions. These define the minimum and maximum contours of the function, and are given by

$$\theta_{max} = \frac{1}{2}\beta_2, \frac{1}{2}\beta_2 + \pi \quad , \quad \theta_{min} = \frac{1}{2}(\pi - \beta_2), \frac{1}{2}(3\pi - \beta_2). \tag{A.16}$$

Figure A.1 shows a contour plot of the function, with the value of $\beta_2 = \pi/8$ used as an arbitrarily chosen example and the amplitude normalised to its peak. The angles where the function rises and falls as steeply as possible to and from the saddle point are of interest. The deformed contour must therefore pass through the saddle point at an angle θ_{min}. The imaginary component of the function will have a contour along this line. It was shown earlier that the directions of maximum variation of one of the component functions is always perpendicular to the contours of the other.

At this point several comments about the analysis thus far can be made. The first is that the detailed description of the geometry of the function $f(\xi)$ in the complex plane has been achieved whilst leaving the function completely general. This is quite remarkable, and is a consequence of the strict constraints imposed upon analytic functions by the Cauchy-Riemann conditions.

The second point to make is that in specifying that the contour of integration may be deformed through this saddle point at the specified angle non-analytic regions of function $f(\xi)$ that frequently occur have not been accounted for. These include singularities and branch cuts, and the contour must be further appropriately deformed, with suitable compensating contributions made to the integral, in order for the deformed contour to remain valid. As the method for accounting for the non-analytic regions varies substantially with their location and the path of the contours, treatment of functions exhibiting these complications is omitted from the general derivation of the method.

As the deformed contour is along a contour line of the imaginary component function Equation (A.2) can be reduced to;

$$f(\xi) = f_1(\xi) + f_2(\xi_0). \tag{A.17}$$

A new variable is defined along the contour, and is given by the difference between the function at a given point and its maximum at the saddle point. Denoting the variable as u^2 for convenience

$$f_1(\xi_0) - f_1(\xi) = u^2, \tag{A.18}$$

it is noted that u^2 must be positive and real as it is the difference in the real component from the maximum. Substitution into Equation (A.17) leads to the condition that

$$f\left(\xi\right) = f\left(\xi_0\right) - u^2 . \tag{A.19}$$

Performing the change of variables in the original integral of Equation A.1 results in the new integral

$$I = \frac{1}{2} \mathrm{e}^{Rf(\xi_0)} \int_{-\infty}^{+\infty} \mathrm{e}^{-Ru^2} g\left\{\xi\left(u\right)\right\} \frac{\mathrm{d}\xi}{\mathrm{d}u} \mathrm{d}u \tag{A.20}$$

The limits have been taken to infinity in the knowledge that the contribution to the integral rapidly reduce away from the saddle point and are therefore assumed to become negligible. The new variable, u^2, can never be negative, and by definition must be greater than zero except at ξ_0. It can be seen from Equation (A.20) that it is valid to take the limit to $+\infty$, as the value of the real component $f_1\left(\xi\right)$ decreases in an unbounded manner (to second order approximation that has been taken here at least). The validity of taking the negative limit of the integral is not as obvious, and is provided by noting that that difference from the maximum was defined as u^2, not u. As u^2 is an odd function, the lower limit can be extended symmetrically, provided a factor a half is included in Equation (A.20) to account for this.

Before the integral can be evaluated an expression relating ξ and u must be derived. Combining Equations (A.11) and (A.19) results in a relation between the new variable of integration and the second derivative of the complex variable ξ:

$$u^2 = -\frac{1}{2} f''\left(\xi_0\right)\left(\xi - \xi_0\right)^2 . \tag{A.22}$$

Equation (A.12) can be substituted to transform the equation to the polar coordinate system with the origin at the saddle point. This gives

$$u^2 = -\frac{1}{2} r^2 f''\left(\xi_0\right) \mathrm{e}^{2\mathrm{j}\theta} . \tag{A.23}$$

As in Equation (A.13), it is possible to separate the second derivative of the function at the saddle point into a magnitude and phase component. The phase has already been specified in Equation (A.13) as β_2. Equation (A.23) then becomes

$$u^2 = -\frac{1}{2} r^2 \left| f''(\xi_0) \right| \mathrm{e}^{\mathrm{j}(2\theta+\beta_2)}. \tag{A.24}$$

As u^2 was defined as the difference between the real component and the maximum it must be real and positive. For this to be the case, Equation (A.24) means that a value of θ must be chosen such that the complex exponential of Equation (A.24) reduces to a real and negative number. This implies that:

$$\theta = \frac{1}{2}(\pm\pi - \alpha_2), \tag{A.25}$$

and furthermore gives

$$u = \pm\frac{1}{\sqrt{2}} r \left| f''(\xi_0) \right|^{\frac{1}{2}}. \tag{A.26}$$

The ambiguity in the plus/minus of the phase angle is simply a consequence of there being two angles separated by a factor π through which the path of steepest descent intersects the saddle point. Using Equation (A.12) to remove the factor of r and differentiating yields

$$\frac{\mathrm{d}u}{\mathrm{d}\xi} = \pm\frac{1}{\sqrt{2}} \mathrm{e}^{-\mathrm{j}\theta} \left| f''(\xi_0) \right|^{\frac{1}{2}}. \tag{A.27}$$

This can finally be substituted back into Equation (A.20) to obtain

$$I = \frac{\mathrm{e}^{Rf(\xi_0)} \mathrm{e}^{\mathrm{j}\theta}}{\sqrt{2}\left| f''(\xi_0) \right|^{\frac{1}{2}}} \int_{-\infty}^{+\infty} \mathrm{e}^{Ru^2} g\{\xi(u)\} \mathrm{d}u. \tag{A.28}$$

Solutions to the integral of Equation (A.28) are obtained by the use of Watson's Lemma. This states that an asymptotic expression exists for integrals of the form

$$\tilde{I} = \int_{-\infty}^{+\infty} \mathrm{e}^{-\frac{1}{2}a^2 z^2} f(z)\,\mathrm{d}z\,. \tag{A.29}$$

Substituting in a series expansion so that $f(z) = a_i z^i$ and using the standard integral results in

$$\int_{-\infty}^{+\infty} \mathrm{e}^{-\frac{1}{2}a^2 z^2} z^{2n}\,\mathrm{d}z \approx \sqrt{2\pi}\,\frac{(2n)!}{2^n n! a^{2n+1}}, \tag{A.30}$$

which means that the integral of Equation (A.29) can be written as

$$\tilde{I} = \sqrt{2\pi}\left(\frac{a_0}{a} + \frac{a_2}{a^3} + \frac{1.3a_4}{a^5} + \ldots\right). \tag{A.31}$$

This result must now be applied to the integral of Equation (A.28). For notational simplicity let $g\{\xi(u)\} = G(u)$. Using a Taylor expansion of $G(u)$ about the saddle point at $u = 0$ gives the power series

$$G(u)\big|_{u=0} = G(0) + G'(0)u + \frac{1}{2}G''(0)u^2 + \ldots \tag{A.32}$$

Substitution of this expansion into the integral of Equation (A.28), truncating the series expansion at the first term, and applying Equation (A.30) gives

$$\int_{-\infty}^{+\infty} \mathrm{e}^{Ru^2} G(u)\,\mathrm{d}u = \frac{\sqrt{\pi}G(0)}{R^{1/2}}. \tag{A.33}$$

Substitution of Equation (A.33) into Equation (A.28) gives the final approximation to the integral

$$I = \frac{\sqrt{\pi}\mathrm{e}^{Rf(\xi_0)}\mathrm{e}^{\mathrm{j}\theta}G(0)}{\left|2Rf''(\xi_0)\right|^{\frac{1}{2}}}. \tag{A.34}$$

An approximate solution to the integral of Equation (A.1) has thus been found in terms of quantities calculable from the various generic functions of the integral, with the approximation valid in the limit of $R \to \infty$. This result requires additional terms if the integrand of Equation (A.1) contains non-

analytic regions, such as branch points or singularities, and the deformation of the contour of integration required by the method of steepest descent passes through these points.

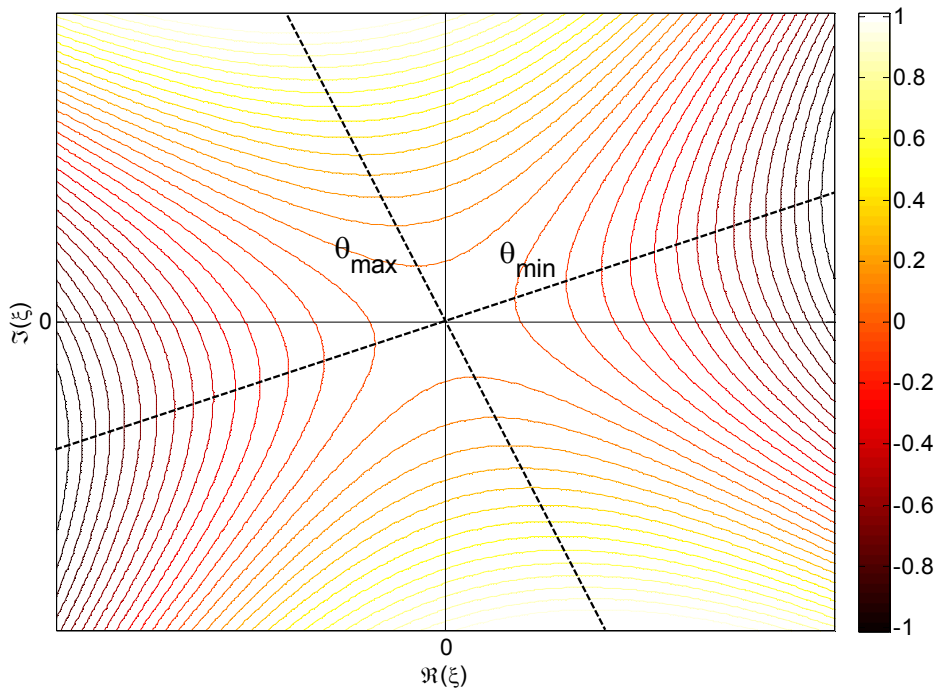

Figure A.1 - Example contour plot of the real part of the analytic function, $f_1(\xi)$, as a function of the real and imaginary parts of ξ. The scale is amplitude scale is normalised to its peak, and the value of $\beta_2 = \pi/8$ is selected arbitrarily for the purposes of example.

Appendix B - Application of the Method of Steepest Descent to the Infinite SH Line Source

Solutions to Equation (2.29) are sought using the asymptotic approximation of Equation (A.34). Equation (2.29) must be recast in the required general form given by Equation (A.1). This is achieved by first rewriting the integral of Equation (2.29) in polar coordinates;

$$I = \int_{-\infty}^{+\infty} \frac{\mathrm{e}^{R\left(-\sqrt{\xi^2 - k_s^2}\sin\theta + \mathrm{j}R\cos\theta\xi\right)}}{\sqrt{\xi^2 - k_s^2}}\,\mathrm{d}\xi \,. \tag{B.15}$$

By comparison with Equation (A.1) the generic functions of the complex variable are found to be

$$f\left(\xi\right) = \mathrm{j}R\cos\theta\xi - \sqrt{\xi^2 - k_s^2}\,\sin\theta \quad ; \quad g\left(\xi\right) = \frac{1}{\sqrt{\xi^2 - k_s^2}} \,. \tag{B.2}$$

The saddle point can be found by setting the derivative of the function to zero;

$$\frac{\mathrm{d}f}{\mathrm{d}\xi} = \mathrm{j}R\cos\theta - \xi_0\left(\xi_0^2 - k_s^2\right)^{-\frac{1}{2}}\sin\theta = 0 \,. \tag{B.3}$$

After rearrangement and using the trigonometric relation that $1 + \tan\theta = \sec^2\theta$ this reduces to

$$\xi_0 = \pm k_s\cos\theta \,. \tag{B.4}$$

The branch points of the integrand occur at $\pm k_s$. By choosing branch cuts extending to positive and negative infinity the deformed integration path will not require additional deformation around the branch cuts. The second derivative of the function is

$$\frac{\mathrm{d}^2 f}{\mathrm{d}\xi^2} = \frac{-\sin\theta}{\left(\xi^2 - k_s^2\right)^{\frac{1}{2}}} + \frac{\xi^2\sin\theta}{\left(\xi^2 - k_s^2\right)^{\frac{3}{2}}} \,. \tag{B.5}$$

The negative result from Equation (B.4) is chosen as the saddle point. The justification for follows after the result is shown. Thus

$$f\left(\xi_0\right) = -\mathrm{j}k_s \,, \tag{B.6}$$

and using the trigonometric relation that $\mathrm{cosec}^2\theta = 1 + \cot^2\theta$ the second derivative at the saddle point is found to be

$$f''(\xi_0) = \mathrm{j}\frac{1}{k_s \sin^2\theta}. \tag{B.7}$$

Before implementation of the general result of Equation (A.34) the two quantities $\mathrm{e}^{\mathrm{j}\theta}$ and $G(0)$ must still be found. The former of these can be found from Equation (A.26). The phase component of the second derivative is the inverse tangent of the imaginary and real parts, which gives β_2 as $\pi/2$, and therefore

$$\theta = \frac{\pi}{2} - \frac{\pi}{4} = \frac{\pi}{4}. \tag{B.8}$$

When considering $G(0)$ it must be noted that this is the first term of the Taylor expansion about $u = 0$, and therefore the value of ξ that this corresponds to must be found. The relationship between these two variables is given by Equation (A.25). Substitution of the relevant quantities from Equations (B.4) and (B.7) gives

$$u^2 = -\frac{1}{2}\mathrm{j}\frac{1}{k_s \sin^2\theta}\left(\xi + k_s \cos\theta\right)^2. \tag{B.9}$$

Expressing j in complex exponential form taking the root of Equation (B.9) and rearranging in terms of ξ leads to two solutions;

$$\xi = \mathrm{e}^{\frac{-\mathrm{j}\pi}{4}}\sqrt{2k_s}u\sin\theta - k_s\cos\theta \quad ; \quad \xi = \mathrm{e}^{\frac{-3\mathrm{j}\pi}{4}}\sqrt{2k_s}u\sin\theta - k_s\cos\theta, \tag{B.10}$$

which upon evaluation for $u = 0$ collapse to the identical result of

$$\xi = -k_s\cos\theta. \tag{B.11}$$

Using the definition of $g(\xi)$ given in Equation (B.2)

$$G(0) = -\mathrm{j}\frac{1}{k_s \sin^2\theta}. \tag{B.12}$$

Substituting all of the relevant quantities from Equations (B.6-8) and (B.12) into the general solution of Equation (A.34) gives a solution of

$$I = \frac{-\sqrt{\pi}\mathrm{e}^{-\mathrm{j}Rk_s}\mathrm{e}^{\mathrm{j}\frac{\pi}{4}}\mathrm{j}\frac{1}{k_s \sin^2\theta}}{\left|\frac{2R\mathrm{j}}{k_s \sin^2\theta}\right|^{\frac{1}{2}}}, \tag{B.13}$$

which reduces to

$$I = -\sqrt{\frac{\pi}{2k_s R}}\mathrm{e}^{-\mathrm{j}Rk_s}\mathrm{e}^{\mathrm{j}\frac{3\pi}{4}} \tag{B.14}$$

The desired displacement function of Equation (2.29) can thus be approximated in the far-field to

$$u_z(R,t) = \frac{\tau_0}{2\mu\sqrt{2\pi k_s R}}\mathrm{e}^{-\mathrm{j}\left(k_s R - \frac{3\pi}{4}\right)}\mathrm{e}^{\mathrm{j}\omega t} \tag{B.15}$$

References

1. Heald, M.A. and Marion, J.B., *Classical Electromagnetic Radiation*. 3rd ed. 1994: Brooks Cole.

2. Jackson, J.D., *Classical Electrodynamics*. 1998: John Wiley & Sons.

3. Bruschini, C., *Metal Detectors in Civil Engineering and Humanitarian Demining: Overview and Tests of a Commercial Visualizing System.* Insight: Non-Destructive Testing and Condition Monitoring, 2000. **42**(2): p. 89-97.

4. MacDonald, J., *Alternatives for Landmine Detection*. 2003: RAND Corporation.

5. Bruce, R.V., *Alexander Graham Bell and the Conquest of Solitude*. 1973: Cornell University Press.

6. Linford, N., *The Application of Geophysical Methods to Archaeological Prospection.* Reports on Progress in Physics, 2006. **69**(7): p. 2205-2257.

7. Gebicke, M.E., *Mine Detection: Army Detector's Ability to Find Low-Metal Mines Not Clearly Demonstrated*, U.S.G.A. Office. 1996.

8. Muggleton, J.M. and Brennan, M.J., *The Design and Instrumentation of an Experimental Rig to Investigate Acoustic Methods for the Detection and Location of Underground Piping Systems.* Applied Acoustics, 2008. **69**(11): p. 1101-7.

9. *Mine Action Equipment: Study of Global Operational Needs*. 2002, Geneva International Centre for Humanitarian Demining.

10. O'Neill, K. and Fernandez, J.P., *Electromagnetic Methods for UXO Discrimination.* NATO Science for Peace and Security Series B: Physics and Biophysics, 2009: p. 197-221.

11. Won, I.J., Keiswetter, D.A. and Bell, T.H., *Electromagnetic Induction Spectroscopy for Clearing Landmines.* IEEE Transactions on Geoscience and Remote Sensing, 2001. **39**(4): p. 703-9.

12. Shubitidze, F., O'Neill, K., Shamatava, I., Sun, K. and Paulsen, K.D., *Fast and Accurate Calculation of Physically Complete EMI Response by a Heterogeneous Metallic Object.* IEEE Transactions on Geoscience and Remote Sensing, 2005. **43**(8): p. 1736-1750.

13. Das, Y., *Effects of Soil Electromagnetic Properties on Metal Detectors.* IEEE Transactions on Geoscience and Remote Sensing, 2006. **44**(6): p. 1444-1453.

14. Eblagh, K. *Practical Problems in Demining and their Solutions*, in *EUREL International Conference on the Detection of Abandoned Land Mines: A Humanitarian Imperative Seeking a Technical Solution* 1996. Edinburgh, UK: IEE.

15. Vales, B.R., Harneit, S., Reuter, M. and Skorupskaite, V. *Moisture Effects in Soils Using a Frequency Domain Metal Detector*. 2007. Budapest, Hungary: Institute of Electrical and Electronics Engineers Computer Society.

16. Annan, A.P., *GPR - History, Trends and Future Developments.* Subsurface Sensing Technologies and Applications, 2002. **3**(4): p. 253-270.

17. Knight, R., *Ground Penetrating Radar for Environmental Applications.* Annual Review of Earth and Planetary Sciences, 2001. **29**: p. 229-255.

18. Metje, N., Atkins, P., Brennan, M., Chapman, D., Lim, H., Machell, J., Muggleton, J., Pennock, S., Ratcliffe, J., Redfern, M., Rodgers, C., Saul, A., Shan, Q., Swingler, S. and Thomas, A., *Mapping the Underworld - State-of-the-Art Review.* Tunnelling and Underground Space Technology, 2007. **22**: p. 568-586.

19. Daniels, D.J., Gunton, D.J. and Scott, H.F., *Introduction to Subsurface Radar.* IEE Proceedings, 1988. **135, Pt. F** (4): p. 278 - 320.

20. Annan, A.P., *Electromagnetic Principles of Ground Penetrating Radar*, in *Ground Penetrating Radar Theory and Applications*, H.M. Jol, Editor. 2009, Elseveir.

21. Cassidy, N.J., *Electrical and Magnetic Properties of Rocks, Soils and Fluids*, in *Ground Penetrating Radar Theory and Applications*, H.M. Jol, Editor. 2009, Elseveir.

22. Arcone, S.A., *Glaciers and Ice Sheets*, in *Ground Penetrating Radar Theory and Applications*, H.M. Jol, Editor. 2009, Elseveir.

23. D'Amico, A. and Pittenger, R., *A Brief History of Active Sonar.* Aquatic Mammals, 2009. **25**(4): p. 426-434.

24. Evans, P.G.H. and Miller, L.A. *Proceedings of the Workshop on Active Sonar and Cetaceans*, in *European Cetacean Society's 17th Annual Conference*. 2003. Las Palmas, Gran Canaria.

25. Harrison, C.H. and Siderius, M., *Bottom Profiling by Correlating Beam-Steered Noise Sequences.* Journal of the Acoustical Society of America, 2007. **123**(3): p. 1282-1296.

26. Siderius, M., Song, H., Gerstoft, P., Hodgkiss, W.S., Hursky, P. and Harrison, C., *Adaptive Passive Fathometer Processing.* Journal of the Acoustical Society of America, 2010. **127**(4): p. 2193-2200.

27. Lemon, S.G., *Towed-Array History, 1917-2003.* IEEE Journal of Oceanic Engineering, 2004. **29**(2): p. 365-373.

28. Burdic, W.S., *Underwater Acoustic System Analysis*. Prentice-Hall Signal Processing Series, ed. A.V. Oppenheim. 1984: Prentice-Hall.

29. Waite, A.D., *Sonar for Practising Engineers*. 2002: John-Wiley & Sons.

30. Krim, H. and Viberg, M., *Two Decades of Array Signal Processing*, in *IEEE Signal Processing Magazine*. 1996. p. 67-94.

31. Unnikrishna Pillai, A., *Array Signal Processing*. 1989: Springer-Verlag.

32. Knight, W.C., Pridham, R.G. and Kay, S.M., *Digital Signal Processing for Sonar.* Proceedings of the IEEE, 1981. **69**(11): p. 1451-1506.

33. Capon, J., *High-Resolution Frequency-Wavenumber Spectrum Analysis.* Proceedings of the IEEE, 1969. **57**(8): p. 1408-1418.

34. Schmidt, R.O., *Multiple Emitter Location and Signal Parameter Estimation.* IEEE Transactions on Antennas and Propagation, 1986. **AP-34**(3): p. 276-80.

35. Allen, S.J., *Seismic Method.* Geophysics, 1980. **45**(11): p. 1619-1633.

36. Klipsch, P.W., *Some Aspects of Multiple Recording in Seismic Prospecting.* Geophysics, 1936. **1**(3): p. 365-377.

37. Mayne, W.H., *Method for Seismic Surveying*, Patent No. 3280936, U.S.P. Office. 1956: United States.

38. Mayne, W.H., *Common Reflection Point Horizontal Data Stacking Techniques.* Geophysics, 1962. **27**(6): p. 927-938.

39. Al-Sadi, H.N., *Seismic Exploration Techniques and Processing*. 1980: Birkhauser Verlag.

40. Kearey, P., Brooks, M. and Hill, I., *An Introduction to Geophysical Exploration*. 2002: Blackwell Publishing.

41. Telford, W.M., Geldart, L.P. and Sheriff, R.E., *Applied Geophysics*. 2nd ed. 1990: Cambridge University Press.

42. Schnieder, W.A., *The Common Depth Point Stack.* Proceedings of the IEEE, 1984. **72**(10): p. 1238 - 1256.

43. Marsden, D., *Static Corrections - A Review.* The Leading Edge, 1993. **43**.

44. Rogers, A.W., *Determination of Static Corrections*, in *Developments in Geophysical Exploration Methods*, A.A. Fitch, Editor. 1981, Applied Science Publishers.

45. Bang, E.-S. and Kim, D.-S., *Evaluation of Shear Wave Velocity Profile Using SPT Based Uphole Method.* Soil Dynamics and Earthquake Engineering, 2007. **27**(8): p. 741-758.

46. Gazdag, J. and Sguazzero, P., *Migration of Seismic Data.* Proceedings of the IEEE, 1984. **72**(10): p. 1302-15.

47. Berkhout, A.J., *Wave Field Extrapolation Techniques in Seismic Migration, a Tutorial.* Geophysics, 1981. **46**(12): p. 1638-1656.

48. Hatton, L., Worthingon, M.H. and Makin, J., *Seismic Data Processing - Theory and Practice*. 1986: Blackwell Scientific.

49. Hood, P., *Migration*, in *Developments in Geophysical Exploration Methods*, A.A. Fitch, Editor. 1981, Applied Science Publishers.

50. Claerbout, J.F., *Towards a Unified Theory of Reflector Mapping.* Geophysics, 1971. **36**.

51. Buske, S., Gutjahr, S. and Sick, C., *Fresnel Volume Migration of Single Component Seismic Data.* Geophysics, 2009. **74**(6): p. WCA47-WCA55.

52. Leuschen, C. and Plumb, R., *A Matched-Filter Approach to Wave Migration.* Journal of Applied Geophysics, 2000. **43**(2-4): p. 271-280.

53. Steeples, D.W. and Miller, R.D., *Avoiding Pitfalls in Shallow Seismic Reflection Surveys.* Geophysics, 1998. **63**(4): p. 1213-1224.

54. March, D.W. and Bailey, A.D., *A Review of the Two Dimensional Transform and its use in Seismic Processing.* First Break, 1983. **1**(1): p. 9-21.

55. Brown, A.R., *Interpretation of Three-Dimensional Seismic Data*. 6th ed. 2004: The American Association of Petroleum Geologists and the Society of Exploration Geophysicists.

56. Lumley, D.E., *Time Lapse Seismic Reservoir Monitoring.* Geophysics, 2001. **66**(1): p. 50-53.

57. Crawford, J.M., Doty, W.E.N. and Lee, M.R., *Continuous Signal Seismograph.* Geophysics, 1960. **25**(1): p. 95-105.

58. Goupillaud, P.L., *Signal Design in the Vibroseis Technique.* Geophysics, 1976. **41** (6): p. 1291-1304.

59. Kirk, P., *Vibroseis Processing*, in *Developments in Geophysical Exploration Methods*, A.A. Fitch, Editor. 1981, Applied Science Publishers.

60. Helbig, K. and Thomsen, L., *75-Plus Years of Anisotropy in Exploration and Reservoir Seismics: A Historical Review of Concepts and Methods.* Geophysics, 2005. **70**(6): p. 9-23.

61. Crampin, S., *Seismic Wave Propagation Through a Cracked Solid: Polarisation as a Possible Dilatancy Diagnostic.* Geographical Journal of the Royal Astronomical Society, 1978. **53**(3): p. 467-496.

62. Crampin, S., *Evaluation of Anisotropy by Shear Wave Splitting.* Geophysics, 1985. **50**(1): p. 142-152.

63. Thomsen, A., *Reflection Seismology Over Azimuthally Anisotropic Media.* Geophysics, 1988. **53**(3): p. 304-313.

64. Graff, K., *Wave Motion in Elastic Solids*. 1991: Dover Publications.

65. Griffiths, D.H. and King, R.F., *Applied Geophysics for Geologists and Engineers*. 1981: Pergamon Press.

66. Hagedoorn, J.G., *The Plus-Minus Method of Interpreting Seismic Refraction Sections.* Geophysical Prospecting, 1959. **7**(2): p. 158-182.

67. Van Overmeeren, R.A., *Hagedoorn's Plus-Minus Method: The Beauty of Simplicity.* Geophysical Prospecting, 2001. **49**(6): p. 687-696.

68. Palmer, D., *An Introduction to the Generalised Reciprocal Method of Seismic Refraction Interpretation.* Geophysics, 1981. **46**(11): p. 1508-1518.

69. Cerveny, V. and Psensik, I., *Geometrical Spreading of Seismic Body Waves in Laterally Inhomogeneous Media with Curved Interfaces of the Second Order.* Geophysical Journal International, 1974. **38**(1): p. 9-19.

70. Whiteley, R.J. and Greenhalgh, S.A., *Velocity Inversion and the Shallow Seismic Refraction Method.* Geoexploration, 1979. **17**: p. 125-141.

71. Soske, J.L., *The Blind Zone Problem in Engineering Geophysics.* Geophysics, 1959. **24**(2).

72. Redpath, B.B., *Seismic Refraction Exploration for Engineering Site Investigations*. 1973, US Army Engineer Waterways Experiment Station Explosive Excavation Research Laboratory: Livermore, California.

73. Zagrai, A., Donskoy, D. and Ekimov, A., *Structural Vibrations of Buried Land Mines.* Journal of the Acoustical Society of America, 2005. **118**(6): p. 3619-3628.

74. Scott, W., Jr., Martin, J.S. and Larson, G.D., *Experimental Model for a Seismic Landmine Detection System.* IEEE Transactions on Geoscience and Remote Sensing, 2001. **39**(6): p. 1155-1164.

75. Scott, W.R., Jr., Schroeder, C. and Martin, J.S. *A Hybrid Acoustic/Electromagnetic Technique for Locating Land Mines*. 1998. Seattle, WA, USA: IEEE.

76. Scott, W.R., Jr., Schroeder, C.T., Martin, J.S. and Larson, G.D., *Use of Elastic Waves for the Detection of Buried Land Mines*, in *IEEE International Geoscience and Remote Sensing Symposium*. 2001.

77. Bachrach, R. and Nur, A. *Ultra Shallow Seismic Reflection in Unconsolidated Sediments: Rock Physics Base for Data Acquisition.*, in *SEG expanded abstract*. 1998. New Orleans, USA.

78. Cook, J.C. and Wormser, J.J., *Semi-Remote Acoustic, Electric, and Thermal Sensing of Small Buried Non-Metallic Objects.* IEEE Transactions on Geoscience Electronics, 1973. **GE-11**(3): p. 135-152.

79. Sabatier, J.M., Bass, H.E., Bolen, L.N. and Attenborough, K., *Acoustically Induced Seismic Waves.* Journal of the Acoustical Society of America, 1986. **80**(2): p. 646-9.

80. Sabatier, J.M., Bass, H.E., Bolen, L.N., Attenborough, K. and Sastry, V.V.S.S., *The Interaction of Airborne Sound with the Porous Ground: the Theoretical Formulation.* Journal of the Acoustical Society of America, 1986. **79**(5): p. 1345-52.

81. Abe, T. and Sugimoto, T., *Extremely Shallow Underground Imaging Using Scanning Laser Doppler Vibrometer.* Japanese Journal of Applied Physics, 2009. **48**.

82. Sabatier, J. and Gilbert, K., *Method for Detecting Buried Objects By Measuring Seismic Vibrations Induced by Acoustical Coupling with a Remote Source of Sound*, Patent No. 6081481, U.S.P. Office. 2000: United States.

83. Xiang, N. and Sabatier, J., *Land Mine Detection Measurements Using Acoustic-to-Seismic Coupling.* Proceedings of the SPIE, 2000. **4038** (Detection and Remediation Technologies for Mines and Mine-like Targets V): p. 645-655.

84. Xiang, N. and Sabatier, J.M., *An Experimental Study on Antipersonnel Landmine Detection Using Acoustic-to-Seismic Coupling.* Journal of the Acoustical Society of America, 2003. **113**(3): p. 1333-41.

85. Biot, M., *Theory of Propagation of Elastic Waves in a Fluid-Saturated Porous Solid. II. Higher Frequency Range.* Journal of the Acoustical Society of America, 1956. **28**(2): p. 179-191.

86. Fokin, V.N., Fokina, M.S., Sabatier, J.M. and Zhiqu, L., *Effect of Ground Variability on Acoustic-to-Seismic Transfer Function and False Alarms in Landmine Detection.* Journal of the Acoustical Society of America, 2006. **120**(2): p. 621-30.

87. Arnott, W. and Sabatier, J., *Laser-Doppler Vibrometer Measurements of Acoustic to Seismic Coupling.* Applied Acoustics, 1990. **30**: p. 279-291.

88. Martin, J.S., Larson, G.D. and Scott Jr., W.R., *An Investigation of Surface-Contacting Sensors for the Seismic Detection of Buried Landmines.* Journal of the Acoustical Society of America, 2006. **120**(5): p. 2676-2685.

89. Bellan, F., Bulletti, A., Capineri, L. and Bruschini, C., *(Non-Linear) Acoustic Landmine Detection Study*. 2004, EUDEM2.

90. Donskoy, D.M., *Non-Linear Seismo-Acoustic Technique for Land Mine Detection and Discrimination*, in *Second International Conference on the Detection of Abandoned Land Mines*. 1998, IEEE: Edinburgh, UK. p. 244-248.

91. Donskoy, D., Reznik, A., Zagrai, A. and Ekimov, A., *Nonlinear Vibrations of Buried Mines.* Journal of the Acoustical Society of America, 2005. **117**(2): p. 690-700.

92. Korman, M.S. and Sabatier, J.M., *Nonlinear Acoustic Techniques for Landmine Detection.* Journal of the Acoustical Society of America, 2004. **116**(6): p. 3354-69.

93. Bachrach, R. and Nur, A., *High-Resolution Shallow-Seismic Experiments in Sand. Part I: Water Table, Fluid Flow, and Saturation.* Geophysics, 1998. **63**(4): p. 1225-33.

94. Hasbrouck, W.P., *Four Shallow-Depth, Shear-Wave Feasibility Studies.* Geophysics, 1991. **56**(11): p. 1875-1885.

95. Steeples, D.W., *Near-Surface Geophysics: 75 Years of Progress*. 2005, Society of Exploration Geophysicists: Tulsa.

96. Dasios, A., McCann, C., Astin, T.R., McCann, D.M. and Fenning, P., *Seismic Imaging of the Shallow Subsurface: Shear-Wave Case Studies.* Geophysical Prospecting, 1999. **47**: p. 565-591.

97. Hill, I.A., *Better Than Drilling? Some Shallow Seismic Reflection Case Histories* Quarterly Journal of Engineering Geology, 1992. **25**: p. 239-248.

98. Jeng, Y., Chen, C., Yu, H., Jeng, A.S., Tang, C. and Lin, M., *Ultra-shallow Seismic Experiment on a Trenched Section of the Chelunpu Fault Zone, Taiwan.* Tectonophysics, 2007. **443**: p. 255-270.

99. Schmelzbach, C., Green, A.G. and Horstmeyer, H., *Ultra-Shallow Seismic Reflection Imaging in a Region Characterized by High Source-Generated Noise.* Near Surface Geophysics, 2005. **3**(1).

100. Bachrach, R., Dvorkin, J. and Nur, A., *High-Resolution Shallow-Seismic Experiments in Sand. Part II: Velocities in Shallow Unconsolidated Sand.* Geophysics, 1998. **63**(4): p. 1234-40.

101. Miller, R.D. and Xia, J., *Large Near-Surface Velocity Gradients on Shallow Seismic Reflection Data.* Geophysics, 1998. **63**(4): p. 1348-1356.

102. Kimura, M. and Kawashima, S., *Depth Dependence of Shear Wave Velocity in Sands.* Japanese Journal of Applied Physics, 1995. **34**: p. 2936-3936.

103. Deidda, G.P. and Balia, R., *An Ultra-Shallow SH-Wave Seismic Reflection Experiment on a Subsurface Ground Model.* Geophysics, 2001. **66**(4): p. 1097-1104.

104. Ha, E.S., Kawamura, Y., Mizutani, K., Okawa, H. and Asaka, M., *Detection of Underground Concrete Block Using Giant-Magnetostriction Vibrator Applying Magnified Cross-Correlation Analysis.* Japanese Journal of Applied Physics, Part 1, 2007. **46**(7B): p. 4500-3.

105. Sugimoto, T. and Okujima, M., *Underground Imaging Using Shear Waves: Stacking Method of the Reflected Scattered Waves* Japanese Journal of Applied Physics, 1996. **35**: p. 3105-3108.

106. Sugimoto, T., Saito, H. and Okujima, M., *Improvement of Underground Image: Underground imaging using shear waves.* Japanese Journal of Applied Physics, Part 1: Regular Papers & Short Notes & Review Papers, 1997. **36**(5B): p. 3197-3198.

107. Sugimoto, T. and Saitou, H., *Improvement of Underground Image (II): Underground Imaging Using Shear Waves.* Japanese Journal of Applied Physics, 1998. **37**: p. 3120-3121.

108. Yoshizumi, N. and Sugimoto, T., *Improvement of Underground Image (III): Underground Image Using Shear Waves.* Japanese Journal of Applied Physics, 2001. **40**: p. 3621-3622.

109. Grice, R. and Pinnington, R., *The Detection of Objects Buried in Sand Using Vibrations Generated by Shakers Located at the Sand Surface: Results of Experimental Investigations in the Laboratory*. 1997, ISVR, University of Southampton.

110. Shin and Hammond, *Fundamentals of Signal Processing for Sound and Vibration Engineers*. 2008: John Wiley & Sons.

111. House, L. and Pape, D., *Method and Apparatus for Acoustic Energy Identification of Objects Buried in Soil*, Patent. 1994: United States.

112. White, P., *Cross Correlation in Structural Systems: Dispersion and Nondispersion Waves.* Journal of the Acoustical Society of America, 1969. **45**(5): p. 1118-1128.

113. ION Geophysical Corporation, *XVib Track Chassis Vibrator*. 2009.

114. Sugimoto, T., Saitou, H. and Okujima, M., *Study of Underground Imaging Using Shear Waves: the Stacking Method of the Reflected Scattered Wave.* Archaeological Prospection, 2000. **7**: p. 249-261.

115. Cremer, L., Heckl, M. and Petersson, B., *Structure-Borne Sound*. 3rd ed. 2005: Springer-Verlag.

116. Kolsky, *Stress Waves in Solids*. 1963: Dover Publications.

117. Timoshenko, S., *Theory of Elasticity*. 1934: McGraw-Hill.

118. Morse, P. and Feshbach, H., *Methods of Theoretical Physics*. 1953: McGraw-Hill.

119. Schroder, C.T. and Scott W.R, Jr., *On the Complex Conjugate Roots of the Rayleigh Equation: The Leaky Surface Wave.* Journal of the Acoustical Society of America, 2001. **110**(6): p. 2867-2877.

120. Pennisi, L., *Elements of Complex Variables*. 1967: Holt, Rinehart and Winston.

121. Gutowski, T.G. and Dym, C.L., *Propagation of Ground Vibration: A Review.* Journal of Sound and Vibration, 1976. **49**(2): p. 179-193.

122. McLachlan, N.W., *Bessel Functions for Engineers*. 1955: Clarendon Press.

123. Miller, G.F. and Pursey, H., *The Field and Radiation Impedance of Mechanical Radiators on the Free Surface of a Semi-Infinite Isotropic Solid.* Proceedings of the Royal Society of London. Series A, Mathematical and Physical Sciences, 1954. **223**(1155): p. 521-541.

124. Miller, G.F. and Pursey, H., *On the Partition of Energy between Elastic Waves in a Semi-Infinite Solid.* Proceedings of the Royal Society of London. Series A, Mathematical and Physical Sciences, 1955. **233**(1192): p. 55-69.

125. Felsen, L. and Marcuvitz, N., *Radiation and Scattering of Waves*. The IEEE Series on Electromagnetic Wave Theory, ed. D. Dudley. 2003: John Wiley & Sons.

126. Woods, R.D., *Screening of Surface Waves in Soils.* American Society of Civil Engineering, Journal of Soil Mechanics, 1968. **94**(4): p. 951-979.

127. Cherry, J.T., Jr, *The Azimuthal and Polar Radiation Patterns Obtained from a Horizontal Stress Applied at the Surface of an Elastic Half Space.* Bulletin of the Seismological Society of America, 1962. **52**(1): p. 27-36.

128. Bycroft, G.N., *Forced Vibrations of a Rigid Circular Plate on a Semi-Infinite Elastic Space and on an Elastic Stratum.* Philosophical Transactions of the Royal Society of London, 1956. **248**(948): p. 327-368.

129. Bullen, K.E., *Seismology*. 1954: John Wiley & Sons.

130. Love, A.E.H., *Some Problems of Geodynamics*. 1911: Cambridge University Press. 180.

131. Deidda, G.P. and Ranieri, G., *Some SH-Wave Seismic Reflections from Depths of Less than Three Metres.* Geophysical Prospecting, 2001. **49**(5): p. 499-508.

132. Heisey, J.S., Stokoe II, K.H., Hudson, W.R. and Meyer, A.H., *Determination of In-Situ Shear Wave Velocities from Spectral Analysis of Surface Waves*. 1982, Centre for Transportation Research, University of Texas.

133. Stokoe, K.H., Wright, S.G., Bay, J.A. and Roesset, J.M., *"Characterization of Geotechnical Sites by SASW Method.* Geophysical Characterisation of Sites, ISSMFE Technical Committee 10, 1994.

134. Onda, I. and Komaki, S., *Waves Generated from a Linear Horizontal Traction with Finite Source Length on the Surface of a Semi-Infinite Elastic Medium, with Special Remarks on the Theory of Shear Wave Generation* Bulletin of the Earthquake Research Institute, 1968. **46**.

135. Roth, M. and Holliger, K., *The Non-Geometric PS Wave in High Resolution Seismic Data: Observations and Modelling.* Geophysical Journal International, 2000. **140**(F5-F11).

136. McQuillin, R., Bacon, M. and Barclay, W., *An Introduction to Seismic Interpretation*. 1984: Graham & Trotman.

137. Bendat and Piersol, *Engineering Applications of Correlation and Spectral Analysis*. 1993: John Wiley & Sons.

138. Knapp, C.H. and Carter, G.C., *The Generalised Correlation Method for Estimation of Time Delay.* IEEE Transactions on Acoustics, Speech and Signal Processing, 1976. **ASSP-24**(4): p. 320-7.

139. Gao, Y., Brennan, M.J. and Joseph, P.F., *A Comparison of Time Delay Estimators for the Detection of Leak Noise Signals in Plastic Water Distribution Pipes.* Journal of Sound and Vibration, 2006. **292**(3-5): p. 552-70.

140. Carter, G.C., Nuttall, A.H. and Cable, P.G., *The Smoothed Coherence Transfrom.* Proceedings of the IEEE, 1930. **61**(10): p. 2.

141. Cohen, L., *Time-Frequency Analysis*. Prentice Hall Signal Processing Series, ed. A.V. Oppenheim. 1995: Prentice Hall.

142. Pitas, I., *Digital Image Processing Algorithms and Applications*. 2000: Wiley & Sons.

143. MacDougall, E.B., *Spatial Filtering.* Economic Geography, 1970. **46**: p. 425-434.

144. Van Vossen, R., Curtis, A. and Trampert, J., *Subsonic Near Surface P Velocity and Low S Velocity Observations Using Propagtor Inversion.* Geophysics, 2005. **70**(4): p. R15 - R23.

145. Morse, P. and Ingard, K., *Theoretical Acoustics*. 1986: Princeton University Press. 927.

146. Schroder, C.T., Scott, W.R., Jr. and Larson, G.D., *Elastic Waves Interacting with Buried Land Mines: A Study Using the FDTD Method.* IEEE Transactions on Geoscience and Remote Sensing, 2002. **40**(6): p. 1405-15.

147. Santamarina, J.C., Klein, K.A. and Moheb, A.F., *Soils and Waves*. 2001: John Wiley & Sons.

148. Auld, B.A., *Acoustic Fields and Waves in Soils*. Vol. 2. 1973: John Wiley and Sons.

149. Pinnington, R. and Briscoe, A., *Feasibility Study for the Detection of Buried Objects - Phase 2A*. 1998, ISVR, University of Southampton.

150. Kirkup, L., *Experimental Methods: An Introduction to the Analysis and Presentation of Data*. 1994: John Wiley & Sons.

151. Pinnington, R., *Feasibility Study to Investigate the Detection of Objects Buried in the Ground*. 1996, ISVR, University of Southampton.

152. Arfken, G.B. and Weber, H.J., *Mathematical Methods for Physicists*. 2005: Elsevier.

153. Titchmarsh, E.C., *The Theory of Functions*. 1932: Oxford University Press.